EVALUATION AND MODELLING PERFORMANCE OF CAPPING LAYER IN RAIL TRACK SUBSTRUCTURE

A THESIS SUBMITTED IN FULFILLMENT OF THE REQUIREMENTS FOR THE AWARD OF THE

DEGREE

DOCTOR OF PHILOSOPHY

BY

SENANIE SUJEEWA RADAMPOLA

BSc(Eng), ME, MIE(SL), MIEAust

CENTRE FOR RAILWAY ENGINEERING

CENTRAL QUEENSLAND UNIVERSITY

ROCKHAMPTON, QUEENSLAND, AUSTRALIA

FEBRUARY, 2006

DECLARATION

I declare to the best of my knowledge that this thesis does not contain any material previously published or written by another person, except where due reference is made in the text. The contents of this thesis have not been included in any other work submitted by the author for another degree or diploma at any other tertiary Institution.

Senanie Sujeewa Radampola

February, 2006

TABLE OF CONTENTS

ABSTRACT I

ACKNOWLEDGEMENTS II

PUBLICATION RELATED TO THESIS IV

LIST OF FIGURES V

LIST OF TABLES XIII

MAJOR SYMBOLS XV

CHAPTER 1 1

1. INTRODUCTION 1

1.1 Research Aims 1

1.2 Scope and Limitation of Research 2

1.3 Thesis Structure 3

CHAPTER 2 5

2. REVIEW OF THE RAIL TRACK SUBSTRUCTURE 5

2.1 Introduction 5

2.1.1 Capping Layer 7

2.2 Track Degradation and Failure 11

2.2.1 Track Degradation 11

2.2.2 Subgrade Failure Modes 12

2.3 Response of Subgrade Layer to Rail Traffic 15

2.3.1 Mechanics of Load Transfer into Subgrade Layer 15

2.3.1.1 Effect of Compaction and Moisture Content 22

2.3.2 Effect of Loading Cycles 27

2.3.3 Stress-Strain Characteristics of Subgrade Layer 30

2.4 Material Models for Soils Subjected to Repeated Loading 40

2.4.1 Non-cohesive Soils 40

2.4.2 Cohesive Soils 46

2.4.3 Typical Subgrade Layer Materials 51

2.4.3.1 Elastic Models 52

2.4.3.2 Elasto-plastic Models 53

2.5 Modelling of Railway Substructure 59

2.5.1 Conventional Models 59

2.5.2 Numerical Models 65

2.5.3 Backcalculation Techniques 73

2.6 Summary 74

CHAPTER 3 78

3. EXPERIMENTAL METHOD OF CHARACTERISING CAPPING LAYER PROPERTIES 78

3.1 Introduction 78

3.2 Semi-Confined Cylinder Test (SCT) 86

3.2.1 Aim of Testing 86

3.2.2 Design of experiments 87

3.3 Material Selection 91

3.4 Experimental Setup 93

3.4.1 Test Procedure 94

3.4.2 Testing Program 95

3.4.3 Density and Moisture Contents of the Specimens Tested 96

3.5 Results of Semi-Confined Cylinder Test (SCT) 97

3.5.1 Behaviour of Material under SCT Setup 97

3.5.2 Monotonic and Cyclic Loading Behaviour 100

3.5.3 Effect of Moisture Content 106
3.5.4 Effect of Penetration Rate 108
3.5.4.1 Dimensional Analysis 109
3.5.5 Ternary Plots 114
3.6 Summary 116
CHAPTER 4 118
4. FINITE ELEMENT MODELLING (FEM) OF CAPPING LAYER MATERIAL 118
4.1 Introduction 118
4.2 Brief Review of Theory of Plasticity 120
4.3 Constitutive Modelling of the Capping Layer Material 123
4.3.1 Stress Dependent Elastic Modulus 132
4.3.2 Stress Dependent Friction Angle 134
4.4 Finite Element (FE) Analysis of SCT Setup 137
4.4.1 Explicit Solution Algorithm (ABAQUS 2002) 137
4.4.2 Stability Limit (ABAQUS 2002) 138
4.4.3 Quasi-static Analysis (ABAQUS 2002) 141
4.4.4 Finite Element Model 142
4.4.4.1 Loading Rates 144
4.4.4.2 Steps 145
4.4.4.3 Amplitude Curves 145
4.4.5 Mesh Refinement and Adaptive Meshing 145
4.4.6 Sensitivity of the Modelling Parameters 148
4.4.6.1 Total Step Time and Energy Balance 148
4.5 Output and Discussion 151
4.6 Summary 156

CHAPTER 5 157

5. BACKCALCULATION OF THE CAPPING LAYER MATERIAL PROPERTIES 157

5.1 Introduction 157

5.2 Backcalculation Process 158

5.2.1 Results of the ABAQUS Simulations 169

5.2.1.1 Model Predictions – OMC State (M) 169

5.2.1.2 Model Predictions – Saturated State (S) 170

5.2.1.3 Model Predictions – Dry State (D) 171

5.2.1.4 Final Output 172

5.2.2 Effect of Moisture Content on Predicted Parameters 177

5.2.3 Parametric Study 181

5.3 Viability of the Model 186

5.4 Summary 188

CHAPTER 6 190

6. APPLICATION OF THE FE MODEL FOR CAPPING LAYER IN PRACTICE 190

6.1 Introduction 190

6.2 Design of Experiments for Plane Strain Conditions 192

6.3 FE Modelling of the Capping Layer under Plane Strain Conditions 196

6.3.1 FE Model 196

6.3.2 Mesh Convergence Studies 197

6.3.3 Analysis, Results and Discussions 201

6.4 Validation Experiments 204

6.4.1 Test Procedure 205

6.4.2 Failure Mechanism 214

6.4.3 Deformations and Strains 215

6.4.4 Spatial Variation of Density 218

6.5 Results and Discussions 219

6.6 Summary 222

CHAPTER 7 223

7. SUMMARY, CONCLUSIONS AND RECOMMENDATIONS 223

7.1 Summary 223

7.2 Major Conclusions 224

7.3 Specific Conclusions 226

7.4 Recommendations for Future Studies 228

Bibliography 230

Appendices 243

ABSTRACT

In the design of rail track structures where the subgrade cannot achieve the desired capacity, enabling the required standard of track geometry to be maintained for the speed, axle load and tonnage to be hauled, a *capping layer* of granular material is placed between the natural ground or the embankment fill material and the ballast to protect the underlying weaker layers.

In spite of the important role played by the capping layer, very little research has been carried out on its performance. The current practice of design of the capping layer, therefore, is based on working stress philosophy where reduced levels of stresses are assumed not to degrade the subgrade. Even on tracks containing a thick ballast layer that ensures allowable levels of working stress the subgrade has been found to have permanently deformed. Design of capping layers based on plastic deformation, therefore, appears appropriate. This thesis aims at determining the load levels that cause detrimental plastic deformation in the capping layer.

The suite of material properties that characterise plastic deformations of capping layer is neither readily available nor easily determined. This thesis proposes a cheaper method of evaluating a range of capping layer material properties using penetration tests on specimens contained in California Bearing Ratio (CBR) test moulds coupled with a finite element modelling based back calculation technique. The suite of material properties thus determined are used for the simulation of the behaviour of capping layers under the boundary and loading conditions similar to those in practice. The predicted results are validated using laboratory experiments on large size capping layer specimens.

ACKNOWLEDGEMENTS

My thanks and gratitude to Associate Professor Manicka Dhanasekar, Director, Centre for Railway Engineering (CRE), my main supervisor for this PhD project for his encouragement, advice, guidance and the provision of all necessary assistance and facilities with kindness throughout the project.

Encouragement, guidance, comments and suggestions by Mr. Tim McSweeney, my co-supervisor, throughout my research need grateful recording.

Advice on geotechnical matters and continuous briefing by Dr. Netra Gurung, Project Design Engineer, Queensland Rail (QR), my second co-supervisor needs special mention.

The inspirational discussions and productive suggestions by M/s. Mike Martin and Damien Foun, Track Geotechnical Engineers, QR, during proof reading my confirmation report, thesis and experiments are acknowledged with gratitude.

All the support and suggestions given in Finite Element Modelling (FEM) and carrying out triaxial tests by Dr. Kan Ding is gratefully acknowledged. Dr. Jian Jun Han is also mentioned for his friendship, support and suggestions in FEM. Ke-yong Wang is thankfully mentioned for his contributions in the FEM.

My considerate colleague, Greg Nigel of Queensland University of Technology (QUT) needs special mention for his valuable suggestions and help extended using ABAQUS/Explicit.

The invaluable assistance and friendship extended by the students and staff in the Faculty of Engineering was a source of encouragement.

The assistance by Paul Furber, Mark Steedman, Gary Hoare, Ian Major, Bernard Jansen, and Ken Morisson in the laboratories made this task a reality. The help by Mark Doran and Brett Scofield in preparing samples for experiments needs special mention. Special thanks go to Mike Gorman for the help extended in organizing assistance for experiments.

Dr Colin Cole for his contribution in programming cyclic tests is mentioned with thanks.

My gratitude to Geoff Bloxsom of CSR Quarry, Nerimbera, Queensland, for allowing the use of material as samples for all my experiments.

Provision of lab facilities to do triaxial tests for higher confining pressures (over 1MPa) at the University of Sydney by A/Prof David Airey, Dept. of Civil Engineering, University of Sydney, NSW, is acknowledged with gratitude.

M/s Chris Bloxsom, Engineer, and Mark Walters, Technical Officer, Road Test, Rockhampton, need special mention with gratitude for the density tests.

My sincere gratitude to the CRE, CQU, for sponsoring this project.

My family, colleagues and friends, both new and old, have provided a lot of inspiration throughout the project. It is amazing how discussions with them clear and calm the mind and help resolve tricky problems.

Thank you all for the loving-kindness extended to me.

PUBLICATION RELATED TO THESIS

Radampola, S. S., McSweeney, T., Dhanasekar, M., and Gurung, N. (2004). "A New Method for Evaluating the Characteristics of Railway Capping Layer." Cyclic Behaviour of Soils and Liquefaction Phenomena, 31 March - 02 April 2004, Bochum, Germany, T. Triantafyllidis, ed., A. A. Balkema, 641 - 647.

LIST OF FIGURES

Figure 2.1 Types and components of track substructure 5

Figure 2.2 Particle size distribution envelopes of ballast material used in Queensland 6

Figure 2.3 Capping layer design chart for 22.5 tonne axle loads (Foun and Williams 2003) 8

Figure 2.4 Approximate correlation of bearing capacity and CBR from Casagrande Chart (Jeffs and Tew 1991) 10

Figure 2.5 Effect of twist defect in track geometry 12

Figure 2.6 Subgrade deterioration factors 13

Figure 2.7 Subgrade progressive shear failure 14

Figure 2.8 Ballast pocket formation 14

Figure 2.9 Stress due to strip load 18

Figure 2.10 Ballast bed and formation represented as two-layer system (Esveld 2001) 18

Figure 2.11 Load spread method 19

Figure 2.12 Comparison of vertical stress distribution under a uniformly loaded circular area by load spread methods and Boussinesq's equation (Jeffs and Tew 1991) 21

Figure 2.13 Illustration of compaction 23

Figure 2.14 Effect of continued compactive effort (Lay 1990) 23

Figure 2.15 Effect of density on stress-strain behaviour of sand (Selig and Waters 2000) 24

Figure 2.16 CBR vs. moisture content at various dry densities (Janssen and Dempsey 1981) 25

Figure 2.17 Effect of soil type on variation of percent compaction and soil stiffness with compaction effort (Selig and Waters 2000) 27

Figure 2.18 Effect of repeated loading (Means and Parcher 1964) 28

Figure 2.19 Increase in secant constrained modulus with successive cycles of loading (Lambe and Whitman 1979) 28
Figure 2.20 Stress strain curves for cyclic loading in oedometer test after Seamen et. al. 1963 (Lambe and Whitman 1979). 29
Figure 2.21 Oedometer test results for well graded calcareous sand from Libya (Lambe and Whitman 1979). 29
Figure 2.22 Stress-strain behaviour of soils 31
Figure 2.23 Stress beneath rolling wheel load (Lekarp et al. 2000) 32
Figure 2.24 First cycle stress-strain curve 34
Figure 2.25 Schematic diagrams of the triaxial test setup (Kim et al. 2001a) 37
Figure 2.26 Stress-strain curves for clay and sand (Lambe and Whitman 1979) 38
Figure 2.27. Typical variation in resilient modulus with deviator stress (Thompson and Robnett 1979) 47
Figure 2.28. Real soil behaviour involving hardening and softening 51
Figure 2.29 Hyperbolic stress-strain curve 53
Figure 2.30 Mohr-Coulomb criterion 56
Figure 2.31 Drucker-Prager criterion 57
Figure 2.32 Cumulative strain resulting from repeated load tests of London clay (Heath et al. 1972) 61
Figure 2.33 Modified SN curve (Heath et al. 1972) 62
Figure 2.34 Relationship between induced stresses and soil strength (Heath et al. 1972) 63
Figure 2.35 Thickness of sub-ballast layer according to DB (Esveld 2001) 64
Figure 2.36 Beam on elastic foundation model (Selig and Waters 2000) 65
Figure 2.37 Comparison of distribution of vertical pressure with depth under single axle load: MULTA, PSA, and ILLI-TRACK (Adegoke et al. 1979) 68

Figure 2.38 Comparison of distribution of vertical displacement with depth under single axle load: MULTA, PSA, and ILLI-TRACK (Adegoke et al. 1979) 69

Figure 3.1 Equipment set up for the ATM device (Drumm et al. 1996) 79

Figure 3.2 Comparison of cyclic triaxial and ATM resilient modulus test results (Drumm et al. 1996) 80

Figure 3.3 Comparison of mean effective stresses during static triaxial and M_R tests (Kim *et al.* 2001a) 81

Figure 3.4 Comparison of M_R values with alternative method (Kim *et al.* 2001a) 82

Figure 3.5 Evaluation of reliability of moduli determined by the alternative method (Kim *et al.* 2001a) 82

Figure 3.6 Cyclic penetration test apparatus (Okada and Ghataora 2002) 83

Figure 3.7 Relationship between moisture content and plunger pressure (Okada and Ghataora 2002) 84

Figure 3.8 Monotonic and cyclic loading sequences 88

Figure 3.9 Maximum train vibration levels reported at Sacramento, CA, USA (Hendriks 2002) 89

Figure 3.10 Vertical particle velocity response reported at high-speed project of Banverket, Sweden (Hall 2003) 90

Figure 3.11 Particle size distribution of Type 2.4 Unbound Material 92

Figure 3.12 Experimental Setup 93

Figure 3.13 Typical load-penetration behaviour in a test 98

Figure 3.14 Dilatancy and Collapsing effects under shear of cohesionless soils (Bowles 1979) 99

Figure 3.15 Behaviour during reloading at 2.5mm/min loading rate 101

Figure 3.16 Behaviour during reloading at 5.0mm/min penetration rate 101

Figure 3.17 Behaviour during reloading at 10.0mm/min penetration rate..... 101

Figure 3.18 Behaviour during reloading at 15.0mm/min penetration rate..... 102

Figure 3.19 Behaviour during reloading at 20.0mm/min penetration rate..... 102

Figure 3.20 Behaviour during monotonic and cyclic loading at all penetration rates 103

Figure 3.21 Typical unloading-reloading behaviour after the first loading..... 104

Figure 3.22 Stiffness during initial loading and reloading 105

Figure 3.23 Penetration against cycle number..... 106

Figure 3.24 Effect of moisture content (dry specimens)..... 107

Figure 3.25 Effect of moisture content on the initial loading stiffness..... 107

Figure 3.26 Effect of penetration rate 108

Figure 3.27 Effects of penetration rate on initial stiffness..... 109

Figure 3.28 Dimensional Relationships of dry, OMC and saturated data 110

Figure 3.29 Monotonic envelope and best fit curves for dry specimens 111

Figure 3.30 Cyclic envelope and best fit curves for dry specimens 112

Figure 3.31 Monotonic envelope and best fit curves for OMC specimens..... 112

Figure 3.32 Cyclic envelope and best fit curves for OMC specimens..... 113

Figure 3.33 Monotonic envelope and best fit curves for saturated specimen..... 113

Figure 3.34 Cyclic envelope and best fit curves for saturated specimen..... 114

Figure 3.35 Relationship between the moisture content, rate of penetration and penetrated depth in monotonic tests 115

Figure 3.36 Relationship between the moisture content, rate of penetration and penetrated depth in cyclic tests..... 116

Figure 4.1 Isotropic hardening (a) uniaxial stress-strain diagram (b) evolution of the yield surface in the biaxial stress plane (Jirasek and Bazant 2002)..... 122

Figure 4.2 Kinematic hardening (a) uniaxial stress-strain diagram (b) evolution of the yield surface in the biaxial stress plane (Jirasek and Bazant 2002) 123
Figure 4.3 Drucker-Prager approximations (Wang and Sitar 2004) 132
Figure 4.4 Stress dependency of the friction angle 136
Figure 4.5 Plan view of a typical test showing the indentation created by the loading piston 142
Figure 4.6 ABAQUS Finite element mesh 143
Figure 4.7 Original mesh configuration 146
Figure 4.8 Deformed mesh configuration at 100mm penetration of the loading piston . 147
Figure 4.9 Load-penetration response of the SCT setup, ABAQUS/Explicit; influence of mesh refinement 147
Figure 4.10 Effect of total step time on load-penetration profiles in ABAQUS model . 149
Figure 4.11 Kinetic and internal energy ratio histories for the speedups of 0.0218s, 0.109s and 0.218s 150
Figure 4.12 Deformed configurations at different percentages of the total piston penetration of 100mm 151
Figure 4.13 Physical configuration of the penetration of the piston throughout a typical test 152
Figure 4.14 Typical stress distributions at 10% of the total piston penetration of 100mm 154
Figure 4.15 Typical stress distributions at 100% of the total piston penetration of 100mm 155
Figure 5.1 Three distinctive groups of experimental data obtained from SCT 159
Figure 5.2 Triaxial setup 164
Figure 5.3 Calibration of K_a and n 165

Figure 5.4 Effective stress-effective strain curves of the OMC samples 166

Figure 5.5 Flow chart of simulation process 168

Figure 5.6 Predicted boundary envelopes of OMC state 170

Figure 5.7 Predicted boundary envelopes of saturated state 171

Figure 5.8 Predicted boundary envelopes of dry state 172

Figure 5.9 Strength line of cemented granular soils (Means and Parcher 1964) 174

Figure 5.10 Typical Mohr-Coulomb envelopes of the material tested 177

Figure 5.11 Effect of moisture on the tangent modulus 178

Figure 5.12 Effect of moisture on friction angle 178

Figure 5.13 Effect of moisture on cohesion 179

Figure 5.14 Effect of moisture on dilation angle 179

Figure 5.15 Effect of moisture on hardening modulus 180

Figure 5.16 Effect of E_t : SCT Specimen Behaviour 182

Figure 5.17 Effect of changes to ϕ : SCT Specimen Behaviour 183

Figure 5.18 Effect of c : SCT Specimen Behaviour 184

Figure 5.19 Effect of changes to ψ : SCT Specimen Behaviour 185

Figure 5.20 Effect of H_p : SCT Specimen Behaviour 185

Figure 5.21 Normal stress development along a selected level with the penetration of the loading piston 187

Figure 5.22 Confining stress development along a selected level with the penetration of the loading piston 187

Figure 6.1 Plane strain conditions in a railway embankment 191

Figure 6.2 Boxes used for the testing of large scale capping layer material 193

Figure 6.3 Load distribution method and instrumentation layout 194

Figure 6.4 ABAQUS plane strain model 197

Figure 6.5 Original mesh configurations at different mesh densities of 300mm layer... 198

Figure 6.6 Original mesh configurations at different mesh densities of 600mm layer... 199

Figure 6.7 Load-displacement profiles of the large-scale set-up, ABAQUS/Explicit; influence of mesh refinement 200

Figure 6.8 Plane strain model predictions and deformations at a 500kN wheel load..... 202

Figure 6.9 Plane strain model predictions and limit loads at a 20mm deformation 203

Figure 6.10 Experimental setup 204

Figure 6.11 Loading plates stack with deformation transducers and strain gauges..... 206

Figure 6.12 Sieving large material volumes using a motor driven sieve..... 207

Figure 6.13 Mixing at required moisture level using a back hoe..... 207

Figure 6.14 150mm thick layers marked on the walls of the box and a levelled material layer ready for compaction 209

Figure 6.15 Compaction using a 40kg plate compactor 209

Figure 6.16 Application of a thin layer of chalk dust 210

Figure 6.17 Centred loading plates 211

Figure 6.18 Covered top surface hindering moisture evaporation..... 211

Figure 6.19 Centred sample under the load cell ready for instrumentation..... 212

Figure 6.20 Instrumented setup ready for testing 212

Figure 6.21 Preparation for the Moisture-density gauge measurement taking..... 213

Figure 6.22 Obtaining the Moisture-density gauge measurement from SMDG (Troxler Electronic Laboratories Inc 1990-2001)..... 213

Figure 6.23 Obtaining core samples along the centre line of the specimen using a 50mm diameter sampler..... 214

Figure 6.24 Heaving and pushing of material due to applied loading 215

Figure 6.25 Displacement transducer (D_1-D_4) and strain gauge (S_1-S_6) readings relative to the normal load applied on the plate 216

Figure 6.26 Vertical displacement profiles of the side walls 217

Figure 6.27 Dry density recordings obtained from SMDG 218

Figure 6.28 Comparison of load-displacement profiles of varying thicknesses 220

Figure 6.29 Comparison of experimental data with FEM predictions 221

LIST OF TABLES

Table 2.1 Values of t and φ (Esveld 2001) 16

Table 2.2 Percentage of reduction in moduli due to moisture contents (Ksaibati et al. 2000) 26

Table 2.3 Merits and Demerits of the methods of measuring subgrade parameters (Okada and Ghataora 2002) 35

Table 2.4 Design limit bearing pressures of subgrades (Jeffs and Tew 1991) 60

Table 2.5 Permissible stresses on formations (Esveld 2001) 64

Table 3.1 Properties of Type 2.4 Unbound Material 92

Table 3.2 Laboratory testing program 95

Table 3.3 Specimen properties 96

Table 4.1 Model Parameters α_1, α_2, and k (Wang and Sitar 2004) 132

Table 4.2 Results of mesh refinement study 146

Table 5.1 User input parameters 161

Table 5.2 Values of dilation angle (ψ) suggested by Vermeer and de Borst in 1984 (Liao 2003) 162

Table 5.3 Material properties obtained from triaxial tests 164

Table 5.4 Variation in ϕ at different stress levels 165

Table 5.5 E_0 and H_p of the capping layer material at OMC state 166

Table 5.6 Classification of user input parameters as primary, secondary or tertiary 167

Table 5.7 Model predicted properties – OMC state 169

Table 5.8 Model predicted properties – Saturated state 170

Table 5.9 Model predicted properties – Dry state 172

Table 5.10 Predicted material properties from simulations 173

Table 5.11 Comparison of model predicted data with published, triaxial and uniaxial test data 176

Table 5.12 Average parameter values of OMC state used in sensitivity analysis 181

Table 6.1 Mesh refinement results 198

Table 6.2 Model predictions of SCT setup for OMC state 201

Table 6.3 Density and moisture content of the layers 218

Table 7.1 Summary of predicted capping layer properties 226

MAJOR SYMBOLS

Stresses and Strains

σ_{ij} stress tensor

s_{ij} stress deviator tensor

ε_{ij} strain tensor

e_{ij} strain deviator tensor

Invariants

$I_1 = \sigma_1 + \sigma_2 + \sigma_3 = \sigma_{ii} =$ first invariant of stress tensor

$J_2 = \frac{1}{2} s_{ij} s_{ij} =$ second invariant of stress deviator tensor

Material Parameters

E_i initial modulus

E_t tangent modulus

E Young's modulus

ν Poisson's ratio

K $\frac{E}{3(1-2\nu)} =$ bulk modulus

G $\frac{E}{2(1+\nu)} =$ shear modulus

H_p Hardening modulus

c, ϕ cohesion and friction angle in Mohr-Coulomb criterion

α, k constants in Drucker-Prager criterion

ψ dilation angle

Miscellaneous

$f(\,)$ yield function

$g(\,)$ potential function

C_{ijkl} material stiffness tensor

δ_{ij} Kronecker delta

CHAPTER 1

1. INTRODUCTION

Rail track structures are designed with an objective of achieving a minimum standard of capacity and track geometry to ensure safer operation of trains at specified levels of speed, axle load and tonnage to be hauled. To realise these design objectives both the strength and stability of the quality of the upper subgrade and the subgrade soils must be carefully assessed. If the subgrade soil cannot achieve these requirements, then a *capping layer* of granular material is placed between the natural ground or the embankment fill material and the ballast to improve the capacity of the track structure and to minimise its ongoing costs of maintenance, especially issues related to track geometry. The basic functions of a capping layer are therefore, i) to act as a working platform for the construction of the ballast layer in the short term, ii) to act as a structural layer with the capability of protecting the natural ground or the embankment fill material by minimising long term permanent and uneven deformations, and iii) to protect the subgrade from rainwater ingress.

1.1 Research Aims

The research described in this thesis aims to improve understanding of the behaviour of the capping layer material in addition to developing an inexpensive method of evaluating the elasto-plastic properties of such materials. These aims are achieved through the following enabling objectives:

- A critical review of the literature in this field and a discussion of the findings of this literature.

- Laboratory study of material behaviour through a simple method which can be used instead of the expensive cyclic triaxial tests.
- Numerical modelling of the experiments through a backcalculation technique coupled with finite element approximation incorporating suitable material constitutive relations for predicting the fundamental elasto-plastic material constants.
- Extending the finite element model with the predicted constitutive properties to evaluate the behaviour of the capping layer material subjected to boundary and loading conditions that approximately simulate the field conditions.
- Validating the finite element predictions using full-scale laboratory testing.
- Examining the sensitivity of the elasto-plastic material properties to permanent deformation as a basis for drawing useful, practical conclusions.

Through the above objectives the thesis presents many important aspects of capping layer behaviour that can be applied in practical situations for the design and analysis of an upper subgrade zone.

1.2 Scope and Limitation of Research

The research described in this thesis contributes to significantly extending the knowledge of the capping layer behaviour through the following approaches:

1. The development of a small-scale experimental method describing the behaviour of non-cohesive granular layers. This experimental method will be inexpensive and can be used as an alternate method to the conventional cyclic triaxial tests that are expensive.

2. Development of a numerical model that accounts for the pressure dependency of the properties of the non-cohesive capping layer soils.
3. Large scale testing of capping layer in a purpose built large-scale testing apparatus.

This thesis is mainly concerned with the time-independent plasticity of the capping layer material. It does not account for long term consolidation and/or high cycle fatigue failure of the capping layer material.

1.3 Thesis Structure

The research described in this thesis begins with a "Review of the Rail Track Substructure", presented in Chapter 2. This review describes the behaviour of support substructure material including both empirical research and analytical methods.

Chapter 3 on "Experimental Method of Characterising Capping Layer Properties" describes the laboratory experiments carried out for examining the behaviour of capping layer material. These tests were intended to develop an alternative economical method to determine elasto-plastic material parameters for capping layer design.

Chapter 4 is dedicated to "Finite Element Modelling (FEM) of Capping Layer Material". The theory behind the modelling of material characterisation is described. This Chapter is subdivided to describe the development of the model with a brief introduction to the theory of plasticity.

Chapter 5 describes the “Backcalculation of the Capping Layer Material Properties”. This Chapter describes the method of prediction of the properties using the capping layer material and compares the predictions with published and other available data.

Chapter 6 presents an “Application of the FE Model for Capping Layer in Practice”. This Chapter presents the application of the FE model to plane strain cases of capping layer material that approximately simulate the boundary and loading conditions that exist in the field operating environment. Large-scale experimental setup has been used for validating the results obtained through the application of the FE model.

Chapter 7 presents the “Conclusions and Recommendations”. This Chapter sets out the main research findings and some future directions for further research in this field.

CHAPTER 2

2. REVIEW OF THE RAIL TRACK SUBSTRUCTURE

2.1 Introduction

Conventional railway track substructure is a layered system; its components include ballast, sub-ballast, and subgrade soil providing support to the rail and sleepers (Fig. 2.1). In some literature the ballast and sub-ballast layers are defined as a combined "track support" layer. It could be observed from Fig. 2.1 that not all substructure systems include capping layers. Capping layer is provided to protect the natural ground or fill from moisture ingress and to form a unified subgrade layer.

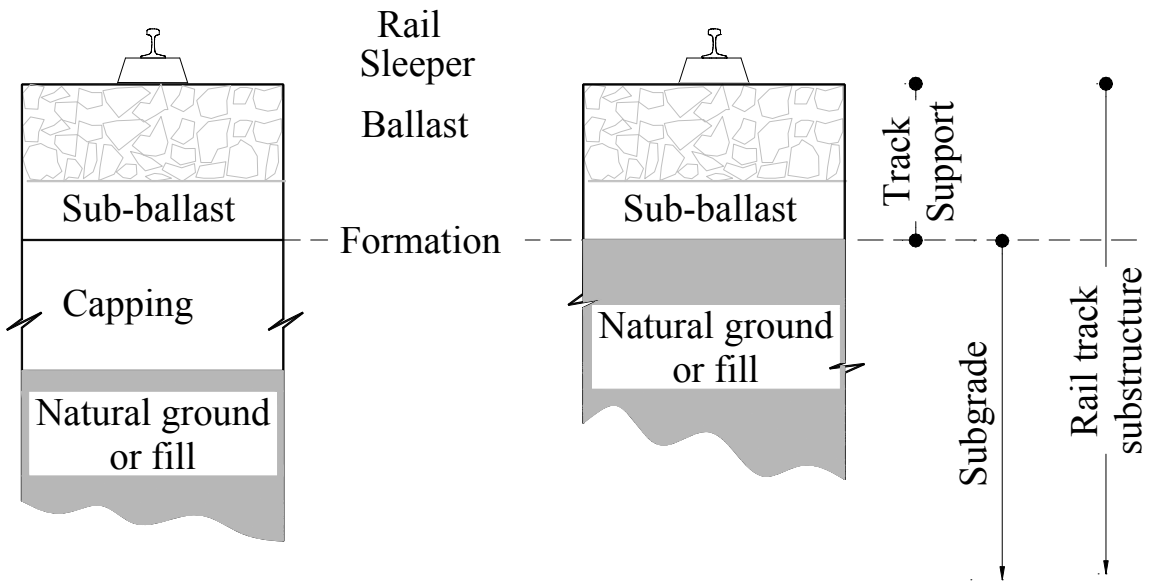

a) with capping layer b) without capping layer

Note:
Except for new construction, the boundaries between strata, as defined, may not be distinct.

Figure 2.1 Types and components of track substructure

Ballast or the track support layer keeps the rail and sleepers intact at the required position by resisting and dissipating the vertical, transverse and longitudinal forces transmitted by

the sleepers. It distributes the loads to the layers below, protecting the subgrade from high stresses and attenuates the noise and shock in addition to providing immediate drainage. The ideal ballast must be of uniform quality, preferably angular in shape with hard corners, usually with all dimensions nearly equal, and clean and free from dust and other contaminants. An appropriate thickness of the ballast layer helps in preventing track buckling.

Fig. 2.2 illustrates the Particle sizes for ballast specified by Queensland Rail (QR); at least 80% by weight of particles forming ballast shall be of crushed rocks (Specification No CT147 2001, QR).

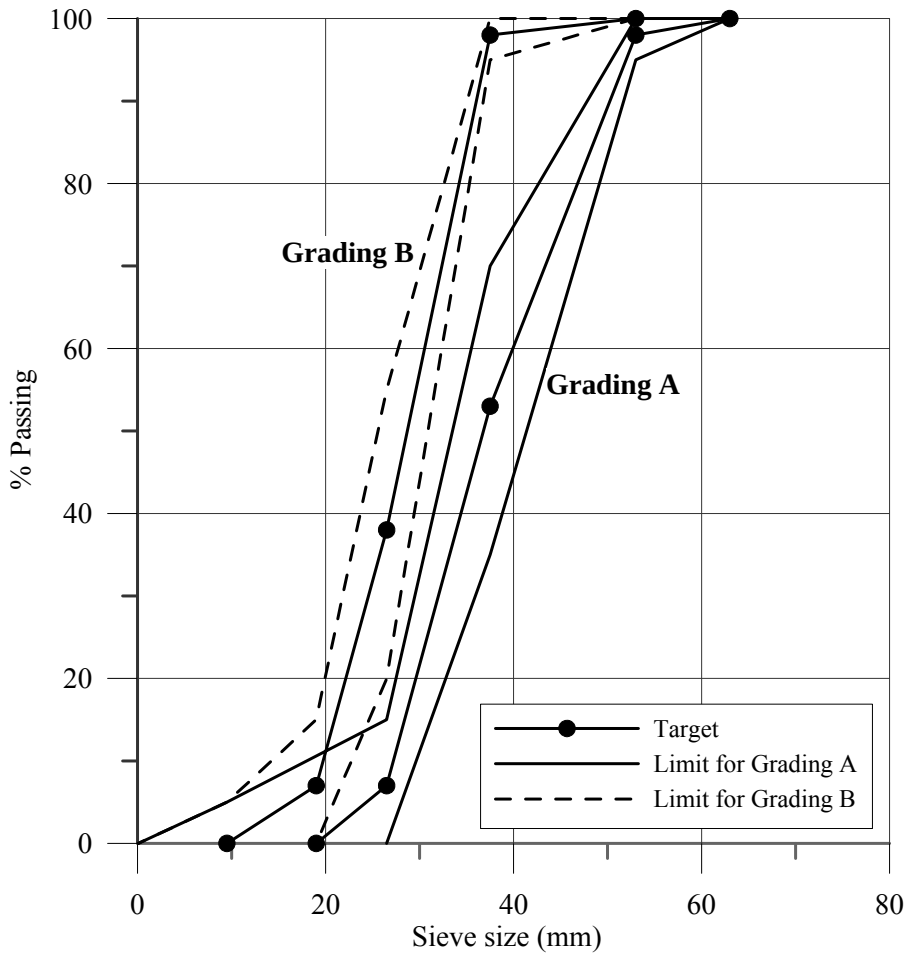

Note: Grading A: Used for concrete sleepers; Grading B: Used for steel sleepers

Figure 2.2 Particle size distribution envelopes of ballast material used in Queensland

Sub-ballast may or may not be present in rail track. In the absence of the sub-ballast layer, high maintenance efforts are likely as sub-ballast helps in protecting the upper surface of subgrade from the intrusion of ballast stones and acts as an inverted filter in the case of mud pumping while facilitating rainwater runoff and further distribution of loads. Suitable sub-ballast materials are broadly graded naturally occurring or processed sand-gravel mixtures, or broadly graded crushed natural aggregates or slag (Selig and Waters 2000).

Subgrade is the load-bearing layer of a track structure, either compacted natural ground or an imported fill embankment, which provides a permanent way to support the ballast layer. Subgrade soils are subjected to lower stresses than the ballast layer. The stress decreases with depth, and the controlling subgrade stress is usually at the top zone of the subgrade unless unusual conditions such as a layered subgrade of sharply varying water contents or densities may change the locations of the controlling stress. The soil investigation prior to design should check for these conditions. In some cases poor support is best avoided by changing the site or by removing unsuitable soil and replacing it with desirable soil or by chemical stabilisation (e.g. lime or cement).

2.1.1 Capping Layer

Capping layer (or an improvement layer) is a higher strength and higher stiffness layer introduced to protect weak natural ground or embankment fill by using a granular material. It serves as a temporary haul way which helps in solving the problem of subgrades wetting up and losing strength during construction by protecting the subgrades from the damage caused by site traffic. However, care and design must be undertaken not to instigate shear failure in both the capping layer and the subgrade. Practically it is not possible to build upon subgrades whose California Bearing Ratio (CBR) value is less than 3. It is, therefore,

necessary to improve the CBR value either by installation of a capping layer or stabilization of the natural ground or embankment fill.

Functions of capping layer are:

- to distribute loads over a sufficient area of the base preventing overstressing;
- to facilitate good drainage; and
- to prevent intrusion of ballast into subgrade.

The best material with which to construct a capping layer is a low plasticity well graded coarse-grained gravely material consisting of sand and gravel particles. It usually comprises of locally available low cost material such as crushed concrete, hardcore or poorly graded crushed rock, possibly with a binder included. In some instances a sub-ballast layer is also termed as a capping layer. In some railways, lime or cement stabilization of capping layer or subgrade is also common in practice.

QR uses capping layer design charts. These are based on CBR values, rail traffic loadings, maximum axle loads for the particular line, and operational parameters such as rail traffic, volume, speed and maintenance standards (Foun and Williams 2003). An example of a design chart for track with 22.5 tonne axle loads is shown in Fig. 2.3.

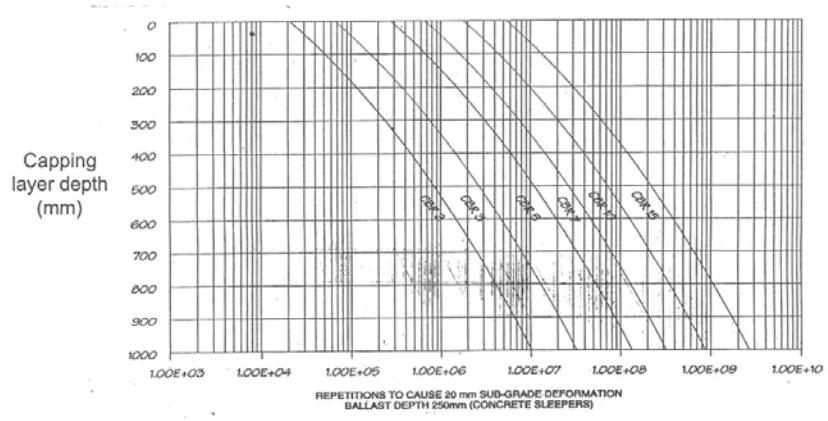

Figure 2.3 Capping layer design chart for 22.5 tonne axle loads (Foun and Williams 2003)

Subgrade failure usually occurs due to over-stressed conditions, poor construction or maintenance practices such as inadequate foundation preparation or inadequate compaction or excessive moisture content of the filling material. Similarly, natural conditions such as a weak subgrade soil (silt, clay), high groundwater tables and erosion or sliding of embankment also affect the performance of the subgrade. Therefore, it is essential that a sufficient crossfall between 1 in 20 and 1 in 40 is maintained on the upper surface of the subgrade to direct runoff from ballast towards a drain or cesspit to prevent water accumulation within the track structure. The subgrade is usually proof rolled to improve uniformity and reduce permeability and a proper drainage system will also accommodate the runoff from adjacent catchments as well as any ground water which could be present.

Although not wholly satisfactory, the main subgrade parameter commonly used in the design of railway tracks or road pavements is the CBR, which is an empirical measure of stiffness and the shear strength of the material tested. In the CBR test a standardised plunger of 50mm diameter is forced into the prepared soil specimen (contained in a rigid mould of approximately 150mm diameter and 200mm height) or in-situ ground and the load required to cause 2.5mm and/or 5mm penetration is measured. The penetration is standardised against the load required to cause the same penetration into a high quality crushed stone that is considered to have a CBR value of 100. The ratio of these loads is then used to calculate the CBR of the material.

$$\text{CBR}\% = \frac{\text{Load (or pressure) sustained by the specimen at 2.5 or 5.0mm penetration}}{\text{Load (or pressure) sustained by standard aggregates at the corresponding level}} \times 100$$

Australia Standards, AS1289.6.1.1-1998, AS1289.6.1.2-1998 and AS1289.6.1.3-1998 describe the method of measurement of CBR in laboratory and field. The CBR values are

then related to safe bearing pressures for different types of soil classification. Fig. 2.4 shows the approximate correlation of bearing capacity and CBR from Casagrande Chart.

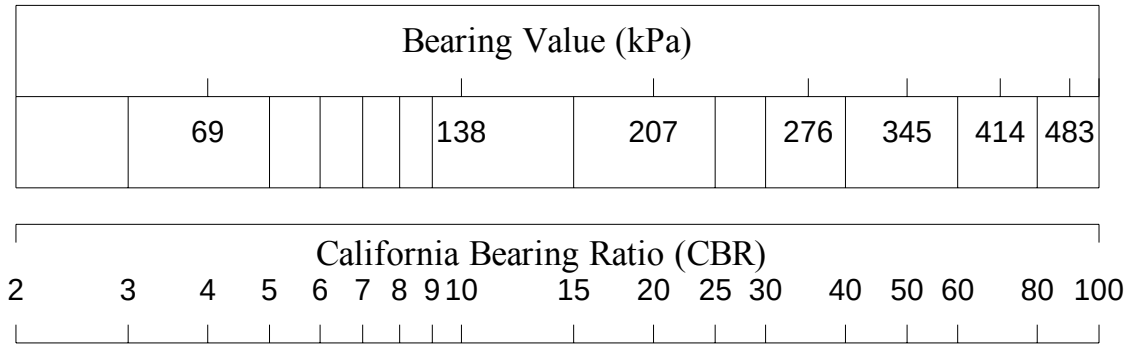

Figure 2.4 Approximate correlation of bearing capacity and CBR from Casagrande Chart (Jeffs and Tew 1991)

The soaked CBR is obtained by immersing specimens in water and allowing free access of water to the top and bottom of samples. The specimens are allowed to soak for 4days or the specified soaking period required. Soaked laboratory CBR values may not necessarily indicate the equilibrium situation or the stress history, but they do give an indication of the worst conditions of a soil. The natural soil moisture content after drainage is the correct moisture content for determining CBR values for railway designs. This is because during the course of time such natural soil conditions have been re-established. The drainage must be kept operating efficiently during the life of the rail track to prevent weakening of foundation due to loss of strength or decrease in CBR value due to rising water table. The use of CBR values is specified in the Railway Specifications for Earthworks (Queensland Rail - Civil Engineering Section 1998). For example, for new embankments a CBR of not less than 20 (soaked) is specified for capping layer materials. CBR tests on material with large aggregates can be very misleading if the resistance to the plunger penetration is provided by isolated larger particles. Similarly the only justification that a compacted clay

material be compared with crushed rock is that the test has a record of relative reliability and usefulness (Lay 1990)

To predict the gross behaviour of the track structure, a parameter known as the track modulus is used. Track modulus is a measure of stiffness of the gross track structure and is usually defined as the force per unit of deflection per unit of track length per rail. Zhang (2000) has indicated that the accuracy of track modulus evaluation is dependent on the theory and track models used. The properties of the subgrade are the dominant factors that influence the track modulus. The reason for this is that the influencing depth of subgrade is thicker relative to thin layers of ballast and sub-ballast. Selig and Waters (2000) state that the influence of traffic induced stresses extend downwards as much as 5m below the bottom of the sleepers. With low modulus, track substructure deflections will increase resulting in a decrease in riding quality as well as a significant increase in maintenance.

2.2 Track Degradation and Failure

2.2.1 Track Degradation

The development of irregularities of the top surface of rails or track alignment with increase in the number of load cycles is termed as track degradation. These irregularities lead to deterioration in riding quality. Track degradation parameters are usually measured by a track geometry-recording car, which detects rail level (top) variation, the curvature in horizontal alignment (versine), the difference in level of the rail (superelevation or cant), and the difference in cant over a given length (twist).

Of these track degradation parameters, twist is the most critical in terms of the risk of derailment. If a trailing axle of a wagon runs into a depression on the track, the diagonally opposite wheel is unloaded due to loss of contact with the rail as shown in Fig. 2.5. The danger in this phenomenon is that the lateral force acting on the wheels undergoing unloading of the vertical load may be sufficient to cause wagon derailment. Therefore, maintenance of the track geometry at specified standards is essential for a safe ride.

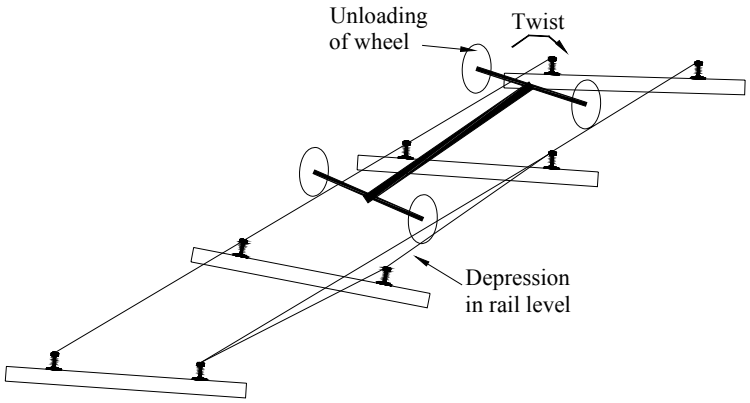

Figure 2.5 Effect of twist defect in track geometry

As per the discussion in Section 2.1, a key contributor to track degradation is the performance of the subgrade. This is due to the fact that natural ground properties can have a considerable variation within a few meters and are easily affected by seasonal moisture changes causing differential settlements. This phenomenon is aggravated by the repeated nature of the wheel passage or load cycle.

2.2.2 Subgrade Failure Modes

Fig. 2.6 shows a few factors that contribute to subgrade deterioration. The factors are repeated dynamic loading, excessive moisture and fine grained or poor quality soil. Selig and Waters, (2000) describe subgrade failure modes as follows:

- Excessive progressive settlement from repeated traffic loading;

- Consolidation settlement and massive shear failure under the combined weights of the train, track structure, and earth;
- Progressive shear failure from repeated wheel loading;
- Shrinking and swelling from moisture change;
- Frost heave and thaw softening; and
- Subgrade attrition.

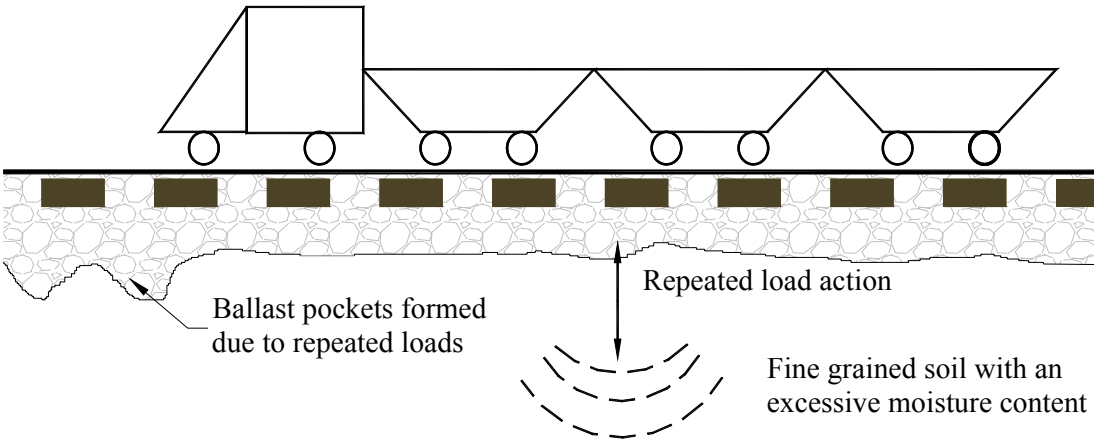

Figure 2.6 Subgrade deterioration factors

Firstly, the plastic flow of soil caused by excessive repeated loading at the subgrade/ballast interface leads to heave at the trackside through progressive shear failure (Fig. 2.7). This failure is prominent in subgrades of fine-grained soils with high clay contents. Secondly, non-uniform track settlement and unacceptable track geometry changes occur due to excessive plastic deformation caused by progressive soil compaction and consolidation.

Fig. 2.8 illustrates ballast pocket formation as a result of the vertical component of progressive shear deformation. This failure is caused by progressive compaction or consolidation of the entire subgrade layer because of repeated loading. Often this type of failure contributes to the development of non-uniform track settlement and unacceptable

track geometry changes. The other types of subgrade failures are subgrade attrition with mud pumping caused by high moisture content and repeated loading at the ballast and subgrade interface leading to ballast fouling and associated drainage problems, slope stability failures and excessive consolidation settlement due to self-weight.

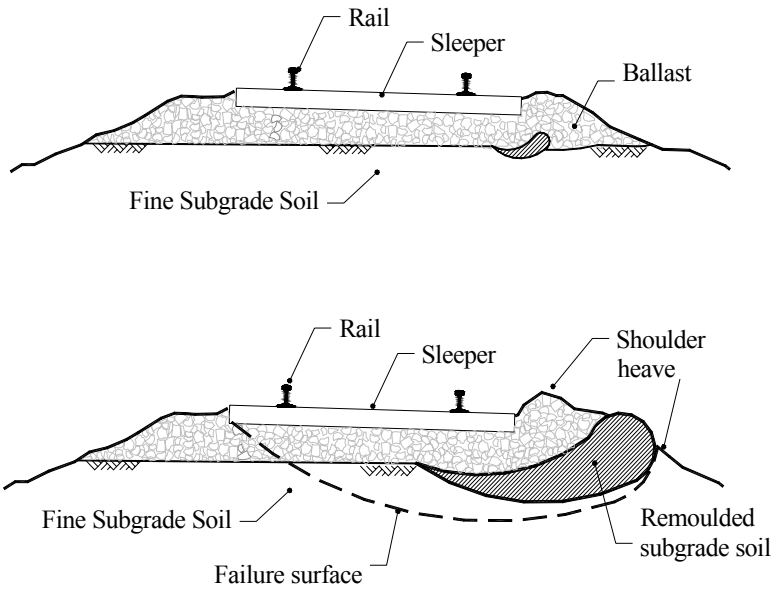

Figure 2.7 Subgrade progressive shear failure

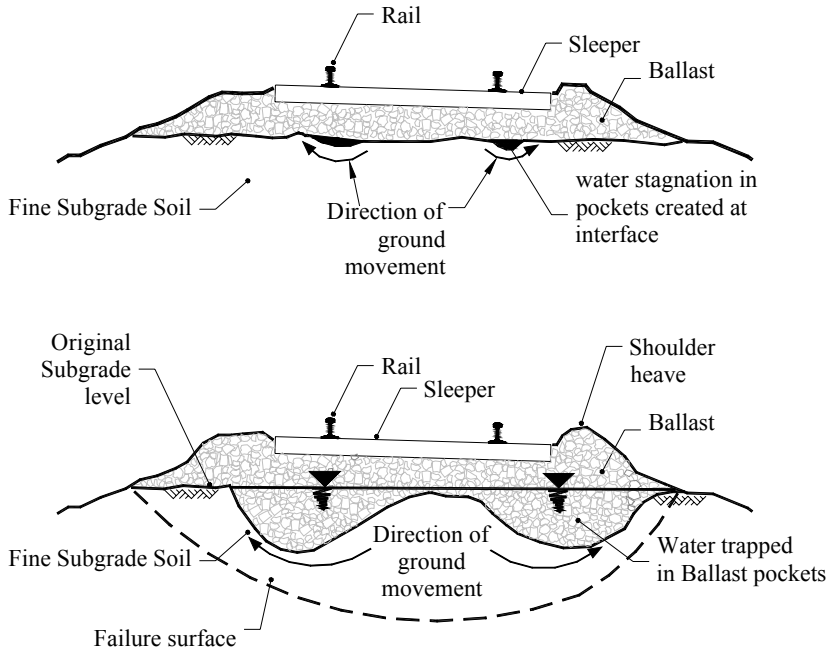

Figure 2.8 Ballast pocket formation

The most commonly used remedial measure, which is considered the most economical, is to increase the ballast thickness to reduce subgrade stresses. However, this method of remediation in association with excessive plastic deformation can also lead to formation of ballast pockets. The other possible remedial measures are constructing new track, increased rail weight, using a hot asphalt mix layer and modifying subgrade to permit higher stresses (Li and Selig 1998a; Li and Selig 1998b). These remedial measures adopted by the industry appear to provide only a short term solution by only treating the symptoms of the problems rather than analysing its root cause for longer term eradication. This thesis is an attempt to provide assistance towards developing a long lasting solution.

2.3 Response of Subgrade Layer to Rail Traffic

2.3.1 Mechanics of Load Transfer into Subgrade Layer

To calculate the vertical pressure on the subgrade layer resulting from sleeper loading, the load transfer through the ballast layer should be investigated. A comprehensive discussion of simplified theoretical models (Boussinesq elastic theory and stress below an evenly distributed strip load), semi-empirical (load spread methods and Schramm's solution) and empirical solutions (Talbot equation and Japanese National Railway equations) can be found in Jeffs and Tew (1991). Esveld (2001) has described the calculation of stresses based on Zimmermann's theory. The following gives a brief introduction to some of the above mentioned methods.

It is common in practice to analyse the rail track system for a static load, taking into account the dynamic effects of running speed on load by a Dynamic Amplification Factor

(DAF) also sometimes called the impact factor. The Eisenmann formula is the most recognised, based on track quality, and is given in Eq. (2.1) (Esveld 2001).

$$\text{DAF} = 1 + t\varphi \text{ if V} < 60 \text{ km/h}$$
$$\text{DAF} = 1 + t\varphi(1 + \frac{V - 60}{140}) \text{ if } 60 \le \text{V} \le 200 \text{ km/h} \quad (2.1)$$

where V = train speed km/h, φ = factor depending on track quality, and t = multiplication factor of standard deviation which depends on the confidence interval (Table 2.1).

Table 2.1 Values of t and φ (Esveld 2001)

Probability of occurrence in the field	t	Application
68.3%	1	Contact stress, subgrade
95.4%	2	Lateral load, ballast bed
99.7%	3	Rail stresses, fastenings, supports

Track condition	φ
Very Good	0.1
Good	0.2
Poor	0.3

Since the rail is so important for safety and reliability of rail traffic, a value of t = 3 is recommended as the chance of exceeding the maximum calculated stress is only ± 0.15%. On the other hand for subgrade stress calculation, a value of t =1 (corresponding to the chances of exceeding of ± 15.85%) is suggested.

Boussinesq elastic theory

This theory assumes that the ballast and the subgrade form a half space that is semi-finite, elastic and homogeneous and that the rail seat load is uniformly distributed over a circular area equivalent to the assumed contact area between the sleeper and the ballast.

$$\text{vertical stress} = P_a\left[1 - \frac{z^3}{(a^2 + z^2)^{1.5}}\right] \quad (2.2a)$$

$$\text{horizontal stress} = \frac{P_a}{2}\left[(1 - 2\nu) - \frac{2(1+\nu)z}{(a^2 + z^2)^{0.5}} + \frac{z^3}{(a^2 + z^2)^{1.5}}\right] \quad (2.2b)$$

where P_a = average uniform pressure over the loaded area (kPa), a = radius of the loaded area (m), ν = Poisson's ratio, z = vertical depth to any point beneath the surface.

Zimmermann's theory based stress calculation

The maximum vertical stress on the formation is calculated by superimposing contributions from the adjacent sleepers, which is assumed as uniformly distributed over each sleeper surface (Esveld 2001). The magnitude of this stress beneath the various sleepers caused by effective wheel load Q is given by

$$\sigma_i = \sigma_{\max} \eta(x_i) \tag{2.3}$$

in which

$$\sigma_{\max} = \text{DAF}.\frac{Qa}{2LA_{sb}} \tag{2.4}$$

$$\eta(x_i) = e^{-x_i/L}\left[\cos\frac{x_i}{L} + \sin\frac{x_i}{L}\right] \quad x_i \geq 0 \tag{2.5}$$

where a = sleeper spacing (centre - to - centre distance), A_{sb} = contact area between sleeper and ballast bed for half sleeper, DAF = dynamic amplification factor, and L= characteristic length determined by $L = \sqrt[4]{4EI/k}$ where EI = bending stiffness of rail and k = modulus of subgrade reaction.

As adjacent sleepers cannot all be subjected to an unfavourable load at the same time, the value of factor t is taken as unity when calculating DAF. The vertical stress at any location (x,z) is given by

$$\sigma_z = \frac{\sigma_i}{\pi}\left[\alpha_1 - \alpha_2 - \frac{1}{2}(\sin 2\alpha_1 - \sin 2\alpha_2)\right] \tag{2.6}$$

where σ_i = average uniform contact pressure between the sleeper and the ballast (kPa) and α_1, α_2 = as depicted in Fig. 2.9. Fig. 2.10 shows the stress pattern on the ballast bed along the length of the track.

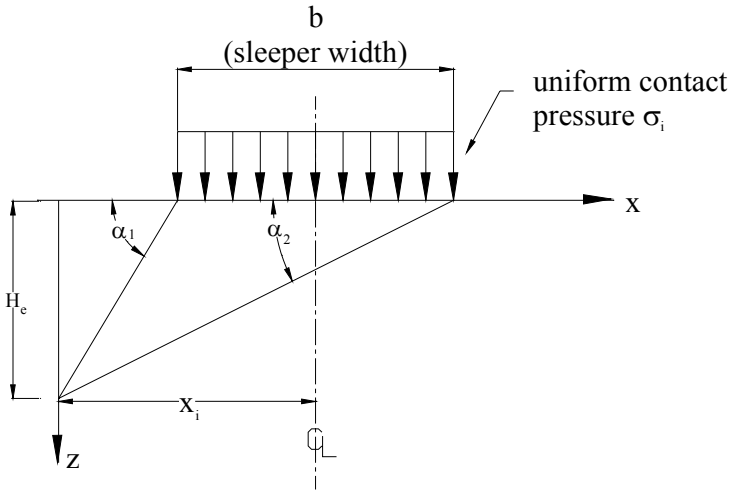

Figure 2.9 Stress due to strip load

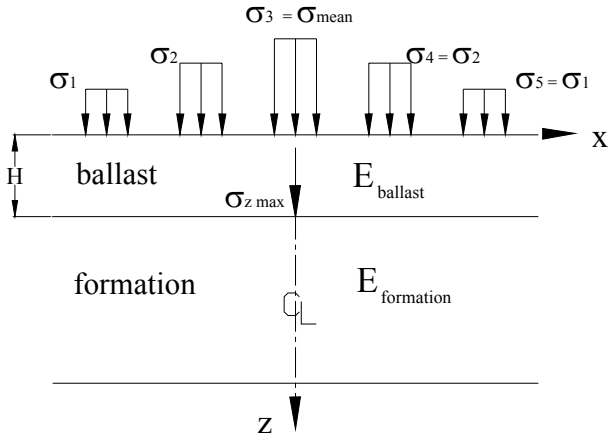

Figure 2.10 Ballast bed and formation represented as two-layer system (Esveld 2001)

In the Odemark's equivalence method, the two layered system is converted into a single layered system by

$$H_e = 0.9H \sqrt[3]{\frac{E_{ballast}}{E_{formation}}} \qquad (2.7)$$

where H_e = equivalent ballast depth, H = actual ballast depth under the sleeper, $E_{ballast}$ = modulus of elasticity of ballast, and $E_{formation}$ = modulus of elasticity of formation.

The maximum vertical stress on the formation in the actual two layered system then correlates with the maximum vertical stress in the equivalent half space at a distance H_e from the surface as shown in Fig. 2.9.

Load spread method

The assumption that vertical load is distributed vertically with a load spread slope of 1:1 or 2:1(vertical : horizontal) is the most commonly used simplified method in practice. Fig. 2.11 shows the mechanism of load transfer from the wheel to formation.

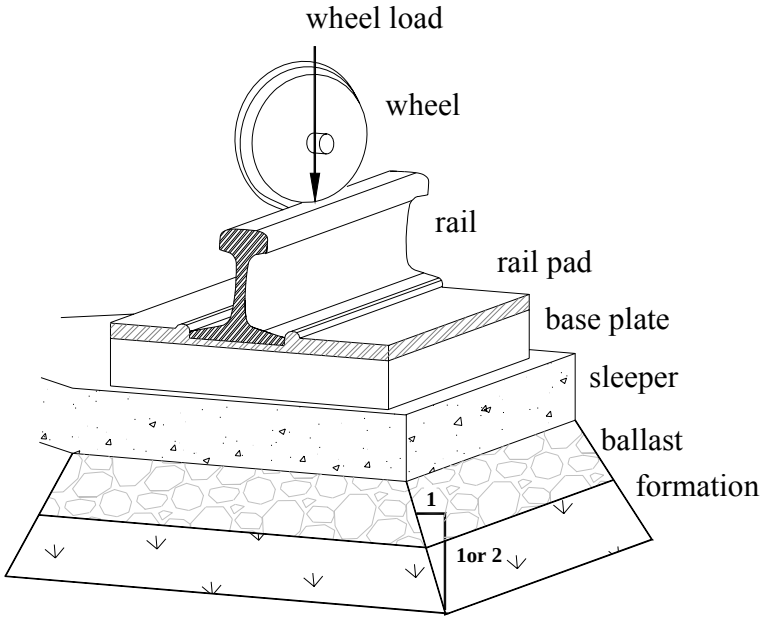

Figure 2.11 Load spread method

Jeffs and Tew (1991) indicated that the load spread method gives an average value of vertical stress at any given horizontal plane within the loaded area below the sleeper, while Boussinesq's method finds a maximum vertical stress. A comparison of these two methods (considering loaded area as circular) carried out by the Department of Industrial

Research, UK in 1991 is shown in Fig. 2.12. It was found that load spread of 2:1 is closer to Boussinesq than 1:1 load spread. The equations for 1:1 and 2:1 spreads can be derived in few steps as $\sigma_{average} = \frac{P_a}{\left[1+\frac{z}{a}\right]^2}$ and $\sigma_{average} = \frac{P_a}{\left[1+0.5\frac{z}{a}\right]^2}$ respectively.

Talbot Equation

The most commonly used empirical relationship to limit the subgrade stresses is the American Railway Engineering Association (AREA) recommended Talbot Equation developed in 1991. Li and Selig (1998a) have presented the Talbot equation shown in Eq. 2.8.

$$H = 0.24\left(\frac{P_m}{P_c}\right)^{0.8} \qquad (2.8)$$

where H = granular layer thickness (m), P_c = allowable subgrade pressure (138kPa recommended by AREA) and P_m = vertical stress applied on the ballast surface.

Li and Selig (1998a,1998b) identified the limitations of Eq. 2.8 as follows:

- Oversimplification of actual situation for tracks under heavier axle loads and higher train speeds;
- Not reflecting the effect of repeated dynamic loads on subgrade condition;
- Not considering the granular layer properties; and
- Assumption of a homogeneous half space that represents ballast, sub-ballast and subgrade layers without considering properties of individual layers.

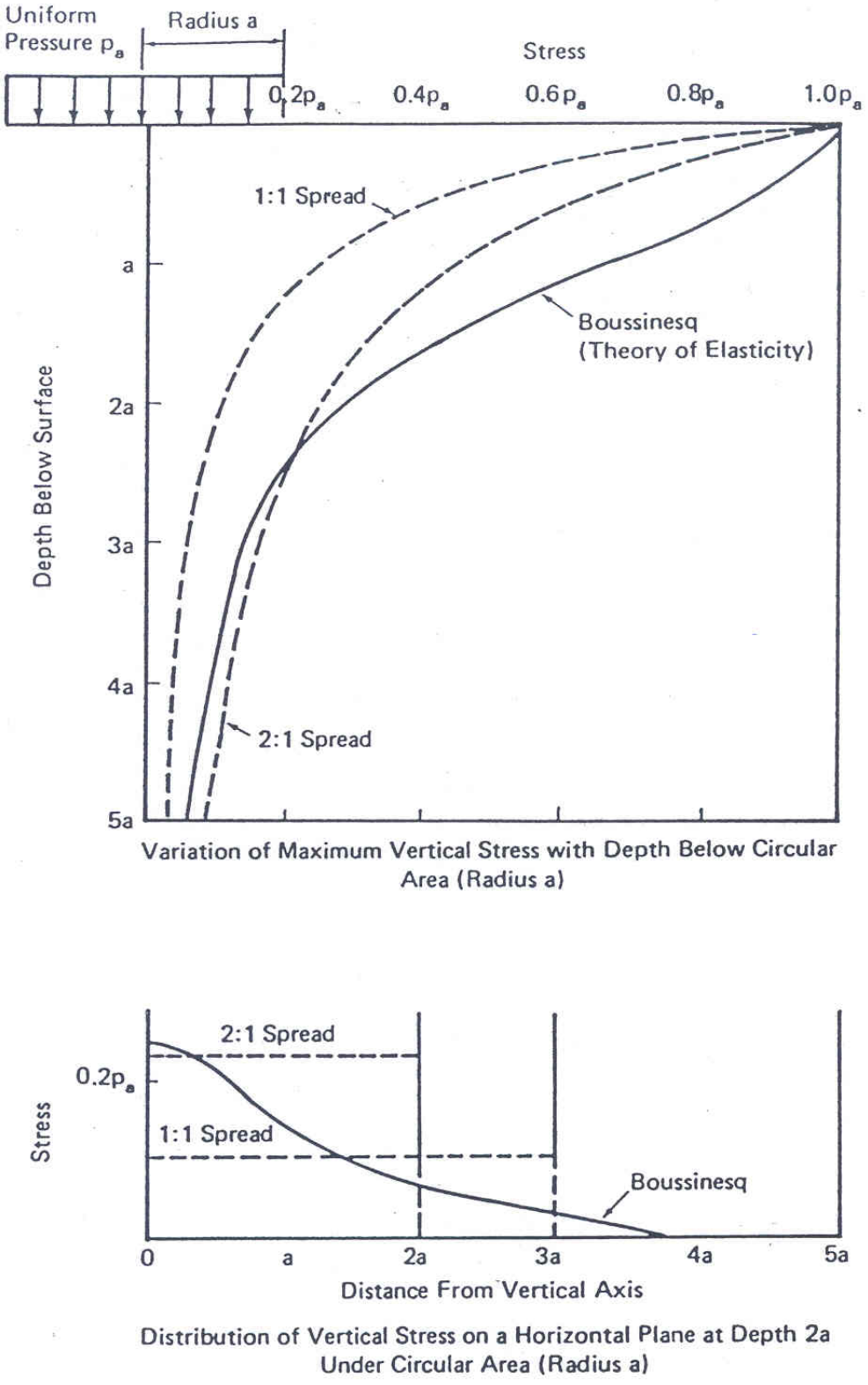

Figure 2.12 Comparison of vertical stress distribution under a uniformly loaded circular area by load spread methods and Boussinesq's equation (Jeffs and Tew 1991)

In fact all the methods described above have the limitations discussed by Li and Selig (1998a,1998b). Yet these methods provide simple, easy to use solutions in comparison with complex tedious multilayer theories or finite element techniques. Jeffs and Tew (1991) state that in 1968, Office of Research and Experiments (ORE) of the International Union of Railways (UIC) found the following important factors:

- The vertical stress distribution in the subgrade becomes practically uniform at a thickness of construction greater than 600mm.
- Sleeper spacing in the range 630 to 790mm had a negligible influence on the vertical stress level in the subgrade for a unit load applied to the sleeper.

2.3.1.1 Effect of Compaction and Moisture Content

Compaction is the process of increasing soil density or unit weight, accompanied by a decrease in air volume as shown in Fig. 2.13. There is usually no change in water content**.** The degree of compaction is measured by dry unit weight and depends on the water content and compactive effort (laboratory - weight of rammer, number of blows; field - weight of rollers, number of passes, frequency and amplitude of vibration).

The objective of compaction is to improve the engineering properties either of an existing soil or during the process of placing a fill. The main outcomes being sought are to:

- increase shear strength and therefore bearing capacity;
- decrease void ratio and therefore reduce future settlement and permeability;
- decrease swelling or shrinkage.

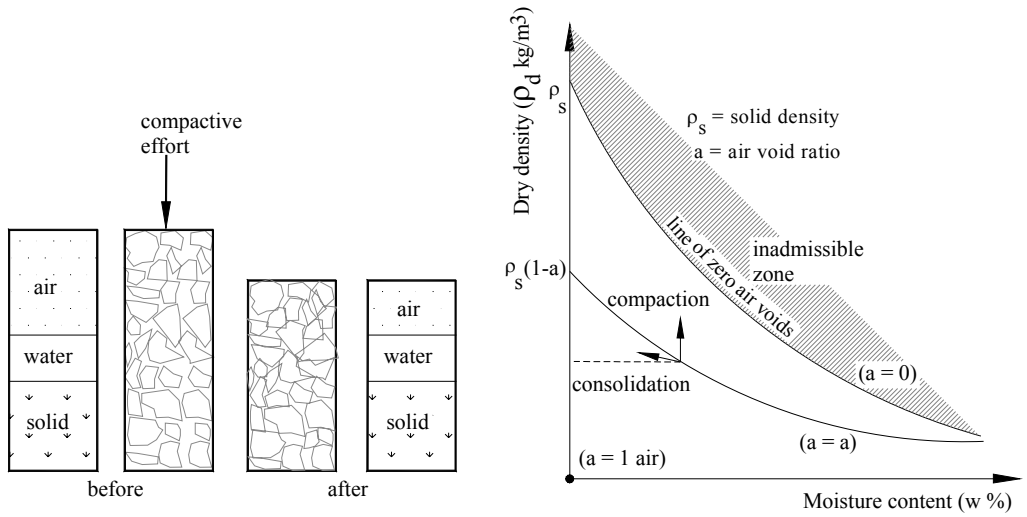

(a) material phases in soil

(b) basic density, moisture content variation (Lay 1990)

Figure 2.13 Illustration of compaction

Fig. 2.14 shows that for a given compactive effort, there will be an Optimum Moisture Content (OMC) at which the dry density attains its maximum value. The higher the compactive effort, the lower will be the OMC and the higher will be the maximum dry density, which is the shift from curve b to curve c. Fig. 2.14 also shows how the effect of increased compactive effort will produce little increase in densification after a relevant stage until no further compaction is possible. Usually, reduction in densification at constant moisture occurs for equal incremental increases in compaction energy and it all stops as about 1% voids is approached.

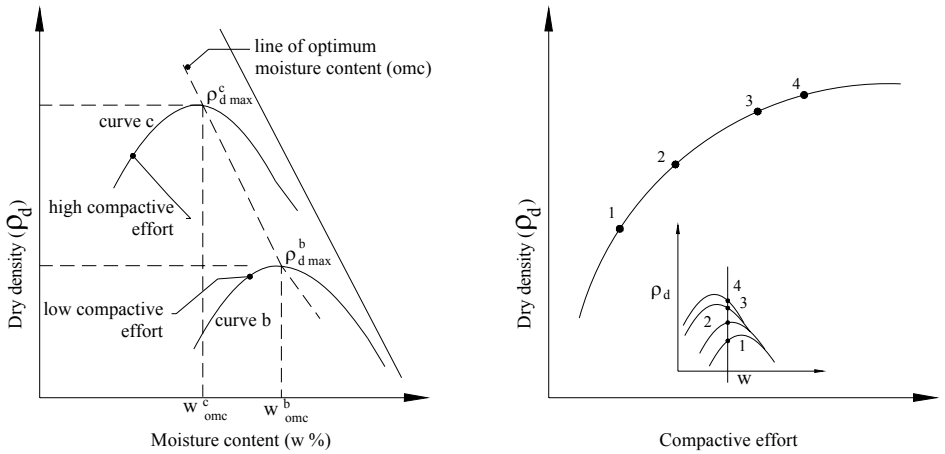

Figure 2.14 Effect of continued compactive effort (Lay 1990)

The increase in the moulding moisture content would results in a decrease in permeability on the dry side of OMC and a slight increase in permeability on the wet side of OMC. An increase in the compactive effort reduces the permeability and increases the dry density, thereby reducing the voids available for flow and increases the orientation of particles. Compaction rearranges soil particles and moves them closer together resulting generally an increase in the ratio of horizontal effective stress to vertical effective stress of soil (Lambe and Whitman 1979).

Well-graded coarse soils can be compacted to a high density compared to fine grained soils. OMC for fine grained soils is greater than that for coarse grained soils because finer particles have larger surface area and need more water to wet them. Thus for the same compactive effort, maximum dry density of fine grained soils will be less than that for coarse grained soils.

Fig. 2.15 shows the effect of three different densities on stress-strain characteristics curves obtained from consolidated undrained triaxial tests on sand specimens.

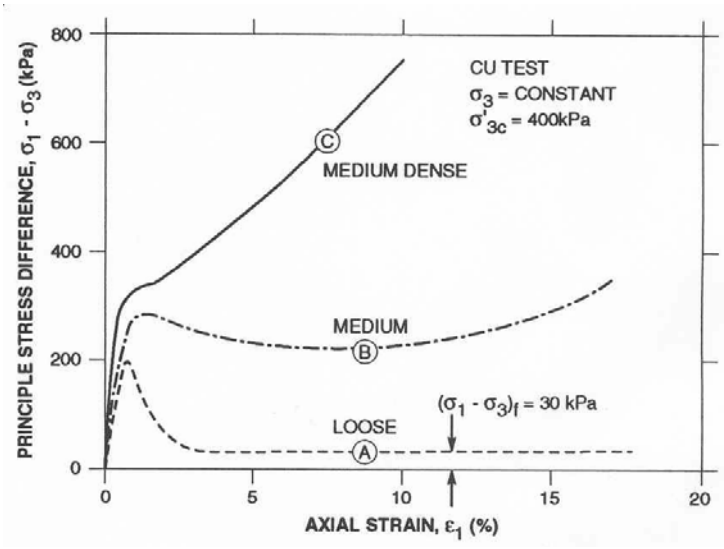

Figure 2.15 Effect of density on stress-strain behaviour of sand (Selig and Waters 2000)

Fig. 2.15 shows that there exists an increase in peak deviator stress with the increase in density for any given level of strain. This could be interpreted as indicating that, with an increase in density, the strength tends to increase due to closer packing of particles, increased friction angles and dilatency effects.

Natural subgrade moisture content is a direct function of seasonal fluctuations in the natural water table. Although the compacted moisture content is known at the time of construction, after a few years of service a substantial difference in moisture content is normally observed. Janssen and Dempsey (1981) explained the performance of subgrade due to different moisture conditions. Three major factors described by them are:

- shear strength (indicated by CBR) is inversely proportional to the moisture content (Fig. 2.16);
- dynamic and resilient modulus of unsaturated soils decreases with increased moisture content;
- frost heaving is influenced directly by already available water and indirectly by affecting the unsaturated hydraulic conductivity.

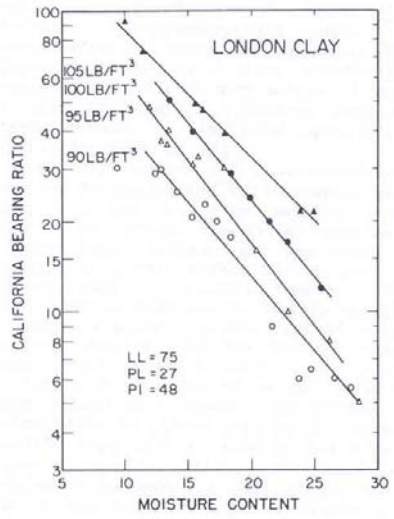

Figure 2.16 CBR vs. moisture content at various dry densities (Janssen and Dempsey 1981)

Ksaibati et. al. (2000) found that increasing moisture in subgrade and base layers of road pavements can significantly reduce the modulus values. The study was conducted using Dynaflect and Falling Weight Deflectometer (FWD) tests on Florida state roads, USA and the layer moduli were backcalculated. Table 2.2 tabulates their findings.

Table 2.2 Percentage of reduction in moduli due to moisture contents (Ksaibati et al. 2000)

State Road	Base			Subgrade		
	Range in moisture content (%)	Percent decrease in Dynaflect modulus	Percent decrease in FWD modulus	Range in moisture content (%)	Percent decrease in Dynaflect modulus	Percent decrease in FWD modulus
200	3.5	17.2	91.0	11	17.3	36.9
26	8.5	10.9	96.3	9.3	10.6	22.2
207	0.9	5.0	26.5	3.4	6.4	21.8
24	4.1	35.0	13.8	6.9	31.3	53.6
62	6.2	19.0	43.7	7.5	15.0	23.6

The effect of three different soil types (sand, silt and clay) on variation of compaction and stiffness achieved for increasing compactive effort are shown in Fig. 2.17. The percent compactive effort is the density expressed as a percent of maximum dry density in the ASTM standard compaction test. Effort is the work done by the compactor per unit volume of soil expressed as a percent of the effort in the ASTM test (Selig and Waters 2000). The main factors obtained from the excercise are:

- the coarser the material, the greater the percent compaction achieved;
- the finer the material, to achieve the same percent compaction requires greater compactive effort;
- the coarser the material, the greater the stiffness achieved due to compaction.

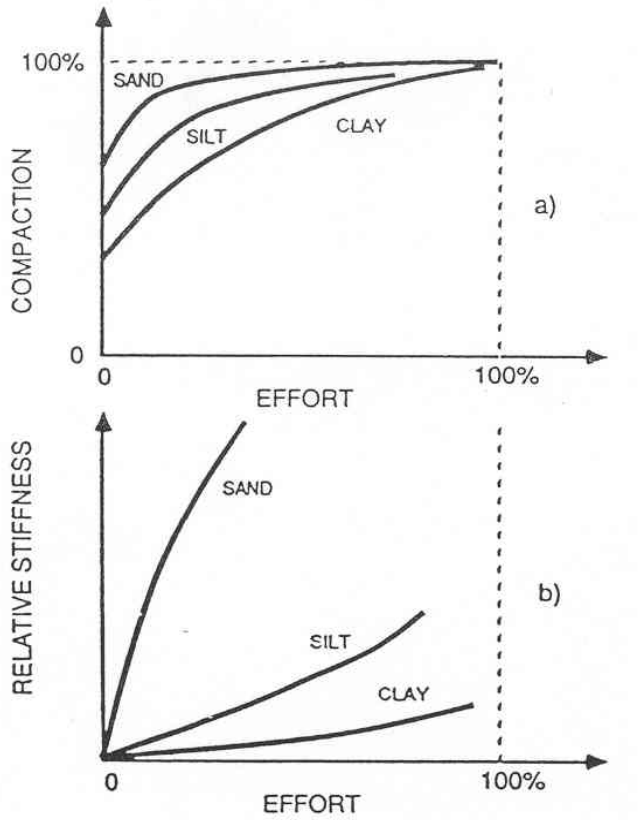

Figure 2.17 Effect of soil type on variation of percent compaction and soil stiffness with compaction effort (Selig and Waters 2000)

2.3.2 Effect of Loading Cycles

Means and Parcher (1964) discussed the effect of repeated loading, illustrating the typical stress-strain curves for initially identical specimens, one subjected to several thousands of repeated stress applications and the other in its initial compacted state before both being subjected to failure in a normal undrained test (Fig. 2.18), based on tests carried out by Seed and co-workers at the University of California on compacted clays. It was observed that the shear strength of clay increased due to a large number of repetitions of relatively low stress. However, if the stress intensities are too high, the cumulative deformation after a few repetitions will result in failure.

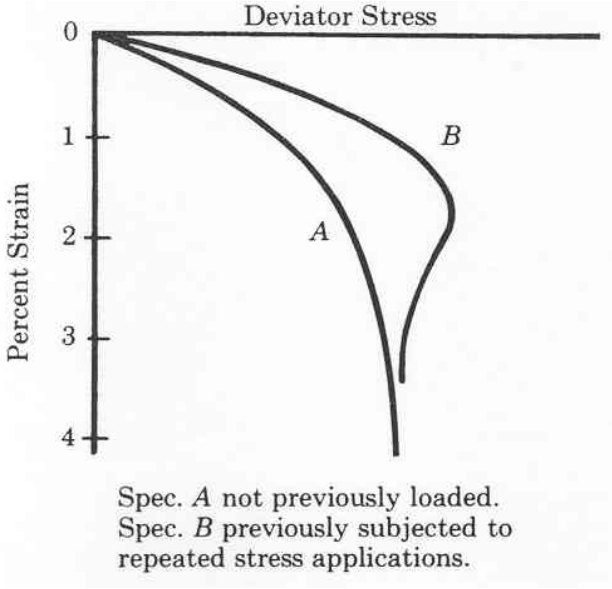

Figure 2.18 Effect of repeated loading (Means and Parcher 1964)

Fig. 2.19 illustrates the increase in constrained modulus during successive cycles of loading of Ottawa sand. The modulus is very sensitive to the early stages of loading, but this effect gradually decreases during successive loadings, stabilizing after several hundreds of cycles (Lambe and Whitman 1979).

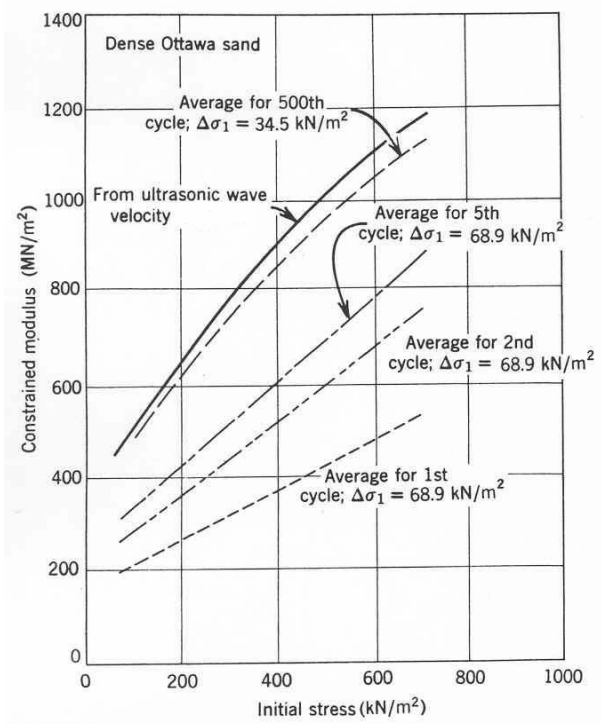

Figure 2.19 Increase in secant constrained modulus with successive cycles of loading (Lambe and Whitman 1979)

Fig. 2.20 shows stress strain behaviour of soil in oedometer test under repeated loading. At the first 10-50 cycles of a constant load application, a small amount of permanent strain is observed in sand which stabilized after several numbers of loading cycles (Fig. 2.20). As shown in Fig. 2.21, a sand sample becomes stiffer after the initial loading (Lambe and Whitman 1979).

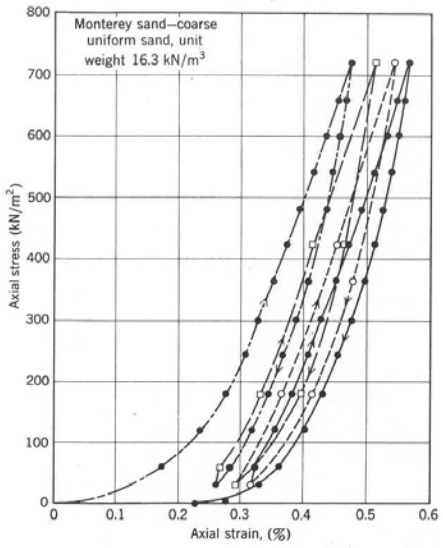

Figure 2.20 Stress strain curves for cyclic loading in oedometer test after Seamen et. al. 1963 (Lambe and Whitman 1979).

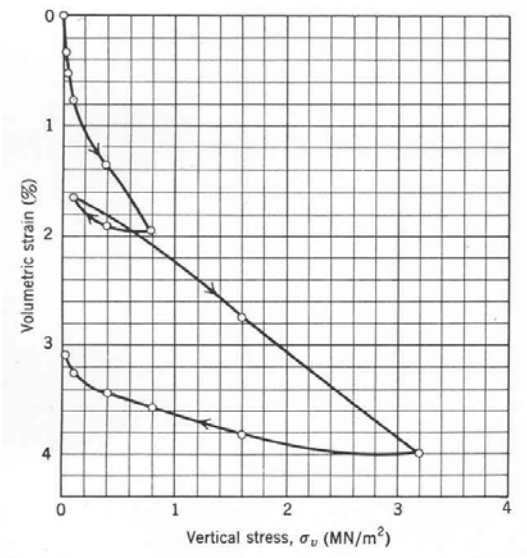

Figure 2.21 Oedometer test results for well graded calcareous sand from Libya (Lambe and Whitman 1979).

The stress strain characteristic of the railway substructure is dependent on the frequency and the size of the individual axle load applications. Profillidis (2000) has suggested that Dormon's rule, established in highway engineering, can be used for railways as well. Accordingly, the loading on the subgrade is inversely proportional to the number of loading cycles raised to a power λ, given by

$$\frac{\sigma_1}{\sigma_2} = \left(\frac{N_2}{N_1} \right)^{\lambda} \qquad (2.9)$$

where σ_1, σ_2 = stresses corresponding to N_1, N_2 loading cycles respectively and λ = an exponent with a mean value of 0.2.

If P = load per axle and T = daily traffic tonnage, from Eq. 2.9 it follows that

$$\frac{\sigma_1}{\sigma_2} = \left(\frac{T_2 / P_2}{T_1 / P_1} \right)^{\lambda} \qquad (2.10)$$

For constant axle loads, $P_1 = P_2$ and Eqn. 2.10 becomes

$$\frac{\sigma_1}{\sigma_2} = \left(\frac{T_2}{T_1} \right)^{\lambda} \qquad (2.11)$$

2.3.3 Stress-Strain Characteristics of Subgrade Layer

The appropriate measure of evaluating subgrade layer characteristics and its behaviour is dependent on its composition, structure, density and moisture content as well as the application. The material is usually tested for its performance under in-service conditions as much as possible. Behaviour of soils is very difficult to entirely match with simple elastic theory as they depart from it due to non-linearity, hysteresis and irreversible or plastic deformations when loaded as indicated in Fig. 2.22.

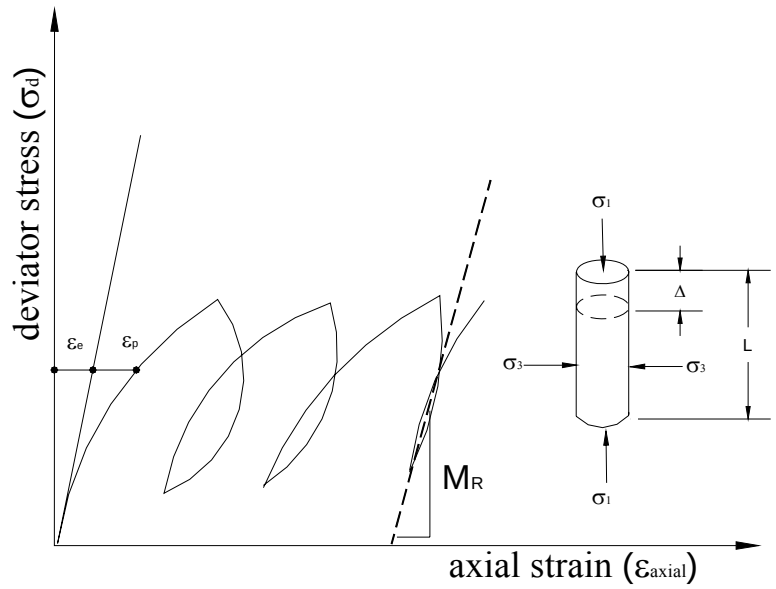

Figure 2.22 Stress-strain behaviour of soils

Fig. 2.22 shows the typical deviator stress and axial strain behaviour observed in a triaxial test, where a cylindrical soil sample is first consolidated to an isotropic stress and then subjected to an axial stress while holding the horizontal stress constant to cause shear failure. The axial stress is referred to as deviator stress. The axial deformation (Δ) on the original axial length (L) is also measured during the application of deviator stress. Thus, the vertical stress is the major principal stress (σ_1) and the minor (and intermediate) principal stress (σ_3) is the horizontal stress

The complex nature of the vertical, horizontal and shear stress patterns induced when a moving load approaches and departs a pavement is illustrated in Fig. 2.23. As shown an element in a pavement structure is subjected to positive vertical and horizontal stress components while the shear stress component is reversed as the load passes causing a rotation of the principal stress axes (σ_1) and (σ_3) (Lekarp et al. 2000).

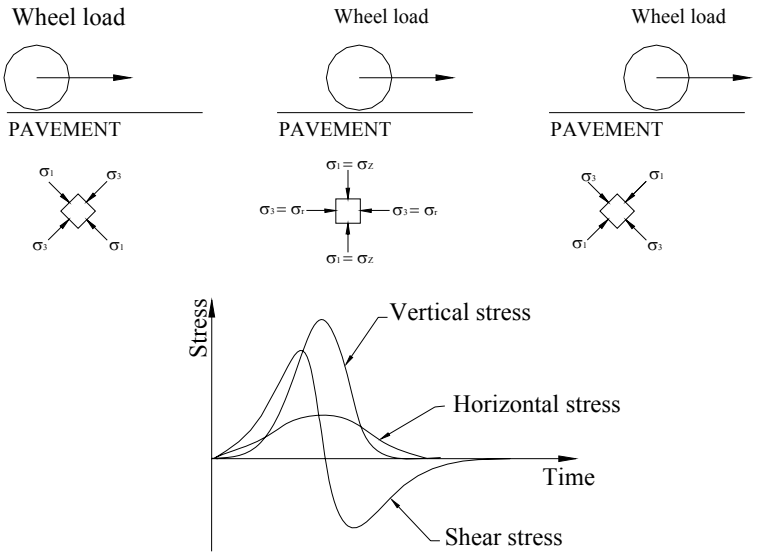

Figure 2.23 Stress beneath rolling wheel load (Lekarp et al. 2000)

Elastic behaviour

A soil is said to be elastic when it suffers a reduction in volume when a compressive load is applied but recovers its initial volume immediately when the load is removed. At the beginning of the stress-strain curve, soils present an approximate elastic behaviour since the strains are recoverable when the load is removed. Linear elasticity can be assumed if the loading is small enough to keep stresses and strains at low levels. The simplicity of this model has made it easy to produce closed-form solutions for many situations in engineering applications. The linear characteristics of a soil can generally be observed at very low strains in the order of 10^{-4} and smaller (Bowles 1979).

Resilient or recoverable behaviour

Resiliency is defined as the extreme limit to which a soil body can repeatedly be strained without fracture or permanent deformation. In the literature Resilient Modulus is considered as the most important property for both railway track and road pavement designs. It is defined as the rebound deformation from repeated load applications. *This is*

because permanent deformation is considered relatively insignificant to the resilient behaviour and is ignored in subgrade designs. As illustrated in Figure 2.22 the Resilient Modulus (M_R) is defined by the secant slope of the deviator stress (σ_d)-axial strain (ε_{axial}) curve given by:

$$M_R = \frac{\sigma_d}{\varepsilon_{axial}} \qquad (2.12)$$

where $\sigma_d = \sigma_1 - \sigma_3$ and $\varepsilon_{axial} = \frac{\Delta}{L}$ = axial strain in the direction of σ_1

σ_1 and σ_3 are the major and minor principal stresses.

Plastic or non-recoverable behaviour

Plasticity is defined as the ability of soil to undergo large deformations without crumbling or cracking under stresses. To define the permanent deformations, simple elasto-plastic models are generally used. As shown in Fig. 2.22, the stress-strain curve is represented by initial linear-elastic behaviour up to a yield stress, which limits the boundary between elastic and plastic domains. Once this yield stress is reached, plastic strains occur in addition to elastic strains. Usually the total strain is defined as the summation of these two strains:

$$\varepsilon = \varepsilon_e + \varepsilon_p \qquad (2.13)$$

where subscript $_e$ and $_p$ indicate, respectively, elastic and plastic strains.

Dynamic behaviour (Vucetic and Dobry 1991)

The dynamic behaviour of soils depends to a large extent on cyclic stress-strain characteristics of the soil in shear. Fig. 2.24 shows an idealised relationship between shear stress τ and shear strain γ for the first cycle of planar cyclic shear loading.

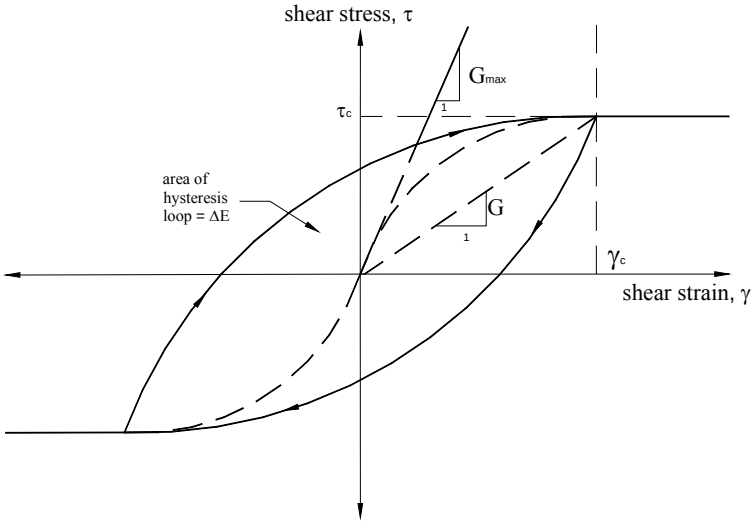

Figure 2.24 First cycle stress-strain curve

The dynamic characteristics are often described by:

a) Shear modulus at small strains, G_{max} given by

$$G_{max} = \rho V_s^2 \qquad (2.14)$$

where ρ = mass density of soil and V_s = shear wave velocity;

b) Secant shear modulus defined as

$$G = \tau_c / \gamma_c \qquad (2.15)$$

where γ_c = cyclic strain amplitude, and τ_c = cyclic stress amplitude corresponding to γ_c; and

c) Material damping ratio λ defining the progressive diminution of dynamic characteristics is given by

$$\lambda = \frac{1}{2\pi} \frac{\Delta E}{G\gamma_c^2} \qquad (2.16)$$

where ΔE = the area enclosed by the hysteresis loop as shown in Fig. 2.23.

Usually, G_{max} is obtained by in-situ seismic measurements of V_s and the influence of number of cycles, N on G is defined as the degradation of the modulus.

Most numerical models of railway track subgrade systems use elastic or elasto-plastic constitutive relationships (Section 2.5.2). Due to the large variability in the subgrade properties and the costs involved in testing, the practitioners experience considerable difficulty in establishing the appropriate resilient modulus for design purposes.

Subgrade moduli can be:

- determined from laboratory testing;
- backcalculated from nondestructive testing data; and
- predicted from soil/granular material properties.

Field/Laboratory Testing

There are basically two modes of testing available for the estimation of subgrade parameters, laboratory and field-testing. The most commonly used methods to determine subgrade material properties are repeated load triaxial tests, CBR tests, plate load tests, and unconfined compressive strength tests (Okada and Ghataora 2002). Table 2.3 lists the advantages and disadvantages of these methods.

Table 2.3 Merits and Demerits of the methods of measuring subgrade parameters (Okada and Ghataora 2002)

Test method	Type of result	Advantage	Disadvantage
Repeated load triaxial test	Secant modulus	Resilient modulus and shear strength can be measured	Time consuming
CBR test	CBR value	Widely used in highway pavement design	Closely related to shear stress
Plate load test	Elastic modulus	Related to CBR value	Slow to perform
Unconfined compression test	Compressive strength	Basic test	Measures static properties only

Nondestructive testing is also common in practice. The Falling Weight Deflectometer (FWD) test is generally used to backcalculate pavement moduli from field data, mostly in pavement design. This method has the advantage over other methods that it can be used to assess railway subgrade quickly without excavating the ballast. Most backcalculation procedures use a static pavement model to reproduce the deflection bowl generated from both static and dynamic surface deflection tests (Collop and Cebon, 1996).

In the case of fine-grained soils, an equivalent to in-situ CBR of subgrade can be assessed economically using the Dynamic Cone Penetrometer (DCP) test. In addition the Atterberg limits and particle size distribution (PSD) curves also are obtained. However, QR experiences show that when DCP is used, the resultant CBR that is estimated only represents the value at the tested fill moisture content. QR also uses ground penetration radar (GPR) tests to investigate the in-situ conditions (Foun and Williams 2003).

Laboratory Methods

Triaxial Test

Triaxial testing is the major laboratory testing for granular and subgrade materials. Elastic moduli, resilient moduli and permanent deformation behaviour can be quantified based on appropriate monotonic or repeated load testing data. A procedure for triaxial tests can be found in Australian Standards AS 1289.6.4.1-1998 and AS 1289.6.4.2-1998 for static load and AS 1289.6.8.1-1995 for repeated loads.

In the triaxial test, pneumatic, mechanical or electro-hydraulic repeated loading equipment is used to apply the required loading cycles (Brown et al. 1975). Computer controlled triaxial testing systems and software are also utilised (Menzies 1988). Specimen

deformation over the entire length, or in some cases, a portion of the specimen, is typically measured with either external or internal linear variable displacement transformers (LVDTs). Total, resilient and plastic deformations are typically recorded. Schematic illustrations of static and repeated load triaxial tests are shown in Fig. 2.25.

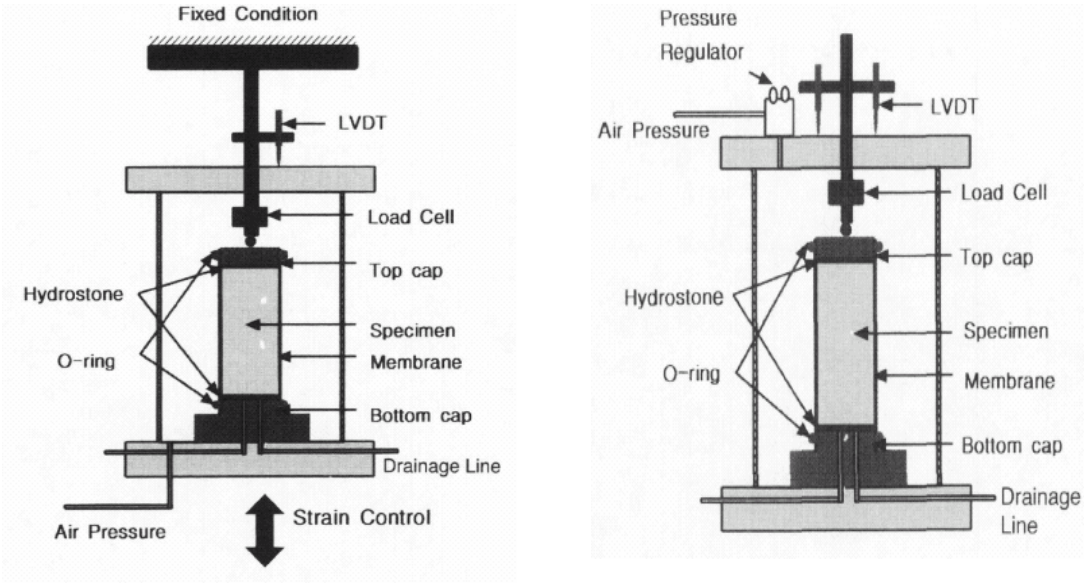

(a) static loading setup (b) cyclic loading setup

Figure 2.25 Schematic diagrams of the triaxial test setup (Kim et al. 2001a)

In drained triaxial tests, pore water is allowed to flow freely into and out of the soil specimen thus dissipating any excess pore pressure. In undrained triaxial tests, pore pressure is allowed to develop but there will be no flow of pore fluid. Fig. 2.26 shows typical stress-strain curves for triaxial compression of clays and sands.

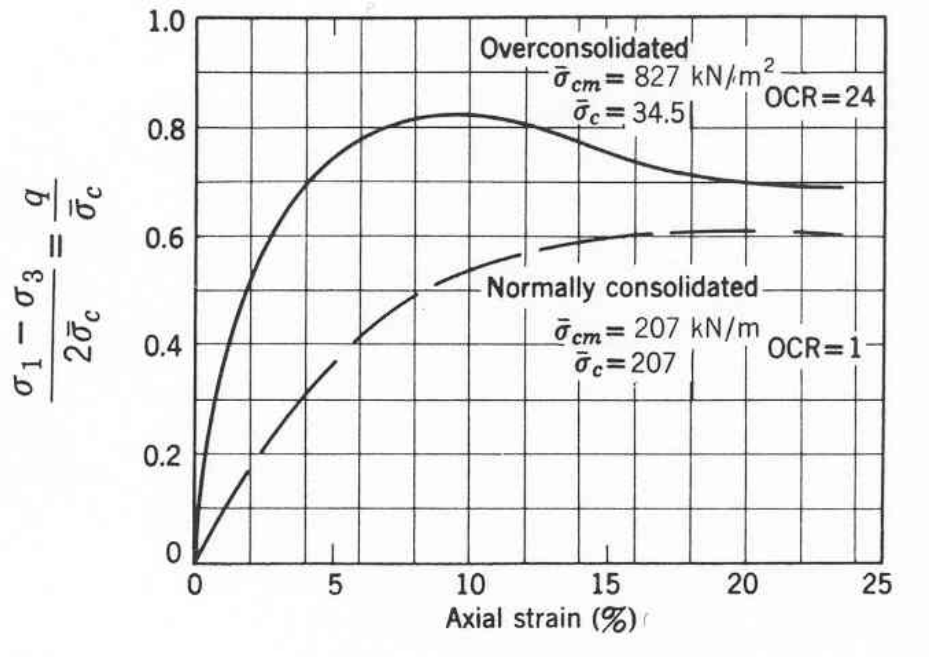

(a) Drained triaxial tests on Weald clay after Henkel, 1956

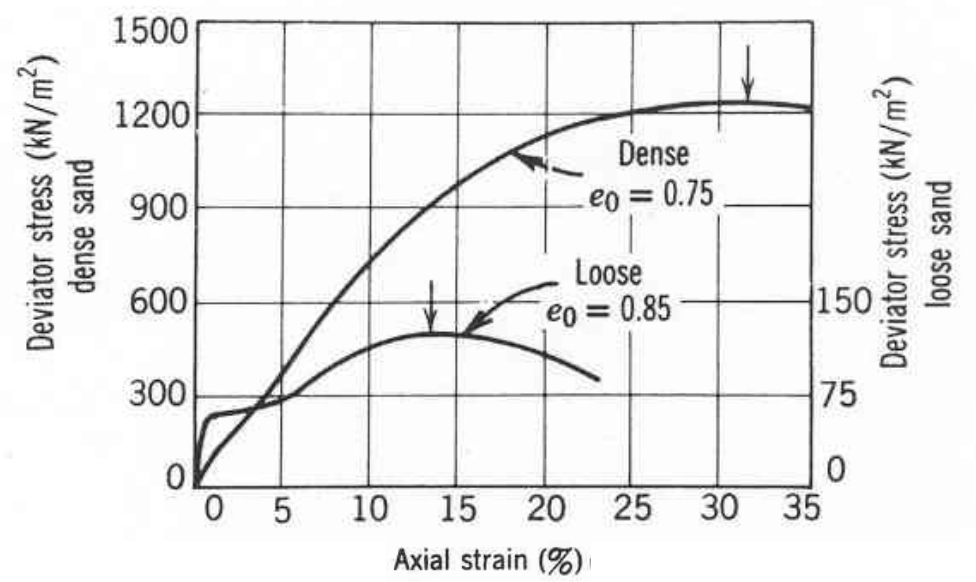

(b) Undrained triaxial tests on a saturated sand after Leonards, 1962

Figure 2.26 Stress-strain curves for clay and sand (Lambe and Whitman 1979)

Lambe and Witman (1979) have mentioned the following factors in their discussions on stress-strain behaviour of soils.

- Undrained strength behaviour of all soils is basically similar to that of clays;

- The effective stress-strain behaviour of granular soil is virtually the same for dry and saturated conditions;
- In granular soils, for normal stresses up to 14MPa the major contribution to the strain development is through the relative movement between adjacent particles and their rearrangement. A major cause of strain occurring above stresses of 14MPa is the crushing of granular particles;
- Dense sand and overconsolidated clays show similar stress-strain characteristics curves. The same similarity is observed in normally consolidated clays and loose sands;
- The stress-strain behaviour of clay is greatly dependent on the stress history of the sample. The higher the overconsolidation ratio, the stiffer the clay.

Field Methods

Dynamic Cone Penetrometer (DCP) Test

This method sets out the procedure for determining the resistance of soil to the penetration of a steel cone of 30 degrees angle and 20 ±0.2mm diameter driven with a 9 kg mass, dropping 510mm (AS 1289.6.3.2—1997). The DCP value is then related to CBR value through a known relationship that will vary for different materials and density. A discussion on various relationships is found in Harison (1989).

One such widely used relationship provided in Eqn. (2.17) is that proposed by Kleyn in 1975.

$$\text{Log } \mathbf{CBR} = 2.62 - 1.27 \log(\text{DCP}) \qquad (2.17)$$

where DCP = penetration mm/blow.

Nondestructive Methods

Falling Weight Deflectometer (FWD) Test

A method to determine the resilient moduli of the various in-situ flexible material layers and the subgrade soil, a nondestructive testing procedure called Falling Weight Deflectometer (FWD), is typically used for pavement evaluation for maintenance scheduling and overlay design. The FWD method measures the deflection basin or bowl (magnitude and curvature) under an impulse load derived from the kinetic energy of a free falling mass to simulate the effect of a moving wheel load. The surface deflection is measured from radially spaced velocity transducers. The moduli of the subgrade or pavement materials are then backcaluculated using these "measured deflection bowls". The principle is used to find a set of moduli to simulate the measured deflection basin through an error-minimisation procedure that locates the optimum solution. If the pavement material and subgrade soils to be encountered on a planned project are similar to those in an existing model then it is possible to utilise the backcalculated moduli in establishing reasonable and representative moduli inputs for a priori mechanistic design.

2.4 Material Models for Soils Subjected to Repeated Loading

2.4.1 Non-cohesive Soils

Models on resilient behaviour

Railway substructure materials characterisation generally includes resilient modulus. The resilient modulus of ballast (unbound granular material), and subgrade (fine grained soil) depends on the state of stresses within the track substructure. Over the years numerous models have been developed, especially in pavement design, which combine applied stress and material properties describing nonlinear stress strain relationships of soils and granular

materials under traffic loading. The following section gives a summary of material models currently available in pavement design, which in turn can be useful in proposing track substructure moduli.

The granular material models can be categorised as linear and nonlinear models. Shackel (1973) has described some of these models evolved based on resilient modulus as early as 1949. Accordingly, the model proposed by Terzaghi and Peck in 1949 is the earliest and the simplest linear stress strain model given by

$$E_t = K\sigma_3 \qquad (2.18)$$

where E_t = tangent modulus of cohesionless soil, K = constant, and σ_3 = confining stress. Shackel (1973) indicates that the model proposed by Biarez in 1962 is the earliest nonlinear model for cyclically stressed granular material given by

$$E_S = K\sigma_3^{\,n} \qquad (2.19)$$

where E_S = secant modulus, σ_3 = confining stress, and K,n = empirical constants.

Hjelmstad and Taciroglu (2000) indicate that the K-θ model of Hicks and Monismith (1971) has been a very popular material model since the late 1970's due to its simplicity. This model suggests that the resilient modulus is proportional to the mean compressive stress raised to a fractional power given by

$$M_R = K\theta^n \qquad (2.20)$$

where M_R = resilient modulus, $\theta = (\sigma_1 + \sigma_2 + \sigma_3)/3$ is the mean compressive stress (hydrostatic stress) acting on a sample in a triaxial test and K, n = empirical constants. σ_1, σ_2 and σ_3 are the major and minor principal stresses as defined in Figure 2.22. In a triaxial test the minor stresses, $\sigma_2 = \sigma_3$.

Hjelmstad and Taciroglu further indicated that Uzan (1985) has observed that the *K-θ* model did not comply with measured triaxial data and proposed a three-parameter model of the form

$$M_R = K\theta^n \sigma_d{}^m \qquad (2.21)$$

where $\sigma_d = (\sigma_1 - \sigma_3)$ and *K, n, m* = empirical constants..

In 1988, Witczak and Uzan generalized the model by Uzan (1985). They observed that σ_d coincides with the octahedral shear stress. The octahedral normal and shear stresses provide a better explanation for the stress state of a material in which normal and shear stress change during loading. This relationship is given in the following mathematical formulation

$$M_R(\theta, \tau) = K\theta^n \tau^m \qquad (2.22)$$

where θ, τ = octahedral normal and shear stress respectively, and *n ,m* = modal constants.

Thompson et. al. (1998) have carried out a comprehensive literature survey on granular material and soil moduli. Other than the above, several other modified models can be found in Thompson et. al. (1998) as follows.

Another approach adopted in predicting the resilient modulus of granular material is based on establishing a relationship to its volumetric and deviator strains (Thompson et al. 1998). The *K-G* model by Boyce (1980) described below is one such model.

Boyce (1980) model gives volumetric and deviator strains in the following forms

$$\varepsilon_V = \left(\frac{1}{K_i}\right) p^{\mu}\left[1-\beta\left(\frac{q}{p}\right)^2\right] \qquad (2.23)$$

$$\varepsilon_q = \left(\frac{1}{3G_i}\right) p^{\mu}\left(\frac{q}{p}\right) \qquad (2.24)$$

where K_i and G_i = initial values of bulk and shear moduli respectively, μ = constant less than 1, $\beta = (1-\mu)K_i/(6\ G_i)$, q = deviator stress and p = mean normal stress.

Statistical correlation between M_R and engineering index properties such as plasticity index, shrinkage index, etc. are useful in practice as basic engineering properties are easy and inexpensive to evaluate. However, the M_R values of granular material are neither related to the plasticity index nor to the conventional classification system. Some factors influencing M_R of granular materials are magnitude of the repeated stress state, gradation and moisture content, cohesion, friction angle, and static material strength properties (Tian et al. 1998).

Thompson et. al. (1998) after a thorough examination of their literature survey have concluded the following on granular material models:

- K-θ model is very simple but neglects the shear stress effect;
- Uzan model and its modifications consider both confining pressure and deviator stress effect; these models are shear stress related, and best for routine use giving reasonable results;
- Volumetric and shear strain related models are fundamentally sound yet complicated and more well suited for theory-related research than routine design use; and

- For a practical, accurate approach at least Uzan or one of its modifications should be employed in designs when characterizing granular material behaviour.

Models on plastic behaviour

The gradual accumulation of large numbers of small plastic deformations could lead either to failure or to stabilisation of a rail/pavement structure leading it to a fully resilient response. Insufficient research has been done to define reliable relationships between stress and plastic strain accumulation under repeated loading.

A comprehensive study on the permanent deformations of unbound granular material can be found in Lekarp and Dawson (1997, 1998) and Lekarp et. al. (2000). The modelling of permanent strain is done either considering the number of load applications or the stress conditions. The following summarises their findings:

- Barksdale (1972) has performed repeated load triaxial tests on different base course material with 10^5 load applications and suggested that the total permanent axial strain $(\varepsilon_{1,p})$ can be expressed by

$$\varepsilon_{1,p} = a + b\log(N) \qquad (2.25)$$

where N = number of load cycles, and a and b = constants for a given level of deviator stress and confining pressure.

- Sweere (1990) has observed that the above log-normal approach did not fit his results after 10^6 cycles and suggested a log-log approach given by

$$\varepsilon_{1,p} = aN^b \qquad (2.26)$$

where a and b are regression parameters.

- Wolff and Visser (1994) further investigated this log-log model for several million load applications and suggested

$$\varepsilon_{1,p} = (c\,N + a)\left(1 - e^{-bN}\right) \qquad (2.27)$$

where a, b and c are regression parameters.

- Paute et. al. (1993) have suggested a new approach to express the influence of number of load applications on the permanent deformations given by

$$\varepsilon^{*}_{1,p} = A\left(1 - \left(\frac{N}{100}\right)^{-B}\right) \qquad (2.28)$$

where $\varepsilon^{*}_{1,p}$ is the permanent strain after first 100 cycles, A and B are regression parameters.

- Lekarp and Dawson (1998) have suggested a relationship considering the maximum shear – normal stress ratio $(q/p)_{max}$, and the length of the stress path in p-q space applied to reach this maximum value given by

$$\frac{\varepsilon_{1,p}\left(N_{ref}\right)}{L / p_0} = a\left(\frac{q}{p}\right)^{b}_{\max} \qquad (2.29)$$

where $\varepsilon_{1,p}\left(N_{ref}\right)$ is the accumulated permanent axial strain after N_{ref} number of cycles, N_{ref} is any given number of load cycles greater than 100, L is the length of the stress path, a and b are regression parameters and p_0 is a reference stress introduced to ensure non-dimensionality of the equation.

Another approach found in pavement literature is the "shakedown theory" (Boulbibane et al. 2000; Collins and Boulbibane 2000; Raad et al. 1989; Sharp and Booker 1984). Shakedown is defined as the process of adaptation to the resilient (elastic) deformations after a certain number of cycles which stabilised permanent strains. If plastic deformations

do not stabilise, then some form of failure will occur. Lekarp and Dawson (1998) stated that the complex numerical models suggested in the literature treat this response of the whole pavement as a single unified structure. Lekarp and Dawson (2000) further state that the model predictions from Eq. (2.29) showed close similarities to the concept of shakedown theory.

2.4.2 Cohesive Soils

Models on resilient behaviour

Li and Selig (1994) categorise factors influencing magnitude of resilient modulus as:

- loading condition or stress state – magnitude of deviator stress and confining pressure, and the load cycles and their sequence;
- soil type and structure – depends on compaction method and compactive effort of a new subgrade; and
- soil physical state – moisture content and dry density which is subject to environmental changes.

Confining pressure was found to have less significant effect on resilient modulus than deviator stress for fine grained subgrade soils.

According to Thompston *et. al*. (1998) empirical models can be found related to soil strength such as the CBR value, and the following models are commonly used.

Model by Heukelom and Klomp, 1962;

$$M_R \text{ (MPa)} = 10 \text{ CBR} \qquad (2.30)$$

and the model by Lister and Powell, 1987.

$$M_R \text{ (MPa)} = 17.6 \text{ (CBR)}^{0.64} \qquad (2.31)$$

Typically, the cohesive soil materials are found to display a decrease in moduli with increasing amplitude of cyclic load, or increasing deviator stress as shown in Fig. 2.27. The nonlinear behaviour was defined in terms of the break point modulus and deviator stress as indicated in Fig. 2.27 and the intersection point was identified (σ_{Di}, E_{Ri}). The response, E_{Ri} was used in defining the subgrade properties and design algorithms (Drumm et al. 1990). These bilinear models are of the form given by

$$M_R = K_2 + K_3 (K_1 - \sigma_d) \quad \text{for } \sigma_d < K_1 \qquad (2.32a)$$

$$M_R = K_2 + K_4 (\sigma_d - K_1) \quad \text{for } \sigma_d > K_1 \qquad (2.32b)$$

where σ_d = deviator stress and K_1, K_2, K_3 and K_4 = modal parameters.

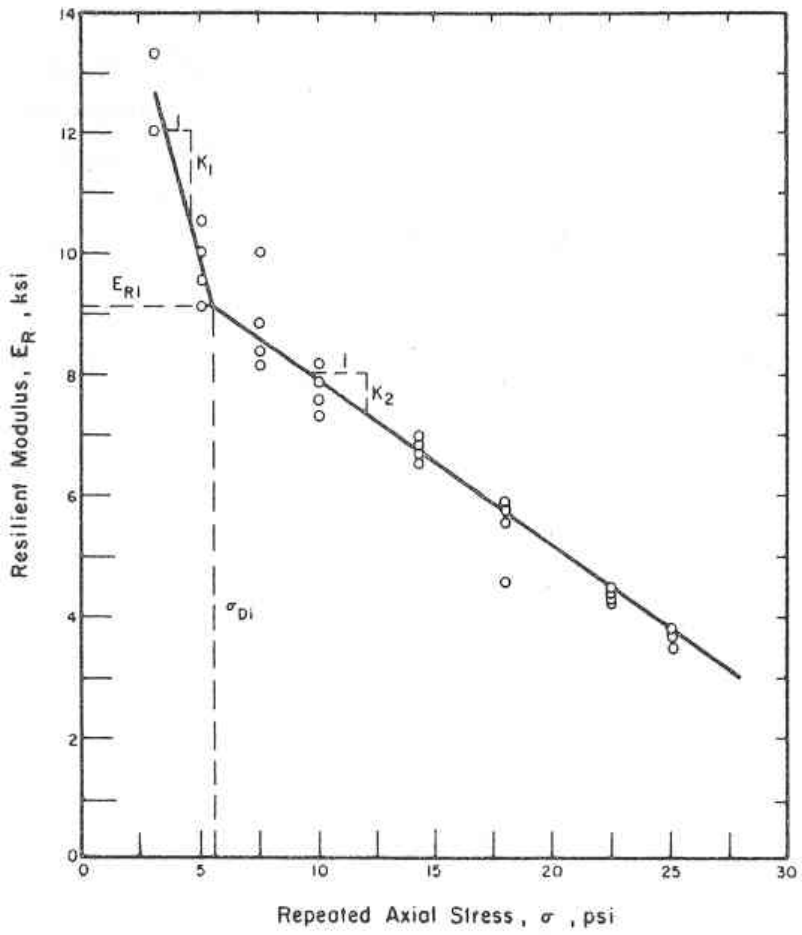

Figure 2.27. Typical variation in resilient modulus with deviator stress (Thompson and Robnett 1979)

Nonlinear models also are found in literature (Drumm et al. 1990; Li and Selig 1994; Thompson et al. 1998). These models are of the form

$$M_R = k\sigma_d^{\ n} \qquad (2.33)$$

where σ_d = deviator stress and k, n = modal parameters.

Drumm *et. al*. (1990) proposed a hyperbolic model. This relationship was arrived at by using the resilient response E_{Ri} proposed by Thompson and Robnett (1979) and correlating it to initial tangent modulus, unconfined compressive strength, plasticity index, dry unit weight, degree of saturation, and the percent passing #200 sieve. The model was given by

$$M_R = \frac{a + b\sigma_d}{\sigma_d} \qquad (2.34)$$

where σ_d = deviator stress and a, b = modal parameters.

Li and Selig (1994) summarised that bilinear, power, semilog, and hyperbolic models were able to fit the relationship between the resilient modulus and stress state for the soil tested by the respective researchers. They found that the best representations could be given in the order of bilinear, power, semilog and hyperbolic.

It was demonstrated in several studies that many factors influence the resilient behaviour of soils, plasticity index, moisture content, CBR value etc. (Drumm et al. 1997; Lee et al. 1997; Li and Selig 1994; Muhanna et al. 1999; Tian et al. 1998). The moisture sensitivity is one of the main factors addressed by the researchers. Li and Selig (1994) provide one such model considering moisture content and dry density

$$M_R = R_{m1} M_{R(opt)} \qquad (2.35)$$

where $R_{m1} = f_1(w - w_{opt})$, M_R = resilient modulus at moisture content w, and $M_{R(opt)}$ = resilient modulus at optimum moisture content w_{opt}.

Models on plastic behaviour

Three mechanisms are mainly responsible for the cumulative plastic deformation of fine grained soils. They are:

- Cumulative plastic shear strain;
- Cumulative consolidation; and
- Cumulative compaction.

The critical level of repeated deviator stress (often called the dynamic strength of soil) is defined as the stress above which the soil plastic deformation increases rapidly with cyclic loading. The dynamic strength of soil is usually smaller than the soil static strength determined under monotonic loading (Li and Selig 1996).

Puppala et. al. (1999) discussed a few of the models available in pavement literature for plastic strains in subsoils . They are:

- Lentz and Baladi (1981) model estimating the accumulated permanent strains (ε_p) of sandy soils which is similar to Equation (2.25) by Barksdale (1972)

  $$\varepsilon_p = a + b \ln N \qquad (2.36)$$

  where *a* and *b* are regression constants and N is the number of load repetitions.

- Thompson and Neumann (1993) have used a logarithmic permanent strain and a logarithmic load repetitions model expressed as:

  $$\log \varepsilon_p = a + b \log N \qquad (2.37)$$

  where a and b are modal constants. The term *a* varies and depends on the soil stress levels. The term *b* varies between 0.12 and 0.20 for the cohesive and granular soils respectively.

- Ullditz (1993) has developed the following plastic strain formulation recognising the limitations in earlier models:

$$\varepsilon_p = AN^{\alpha}\left[\frac{\sigma_z}{\sigma}\right]^{\beta} \qquad (2.38)$$

where σ_z = vertical effective stress, σ = reference stress that is equal to atmospheric pressure and A, α, β = constants.

- Puppala et. al . (1999) have modified the above model to accommodate the influence in confining pressure given by:

$$\varepsilon_p = AN^{\alpha}\left[\frac{\sigma_{oct}}{\sigma_{atm}}\right]^{\beta} \qquad (2.39)$$

where σ_{atm} = reference stress (atmospheric pressure of 100 kPa) and

$$\sigma_{oct} = \frac{\sigma_1 + \sigma_2 + \sigma_3}{3}$$

Li and Selig (1996) stated that the most common method used is the power model given by

$$\varepsilon_p = AN^b \qquad (2.40)$$

where A and b are parameters depending on soil type, soil properties and stress state.

To relate plastic deformations of cohesive soils in railway subgrades, Li and Selig (1998a) have suggested the following expressions:

$$\varepsilon_p = A\left(\frac{\sigma_d}{\sigma_s}\right)^m N^b \qquad (2.41a)$$

$$\rho = \int_0^T \varepsilon_p \qquad (2.41b)$$

where σ_d = soil deviator stress caused by train axle loads, σ_s = soil compressive strength, a,m,b =parameters depending on soil type, ρ = cumulative soil plastic deformation and

T = subgrade layer depth. Their design approach was to limit plastic strain and deformations for the design period.

2.4.3 Typical Subgrade Layer Materials

Subgrade materials also exhibit behaviour similar to other elasto-plastic materials where a yield locus could be defined. Beyond the yield locus significant plastic strains occur and within the locus plastic strains are relatively smaller and recoverable. Traditionally, in engineering practice, simplified and empirical approaches are adopted. Fig. 2.28 illustrates the behaviour of real soil showing complex hardening and softening behaviour.

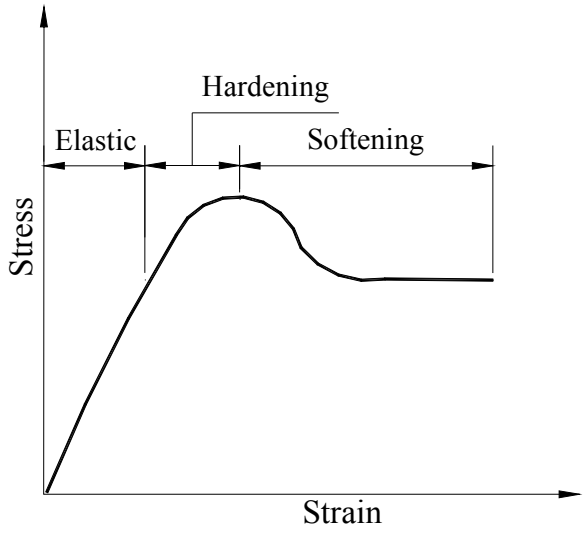

Figure 2.28. Real soil behaviour involving hardening and softening

There does not exist a single constitutive model which can describe the complex soil behaviour fully. The existing models have their own strengths and weaknesses according to the assumptions made to predict the behaviour of soils. The following briefly describes some of the constitutive models used in geotechnical designs. These models can be categorised as elastic and elasto-plastic models.

2.4.3.1 Elastic Models

The characteristic of an elastic model is that the direction of principal incremental stress and incremental strain coincides. These can be either linear or nonlinear models. The advantage of the elastic model is its simplicity. If one decides to explore beyond elasticity more complex numerical solutions on a computer are required.

Linear elastic model

Linear elastic model is based on Hooke's law. The loading and unloading moduli are kept the same in this model. There are four material parameters for an elastic model, elastic modulus (E), Poisson's ratio (ν), bulk modulus (K), and shear modulus (G) of which only two are independent.

K and G are specified as $K = E/3(1-2\nu)$ and $G = E/2(1+\nu)$.

Bilinear model

This model assumes that bulk and shear stiffness are constant until the stress state reaches the failure condition. The model requires two parameters to define pre-failure elastic behaviour and additional parameters to define failure surface. The pre-failure parameters required are either (E, ν) or (K, G). To define the failure surface parameters, for example, if the Mohr-Coulomb failure criterion is used, angle of friction (ϕ) and cohesion (c) are needed (Potts and Zdravkovic 1999).

Hyperbolic model

The hyperbolic model is defined by the following equation assuming a Poisson's ratio of 0.5

$$\sigma_d = (\sigma_1 - \sigma_3) = \frac{\varepsilon}{a + b\varepsilon} \qquad (2.42)$$

where σ_1 and σ_3 are the major and minor principal stresses, ε the axial strain and a and b are material constants as defined in Fig. 2.29.

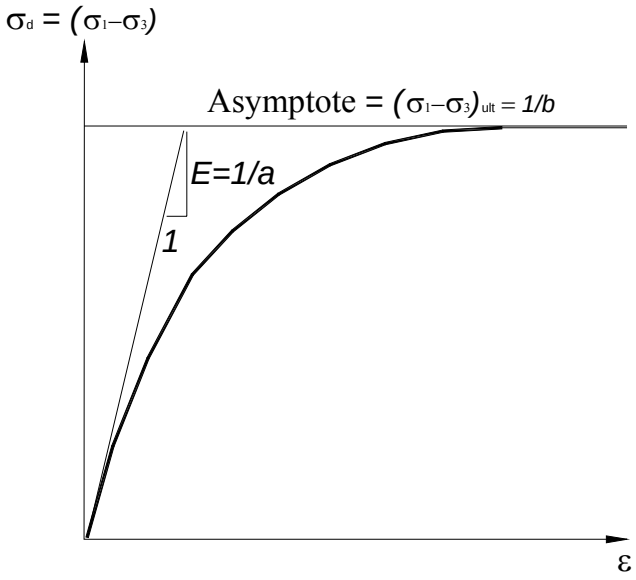

Figure 2.29 Hyperbolic stress-strain curve

2.4.3.2 Elasto-plastic Models

The elasto-plastic models assume that the material behaves in a linear elastic manner prior to yielding. The material behaviour after yielding can be defined as perfectly plastic, or strain hardening or strain softening plasticity. The fundamental difference between the behaviour of elastic and plastic models is that, in elastic behaviour the strain increments are proportional to stress increments (or linear), whereas in plastic behaviour strain increments are a function of the current stress state.

Some definitions associated with elasto-plastic models are given below.

Invariants

The six components for the stress vector (i.e., $\sigma_x, \sigma_y, \sigma_z, \tau_{xy}, \tau_{xz}, \tau_{yz}$) depend on the direction of coordinate axes selected. The principal stresses, generally denoted as $\sigma_1, \sigma_2,$ and σ_3, are invariant to the choice of axes. Therefore it is customary to use alternative invariants quantities in geotechnical designs. Some of the main invariants used as a combination of principal effective stresses are given below (Potts and Zdravkovic 1999).

Mean effective stress: $p' = \dfrac{(\sigma_1' + \sigma_2' + \sigma_3')}{3}$

Deviatoric stress: $J = \dfrac{1}{\sqrt{6}} \sqrt{(\sigma_1' - \sigma_2')^2 + (\sigma_2' - \sigma_3')^2 + (\sigma_3' - \sigma_1')^2}$

Lode's angle: $\theta = \tan^{-1}\left[\dfrac{1}{\sqrt{3}} \left(2\dfrac{(\sigma_2' - \sigma_3')}{(\sigma_1' - \sigma_3')} - 1 \right) \right]$

Flow rules

Plastic deformation depends on the stress state at which yielding of the soil occurs rather than on the route by which that stress state is reached. Yielding is associated with some plastic irrecoverable volumetric strain and some plastic shear strain. The relationship between plastic strain ratio and stress ratio is known as the flow rule governing the mechanism of plastic deformation or flow of the soil. If plastic potential and yield functions of a soil are assumed to be the same, the flow rule is said to be associated. When they differ, the flow rule is said to be non-associated. While there are many models describing plastic flow of materials, only a few models relevant to soils are described further.

Mohr-Coulomb model

The Mohr-Coulomb model is an elastic and perfectly plastic model with associated and non-associated flow rules. A hexagonal pyramid graphically illustrates this model and defines the yield surface (Fig. 2.30). Deformation prior to yielding is assumed to be linear elastic governed by the elastic parameters E and ν.

Yield function for the Mohr-Coulomb model in terms of stress invariants p', J and θ is given by:

$$f = J - \left(\frac{c'}{\tan \phi'} + p' \right) g(\theta) = 0 \qquad (2.43)$$

where $g(\theta) = \dfrac{\sin \phi'}{\cos \theta + \dfrac{\sin \theta \sin \phi'}{\sqrt{3}}}$, c' = cohesion, and ϕ' = angle of shearing resistance.

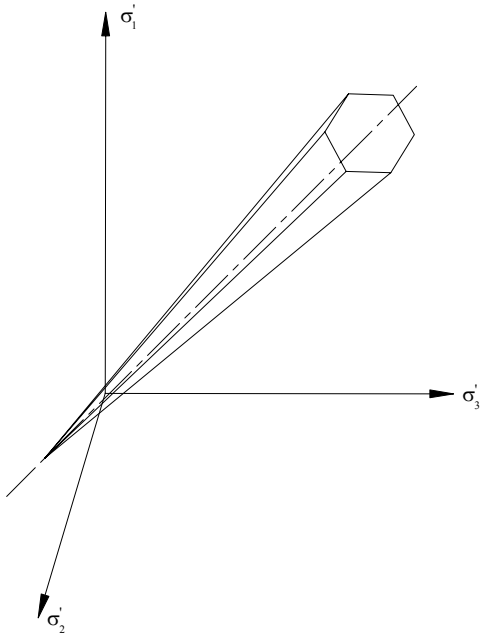

Figure 2.30 Mohr-Coulomb criterion

Drucker-Prager model

The Drucker-Prager model is an elasto-plastic model based on associated and non-associated flow rules. The yield surface is simplified to a cone in this model (Fig. 2.31).

Yield function for the Drucker-Prager model in terms of stress invariants p', J and θ is given by:

$$f = J - \left(\frac{c'}{\tan \phi'} + p' \right) M_{JP} = 0 \qquad (2.44)$$

where M_{JP} = constant independent of θ, c' = cohesion, and ϕ' = angle of shearing resistance.

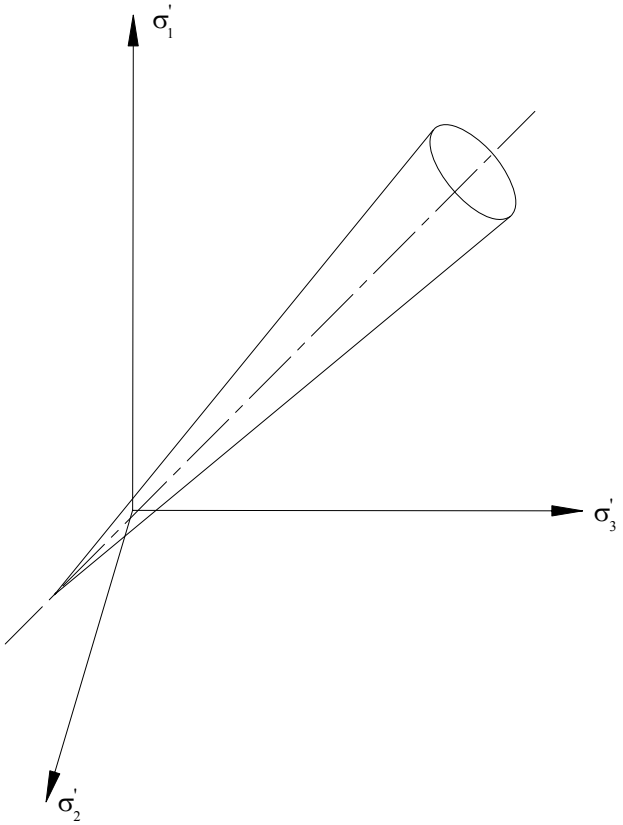

Figure 2.31 Drucker-Prager criterion

Critical state models

There are two critical state models, the modified cam clay model and the double yield surface model. The first is a time dependent model and the latter can be used as a time dependent or time independent model.

Modified cam clay model

The modified cam clay model is an elasto-plastic model with nonlinear elasticity prior to yielding. Elastic deformation is governed by bulk modulus and Poisson's ratio. The bulk modulus is related to the slope of the recompression line given by:

$$K = \frac{(1+e)p'}{\kappa} \qquad (2.45)$$

where e = current void ratio of the material and κ = slope of the recompression line in the plot of void ratio versus natural logarithm of p'.

The plastic deformation is defined by the yield function

$$f = \left(\frac{J}{p'M_J}\right)^2 - \left(\frac{p_0'}{p'} - 1\right) = 0 \qquad (2.46)$$

M_J = critical state parameter, and p'_0 = current isotropic consolidation stress.

Double yield surface model

This model employs the concept of double-yield criteria, which assumes that two yield surfaces are acting simultaneously. The total strain is decomposed into elastic (ε^e) and plastic (ε^p) components as in other models. In addition, the plastic component is subdivided into plastic strains associated with the two yield criteria given by:

$$\Delta\varepsilon = \Delta\varepsilon^e + \Delta\varepsilon^{p1} + \Delta\varepsilon^{p2} \qquad (2.47)$$

The elastic component is divided into time independent and time dependent components. Usually the time dependent component is related to creep and divided into distinct

interdependent volumetric and deviatoric components. The parameters for the model can be determined from triaxial and creep tests.

Constitutive models explore anything beyond elasticity and provide a rationale for the hardening and softening effects undergone by the subgrade material. These models are successfully adopted in a variety of commercially available computer programs.

2.5 Modelling of Railway Substructure

In the past, railway track substructure designs were based on empirical rules or on the beam on elastic foundation theory. With the availability of advanced computational power it is now possible to use advanced techniques such as the finite element methods. The following provides a brief overview of the existing methods.

2.5.1 Conventional Models

Simple elastic theory has been used to predict the mean maximum vertical stress in the subgrade with reasonable accuracy. The safe average bearing pressure (σ_{safe}) is defined as the ultimate subgrade bearing capacity (σ_{ult}) reduced by a factor of safety (x_L) $\leq$1.0. In designs this is used when the effect of settlement is considered negligible and the safety factor takes into account the plastic shear failure of the subgrade.

$$\sigma_{safe} = x_L \sigma_{ult} \qquad (2.48)$$

The most conservative estimate of bearing pressure is the allowable bearing pressure (σ_{des}), which takes into account both the settlement and shear failure. A settlement safety factor (x_s) $\leq$ 1.0 is introduced further reducing the safe bearing pressure.

$$\sigma_{des} = x_s \sigma_{safe} = x_s x_L \sigma_{ult} \quad (2.49)$$

The design limits for the subgrade pressure determined by these methods are based on various static testing methods applied to saturated subgrades representing the worst possible subgrade condition. Jeffs and Tew (1991) further discuss the safety factors, indicating that Clarke (1957) has recommended that the settlement factor (x_s) be equal to 0.60. As a general rule, the maximum bearing pressure should not exceed about 83kPa for un-compacted formations and about 139kPa for compacted formations (Jeffs and Tew 1991). The 0.60 reduction factor is based on the AREA data, which accounts for the variability in sleeper support and track maintenance. Jeffs and Tew (1991) indicate that the AREA (1973) has recommended the calculations of allowable subgrade pressure be based on laboratory tests of saturated and remoulded samples (static triaxial tests).

To estimate the bearing pressure, the design (dynamic) wheel load should be doubled and the estimate be compared with the determined safe bearing pressure resulting in an equivalent settlement factor of 0.5. Table 2.4 illustrates the calculation of the design limit for subgrade pressure using both Clark and AREA settlement factors.

Table 2.4 Design limit bearing pressures of subgrades (Jeffs and Tew 1991)

Subgrade description	Average bearing	Design limit bearing pressure σ_{des} (kPa)

	pressure σ_{safe} (kPa)	Clark (1957) $x_s = 0.6$	AREA (1973) $x_s = 0.5$
Alluvial soil	< 70	< 42	< 35
Prepared ground not compacted	75-105	45-63	37-52
Soft clay, wet or loose sand	110-140	66-84	55-70
Dry clay, firm sand, sandy clay	145-210	87-126	72-105
Dry gravel soils	215-275	129-165	108-137
Compacted soils	> 280	> 165	> 140

Typical safe bearing capacities for compacted static loading of compacted subgrades have been well established in terms of a variety of testing techniques correlating the bearing capacity. The CBR test is considered as an adequate measure of safe bearing pressure of the subgrades.

The British Rail formation design method

British Rail has developed a "threshold stress" design method, limiting the stress on subgrade soils to protect against subgrade failure by excessive plastic deformation (Heath et al. 1972). The threshold stress was determined from repeated load tests on samples of London clay. The cumulative strain was measured as a function of loading cycles applied. Fig. 2.32 shows these results. The results have formed two distinct groups, one in which the deformation is progressive until complete failure and the other where the rate of deformation reduces to a stable condition.

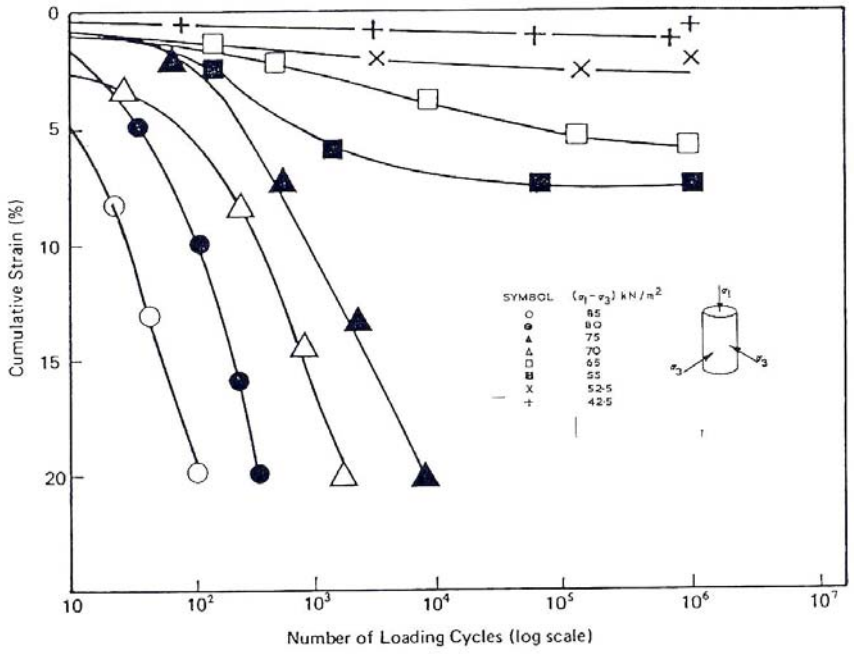

Figure 2.32 Cumulative strain resulting from repeated load tests of London clay (Heath et al. 1972)

Fig. 2.33 shows the modified strain-cycle (SN) relationships derived from repeated load tests on London clay. Here the failure number of cycles is defined at 10% cumulative strain, which is considered as a convenient limit failure (Heath et al. 1972). On this basis a limiting repeated elastic strain has been defined above which the deformation is continuous and below which it is terminating.

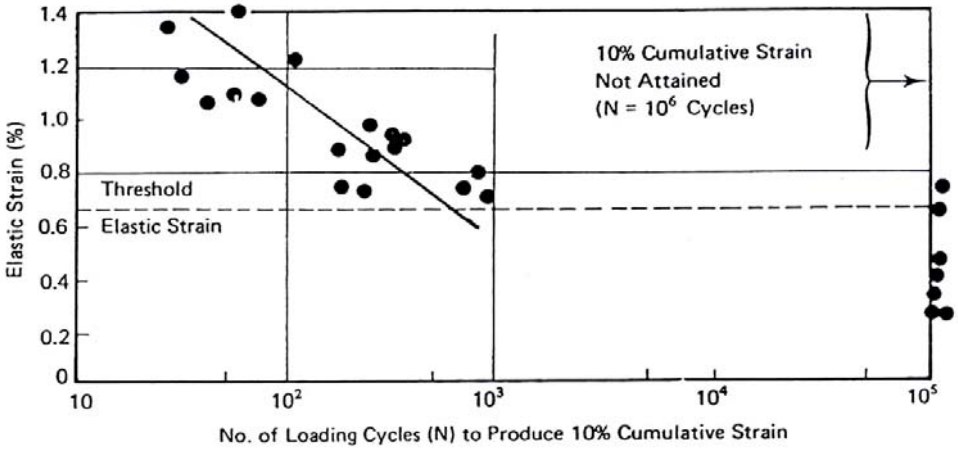

Figure 2.33 Modified SN curve (Heath et al. 1972)

Based on this definition, concept design charts have been developed by British Rail for selecting granular layer thickness for various subgrade soil conditions and axle loads (Fig. 2.34). The threshold stress/depth relationship is also superimposed on these curves, making it possible to determine the ballast depth required for a particular axle load induced threshold value. For example if an axle load of 79kN with a stress threshold of 60kPa is considered, then the required ballast depth would be about 425mm according to the chart. The limitations in applying this method are discussed by Raymond (1978) and Li and Selig (1998a,b). A summary of limitations is:

- Lumping of ballast, sub-ballast and subgrade as a single homogeneous layer neglects much higher stiffness of the top granular layer;
- The design often leads to a conservative granular layer thickness because of calculated stress levels in subgrade;
- This method uses a single value of axle load without considering cumulative tonnage i.e., the granular layer thickness will be the same for 10 million gross tons (MGT) or 100 MGT for the same maximum axle load; and
- The method is developed for clay and if used for gravel, sand, and low compressibility subgrades, the required granular depth is overestimated.

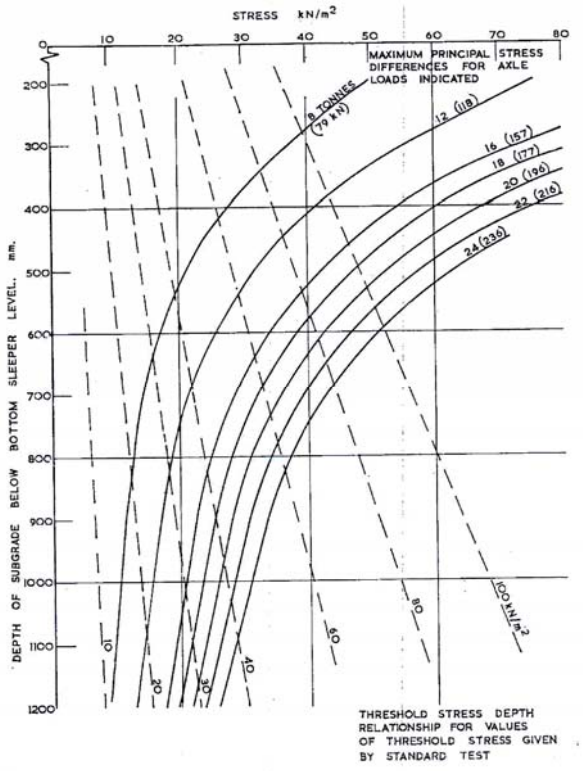

Figure 2.34 Relationship between induced stresses and soil strength (Heath et al. 1972)

German Railways empirical method

German Railways (DB) uses an empirical formula developed by Heukolom and Klomp in formation design. The permissible compressive stress σ_z on the formation related to number of loading cycles is given by:

$$\sigma_z = \frac{0.006E_{v2}}{1+0.7\log n} \qquad (2.50)$$

where E_{v2} = modulus of elasticity taken from the second load step in a plate load testing and n = number of load cycles.

Table 2.5 provides the permissible stresses according to Eq. (2.50) for two million cycles. The table also indicates the order of magnitude of the foundation modulus C when using a 300mm deep ballast bed with E=150MPa.

Table 2.5 Permissible stresses on formations (Esveld 2001)

Classification	E_{v2} (MPa)	C (N/mm^3)	σ_z (MPa) n=2x10^6
Poor	10	0.03	0.011
	20	0.04	0.022
Moderate	50	0.07	0.055
Good	80	0.09	0.089
	100	0.11	0.111

For the above formulation the DB standard demands an E_{v2} modulus of at least 120MPa just beneath the ballast bed. If the measured value from a plate load test does not comply with 120MPa, an intermediate layer is introduced. This intermediate layer in DB is a sub-ballast layer whose depth is determined according to Figure 2.35.

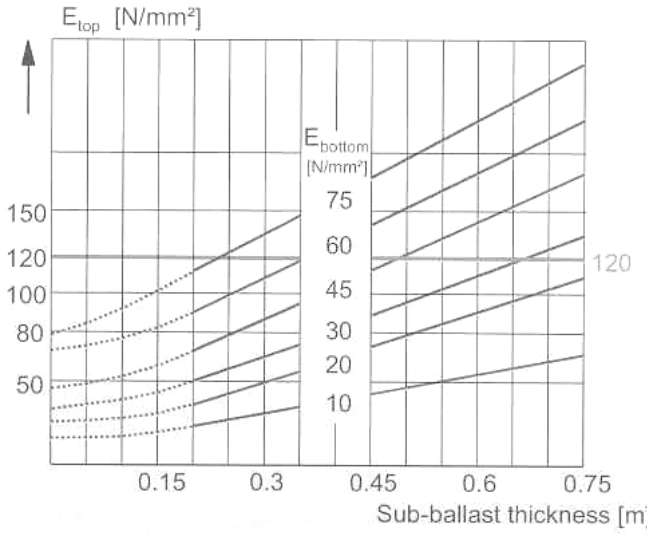

Figure 2.35 Thickness of sub-ballast layer according to DB (Esveld 2001)

According to this chart, if E_{top} = 100MPa & E_{bottom} = 60MPa, a sub-ballast depth of 0.25m is required. If E_{bottom} drops to 20MPa, the required sub-ballast depth is increased to 0.67m.

Beam on elastic foundation model

The beam on elastic foundation is based on the assumption that each rail acts like a continuous beam on an elastic support. The track foundation modulus, u is defined as the

supporting force per unit length of rail per unit vertical deflection of the rail as shown in Fig. 2.36.

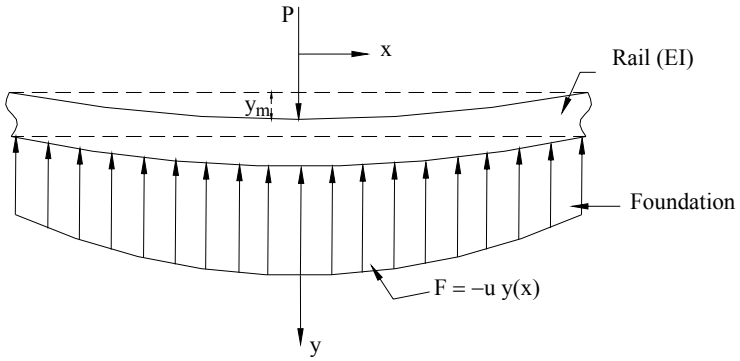

Figure 2.36 Beam on elastic foundation model (Selig and Waters 2000)

The rail foundation represents by u, includes the effect of fastener, sleeper, ballast, sub-ballast and subgrade. The track modulus cannot be calculated from the properties of each of these components and therefore the model is incapable of considering their individual effects. The differential equation of this model is given by:

$$EI\frac{d^4y}{dx^4} + uy = 0 \qquad (2.51)$$

where E = rail modulus of elasticity, I = rail moment of inertia, u = track foundation modulus x = any distance, x along the rail from the single point load P and y = rail deflection.

2.5.2 Numerical Models

As discussed previously, the conventional approaches disregard the effect of the constitutive material models on the behaviour of the track systems. It is advisable not to extrapolate the conventional models unless there is a sound basis on the fundamental approach to the problem. With the advent of numerical models, the analysis procedures have become more effective and reliable, incorporating complexities in geometry,

boundary conditions and material properties, but limited with the computer time and cost required.

The principles and concepts of numerical modelling methods can be found in many references, including Desai and Abel (1972), Smith and Griffiths (1988), Zienkiewicz and Taylor (2002) and an extensive list of references can be found in Desai and Siriwardane (1982). Dahlberg (2001) has summarised the mathematical models currently available in the literature, emphasising that track settlement is mostly considered as a function of loading cycles and/or function of the magnitude of the loading, but very little has been found in the literature on the material properties of track substructure. Following is a brief review of some of the existing numerical models.

Models on mechanical behaviour

The finite element models that consider mechanical behaviour of track and trackbed structure are discussed in this section. These models utilise failure criteria that consider the effects of static/repeated loading and material properties (modulus of elasticity, resilient modulus), but not the dynamic properties (dynamic shear modulus and damping).

Svec and Raymond (1976) developed a three-dimensional finite element model (CIGGT3D), which characterises the behaviour of ballast material stress path and its lack of ability to sustain tension, validated with full-scale model laboratory tests. The study thus concentrates on the effect of the sleeper and sleeper spacing on the contact pressure. Tayabji and Marshall (1977) presented a finite element structural model of conventional railway track support system (CRTSS). Here the finite element analysis was carried out in two stages, viz., a longitudinal analysis followed by a transverse analysis. The pseudo

plane strain technique was used in the analysis. Material non-linearity was accounted for by using the resilient modulus, and the load transfer was defined by two empirical parameters of sleeper-bearing length and angle of distribution.

Adegoke et. al. (1979) have studied three analytical models – MULTA, PSA, and ILLI-TRACK and evaluated their performance by comparing their predicted results with field measurements. The following is a brief description of each model.

MULTA - combines Burmister's three-dimensional elasticity solution with a structural analysis model that solves for the sleeper-ballast reaction. This model is restricted to homogeneous layers of linear elastic ballast and subgrade materials.

PSA – a finite element three-dimensional model with prismatic elements combined with a structural analysis model, which has the ability to incorporate property variations in both longitudinal and transverse directions. It is an expensive model compared to MULTA and ILLI-TRACK.

ILLI-TRACK – same model defined in CRTSS by Tayabji and Marshall (1977). The model has the ability to change material properties in the vertical, longitudinal and transverse direction. The limitations are the pseudo- three-dimensional assumption and the assumed model parameters, effective sleeper bearing length and angle of distortion. However it is the most cost effective method when considering computer cost and input-data preparation.

The three models were compared by Adegoke et. al. (1979) using constant moduli and Poisson's ratios. Figs. 2.37 and 2.38 show comparisons of the vertical pressure and displacement distribution under a single axle load. The results illustrate existence of some differences arising from the assumptions made in the distribution of load under the sleeper. This is reflected in the results of displacement as shown in Figure 2.38. However both MULTA and PSA models predict results of almost the same order while ILLI-TRACK predicts values in the order of 100 percent higher.

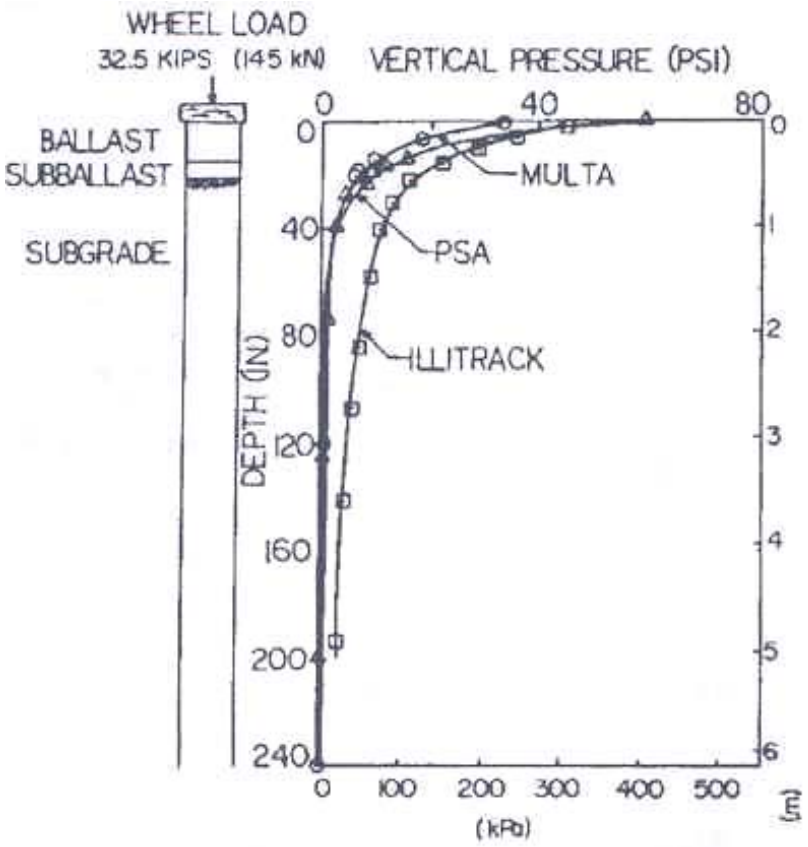

Figure 2.37 Comparison of distribution of vertical pressure with depth under single axle load: MULTA, PSA, and ILLI-TRACK (Adegoke et al. 1979)

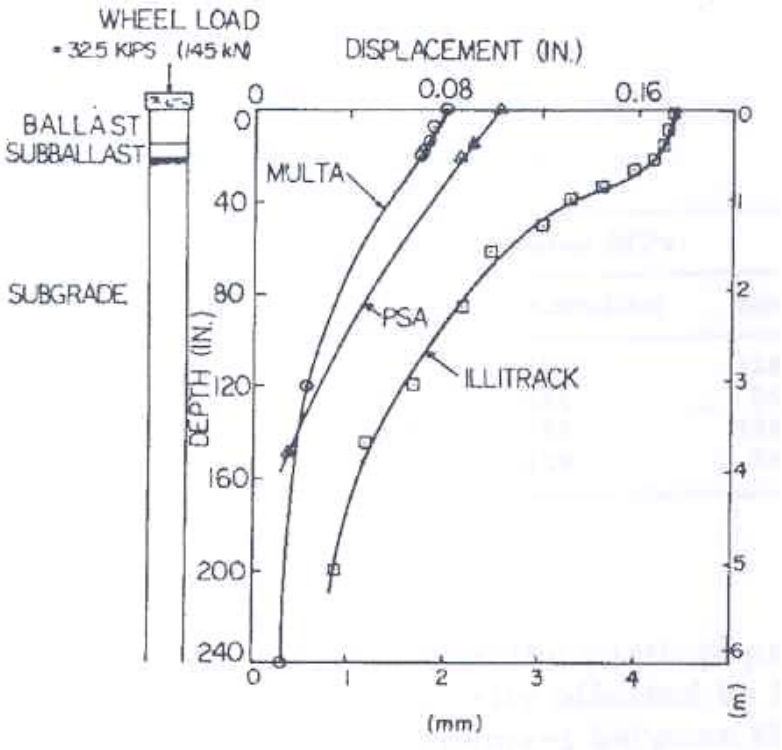

Figure 2.38 Comparison of distribution of vertical displacement with depth under single axle load: MULTA, PSA, and ILLI-TRACK (Adegoke et al. 1979)

The above observations were essentially the same as those obtained by Desai and Siriwardane (1982). The final conclusion reported by them is that irrespective of whether two- or three-dimensional analysis is used, proper care and judgement on factors such as the spacing and the length of the sleepers, and angle of load distribution is essential.

Chang et. al. (1980) have developed the GEOTRACK model – a three-dimensional multi-layer model considering the elastic response of the rail track system incorporating stress dependent material properties and separation of sleeper and ballast. Output of the model includes rail seat load, sleeper-ballast reactions, sleeper and rail deflections and bending moments.

Desai and Siriwardane (1982) developed several finite element formulations based on one-, two- and three-dimensional idealisation of rail track support system. The model procedures have been compared with results from ILLI-TRACK, MULTA and PSA models and with field observations. The main features of the models developed were:

- Provision of non linear elastic and elastic-plastic behaviour for model idealisations;
- Triaxial tests have been used to define model parameters;
- Use of special 'thin' interface elements between various components; and
- Use of special techniques to make computations as economical as possible.

Further, it was commented that though the one- and two-dimensional idealisations are possible in a number of situations, the non-linear three-dimensional analysis is the best to simulate practical problems; viz., loss of sleepers, local failures, sections near curves, fatigue failures due to repeated loading, etc.

Profillidis (1985, 1986) has presented a model to predict stress and strain at subgrade and sleeper and rail level. The method takes into account the different types of sleepers, the thickness of the track bed structure (ballast, sub-ballast and sand) and the quality of the soil of the subgrade.

Li and Selig (1998a,b) have presented a new design method for selecting granular layer thickness intended to prevent progressive shear failure and excessive plastic deformation due to repeated traffic loading developed based on the GEOTRACK model. Design charts have been developed covering various types of soils and granular layer conditions.

Models on Dynamic behaviour

The models that consider dynamic effects as a modelling parameter are discussed below. Here the models available on dynamic variation of loads or inclusion of damping coefficients are emphasised.

Zicha (1989) has developed a vibrating elastoplastic model of a high-speed track structure for the vertical and transverse load. In his discussion Zicha emphasised that with increasing velocity the vibrations penetrate to greater subgrade depths than usual and that subgrade has to be designed to withstand the special loadings induced by the dynamic phenomenon. The objective is to minimise plasticity and Zicha specifies a slightly more elastic subgrade material with careful drainage facilities and special transition zones between flexible and stiff foundations (eg. a tunnel or a rock cutting).

Cai and Raymond (1993) have presented a model incorporating rail and the sleepers as Timoshenko type beams, rail pads as linear springs with viscous damping and stiffness, and the vibration absorbing effect of track bed as a continuous array of linear springs and viscous dashpots. The study was done for a stationary vertical impact load.

Knothe and Wu (1998) have investigated a model that predicts vertical dynamic behaviour of a railway track on an elastic halfspace or on a layered halfspace.

Lei (2001) has developed a three-dimensional model in which rails, sleepers, fasteners and pads, ballast and track substructure are considered as a whole system. First, a wheelset model was used to derive the load spectrum varying with time. Then this load spectrum

was input into the three-dimensional model. Finally the dynamic response of the track structure was analysed under high-speed trains.

Sun (2002) has presented a closed-form solution of beam on viscoelastic subgrade subjected to a moving constant point load. The model has predicted that load velocities have significant effect on the shape of the dynamic deflection and the maximum deflection.

Models on Track response

Frohling (1997) formulated a model to predict differential track settlement due to dynamic wheel loading and spatially varying track support conditions. On-track measurements were used to analyse the model and mathematical simulations were used to predict future performance of the vehicle/track model.

Zhang (2000) has developed a model to predict track degradation. This model takes into account the degradation of each track component enabling prediction of either overall track condition or individual track component condition using various empirical relations approachs.

Shahu et. al. (1999) developed a three-dimensional linear elastic finite element model 3D20N to investigate the effect of track parameters on overall track response. The model was compared with other numerical models and field test data. Subgrade modulus was found to be the most influential track parameter on the overall track response. The parameters such as the depth of sub-ballast, rail moment of inertia, and sleeper spacing are also important.

2.5.3 Backcalculation Techniques

Backcalculation can be described as an inverse problem solution in which characteristics of material are assumed and adjusted until it computes the best fit to the measured deflection basin. Therefore, backcalculation can be defined as an error minimisation procedure. The analysis may be performed using iterations, database searching, closed-formed solutions or simultaneous equations. Usually the minimisation techniques employed use absolute or squared error with or without weight factors (May and Von Quintus 1994; Uzan 1994). Backcalculation analysis is very much sensitive to the assumptions made to interpret measured data in the mechanical model. For example most stress analyses carried out on pavement structures assume linear elastic response and uniform material properties. These assumptions lead to large errors in the best fit of the measured deflection basin and hence errors in the backcalculated moduli (Stolle 1990; Uzan 1994).

Further, the static response models used to reproduce the deflection bowls generated from static and dynamic surface deflection tests assume that the dynamic component of the response is unimportant. Instead these models assume that the deflection bowl is due to quasi-static response of the pavement (Collop and Cebon 1996). Collop and Cebon (1996) state that Tam and Brown (1989) examined the effect of simplification to quasi-static response and they concluded that the inertial effects are insignificant and a static model could be used with confidence in pavement analysis. They also concluded that material damping is a more important parameter than the inertia of the pavement.

In backcalculation, the real modulus or the damping coefficient or the components of the constitutive models used can be derived. The number of parameters is generally kept to a minimum so as not to produce instability in the set of equations to be solved (Uzan 1994).

Present pavement backcalculation models are based on multi-layered or two-layered systems. The moduli predicted from these models are sensitive to the input variables of the pavement such as layer thickness and the depth of bedrock (Uzan 1994). If two adjacent layers have relatively close moduli, it will be difficult to obtain realistic results using trial and error backcalculation methods since divergence or non-uniqueness is likely to render the iterative process ineffective (Shuo et al. 1998; Uzan 1994).

Most backcalculation procedures are developed for finding pavement layer moduli in highway and airport runway designs. Sussmann and Selig (2000) have used backcalculation techniques to find equivalent layer moduli of track layers using GEOTRACK. Elastic and plastic vertical deformations were measured by a multi-depth deflectometer installed to a maximum depth of 3m below top of sleeper. For the comparison of results, the correlated moduli of the cone penetration test (CPT) tip resistance and published results were used. These results were found to be favourable.

Backcalculation was performed in the current research to predict material properties using uniaxial compressive tests on soil samples in a rigid cylinder. The commercially available Finite Element program ABAQUS was used in predicting material properties. Details of this procedure can be found in Chapter 5.

2.6 Summary

Analysis and design of rail track substructure, in particular sub-ballast/capping layer has been reviewed in this Chapter. Effect of track degradation on the ride quality and

derailment potential has also been briefly described. Factors affecting degradation and failure of subgrade (natural ground or fill and capping layer) have been listed.
As the natural ground in subgrade is very complex with variable properties, attention has been focused on the capping layer analysis and design. For effective analysis of the capping layer, the stress level due to operational load is important. Various analytical, empirical and numerical methods used for the determination of stress levels in the capping layer are also provided and their advantages and disadvantages have been examined.

Effect of compaction, moisture content and load cycle on the physical characterisation has been described. Various tests methods used in the determination of the properties of the capping layer material have been provided. Various formulae used in the analysis of these experimental data have also been provided.

Basic theories of plasticity relevant to granular materials (soils) have been briefly presented. Various design methods of rail track substructure have been described in detail in the final section of this Chapter. The information provided in this Chapter will form the basic theory for the development of numerical modelling and experiments developed as part of this thesis.

The conventional track models are limited in their applications, as they do not address the performance of the substructure due to repeated application of axle loads, subgrade quality or ballast quality. Numerical models on the other hand incorporate all major components of track and subgrade (rails, sleepers, pads, ballast, subballast, and subgrade) yet lack proper characterisation of ballast and subgrade material properties, load distribution and the failure criteria chosen to develop the models. As discussed by Desai and Siriwardane

(1982) it is essential to use three-dimensional modelling in some cases to understand practical problems that occur in rail track structures; viz., loss of sleepers, local failures, sections near curves, fatigue failures due to repeated loading, etc.

The economic design and modelling of railway subgrade depends on proper characterisation of load deformation of materials. Resilient modulus has been identified as the concept to properly describe the behaviour of subgrade material subjected to repeated loading. Very few literature references were found on railway subgrade material moduli. However the literature on concepts and designs covered in pavements (highways and airfields) can be utilized for railway subgrades as well.

The most important factor affecting the resilient modulus of fine-grained materials was found to be the deviator stress, and this was identified to be most sensitive to the moisture content of the subgrade soil. As resilient modulus is sensitive to various soil indices, careful consideration must be given when utilising it in substructure analysis and design.

Granular materials display less variable characteristics compared to fine grained soils. Magnitude of repeated stress state, moisture content, degree of compaction and gradation are identified as significant factors influencing granular material resilient moduli.

Most researchers found that permanent deformation and log number of load applications were related in the form $\varepsilon_p = AN^b$. This equation is widely accepted in the practice of pavement design, especially for cohesive soils.

Static testing procedures are inadequate for characterising subgrade and granular material properties subjected to repeated loads. Repeated loading procedures are utilized to quantify the resilient modulus. Different testing procedures yield different M_R values and hence differences in substructure design.

Despite the sophisticated moduli obtained to represent the subgrade behaviour, CBR values and allowable subgrade bearing capacity form a larger content in design practices globally. Various charts related to CBR or allowable bearing capacities are readily available. This is common practice in railways and pavements design.

In characterising material properties, backcalculation techniques are used as a tool. The non-linear stress-strain properties are obtained by elastic layered theory in most of the backcalculation techniques used in pavement design. In the current research also, material properties are evaluated using finite element modelling based backcalculation techniques in which material properties are adjusted to best-fit the load-penetration response obtained from a semi-confined testing. This includes a series of small scale compressive tests. This laboratory study is presented in Chapter 3.

CHAPTER 3

3. EXPERIMENTAL METHOD OF CHARACTERISING CAPPING LAYER PROPERTIES

3.1 Introduction

Deformation of the substructure can be divided into two parts, recoverable elastic deformation which is a measure of the resilient behaviour, and non-recoverable plastic deformation which is a measure of absorbent behaviour. The current characterisation of substructure design and analysis is based on the resilient properties of soil. As such, in the past much emphasis was given to the study of the resilient behaviour of soils, particularly in pavement designs. The use of Resilient Modulus (M_r) as an indicator of the resilient behaviour has been introduced successfully into the design of flexible pavements. The focus of most recent efforts have been on providing better interpretation, understanding and application of M_r into mechanistic design models. A potential parameter which directly governs the plastic deformations is yet to be introduced for practical design considerations.

The current design practice of rail substructure is based on California Bearing Ratio (CBR) and soil bearing capacity. The safe average bearing pressure method (based on static testing techniques applied to saturated soils) and the British Rail formation design method (based on repeated load tests) are the two major methods developed to determine the allowable bearing pressure of the subgrade (Jeffs and Tew, 1991). The experiments such as the CBR test and the repeated load tri-axial test have allowed reliable design procedures but failed to explain global and local failure of the subgrade. Lay (1990) has discussed that, though field bearing tests and CBR tests provide correct in-situ soil strength, they are

slow and cumbersome and only give results specific to the location. Efforts have therefore been made to generalise the available knowledge and experiences using the elastic theories to evaluate the effect of the dynamic and repetitive character of the traffic loading.

Drumm et. al. (1996) introduced an Alternative Resilient Modulus Test Method (ATM) for fine grained soils, based on a falling weight impacting on a Standard Proctor specimen. A falling weight load was used to simulate a moving vehicle and the applied load or stress was controlled by varying the weight and height of fall as shown in Fig. 3.1.

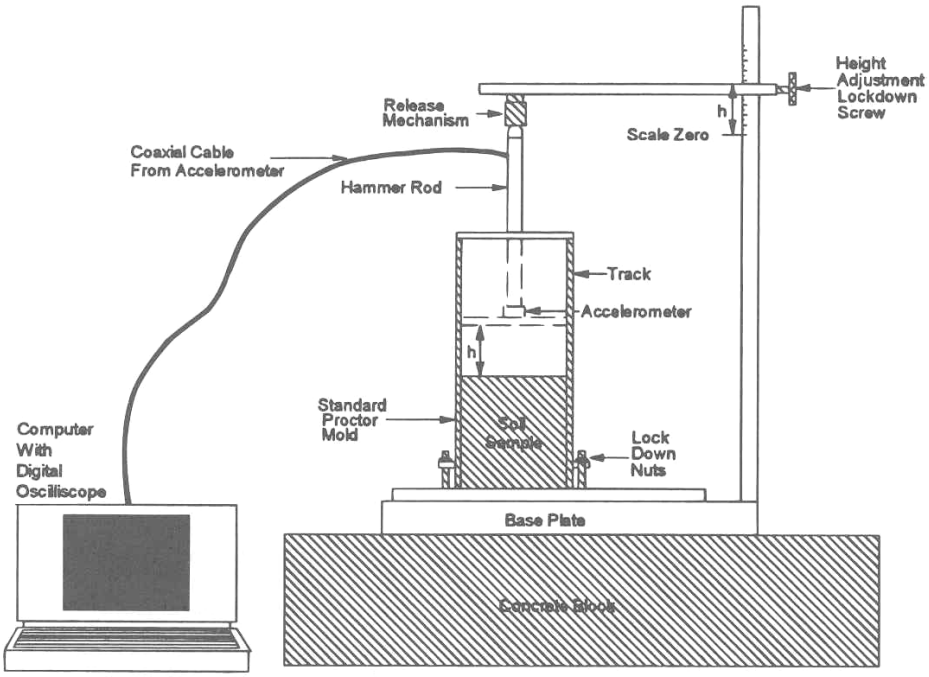

Figure 3.1 Equipment set up for the ATM device (Drumm et al. 1996)

Expressions for the modulus and deviator stress as a function of the measured acceleration during impact were developed using a simple theoretical model by Drumm et. al. (1996). They evaluated the resilient moduli from the new alternative test method for 14 soils from Tennessee and their values compared reasonably with the results from standard repeated load triaxial tests (Fig. 3.2). They also showed that the soils with low and high moduli

were consistently distinguished by the alternative method and the estimates of resilient modulus were considered satisfactory for most pavement design applications. The alternative method developed by Drumm et. al. (1996) was simple and advantageous to use in a production environment favoured by the familiarity of the Proctor test and the limited data collection requirements.

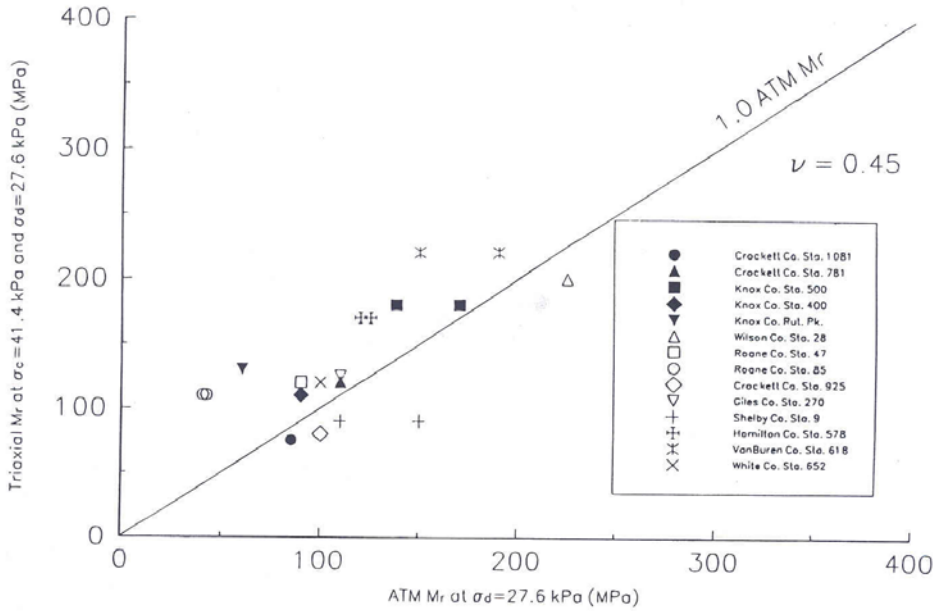

Figure 3.2 Comparison of cyclic triaxial and ATM resilient modulus test results (Drumm et al. 1996)

Kim *et. al.* (2001a,b) have developed an alternative resilient moduli (M_R) testing technique which is simple and reliable, considering the difficulties, complexities and prohibitive costs and time involved in performing the cyclic M_R testing. They proposed static triaxial tests as an alternative considering the effects of loading frequency, mean effective stress, number of loading cycles, and maximum particle sizes. Comparison of results with resonant column –torsional shear stress was also performed on seven subgrade samples (nonplastic sandy soils, plasticity index less than 5%, average CBR value 21) from several pavement projects.

Kim *et. al*. (2001a,b) carried out loading, unloading and reloading stages of the static triaxial test, and the secant modulus was calculated from the slope of lines connecting the reversal origin to the reloading curve (E_r) or unloading curves (E_u) as shown in Fig. 3.3. It was found that the mean effective stress during the reloading stage [$(3\sigma_c + \sigma_{d,r})/3$] of the static triaxial test was equivalent to those in the M_R test [$(3\sigma_c + \sigma_{d,}M_R)/3$] with a given seating pressure. The stiffness therefore was determined from the reloading curve of the static triaxial test with the same seating load as the standard M_R testing method.

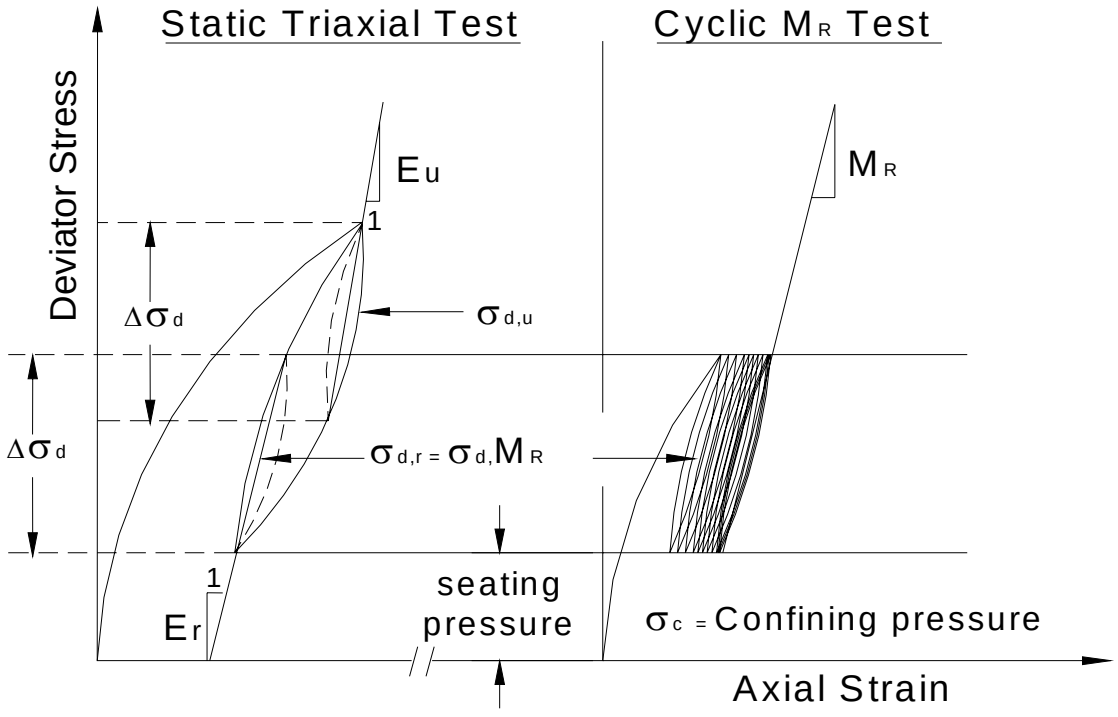

Figure 3.3 Comparison of mean effective stresses during static triaxial and M_R tests (Kim *et al.* 2001a)

Fig. 3.4 shows a typical comparison of this alternate method (Kim *et. al*. 2001a,b) with the standard M_R test, for a non-plastic subgrade type SG-6, which was in good agreement. To evaluate the reliability of applying modulus values, a confidence level was evaluated under working stress conditions. As shown in Fig. 3.5, the 95% confidence interval of moduli obtained from the proposed method was ±3.59%, and the moduli determined from the

proposed method were about 9% larger on average than those obtained from the standard M_R test. Considering the findings of Kim *et.al.* (2001and b), a similar approach was adopted in the current research to find the resilient material properties.

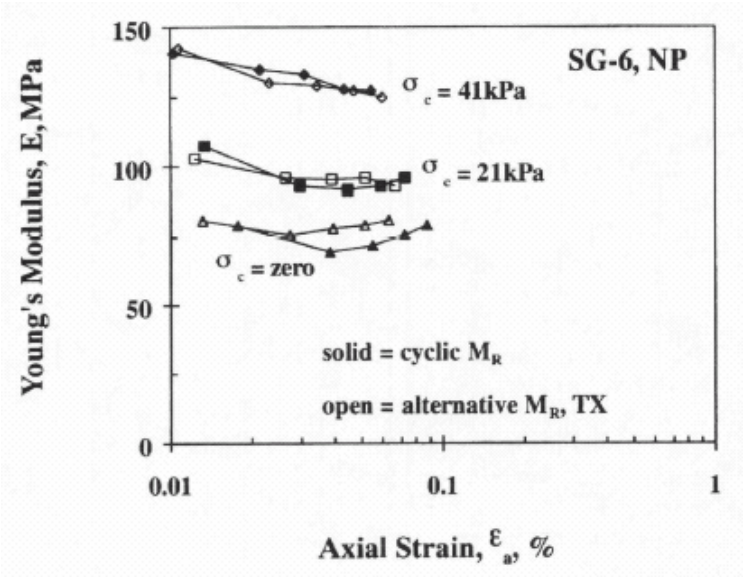

Figure 3.4 Comparison of M_R values with alternative method (Kim *et al.* 2001a)

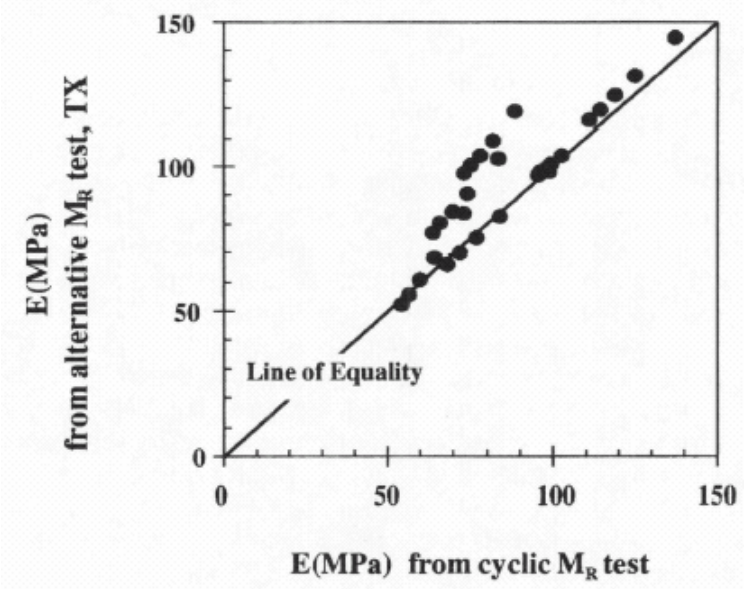

Figure 3.5 Evaluation of reliability of moduli determined by the alternative method (Kim *et al.* 2001a)

Okada and Ghataora (2002) have developed a quick and accurate method for measuring the stiffness of railway subgrades. A cyclic penetration test was introduced using the California Bearing Ratio (CBR) test mould (Fig. 3.6). A finite element analysis was carried out and cyclic stress distribution in the CBR mould was calculated.

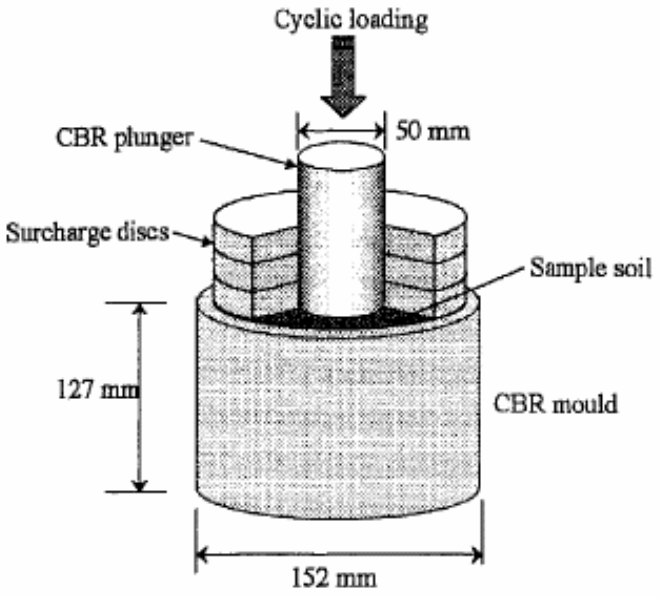

Figure 3.6 Cyclic penetration test apparatus (Okada and Ghataora 2002)

A plastic modulus M_p was defined using the cyclic stresses, which in turn was used to calculate the cumulative plastic deformation (for soil in a CBR mould). These results were then correlated to cumulative settlement of subgrade using the Talbot equation and a power model. The results were compared with measured settlements at actual railway sites by Heath et. al. (1972) and reported to be in good agreement.

The main advantage of this method is that it can be easily used to design ballast depth by limiting allowable subgrade settlement. A reliable indicator for the maximum acceptable soil moisture content defined as 'threshold moisture content' was also determined. The determination of the relationship between the penetration of plunger and moisture content

was by normalising both values, for London clay, Oxford clay and building sand. The normalised moisture content is the ratio of moisture content to optimum moisture content and the normalised penetration is the ratio of penetration to penetration at optimum moisture content. There was a sudden increase in penetration at certain levels of normalised moisture content of 1.1 to 1.4 as illustrated in Fig. 3.7. This sudden changing value was termed the threshold moisture content and it was found that wet subgrades exceeding this threshold value potentially failed prematurely. The significance of maintaining adequate drainage in subgrade to maintain its stiffness is therefore apparent as the plastic deformation of soil significantly increases especially when the soil is nearly saturated.

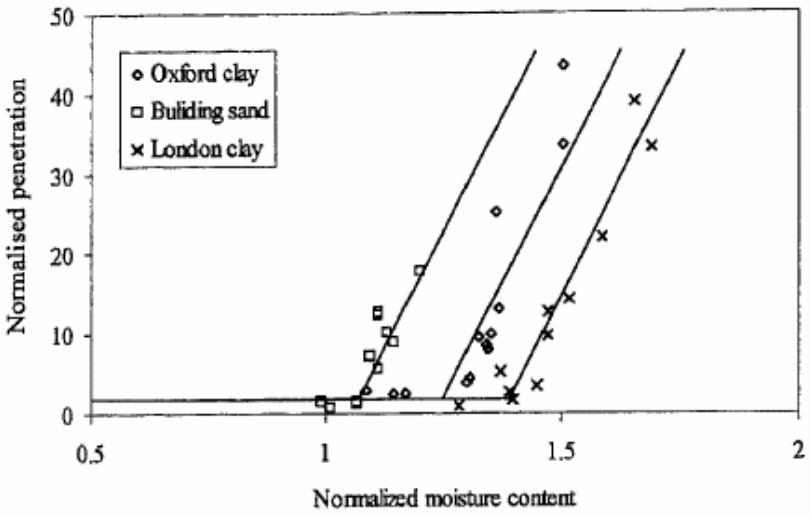

Figure 3.7 Relationship between moisture content and plunger pressure (Okada and Ghataora 2002)

With the advent of modern computerised numerical models, the analysis procedures have become more effective and reliable at incorporating complexities in geometry, boundary conditions and material properties. Dahlberg (2001) has summarised mathematical models currently available in the literature, emphasising that track settlement is mostly considered

as a function of loading cycles and/or a function of the magnitude of the loading, but very little is available in the literature dealing with the material properties of track substructure. The major reasons for current design methodologies not addressing the permanent deformation of substructure are:

- expensive, tedious and time-consuming experiments;
- implicit consideration of subgrade deformations as insignificant; and
- assumptions of the distress caused by loading as highly dependent on the resilient properties rather than plastic properties of subgrade.

However, present trends focus on maintaining the level of the geometry for the top layers of the railway track, sub-ballast and capping layers within very strict tolerance levels. As permanent deformation of these layers is the major contributing factor to the geometry tolerance issues, it would be prudent to include the calculation of deformation of such layers during the design stage itself. This thesis therefore aims at developing an inexpensive method of determining both the recoverable and irrecoverable moduli of the capping layer.

This Chapter first states the aim of the experiments and the methods of testing; second it outlines the selection of material for testing and examination of its properties followed by the experimental setup, typical experimental results and discussions. Dimensional analysis and ternary plots are then detailed for further analysis of the experimental results. The relevant data of Chapter 3 are exhibited in detail in Appendices A.1 – A.7.

APPENDIX A.1	Basic properties of the capping layer material
APPENDIX A.2	Density and saturation calculations- Semi Confined Test (SCT) samples
APPENDIX A.3	SCT experimental data sheets

APPENDIX A.4	Stiffness and penetrated depth against moisture, penetration rate and number of cycles in SCT
APPENDIX A.5	Dimensional analysis data sheets
APPENDIX A.6	Coefficients of the orthogonal polynomials
APPENDIX A.7	Ternary plot calculations

3.2 Semi-Confined Cylinder Test (SCT)

3.2.1 Aim of Testing

In-situ tests normally produce measurable structural responses (for example, load-settlement curves) and the material properties of the constituent layers are determined via backcalculation of layered subgrades. However limitations are prominent in in-situ testing as a large number of un-controllable environmental variables (moisture, temperature, etc.) usually influence the results. Laboratory tests, on the other hand, determine actual parameters without influences from other material layers. The laboratory studies for evaluation of permanent deformation are less advanced than for resilient deformations. The existing test procedures for permanent deformation evaluation are relatively complex and laborious. As such, further development on methods assessing permanent deformation and correlation of resilient behaviour to simpler tests is required.

The main aim of this thesis is to develop an economical method to evaluate the stress-strain relationship of capping layer which would have the potential to be used as a routine assessment approach for the characterisation of granular soils comprising the rail track substructure.

Mathematical models of the behaviour of soils have been developed since late 1940's as discussed in Section 2.4. These methods show that qualitative agreements can be found

with experimental results even by means of simple elasto-plastic models. As such in this research a simple strain controlled penetration testing of soil specimens contained in a rigid cylinder is proposed. The material properties are then predicted via a finite element simulation based backcalculation technique.

3.2.2 Design of experiments

It was decided to perform an extensive series of tests on a benchmark material in order to obtain a complete data base with which to compare the modelling predictions. In developing an economical method, it was also decided to use the typical CBR mould as the apparatus for the testing. The CBR mould is capable of approximating the drained conditions observed in-situ.

Two major parameters that affect the behaviour of railway substructure were considered in the design of experiments. They were the moisture ingress and the train speeds.

Furthermore all categories of test specimens were subjected to two loading sequences; 1) monotonic loading and 2) cyclic loading. In the monotonic tests the penetration was continuously increased to a substantive level at a constant rate. In the cyclic tests the displacement was applied at a constant rate in a sequence of loading, unloading and reloading at pre-decided penetration levels. Fig. 3.8 provides a sketch of these two penetration sequences. It also shows possible load-penetration profiles that can be expected of this form of penetration sequences. In both cases only the vertical penetration was considered.

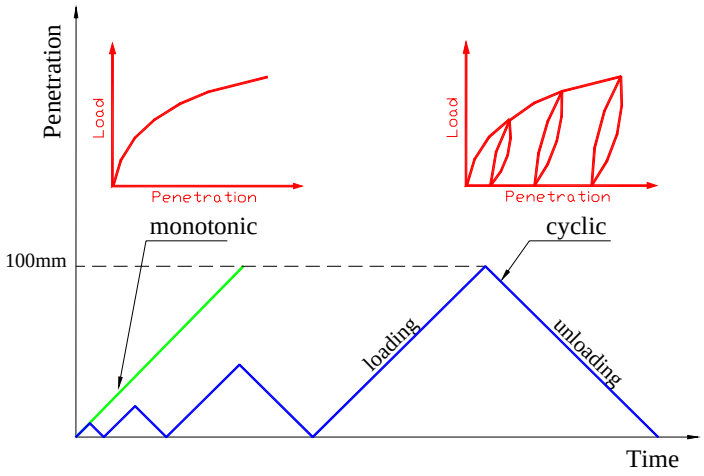

Figure 3.8 Monotonic and cyclic loading sequences

Moisture States

In practice, the compaction of the railway subgrade is carried out at Optimum Moisture Content (OMC). Therefore to assess the effect of the moisture ingress on the behaviour of the capping layer; OMC (moist), dry and saturated (wet) were considered in the experiments. All specimens were made first by compacting at OMC in line with the engineering standard for "modified compaction". In simulating the three states, the samples were tested as-prepared (OMC or moist state) or tested after modifying the level of moisture in them. The moisture levels were modified by soaking for four days (96hrs.) or after drying in an oven at 105^0C for one day (24hrs.), to examine the effect of saturated (wet) and dry conditions respectively. For illustrations in the diagrams, these three conditions OMC, saturated and dry are referred to as M, S and D respectively.

Loading Rates

The effect of train speed has an influence on the behaviour of the substructure. The effect of train speeds are generally investigated in terms of resulting dynamic vertical loads on tracks (Zhang 2000). There are three main wave types caused by the vibrations in soil through which each wave propagates; Surface or Rayleigh waves, P-waves or compression

waves, and S-waves or shear waves. The soil particles will start to move locally when these earthborne waves pass through the soil medium. Usually these particle velocities are measured, analysed or reported as vertical, horizontal longitudinal, horizontal traverse, or the resultant of all three motions. Most often (although not always), the vibrations along the ground are greatest in the vertical direction and usually a Peak Vertical Particle Velocity (PVPV) is reported for earthborne vibrations (Hendriks 2002).

The vibration levels caused by trains will vary depending on the speeds, loads, condition of track and the amount of ballast used to support the track. Fig. 3.9 shows PVPV's caused by the passage of trains, measured at 5m from the train where the PVPV of 7mm/s was observed which diminishes with increasing distance from the train to about 0.25mm/s at about 90m (Hendriks 2002). It also shows some risk levels suggested in literature for various types of buildings.

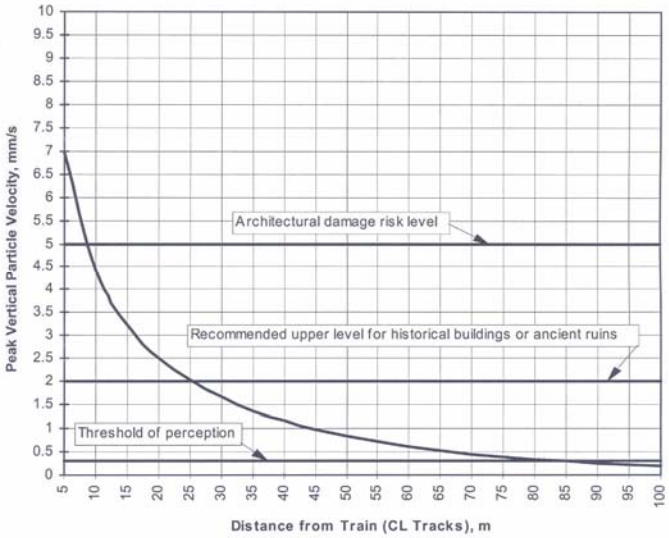

Figure 3.9 Maximum train vibration levels reported at Sacramento, CA, USA (Hendriks 2002)

The peak particle velocities for Japanese and Swedish trains were reported by Dowding (2000). For Japanese trains travelling slower than the wave propagation velocity, the peak

particle velocities recorded were 4mm/s and 7mm/s at a distance of 25m from the train in soft ground and stiff ground respectively. For Swedish trains travelling at greater speeds than the wave propagation velocity the recorded velocities were 200mm/s at a distance of 3m and 17mm/s at a distance of 9m from the train (Dowding 2000).

Hall (2003) too has tested train induced vibrations caused by a trains travelling at various speeds gradually increasing from 10, 70, 120, 140, 160, 180 to 200km/hr at high-speed project of Banverket, Sweden. Fig. 3.10 shows the PVPV's caused by a train travelling at a speed of 142km/hr. It can be seen that the reported PVPV's were between 2.5mm/s to 18mm/s showing a very wide velocity range of the soil particles.

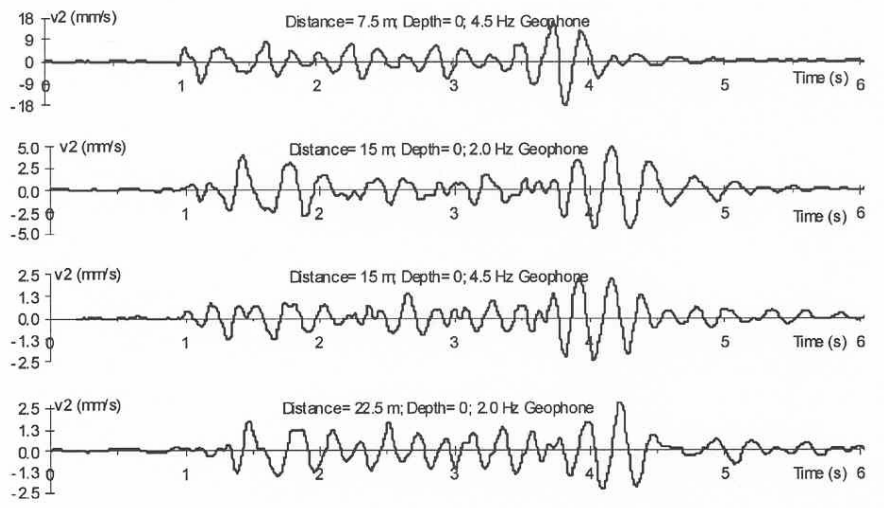

Figure 3.10 Vertical particle velocity response reported at high-speed project of Banverket, Sweden (Hall 2003)

As per the above discussion, by considering the wide range of the PVPV's (2.5-18.0mm/s) caused by the train induced wave propagations and the available test equipment limitations encountered, it was decided to carry out tests for five penetration rates 2.5, 5.0, 10.0, 15.0 and 20mm/min. This range was considered representative enough as usually the tests to measure stress-strain properties of a soil in drained conditions are carried out at low rates.

The wave propagation velocities in all types of soils (granular and cohesive) were influenced by their void ratio and the mean effective confining stress they were subjected to. Saturation also influences the wave propagation velocities. In partially saturated (10-50% saturated) fine granular soils (silty sands) the capillary pressures have increased the shear modulus by 50-100% increasing the wave propagation capacity of the soil (Gazetas 1991)

Thus, thirty (30) experiments were carried out for the above conditions stipulated; two (02) loading sequences × three (03) moisture states × five (05) penetration rates.

3.3 Material Selection

The benchmark material selected for the study is described as MRD Type 2.4 Unbound soil, obtained from the CSR Quarry at Nerimbera, Central Queensland, Australia. The material must meet the requirements of having a minimum soaked CBR of 35 at 100% standard compaction effort and a maximum Plasticity Index (PI) of 12 and maximum Weighted PI of 360 (Main Roads MRS11.05 1999). The Department of Main Roads, Queensland, Australia, uses this material as a base or sub-base layer in road pavements. Queensland Rail (QR) sometimes uses this material as a capping layer in railway substructure. As such, investigation of the behaviour of this material is expected to benefit both the road pavements and the railway subgrades designs.

Fig. 3.11 illustrates the particle size distribution (PSD) envelope of the material used in the laboratory testing. From the PSD curve we could infer that it is a well-graded material; therefore, care was taken to avoid segregation of particles during placement and testing.

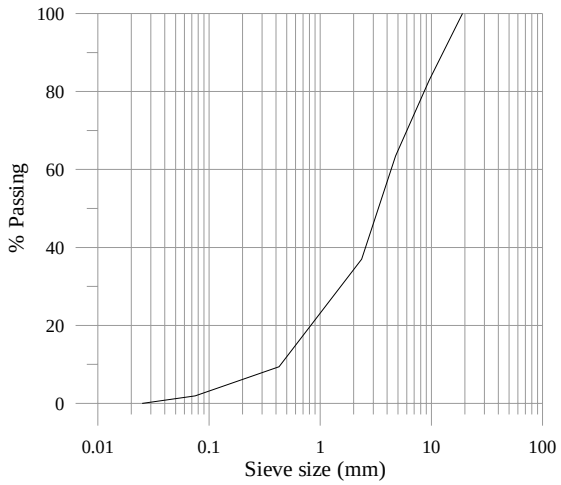

Figure 3.11 Particle size distribution of Type 2.4 Unbound Material

Table 3.1 presents the basic properties of the material selected. The material showed a permeability of 10^{-2}m/sec, which is close to permeability of very fine sands, silts and clay-silt laminate (Craig 1997). From the properties listed, the material can be classified as a *well graded mixture of very sandy gravel with traces of non- plastic fine with a medium permeability.* The corresponding property evaluations are located in Appendix A.1.

Table 3.1 Properties of Type 2.4 Unbound Material

Material property	Measured Value	Reference
Specific gravity from multi-pycnometer test	2.75	(Quantachrome Corporation 1996)
Linear shrinkage	2.4%	(AS 1289.3.4.1 1995)
Liquid limit from cone penetrometer method	20%	(AS 1289.3.9.1. 2002)
Maximum dry density from modified Proctor compaction test (γ_{dmax}) t/m^3	2.31	(AS 1289.5.2.1 2003)
Optimum moisture content at maximum dry density (w_{max})	5.9%	(AS 1289.5.2.1 2003)
Coefficient of uniformity ($C_U = D_{30}^2 / D_{60}D_{10} > 4$)	7	(Craig 1997)
Coefficient of curvature ($1 < C_Z = D_{30}^2 / D_{60}D_{10} < 3$)	1.8	(Craig 1997)
96hrs Soaked California Bearing Ratio (CBR) using modified compactive effort	110	(AS 1289.6.6.1 1998)
Permeability (K) at 20^{0}C of a modified compacted sample m/sec	1.1×10^{-2}	(AS 1289.6.7.2 2001)

Note:
D_{60}, D_{30}, and D_{10}.are the particle size such that 60%, 30% and 10% of the particles are finer than that size respectively.

3.4 Experimental Setup

The CBR mould (152mm diameter, 177.5mm high) was used to prevent overall lateral bulging of the test specimen due to the development of relatively high confining pressures generated by the vertical penetrations. Vertical bulging (Fig. 3.12) through the unconfined top surface of the specimen was, however, possible. Therefore, this test is regarded as semi or partially confined. The vertical penetration was imposed by a servo-hydraulic loading system with a capacity of 500kN fitted to a rigid portal frame, via a rigid solid steel cylinder of length 200mm and diameter 50mm. This provided a solid barrier to the disturbed failed material, not allowing it to fall back into the indentation formed during the process of penetration. The specimen was centred under the load cell and load-penetration behaviour was recorded by the data-acquisition system. The tests were stopped either when the penetration exceeded 100mm or when the load reached the 500kN capacity of the system (equivalent to 255 x 10^3 kN/m^2).

Figure 3.12 Experimental Setup

3.4.1 Test Procedure

Step 1. The material was air dried and sieved through a 19mm sieve to remove any oversize particles.

Step 2. The material was homogenised with the required amount of water at the OMC and thoroughly mixed and cured for a minimum of 2hrs as its liquid limit was low (Table 3.1).

Step 3. The material was then compacted in a greased standard CBR mould in five layers, each of about 35 mm thick subjected to 56 blows with the 4.9kg Proctor hammer falling a distance of 450mm.

Step 4. After compaction, the excess material protruding into the collar was removed with a blade and the top surface was levelled.

Step 5. The sample weight was noted at OMC.

Step 6. To obtain a dry sample, the sample compacted at OMC was oven dried at a temperature of 105^0C for 24hrs. For a saturated sample, the sample, compacted at OMC, was soaked for 96hrs in water.

Step 7. For dry or saturated samples the weight of the sample was noted again prior to testing.

Step 8. The sample was then centred under the load cell of the hydro-servo machine.

Step 9. The load was applied at the required loading sequence and the penetration rate.

Step 10. The load-penetration data were recorded.

Step 11. The tested sample was removed from the mould and void ratio and moisture content were determined.

3.4.2 Testing Program

A total of 30 specimens were tested. Monotonic tests were conducted typically within 10-40 minutes depending on penetration rates. Cyclic tests consisted of 10 cycles minimum and took 20-80 minutes. Table 3.2 illustrates the test program employed. Each specimen was provided with a unique tag of four characters. The first character represents the loading type (C for cyclic; M for monotonic). The second character represents the moisture level (M/S/D as explained before). The third and fourth digits represent the approximate loading rate in mm/minute for 2.5mm/min, and the actual rates used otherwise. That is 02 for 2.5mm/min, 05 for 5.0mm/min, 10 for 10.0mm/min, 15 for 15.0mm/min and 20 for 20.0mm/min.

Table 3.2 Laboratory testing program

Specimen number		Penetration rate (mm/min)	Moisture content	
Monotonic	Cyclic			
MM02	CM02	2.5	Optimum moisture content	**M**
MM05	CM05	5		
MM10	CM10	10		
MM15	CM15	15		
MM20	CM20	20		
MS02	CS02	2.5	96hrs. saturated sample	**S**
MS05	CS05	5		
MS10	CS10	10		
MS15	CS15	15		
MS20	CS20	20		
MD02	CD02	2.5	24hrs. oven dried sample at 105^0C	**D**
MD05	CD05	5		
MD10	CD10	10		
MD15	CD15	15		
MD20	CD20	20		

3.4.3 Density and Moisture Contents of the Specimens Tested

Table 3.3 shows the moisture content and the density of all the specimens tested. The difference between the moisture contents of the OMC and saturated specimens was found to be about 1.0%. The dry specimens showed some amount of moisture contained in them though they were oven dried for 24hrs at 105^0C. The densities of the samples did not vary much although their moisture levels were different. The degree of saturation of each specimen was calculated and presented in Appendix A.2. It can be concluded that the load bearing capacity has reduced with the increase in moisture as the density of the material has been reduced.

Table 3.3 Specimen properties

Monotonic Tests (MT)			Cyclic Tests (CT)			Average of MT & CT		
Specimen Number	Density (kg/m^3)	Moisture content (%)	Specimen Number	Density (kg/m^3)	Moisture content (%)	Density (kg/m^3)	Moisture content (%)	
MM02	2464	5.93	CM02	2394	5.86	2429	5.90	**M**
MM05	2372	5.66	CM05	2396	5.7	2384	5.68	
MM10	2475	5.74	CM10	2502	5.69	2489	5.72	
MM15	2461	5.53	CM15	2471	5.71	2466	5.62	
MM20	2459	5.46	CM20	2477	5.74	2468	5.60	
Average	**2446**	**5.66**	**Average**	**2448**	**5.74**	**2447**	**5.70**	
MS02	2375	7.03	CS02	2405	6.71	2390	6.87	**S**
MS05	2366	7.3	CS05	2411	6.31	2389	6.81	
MS10	2475	7.16	CS10	2496	6.51	2486	6.84	
MS15	2486	6.62	CS15	2471	7.27	2479	6.95	
MS20	2489	6.79	CS20	2411	6.82	2450	6.81	
Average	**2438**	**6.98**	**Average**	**2439**	**6.72**	**2439**	**6.85**	
MD02	2365	0.45	CD02	2332	0.5	2349	0.48	**D**
MD05	2275	0.75	CD05	2353	0.51	2314	0.63	
MD10	2367	1.63	CD10	2343	0.68	2355	1.16	
MD15	2359	1.14	CD15	2381	1.32	2370	1.23	
MD20	2357	1.15	CD20	2276	1.33	2317	1.24	
Average	**2345**	**1.02**	**Average**	**2337**	**0.87**	**2341**	**0.95**	

3.5 Results of Semi-Confined Cylinder Test (SCT)

This section presents the results of the SCT with the discussion highlighting observed behaviour and possible trends. The effect of moisture content and the rate of penetration on the behaviour of specimens are also discussed. Dimensional analysis is used as a tool to analyse the effect of penetration rate. Finally a ternary plot is presented to illustrate the relationship between the density of the sample, penetration rate and the moisture content. The corresponding experimental data sheets are located in Appendix A.3.

3.5.1 Behaviour of Material under SCT Setup

A highly non-linear behaviour with respect to loads was observed in the displacement-controlled tests carried out in the rigid CBR cylinders. The trend indicated in Fig. 3.13 therefore gives the entire picture of the data recorded. Four types of behavioural response were observed in each experiment, namely; hardening, stabilising, softening and remoulding. The initial response of hardening effect is typical of most elasto-plastic materials. This response changed rapidly with the increase in initial confinement stresses generated by the vertical stresses. Following the hardening phase, subsequent increase in penetration of the specimens exhibited a stabilising phase with little or no increase in resistance to penetration. Subsequently a softening in resistance to penetration occurs. With further increase in penetration the specimen then regains stiffness (K') and behaves like a virgin soil, although it does not become as stiff as it was initially (K_0). This range was defined as the "remoulding range" in Fig. 3.13. The specimen exhibited these four phases of behaviour at several stages (*Stage I, Stage II,...*) throughout the penetration path. As illustrated in the inset of Fig. 3.13, the dried samples showed more dominant patterns of the qualitative response described above than the OMC or saturated samples. It can also be

seen that the load carrying capacity has greatly reduced from dry to saturated states as shown in the inset of Fig. 3.13. This can be best described by taking into consideration the adhesive bonding between each point of individual contacts between the soil particles.

Every soil carries an electric charge on its mineral surface and attracts molecules of water or other impurities. As water is introduced the ions hydrate and are less strongly attached to the mineral surfaces (Lambe and Whitman 1979). Thus, in the oven-dried dry samples, the ions are not completely hydrated allowing the actual mineral surfaces to become close together making a strong bond with each other. In the OMC and saturated samples the water has hydrated the ions reducing the effect of the strong bonds between the mineral particles. Thus, the shear resistance has dropped in OMC and saturated samples as water is introduced showing that water acts as a lubricant making the samples weaker.

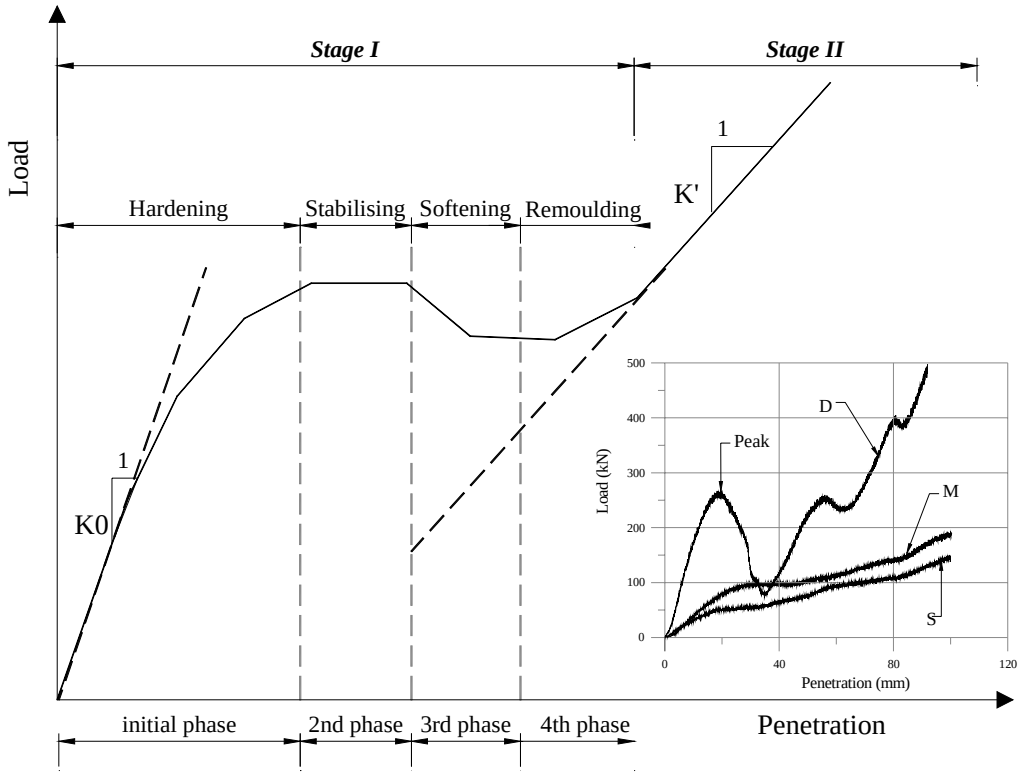

Figure 3.13 Typical load-penetration behaviour in a test

For the initially generated confining pressures, the softening phase is associated with a peak as shown in the dry state of the inset in Fig. 3.13. The lower the confining pressure the more dilatant is the behaviour after the peak. The occurrence of a peak is always associated with the development of a fracture plane in the specimen. For very high confining pressures, hardening starts from the beginning of the shearing phase. Also, for dry specimens it is apparent that the stiffness is lower than the initial stiffness appropriate to tests at much lower initial confining pressures. However, the OMC and saturated specimens show a more "ductile" behaviour compared to the brittle nature of the dry specimens.

The above phenomena can be further explained using the dilation and collapse mechanisms theorised by Bowles (1979). According to the theory the dense soils tend to dilate or expand while the loose soils tend to collapse or densify under shear. In a dense state, dilation occurs with the net effect being an increase in volume (+V) as the particles are forced up, over and around adjacent and confining grains. In a loose state, the net effect is a decrease in volume (-V) as the particles are moved into the voids. Fig. 3.14 illustrates this phenomenon.

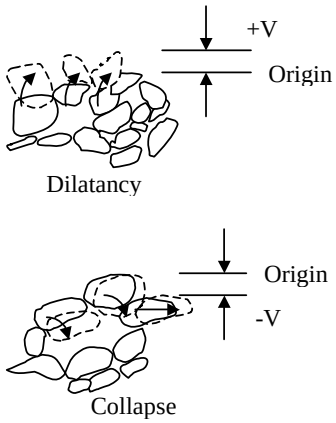

Figure 3.14 Dilatancy and Collapsing effects under shear of cohesionless soils (Bowles 1979)

Lambe and Whitman (1979) discussed similar patterns observed in granular materials in dry conditions. The initial phase of the load-penetration curve shows interlocking of particles with increase in stress, but the second phase shows the onset of a reverse curvature. This appears to be due to yielding causing fracturing of individual particles, which permits large relative motion of individual particles. The fracturing of particles may even cause an incremental momentary collapse range (3rd phase in each stage) and further increase in stress enhances tighter packing of the new and remaining particles making the specimen stiffer. Remoulding phenomenon is also described by Bowles (1979). It is stated that particulate material like soil fails primarily due to rolling and slipping of grains and defines failure as a considerable alteration or state change in soil structure (or remoulding).

3.5.2 Monotonic and Cyclic Loading Behaviour

Figs. 3.15 -3.19 show the results of six specimens under each category of the loading program. In each pair one specimen was monotonically loaded while the other was subjected to many cycles of loading-unloading-reloading.

(i) Envelope response

The saturated specimens subjected to cyclic load exhibited higher resistance to penetration than their monotonic counterparts at 2.5, 5 and 10mm/min penetration rates. At 15 and 20mm/min penetration rates both the monotonic and cyclic load tests exhibited almost equal resistance.

Except for the 2.5mm/min penetration rate OMC specimen, all other OMC specimens subjected to cyclic loads exhibited lower or almost equal envelopes of resistance to penetration than that of monotonic loading.

Dry specimens showed varying levels of envelopes of resistance due to cyclic and monotonic penetrations without any systematic patterns.

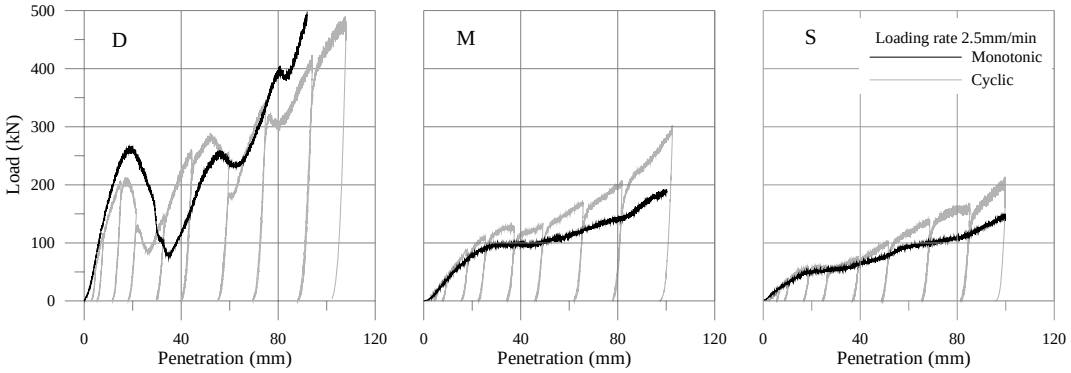

Figure 3.15 Behaviour during reloading at 2.5mm/min loading rate

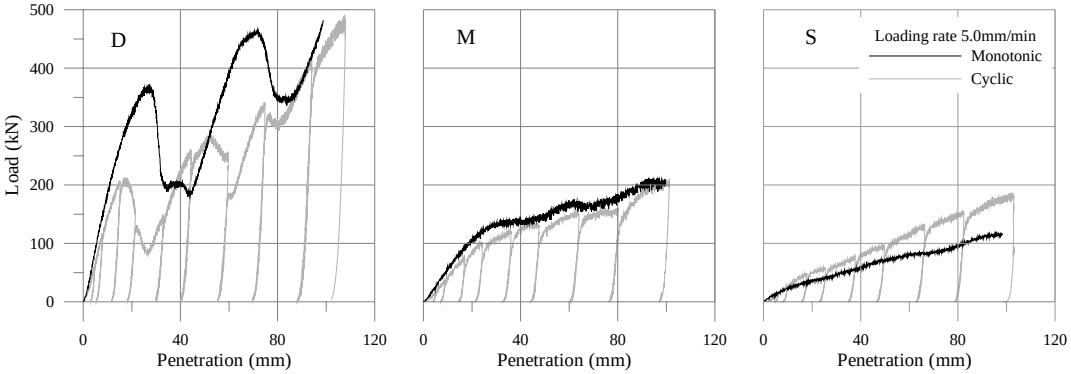

Figure 3.16 Behaviour during reloading at 5.0mm/min penetration rate

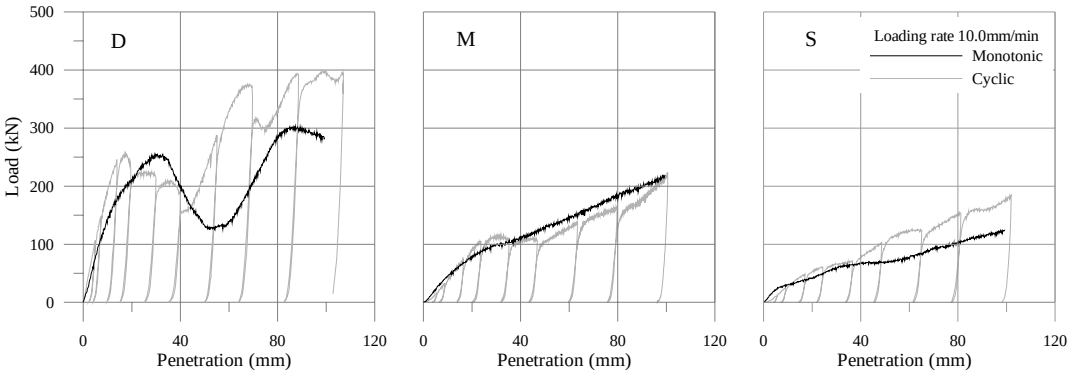

Figure 3.17 Behaviour during reloading at 10.0mm/min penetration rate

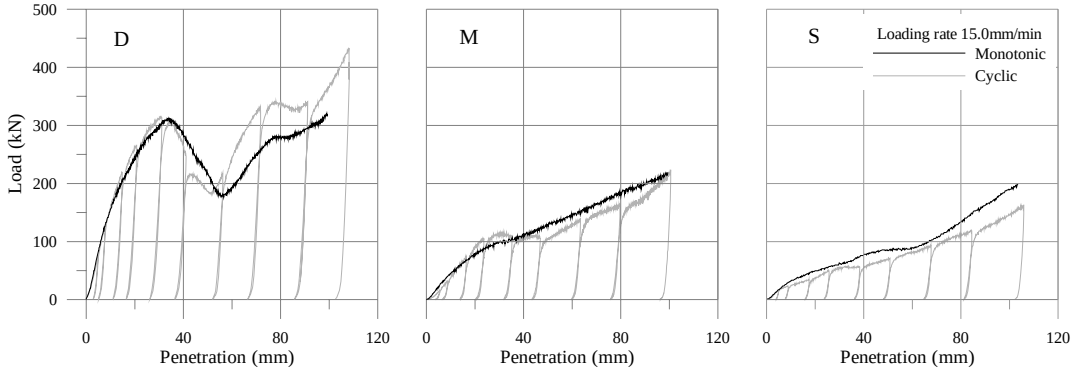

Figure 3.18 Behaviour during reloading at 15.0mm/min penetration rate

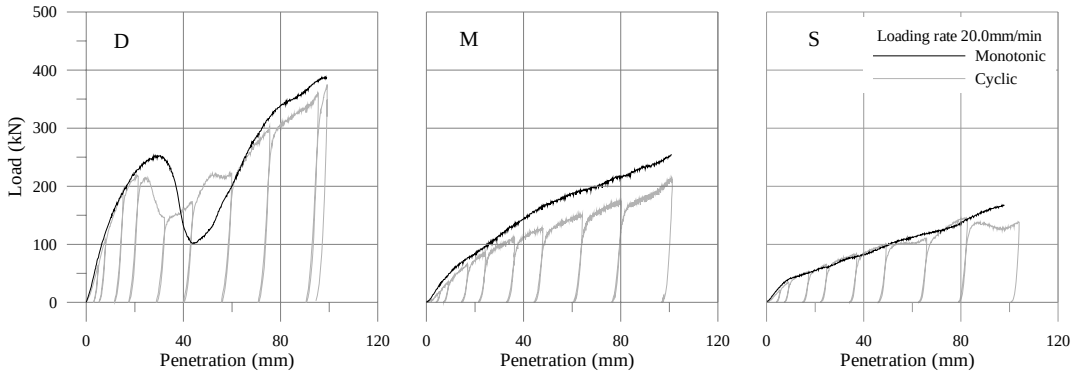

Figure 3.19 Behaviour during reloading at 20.0mm/min penetration rate

In summary, with the limited number of specimens tested (30 samples) in each category, it can be stated that the envelope response of the load-penetration curves could be arranged regardless of the type of loading application (cyclic/monotonic). This statement simplifies evaluation of the material constitutive relations from the monotonic penetration tests that are relatively economical to perform.

It is also evident from the experiments (Fig. 3.20) that three distinctive groups can be formed according to the level of moisture in the specimens irrespective of monotonic/ cyclic load application or penetration rate. The variation caused due to type of loading, penetration rate as well as subjective deviations in density, moisture contents, and compaction while making each of the specimens are all captured in the three data groups

for dry, OMC and saturated states. The variation in all behavioural patterns can be easily accommodated by defining lower and upper bounds for each of these groups. Such simplification is reasonable in geotechnical evaluations as properties of soil directly depend on the soil conditions (initial density, degree of saturation, state of stress, initial grain size and type of restraints they are subjected to) which vary spatially even within relatively small distances in the field.

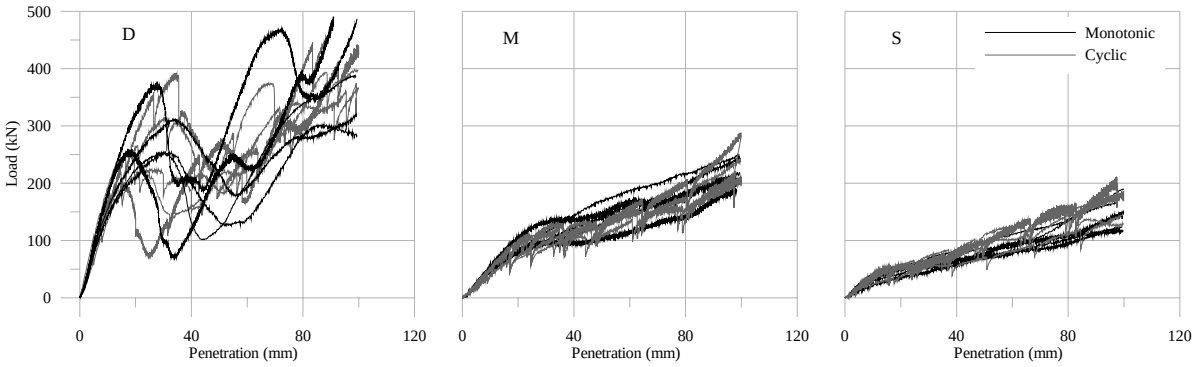

Figure 3.20 Behaviour during monotonic and cyclic loading at all penetration rates

(ii) Unloading-reloading response

The unloading-reloading behaviour is illustrated in Fig. 3.21. The stiffness at initial and various reloading paths are calculated using tangents drawn considering the respective linear parts as shown in Fig. 3.21. The initial loading path OA with initial stiffness K_1 is found to be significantly lower than the reloading path BC with the first reloading stiffness K_2. Further the material showed an elasto-plastic behaviour when load was removed, very little deformation being recovered by elastic rebound as illustrated in Fig. 3.21. Irrespective of the number of loading and reloading cycles, the specimen behaves like a virgin soil during each re-loading cycle.

Moreover the slope of unloading-reloading relationship is only marginally affected by the occurrence of plastic strains. Therefore the occurrence of unloading-reloading cycles of limited amplitude does not influence the behaviour of the material under further loading. At least as a first approximation the unloading-reloading cycles appear to be linear elastic. In brief it could be stated that under unloading-reloading cycles

(i) the reloading stiffness exhibits sequential increase and

(ii) significant plastic deformation accumulates.

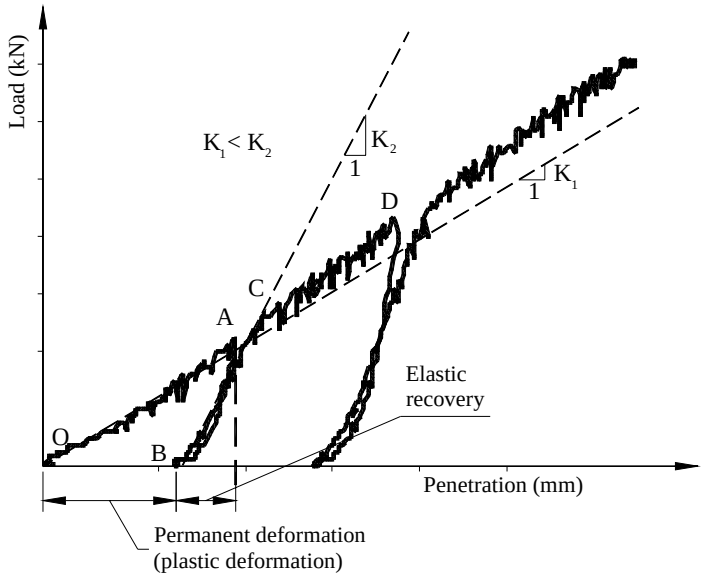

Figure 3.21 Typical unloading-reloading behaviour after the first loading

(iii) Effect of number of load cycles

Fig. 3.22 further elaborates the behaviour explained in (ii) against number of loading cycles. The stiffness increases markedly between the initial loading cycle (K_1) and the first reloading cycle (K_2) as shown in Fig. 3.22. The dry samples showed very stiff behaviour compared to OMC and saturated samples. From K_2 onwards the dry samples showed a stiffness range of 28-70kN/mm at the lower bound. For OMC the lower bound range was 7-30kN/mm, while for saturated samples the range was 5-23kN/mm indicating almost similar behaviour to that of OMC but with a slight reduction in strength. The dry samples

showed a remarkable increase from OMC and saturated while the latter two projected an overlapping region. The relevant data sheets are located in Appendix A.4.

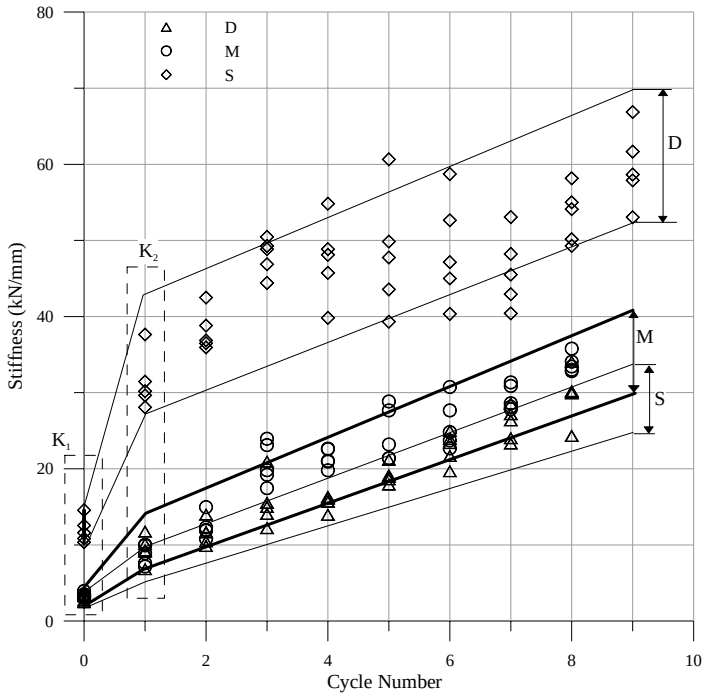

Figure 3.22 Stiffness during initial loading and reloading

In order to determine the effect of the number of load cycles to the predetermined permanent deformation (δ), the deformations were plotted against the cycle number (N) as shown in Fig. 3.23. It can be seen that there is a range in variation from lower penetration rates to higher rates. By considering all data points, irrespective of their rates, the best fit curves are found to be of the power form given by,

$$\ln(\delta) = A \times \ln(N) + B \text{ or}$$
$$\delta = c\, N^{d} \qquad (3.1)$$

where A, B, c and d are constants.

The three relationships obtained are given in Eqs. (3.2)-(3.4) for dry, OMC and saturated samples respectively together with their coefficient of determination R^2 values.

$$\ln(\delta) = 1.48 \times \ln(N) + 0.98 \text{ or}$$
$$\delta = 2.67\, N^{1.48},\ R^2 = 0.97 \qquad (3.2)$$

$$\ln(\delta) = 1.44 \times \ln(N) + 1.23 \text{ or } \delta = 3.43\, N^{1.44},\ R^2 = 0.98 \quad (3.3)$$

$$\ln(\delta) = 1.40 \times \ln(X) + 1.33 \text{ or } \delta = 3.91\, N^{1.41},\ R^2 = 0.98 \quad (3.4)$$

The dry samples showed least permanent deformations with the increasing cycle number while the saturated and OMC samples showed almost similar permanent deformations. Therefore it can be concluded that the moisture content should be the main consideration in any design together with the effect of load cycles.

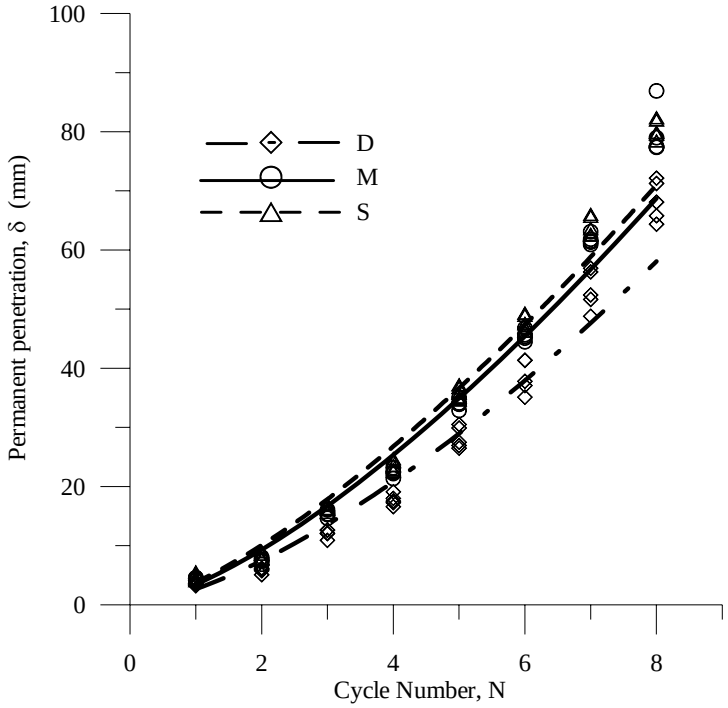

Figure 3.23 Penetration against cycle number

3.5.3 Effect of Moisture Content

In practice the natural phenomena of drying and wetting could lead to brittle and yielding types of failure in a cyclic manner causing differential settlements in the track subgrade. This was very much evident in the respective experiments of dry, OMC and saturated

states as shown in Fig. 3.24. The brittle nature is predominant in dry state while OMC and saturated states showed some ductility in their responses.

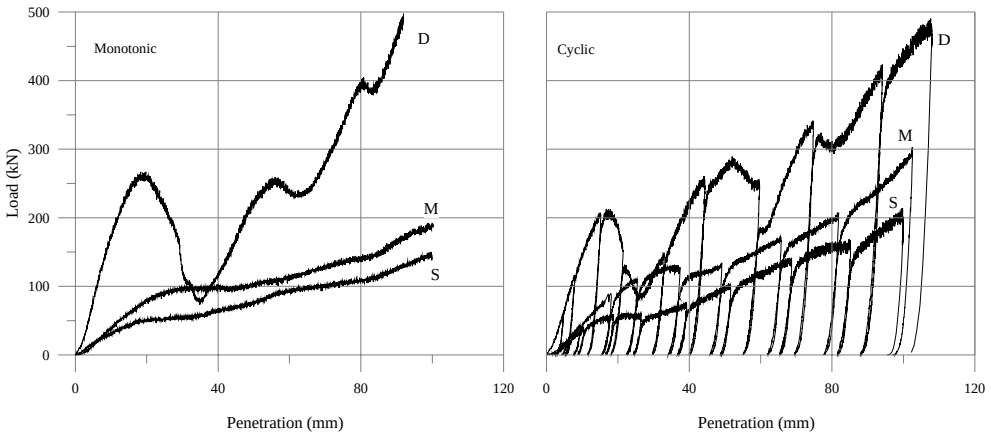

Figure 3.24 Effect of moisture content (dry specimens)

The effect of moisture on the stiffness of specimens was determined by first calculating initial and all reloading stiffnesses as illustrated in Fig. 3.22. Fig. 3.25 shows the comparison of the initial stiffness (K_1) of all tests, both monotonic and cyclic with moisture content (filled symbols show monotonic results and unfilled symbols show cyclic results). The relevant data sheets are given in Appendix A.4.

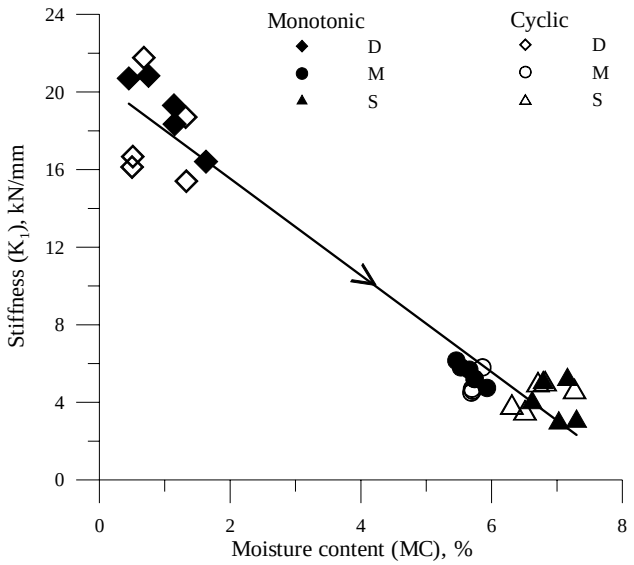

Figure 3.25 Effect of moisture content on the initial loading stiffness

K_1 showed a decreasing trend from dry to saturated condition clustered in three distinct groups.

3.5.4 Effect of Penetration Rate

The penetration rate also influences the behaviour of the soils. Particularly in dry state the behaviour can be affected much more profoundly than in the OMC or saturated states (Fig. 3.22). Thus, the behaviour of the dry specimens at 2.5mm/min and 20mm/min penetration rates for monotonic and cyclic loading are shown in Fig. 3.26. The lower rate (2.5mm/min) caused three distinct stages of material collapse and remoulding (within the entire range of penetration) while the higher rate (20mm/min) caused collapse and remoulding not very distinctly as shown in Fig. 3.26. Therefore, it can be stated that the time available for possible collapse-remoulding operation is low for fast rates. This condition is evident both in monotonic and cyclic experiments.

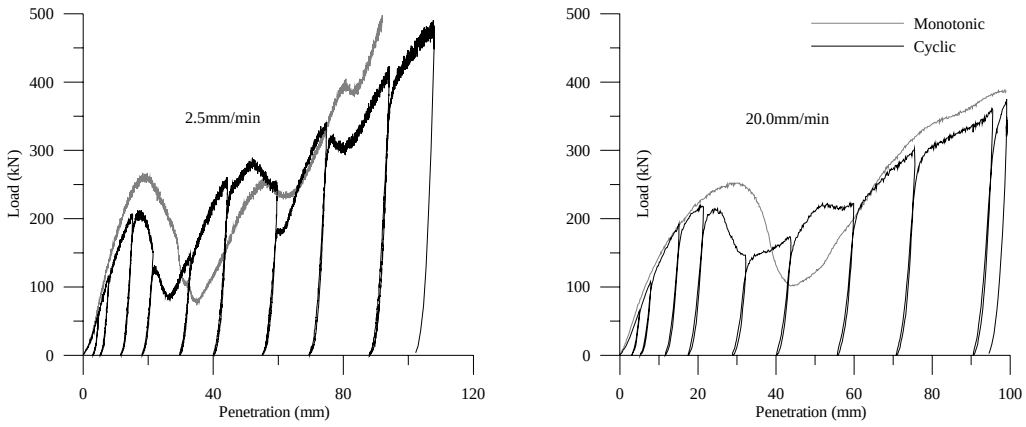

Figure 3.26 Effect of penetration rate

Fig. 3.27 illustrates the comparison of initial stiffness of all tests, both monotonic and cyclic, to the deformation rate (filled symbols show monotonic results and unfilled symbols show cyclic results). The relevant data sheets are given in Appendix A.4.

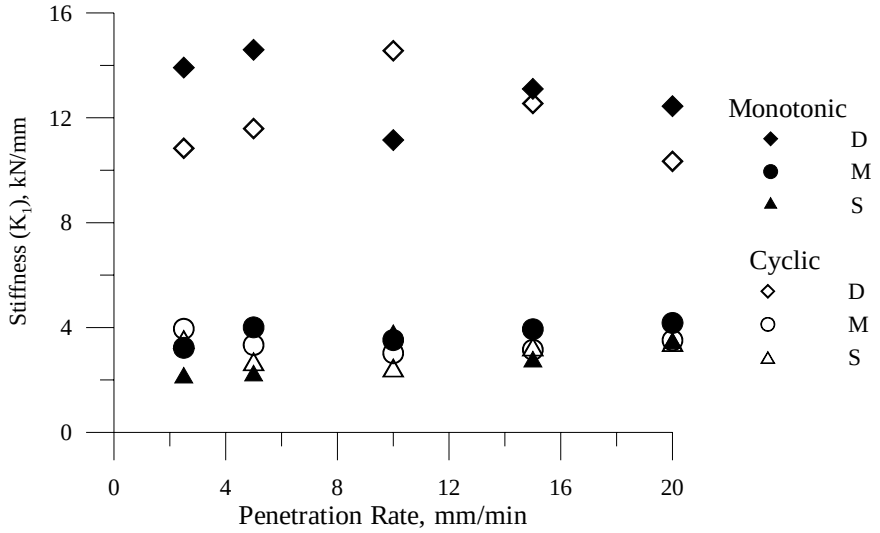

Figure 3.27 Effects of penetration rate on initial stiffness

In contrast, the penetration rate showed little effect on the initial sample stiffness compared to moisture content. However, the trends showed similar patterns of grouping at three distinct plateaus for D (dry), M (OMC) and S (saturated) conditions, where the latter two showed some overlapping.

3.5.4.1 Dimensional Analysis

Dimensional analysis was considered as a tool to differentiate the effect of penetration rate since it was difficult to visualise any marked relationship on the SCT specimens. The relevant data sheets are given in Appendix A.5 and A.6.

By accounting for the important properties a qualitative empirical relationship is established between them in the dimensional analysis (Douglas 1969; Taylor 1974). As such, for the set of experiments conducted, the load obtained (F) was considered as a function of deformation rate (V), dry density of sample (ρ_d) and the permanent deformation (δ) given by

$$F = \oint(V, \rho_d, \delta) \tag{3.6}$$

By assuming an exponential form, Eq. (3.6) is re-written as

$$F = AV^a \rho_d^b \delta^c \tag{3.7}$$

where *A*, *a*, *b*, and c are numerical constants.

Using standard procedure (Douglas 1969; Taylor 1974), the constants a, b, and c have been evaluated as a = 2, b =1 and c = 2. The relationship when these values are substituted is therefore

$$F = A \rho_d V^2 \delta^2 \tag{3.8}$$

Fig. 3.28 illustrates a typical outcome of the relationship between *F* and $(\rho_d V^2 \delta^2)$ of monotonic tests at 2.5mm/min penetration rate for dry, OMC, and saturated conditions.

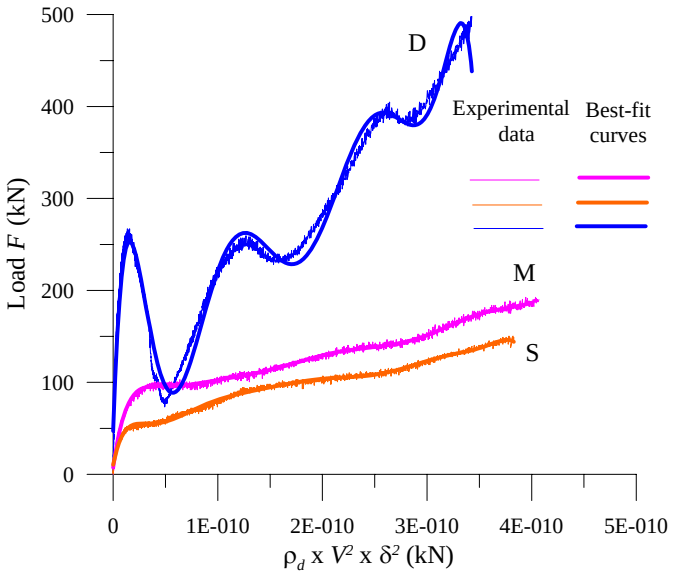

Figure 3.28 Dimensional Relationships of dry, OMC and saturated data

However, the relationship between *F* and $\rho_d V^2 \delta^2$ is found to best fit with a polynomial of degree 8. The dry sample data exhibited zigzag behaviour as shown in Fig. 3.28.

Therefore, to keep the consistency of all regression relationships, the polynomial order was kept at 8 as it was found to be the best fit for the dry sample data. The expressions obtained are of the form given by

$$F = B + pX + qX^2 + rX^3 + sX^4 + tX^5 + uX^6 + vX^7 + wX^8 \qquad (3.9)$$

where $X = (\rho_d V^2 \delta^2)$ and, p, q, r, s, t, u, v, w, and B are numerical coefficients.

The respective relationships between F and $(\rho_d V^2 \delta^2)$ with their best-fit curves for monotonic and cyclic tests are shown in Figs. 3.29 to 3.34. The best-fit constants (p, q, r, s, t, u, v, w and B) and corresponding coefficient of determination R^2 values are located in Appendix A.6. R^2 varied generally between 0.94 and 0.99 suggesting an extremely good fit to the experimental data. However, the anomalies in behaviour patterns in dry conditions are more prominent than that of moist or saturated conditions.

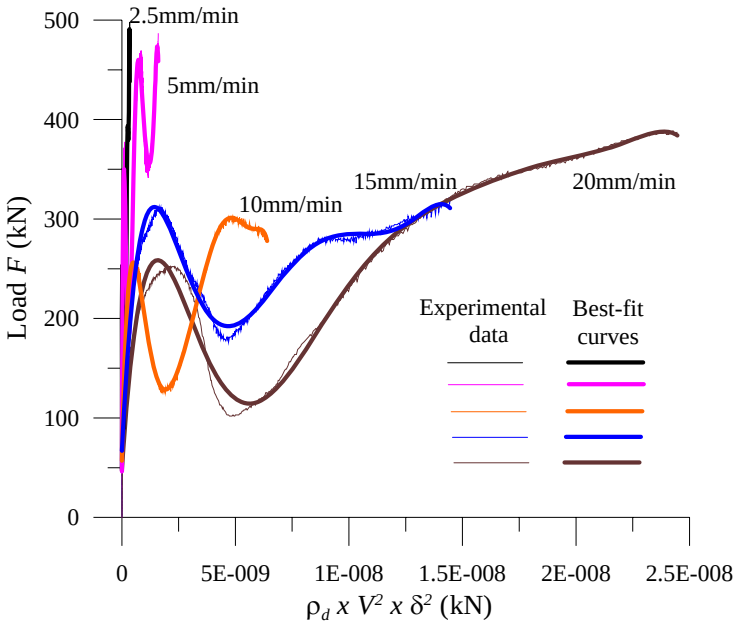

Figure 3.29 Monotonic envelope and best fit curves for dry specimens

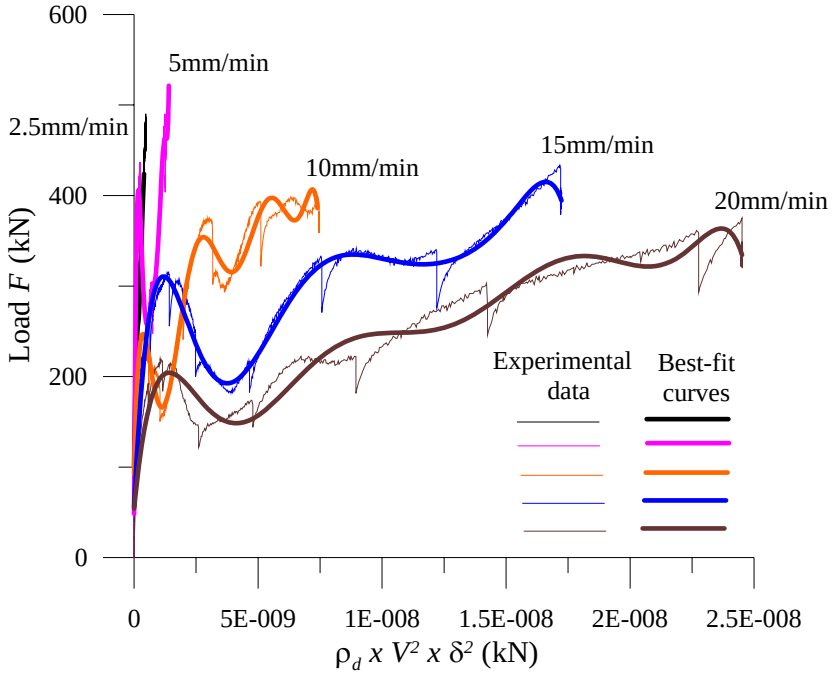

Figure 3.30 Cyclic envelope and best fit curves for dry specimens

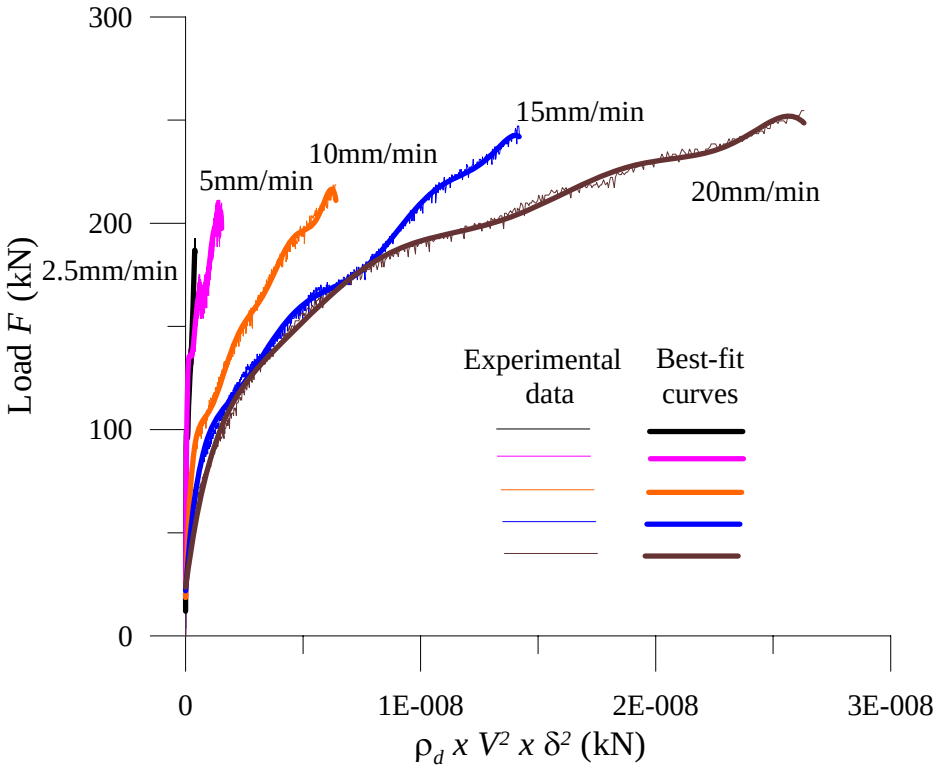

Figure 3.31 Monotonic envelope and best fit curves for OMC specimens

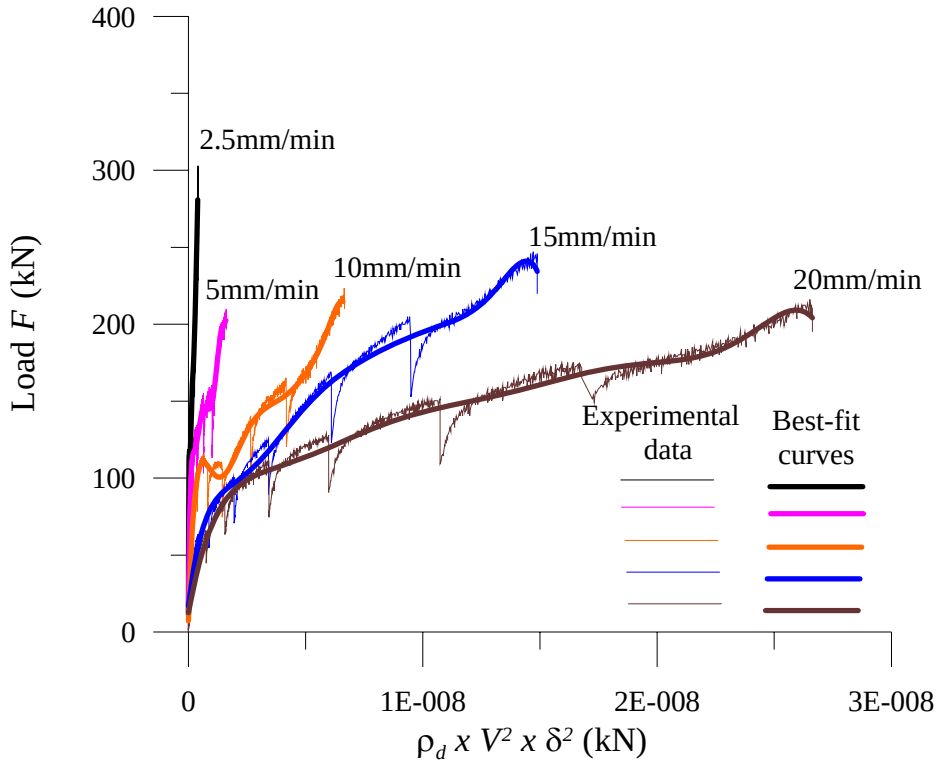

Figure 3.32 Cyclic envelope and best fit curves for OMC specimens

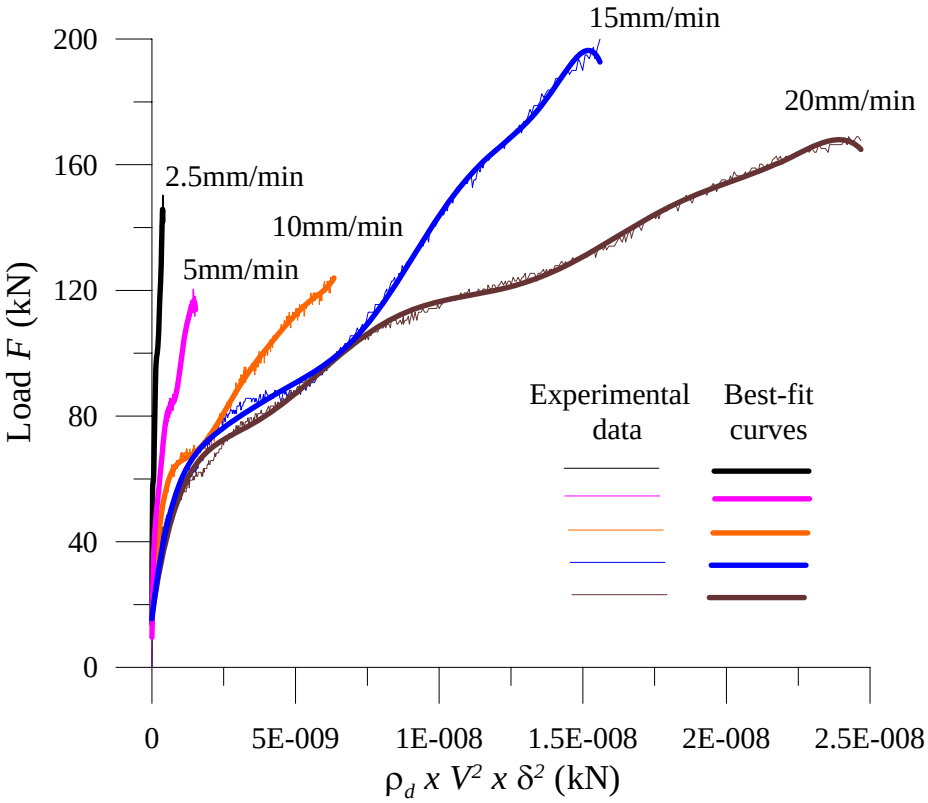

Figure 3.33 Monotonic envelope and best fit curves for saturated specimen

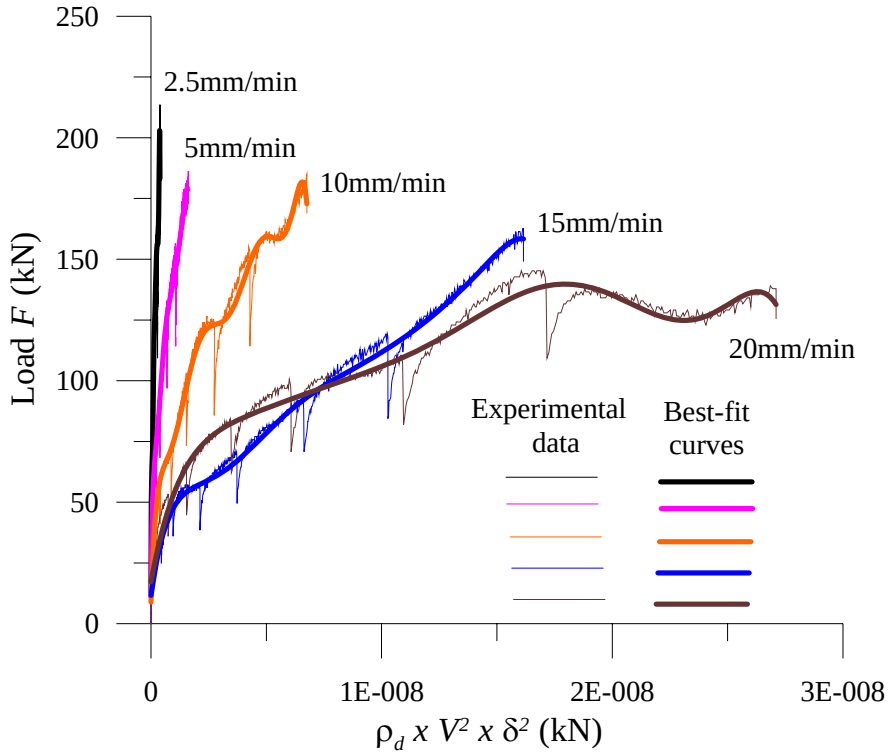

Figure 3.34 Cyclic envelope and best fit curves for saturated specimen

The dimensional analysis has shown the effect of penetration rate more clearly than the load-penetration curves. The higher the penetration rates the lower the limit load response in monotonic and cyclic tests as evident from Figs. 3.29-3.34. However, the sensitivity of load-penetration responses (monotonic or cyclic) due to penetration rates were very much lower compared to that of the moisture levels.

3.5.5 Ternary Plots

A clear and better visualisation of the relationship between the rate of penetration, moisture content and deformation are obtained via ternary plots (Figs. 3.35 and 3.36). Deformations are backcalculated from the above exercise at 25 and 50kN load levels. The loads are considered in the ranges before any secondary effects, i.e., *Stage II* in Fig. 3.13. The effect of each variable is normalised or converted to a percentage. The normalised results for

both monotonic and cyclic tests are located in Appendix A.7. Figs. 3.35 and 3.36 show the ternary plot of the results for monotonic and cyclic loading respectively. Each point in Figs. 3.35 and 3.36 has a (NQ, NF, NL) co-ordinate which denotes the percentage effect of Q, the ratio of rate of penetration to maximum rate of 20mm/min, F, the ratio of sample moisture content to OMC, and L, the ratio of penetrated depth to a deformation of 20mm. The points in Figs. 3.35 and 3.36 are labelled according to the moisture condition of each sample (D = dry, M = OMC and S = saturated).

In both monotonic and cyclic tests, OMC and saturated samples showed little variation in their positions compared to their dry counterparts. The OMC and saturated sample positions are overlapping and clustered towards each other while dry samples are clustered at a different plane altogether which is indicated by a possible boundary shown in Figs. 3.35 and 3.36. This is similar to the trends observed in stiffness calculations (Figs. 3.22, 3.25 and 3.27).

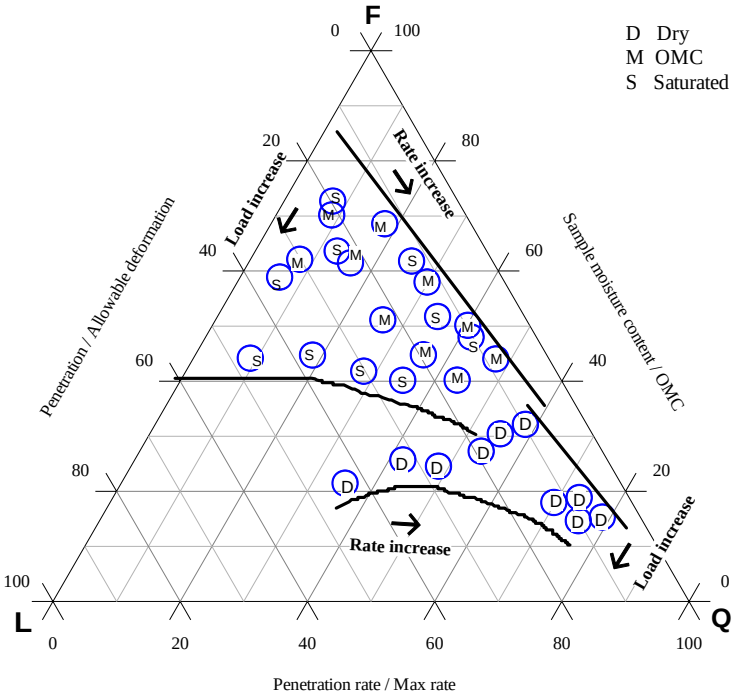

Figure 3.35 Relationship between the moisture content, rate of penetration and penetrated depth in monotonic tests

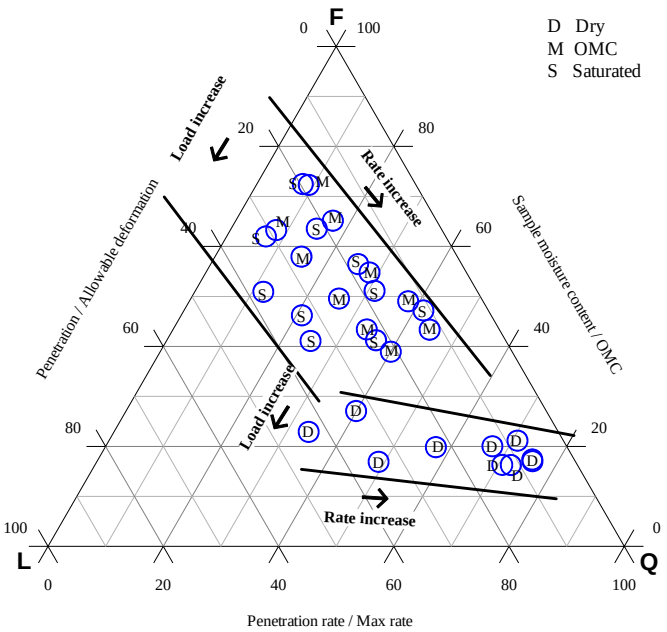

Figure 3.36 Relationship between the moisture content, rate of penetration and penetrated depth in cyclic tests

Thus it could be summarised that to establish material properties through the finite element based backcalculation procedure (described in Chapters 4 and 5), it is sufficient to group the test specimen data according to the moisture level in the specimens. This grouping would be adequate as all the variations expected in the experiments are profoundly described by the upper and lower boundary envelopes of the three groups for this very limited set of test data.

3.6 Summary

This Chapter has presented the findings of the laboratory tests undertaken as part of this thesis. Deformation controlled test results have shown a range of responses for the SCT setup specimens. These responses are categorised into hardening, softening and remoulding ranges. In a highly confined environment the specimens have shown an enhanced ability to resist increase in loading and start remoulding with the increase in the level of penetration.

In summary, these results indicate that the test procedure is capable of characterising the material at very high levels of penetration with permanent deformation in the range of 100mm. This will be more than adequate for practical considerations where a 20mm permanent deformation is usually considered excessive in a railway subgrade, calling for major remediation maintenance. The broad range of stress levels considered in the experiments provided more valuable qualitative and quantitative data than a single or narrow range of stress levels.

The dimensional analysis has shown the effect of penetration rate which otherwise is very difficult to visualise from load-penetration results. The higher the penetration rates the lower the limit load response in monotonic and cyclic tests. However, the sensitivity of load-penetration profiles to penetration rate was low compared with moisture levels irrespective of the type of loading (monotonic/cyclic) as shown in Fig.3.20.

In order to establish material properties from the testing procedure adopted, finite element modelling based back-calculation is used and will be discussed in Chapters 4 and 5. As discussed in Section 3.5.2, with caution based on the limited number of sample tested, the gross simplification of the three groups of dry (Ave m/c = 0.95%), OMC (Ave m/c = 5.7%) and saturated (Ave m/c = 6.85%) states of the material would be adequate in defining the material properties sought in a railway substructure. This is justifiable considering the vast variations in soil properties spatially even within relatively small distances in the field and their behaviour over a wide range of stress states and their mineralogical compositions (Murphy 1987).

CHAPTER 4

4. FINITE ELEMENT MODELLING (FEM) OF CAPPING LAYER MATERIAL

4.1 Introduction

Soils typically behave nonlinearly under loading. Therefore, finding a close-formed solution for problems in soil is a very difficult and complex task. Numerical methods such as the finite element methods are therefore widely used especially in engineering applications. In the finite element method, a solid continuum is reduced to a system of discrete bodies called elements interconnected through their circumferential joints called nodes. The displacements at each nodal point are then solved by equilibrium equations described by mathematical formulations to suit the practical situation. The solution is normally an approximation of the real problem due to the assumptions being made in idealising the geometry, boundary conditions and the constitutive relations. Normally the form of the numerical approximation becomes more accurate as the size of the element is reduced. Several finite element models developed for the analysis of railway track systems during the past decade have been summarised in Section 2.5.2. These models are typically based on one-, two- and three-dimensional idealisation of the rail track support system and consider non-linear behaviour of materials. Some examples of such models are CRTSS (Tayabji and Marshall 1977), MULTA, PSA, ILLI-TRACK (Adegoke et al. 1979) and GEOTRACK (Chang et al. 1980).

Results of non-linear finite element modelling are affected by the idealisation of geometry and material characteristics. As soils are granular materials, modelling of soils using continuum elements inherently simplifies geometric idealisation. Therefore there is a need

to appropriately model the material characteristics. As soils behave highly nonlinearly under loading, the theory of plasticity originally developed for the characterisation of metals has been successfully used with modifications in their modelling (Chen and Mizuno 1990).

Traditionally, railway and pavement substructures have been modelled as static linear elastic systems for structural response analysis (refer to Section 2.5.2). Chen et al. (1995) have studied various FEM pavement analysis programs. ABAQUS is one of the commercially available general purpose programs that have been successfully used in pavement analysis (Chen et al. 1995; Cho et al. 1996; Nazarian and Boddapati 1995; Uddin et al. 1995). ABAQUS offers linear and nonlinear elastic and elasto-plastic material modelling for static, harmonic dynamic and transient dynamic loading simulations, and interface modelling. The infinite element library provided in ABAQUS can be used to represent the semi-infinite boundary conditions in the horizontal, vertical or longitudinal directions of rail track or pavement systems (ABAQUS 2002).

Finite element modelling of the semi-confined cylinder test (SCT) setup described in Chapter 3 is a complex phenomenon. Testing was carried out by penetrating a rigid piston into the capping layer material to a depth of 100mm whilst the height of the specimen itself was only 177.5 mm. This means that the sample was, on average, subjected to large strains which call for extreme care for mesh quality during deformation; an effective re-meshing would be required to minimise or eliminate extreme mesh distortion. Adaptive-meshing tool provided in ABAQUS/Explicit makes it possible to maintain a high-quality mesh under severe material deformation.

The quasi-static analysis method using explicit solution technique provides an economical solution to otherwise time consuming natural time scale solutions. In the quasi-static procedure, the dominant inertial forces evolved by accelerating the analysis speed are made insignificant by modelling the process in the shortest possible time. However, if the analysis speed is increased to a point at which inertial effects dominate, the solution may localise and the results would tend to be unreliable. Another issue, a major one, is appropriate representation of the constitutive material modelling of the capping layer soil under high levels of confining pressure, especially during deeper penetration stages. The material behaviour through any new mechanical constitutive model is implemented by the user defined material routine VUMAT in ABAQUS/Explicit (ABAQUS 2002).

This Chapter provides a brief introduction to the theory of plasticity and constitutive modelling of the capping layer material. It also describes the finite element analysis procedure of the SCT set-up. The relevant data sheets are provided in Appendices B.1-B.4.

APPENDIX B.1	Frequency analysis and step time calculations
APPENDIX B.2	Mesh refinement of SCT FEM
APPENDIX B.3	Typical ABAQUS/Explicit INPUT file/User subroutine
APPENDIX B.4	Sensitivity of modelling parameters in SCT FEM

4.2 Brief Review of Theory of Plasticity

Under low levels of imposed loading, materials behave elastically; in such cases stresses remain proportional to strains. With the increase in load levels, materials undergo significant increase in strain for very small increase in stress; such increase in strain is termed ‘plastic flow’ of the material. In plastic flow theory the total strain of a material is

considered as the sum of recoverable elastic strain and permanent plastic strain components. Therefore, the total strain increment can be written in the form:

$$d\varepsilon_{ij} = d\varepsilon_{ij}^{e} + d\varepsilon_{ij}^{p} \tag{4.1}$$

where $d\varepsilon_{ij}^{e}$ = elastic strain increment and $d\varepsilon_{ij}^{p}$ = plastic strain increment.

Numerical functions that define a material behaviour at the yield limit are termed as yield functions or yield criteria. In general, the initial yield function f is defined as:

$$f(\sigma_{ij}) = f_c \tag{4.2}$$

where f_c is a constant or a function of the accumulated plastic strain.

A plastic material allows yield function f_c to be fixed in the stress space or to expand or contract as plastic strain develops. The fixed yield surface is generalised to a loading surface for a hardening material, and a hardening rule is used to define the kinematics of the yield surface during plastic flow.

The relationship between plastic strain ratio and stress ratio is termed the flow rule governing the mechanism of plastic deformation. The flow rule defines the subsequent increment of the plastic strain of a yielded body subjected to further loading. This is established through the concept of plastic potential function g which defines the direction of plastic strain increment given by:

$$d\varepsilon_{ij} = d\lambda \frac{\partial g}{\partial \sigma_{ij}} \tag{4.3}$$

where $d\lambda$ = positive scalar of proportionality that depends on the state of stress and load history. If the potential and yield functions coincide with each other ($f \approx g$), the flow rule is called the associated flow rule; otherwise the non- associated flow rule applies.

There are a number of hardening rules available to describe the evolution of the loading surfaces, viz., isotropic hardening, kinematic hardening and mixed hardening. In isotropic hardening the loading surface is allowed to expand or contract while affixed to its origin (Fig. 4.1).

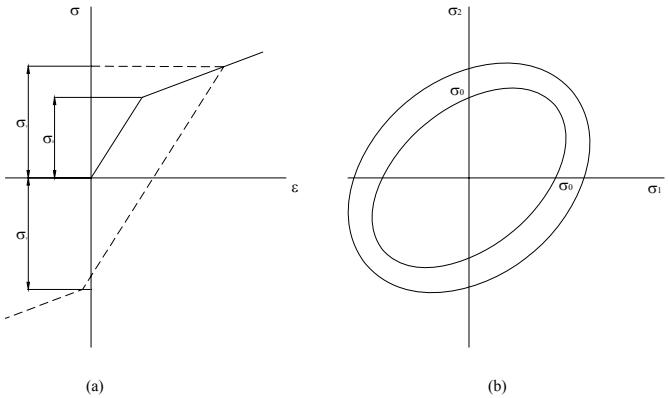

Figure 4.1 Isotropic hardening (a) uniaxial stress-strain diagram (b) evolution of the yield surface in the biaxial stress plane (Jirasek and Bazant 2002)

In kinematic hardening the loading surface is not allowed to expand but allowed to move as a rigid body within the stress space (Fig. 4.2). The mixed rule allows the loading surface to either expand or contact uniformly as well as to translate in the stress space. The kinematic hardening model is suitable for cyclic and reversed type of loading as it takes into account Bauschinger effect (Chen and Mizuno 1990; Jirasek and Bazant 2002).

The Bauschinger effect describes one particular type of directional anisotropy induced by the plastic deformations. The initial plasticity of one sign reduces the resistance of the material with respect to the subsequent plastic deformation of the opposite sign (Chen and Mizuno 1990). This means that the tensile and compressive yield stresses differ when material is subjected to cyclic or reversed type of loading which is pronounced in materials such as soils and steels.

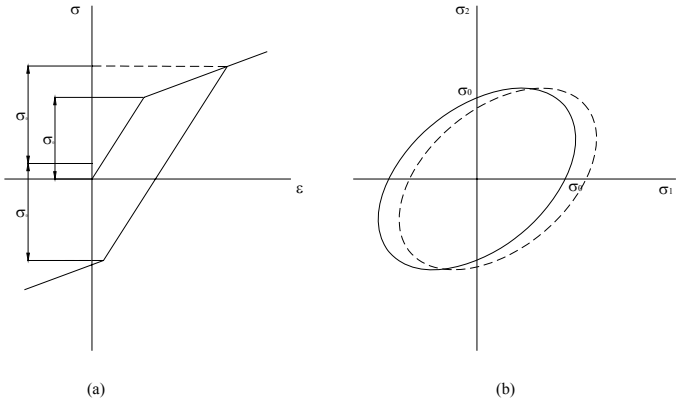

Figure 4.2 Kinematic hardening (a) uniaxial stress-strain diagram (b) evolution of the yield surface in the biaxial stress plane (Jirasek and Bazant 2002)

4.3 Constitutive Modelling of the Capping Layer Material

To express the experimental behaviour of the capping layer material described in Chapter 3 into a mathematical representation, an elasto-plastic constitutive model with hardening parameters is necessary. The Drucker-Prager isotropic hardening model was used to represent the pressure-sensitive capping layer material behaviour. It was noted that the increase in confining pressures obviously influenced the material behaviour. Therefore, a stress-dependent elastic modulus was incorporated in the constitutive model. The constitutive model with variable elastic modulus is described as follows.

As described in Section 4.2, the total strain-increment includes the elastic strain increment $d\varepsilon_{ij}^{e}$ and plastic strain increment $d\varepsilon_{ij}^{p}$. In this section, the theory of plastic constitutive modelling is expressed using tensor notation. Explanation of the symbols used in the definition of tensors is beyond the scope of this thesis. Furthermore, there appears to be no 'standard' form of arranging notations in tensor form. The symbols used in this thesis broadly follow Chen and Mizuno, (1990) and Chen and Han (1988).

The plastic strain increment tensor is obtained from the associated flow rule:

$$d\varepsilon_{ij}^{p} = d\lambda \frac{\partial f}{\partial \sigma_{ij}} \tag{4.4}$$

Where $d\lambda \begin{cases} = 0 \text{ when } (f < 0) \text{ or } (f = 0 \text{ but } df < 0); \\ > 0 \text{ when } (f = 0 \text{ and } df = 0). \end{cases}$

The elastic stress-strain relation is expressed using Hooke's law:

$$d\sigma_{ij} = C_{ijkl} d\varepsilon_{kl}^{e} \tag{4.5}$$

where C_{ijkl} is the tensor of elastic moduli.

Therefore,

$$\begin{aligned} d\sigma_{ij} &= C_{ijkl}(d\varepsilon_{kl} - d\varepsilon_{kl}^{p}) \\ &= C_{ijkl} d\varepsilon_{kl} - d\lambda C_{ijkl} \frac{\partial f}{\partial \sigma_{ij}} \end{aligned} \tag{4.6}$$

The tensor of elastic moduli, C_{ijkl} in Eq. (4.6) can be expressed using shear modulus G and bulk modulus, K as,

$$C_{ijkl} = \left(K - \frac{2}{3} G \right) \delta_{ij} \delta_{kl} + G(\delta_{ik} \delta_{jl} + \delta_{il} \delta_{jk}) \tag{4.7}$$

where $\delta_{ij}, \delta_{kl}, \delta_{ik}, \delta_{jl}, \delta_{il}$, and δ_{jk} are Kronecker deltas.

Substituting Eq. (4.7) into Eq. (4.6) provides,

$$d\sigma_{ij} = 2G d\varepsilon_{ij} + K d\varepsilon_{kk} \delta_{ij} - d\lambda \left[\left(K - \frac{2}{3} G \right) \frac{\partial f}{\partial \sigma_{mn}} \delta_{mn} \delta_{ij} + 2G \frac{\partial f}{\partial \sigma_{ij}} \right] \tag{4.8}$$

For perfectly plastic materials, the general expression of a yield surface has the form

$$f(\sigma_{ij}) = 0 \tag{4.9}$$

The consistency condition is assumed as:

$$df = \frac{\partial f}{\partial \sigma_{ij}} d\sigma_{ij} = 0 \tag{4.10}$$

Now, for Drucker – Prager Model the yield criterion *f* is given by:

$$f = \sqrt{J_2} + \alpha I_1 - k = 0 \tag{4.11}$$

where $I_1 = \sigma_{ii}$ is the first invariant of stress tensor, and $J_2 = \frac{1}{2} s_{ij} s_{ij}$ is the second invariant of deviatoric stress tensor $s_{ij} = \sigma_{ij} - \frac{1}{3} I_1 \delta_{ij}$. α and k are positive material parameters related to soil friction angle and cohesion.

From Eqs. (4.8), (4.10) and (4.11), the most general form of Drucker-Prager elastic-perfectly plastic constitutive relationship is given by:

$$d\sigma_{ij} = \left[2G\delta_{im}\delta_{jn} + \left(K - \frac{2}{3} G \right) \delta_{ij}\delta_{mn} - \frac{\frac{G}{\sqrt{J_2}} s_{ij} + 3K\alpha\delta_{ij}}{G + 9K\alpha^2} \left(\frac{G}{\sqrt{J_2}} s_{mn} + 3K\alpha\delta_{mn} \right) \right] d\varepsilon_{mn} \tag{4.12}$$

Note that the quantity within the outer parenthesis represents the stress dependent material constant.

Also, the stress-strain relation corresponding to the yield function can be expressed as:

$$d\varepsilon_{ij} = \frac{ds_{ij}}{2G} + \frac{dI_1}{9K} \delta_{ij} + d\lambda \left(\frac{s_{ij}}{2\sqrt{J_2}} + \alpha\delta_{ij} \right) \tag{4.13}$$

where

$$d\lambda = \frac{\left(G / \sqrt{J_2} \right) s_{mn} de_{mn} + 3K\alpha d\varepsilon_{kk}}{G + 9K\alpha^2} \tag{4.14}$$

As discussed by Drucker and Prager (1952), a very important feature of Eq. (4.14) is that the plastic rate of cubical dilation is provided by

$$d\varepsilon_{kk}^{p} = 3\alpha d\lambda \,. \tag{4.15}$$

Eq. (4.15) shows that plastic deformation must be accompanied by an increase in volume if $\alpha \neq 0$. This property is known as dilatancy; it is the consequence of the dependency of the yield function on hydrostatic pressure.

The general expression of a yield surface of a hardening material has the form:

$$f(\sigma_{ij}, \varepsilon_{ij}^{p}, k) = 0 \tag{4.16}$$

Hence the consistency condition is assumed as:

$$df = \frac{\partial f}{\partial \sigma_{ij}} d\sigma_{ij} + \frac{\partial f}{\partial \varepsilon_{ij}^{p}} d\varepsilon_{ij}^{p} + \frac{\partial f}{\partial k} dk = 0 \tag{4.17}$$

This ensures that in the plastic loading process, the subsequent stress and deformation states remain on the subsequent yield surface. Thus, the general form of the loading function of the Drucker-Prager isotropic hardening model can be expressed as:

$$f(\sigma_{ij}, \varepsilon_{p}) = \sqrt{J_2} + \alpha(\varepsilon_{p})\, I_1 - k(\varepsilon_{p}) = 0 \tag{4.18}$$

The stress-strain equation for a perfectly plastic material has been presented in Eq. (4.12) with α = constant and k = constant. If we assume that the slope of the loading function in the $I_1 - J_2^{1/2}$ space is a constant, $\alpha(\varepsilon_{p}) = \alpha_1$ and the hardening behaviour can be determined through the hardening parameter $k(\varepsilon_{p})$ given by:

$$f(\sigma_{ij}, \varepsilon_{p}) = \sqrt{J_2} + \alpha_1\, I_1 - k(\varepsilon_{p}) = 0 \tag{4.19}$$

As shown in Eq. (4.15), the plastic deformation of Drucker-Prager material is always accompanied by a dilation of volume if the associated flow rule is considered. In this case, the rate of dilation is controlled by the parameter α . Now the potential function can be defined similarly to the loading function, Eq. (4.19):

$$g(\sigma_{ij}) = \sqrt{J_2} + \alpha_2 \, I_1 \tag{4.20}$$

where $0 \le \alpha_2 \le \alpha_1$ is a constant.

The derivatives of f and g are obtained as:

$$\frac{\partial f}{\partial \sigma_{ij}} = \alpha_1 \delta_{ij} + \frac{1}{2\sqrt{J_2}} s_{ij} \tag{4.21}$$

$$\frac{\partial g}{\partial \sigma_{ij}} = \alpha_2 \delta_{ij} + \frac{1}{2\sqrt{J_2}} s_{ij} \, . \tag{4.22}$$

If $f = g$ or $\alpha_1 = \alpha_2$, the plastic constitutive relation follows the associated flow rule. However, in this thesis we follow the non-associated flow rule ($f \neq g$ or $\alpha_1 \neq \alpha_2$) represented by the inclusion of a dilation angle ψ . Crisfield (1991) also discussed that the non-associated plasticity is mainly relevant to geomechnical material such as soils, stating that the experimental evidence of such materials has shown that flow direction is usually not normal to the yield surface f , but considered normal to some second function g , defined as the plastic potential.

Using the elastic tensor given in Eq. (4.7) we obtain

$$H_{kl} = C_{ijkl} \frac{\partial f}{\partial \sigma_{ij}} = 3K\alpha_1 \delta_{kl} + \frac{G}{2\sqrt{J_2}} s_{kl} \tag{4.23}$$

$$H^*_{kl} = C_{ijkl} \frac{\partial g}{\partial \sigma_{ij}} = 3K\alpha_2 \delta_{kl} + \frac{G}{2\sqrt{J_2}} s_{kl} \tag{4.24}$$

The isotropic hardening parameter, k can be obtained as:

$$dk = \frac{\partial k}{\partial \varepsilon_p} d\varepsilon_p \tag{4.25}$$

where

$$d\varepsilon_p = C\sqrt{d\varepsilon_{ij}^p d\varepsilon_{ij}^p} \tag{4.26}$$

Therefore,

$$dk = \frac{\partial k}{\partial \varepsilon_p} C\sqrt{\frac{\partial f}{\partial \sigma_{ij}}\frac{\partial f}{\partial \sigma_{ij}}} d\lambda \tag{4.27}$$

$d\varepsilon_p$ can be obtained from Eq. (4.4) and $d\sigma_{ij}$ can be obtained from Eq. (4.6) and by substituting these in Eq. (4.27), we obtain:

$$df = \frac{\partial f}{\partial \sigma_{ij}} C_{ijkl} d\varepsilon_{kl} - h d\lambda \tag{4.28}$$

where

$$h = \frac{\partial f}{\partial \sigma_{ij}} C_{ijkl} \frac{\partial g}{\partial \sigma_{kl}} - \frac{\partial f}{\partial \varepsilon_{ij}^p}\frac{\partial g}{\partial \sigma_{ij}} - \frac{\partial f}{\partial k}\frac{\partial k}{\partial \varepsilon_{ij}^p} C\sqrt{\frac{\partial g}{\partial \sigma_{ij}}\frac{\partial g}{\partial \sigma_{ij}}} \,. \tag{4.29}$$

From Eq. (4.28), $d\lambda$ can be solved as:

$$d\lambda = \frac{1}{h}\frac{\partial f}{\partial \sigma_{ij}} C_{ijkl} d\varepsilon_{kl} = \frac{1}{h} H_{kl} d\varepsilon_{kl} \tag{4.30}$$

where the second order tensor H_{kl} is defined as,

$$H_{kl} = \frac{\partial f}{\partial \sigma_{ij}} C_{ijkl} \tag{4.31}$$

for the yield function, f and for the potential function, g

$$H_{kl}^* = \frac{\partial g}{\partial \sigma_{ij}} C_{ijkl} \,. \tag{4.32}$$

For Drucker-Prager material the effective stress σ_e can be written as

$$\sigma_e = \frac{\sqrt{3}(\alpha_1 I_1 + \sqrt{J_2})}{1+3\alpha_1} \tag{4.33}$$

Using Eq. (4.19) k is expressed in terms of σ_e

$$k = \alpha_1 I_1 + \sqrt{J_2} = \frac{1+3\alpha_1}{\sqrt{3}}\sigma_e . \tag{4.34}$$

Therefore,

$$\frac{dk}{d\varepsilon_p} = \frac{1+3\alpha_1}{\sqrt{3}}\frac{d\sigma_e}{d\varepsilon_p} = \frac{1+3\alpha_1}{\sqrt{3}}H_p . \tag{4.35}$$

where hardening modulus H_p can be determined by fitting a tangential modulus at large strains from a uniaxial stress-strain curve, $d\sigma = H_p d\varepsilon$.

Thus, from the work done by an incremental plastic strain,

$$d\varepsilon_p = \frac{dW_p}{\sigma_e} = \frac{\sigma_{kl} d\varepsilon_{kl}^p}{\sigma_e} = C\sqrt{d\varepsilon_{ij}^p d\varepsilon_{ij}^p} . \tag{4.36}$$

Therefore, the parameter C can be obtained as:

$$C = \frac{\sigma_{kl}\dfrac{\partial g}{\partial \sigma_{kl}}}{\sqrt{\dfrac{\partial g}{\partial \sigma_{st}}\dfrac{\partial g}{\partial \sigma_{st}}}\sigma_e} . \tag{4.37}$$

By substituting Eqs. (4.21) to (4.24) and Eqs. (4.33) to (4.37) into Eq. (4.29) we can obtain the scalar function, h as,

$$h = G + 9K\alpha_1\alpha_2 + \frac{\alpha_2 I_1 + \sqrt{J_2}}{3k}(1+\sqrt{3}\alpha_1)^2 H_p . \tag{4.38}$$

Therefore the plastic strain increment, $d\varepsilon_{ij}^{p}$ is given by

$$d\varepsilon_{ij}^{p} = d\lambda \frac{\partial g}{\partial \sigma_{ij}} = \frac{1}{h} \frac{\partial f}{\partial \sigma_{mn}} C_{mnst} \frac{\partial g}{\partial \sigma_{ij}} d\varepsilon_{st} = \frac{1}{h} H_{st} \frac{\partial g}{\partial \sigma_{ij}} d\varepsilon_{st} . \tag{4.39}$$

The elastic-plastic tangent stiffness tensor is obtained as:

$$C_{ijkl}^{ep} = C_{ijkl} - \frac{1}{h} H_{ij}^{*} H_{kl} \tag{4.40}$$

The stress increment $\partial \sigma_{ij}$ can be determined as

$$\begin{aligned} d\sigma_{ij} &= C_{ijkl}(d\varepsilon_{kl} - \frac{1}{h} \frac{\partial f}{\partial \sigma_{mn}} C_{mnst} \frac{\partial g}{\partial \sigma_{kl}} d\varepsilon_{st}) = C_{ijkl}(\delta_{sk}\delta_{tl} - \frac{1}{h} \frac{\partial f}{\partial \sigma_{mn}} C_{mnst} \frac{\partial g}{\partial \sigma_{kl}}) d\varepsilon_{st} \\ &= (C_{ijst} - \frac{1}{h} \frac{\partial f}{\partial \sigma_{mn}} C_{mnst} C_{ijkl} \frac{\partial f}{\partial \sigma_{kl}}) d\varepsilon_{st} = (C_{ijst} - \frac{1}{h} H_{st} H_{ij}) d\varepsilon_{st} \end{aligned} \tag{4.41}$$

Hence, the most general form of Drucker-Prager isotropic hardening elasto-plastic constitutive relationship can be written as

$$d\sigma_{ij} = \left[\begin{array}{l} 2G\delta_{im}\delta_{jn} + \left(K - \frac{2}{3} G \right) \delta_{ij}\delta_{mn} \\ - \left(\dfrac{\dfrac{G}{\sqrt{J_2}} s_{ij} + 3K\alpha_2 \delta_{ij}}{G + 9K\alpha_1\alpha_2 + \dfrac{\alpha_2 I_1 + \sqrt{J_2}}{3k} (1 + \sqrt{3}\alpha_1)^2 H_p} \right) \\ \quad \mathrm{x} \left(\dfrac{G}{\sqrt{J_2}} s_{mn} + 3K\alpha_1 \delta_{mn} \right) \end{array} \right] d\varepsilon_{mn} \tag{4.42}$$

The Drucker-Prager parameters α_1 and α_2 can be obtained by approximating Mohr-Coulomb hexagon in the deviatoric stress plane (Desai and Christian 1977; Wang and Sitar 2004). Fig. 4.3 shows how the compression cone and the extension cone are defined to match Mohr-Coulomb criterion by either triaxial compression or extension tests. An

internal cone is inscribed inside Mohr-Coulomb criterion. An intermediate cone is also defined as an "average" between extension and compression approximations. For various Drucker-Prager approximations, Table 4.1 summaries the determination of model parameters with respect to soil friction angle (angle of shearing resistance) ϕ, cohesion c, and dilatancy angle ψ. For three-dimensional matching, relevant compression cone expressions are used while, for plane strain matching, the internal cone expressions are used (Chen and Mizuno 1990). Accordingly the compression cone expressions for the axisymmetric simulations and internal cone expressions for the plane strain simulations were used in this thesis.

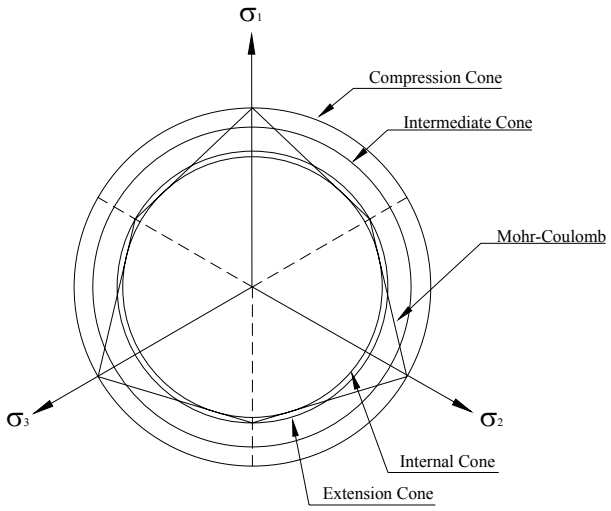

Figure 4.3 Drucker-Prager approximations (Wang and Sitar 2004)

Table 4.1 Model Parameters α_1, α_2, and k (Wang and Sitar 2004)

Drucker-Prager Approximation	Parameter α_1	Parameter α_2	Parameter k
Compression Cone	$\alpha_1 = \frac{2\sin\phi}{\sqrt{3}(3-\sin\phi)}$	$\alpha_2 = \frac{2\sin\psi}{\sqrt{3}(3-\sin\psi)}$	$k = \frac{6c\cos\phi}{\sqrt{3}(3-\sin\phi)}$
Intermediate Cone	$\alpha_1 = \frac{2\sin\phi}{3\sqrt{3}}$	$\alpha_2 = \frac{2\sin\psi}{3\sqrt{3}}$	$k = \frac{6c\cos\phi}{3\sqrt{3}}$
Extension Cone	$\alpha_1 = \frac{2\sin\phi}{\sqrt{3}(3+\sin\phi)}$	$\alpha_2 = \frac{2\sin\psi}{\sqrt{3}(3+\sin\psi)}$	$k = \frac{6c\cos\phi}{\sqrt{3}(3+\sin\phi)}$
Internal Cone	$\alpha_1 = \frac{\sin\phi}{\sqrt{3}\sqrt{(3+\sin^2\phi)}}$	$\alpha_2 = \frac{\sin\psi}{\sqrt{3}\sqrt{(3+\sin^2\psi)}}$	$k = \frac{3c\cos\phi}{\sqrt{3}\sqrt{(3+\sin^2\phi)}}$

4.3.1 Stress Dependent Elastic Modulus

In order to accommodate the varying confining stresses induced in the SCT setup, a stress-dependent elastic modulus is defined instead of a constant elastic modulus. Thus, the shear modulus *G* and bulk modulus, *K* will become stress-dependent in the analysis. The initial modulus (E_i) was assumed to vary with the confining pressure (σ_3) according to the relationship:

$$E_i = K_a p_a \left(\frac{\sigma_3}{p_a} \right)^n \tag{4.43}$$

where p_a = reference pressure (usually taken as atmospheric pressure = 100kPa), K_a and *n* are constants to be determined (Desai and Christian 1977).

Desai and Christian (1997) assumed a hyperbolic model for the stress-strain relationship, the tangent modulus (E_t) at any level of stress or strain being given by:

$$E_t = \frac{\partial \sigma}{\partial \varepsilon} = E_i \left(1 - \frac{R_f \sigma}{s} \right)^2 \tag{4.44}$$

where s = compressive strength and R_f = the ratio of ultimate deviatoric stress of original hyperbolic stress-strain curve to the actual deviatoric stress of soil at failure, a factor between 0.7 and 0.9.

For a Mohr-Coulomb material at failure

$$\left(\sigma_1 - \sigma_3 \right)_f = \frac{2\sigma_3 + 2c\cos\phi}{1 - \sin\phi} \tag{4.45}$$

where c = cohesion, ϕ = friction angle and $\left(\sigma_1 - \sigma_3 \right)_f$ = deviatoric stress at failure.

The term $\frac{\sigma}{s}$ is the ratio between the existing $(\sigma_1 - \sigma_3)$ and s that would be available for the existing σ_3.

Thus,

$$\frac{\sigma}{s} = \frac{(\sigma_1 - \sigma_3)(1 - \sin\phi)}{2\sigma_3 \sin\phi + 2c\cos\phi} \tag{4.46}$$

The tangent modulus in Eq. (4.44) now becomes

$$E_t = E_i \left[1 - \frac{R_f (\sigma_1 - \sigma_3)(1 - \sin\phi)}{2\sigma_3 \sin\phi + 2c\cos\phi} \right]^2 \tag{4.47}$$

By substituting Eq. (4.43) in Eq. (4.47), the complete relationship now becomes

$$E_t = K_a p_a \left(\frac{\sigma_3}{p_a} \right)^n \left[1 - \frac{R_f (\sigma_1 - \sigma_3)(1 - \sin\phi)}{2\sigma_3 \sin\phi + 2c\cos\phi} \right]^2 \tag{4.48}$$

E_t in Eq. (4.48) varies with the stress and could mathematically achieve zero or very high values. But in reality E_t cannot be zero, nor can it have unrealistically high values. Therefore E_t was imposed a range $E_0 \le E_t \le E_{\max}$ in the user subroutine, where E_0 is the minimum E_t and $E_{\max}$ is the maximum E_t. Values for these maxima and minima are user defined. In order to obtain the material parameters K_a and n a series of drained triaxial tests were carried out at 100, 375, 750, 1000 and 2000kPa confining pressures (refer Section 5.2).

4.3.2 Stress Dependent Friction Angle

Murphy (1987) has discussed that the measured angle of shearing resistance ϕ_d (referred as friction angle in this thesis) can be represented in various components given by

$$\phi_d = \phi_u + \phi_r + \phi_\delta + \phi_{\deg} \qquad (4.49)$$

where

ϕ_d = the measured angle of shearing resistance

ϕ_u = the angle of mineral friction

ϕ_r = the component of shearing resistance caused by particle reorientation

ϕ_δ = the dilatancy component of shearing resistance and

$\phi_{\deg}$ = the component of shearing resistance attributable to particle degradation.

Various other authors have discussed the stress-dependency of the friction angle or the angle of shearing resistance (Bolton 1986; Charles and Watts 1980; Murphy 1987; Selig and Waters 2000). Usually, the shear strength of granular material measured in a drained triaxial test with a particular confining pressure is given in terms of

$$\phi = \sin^{-1} \frac{(\sigma_1 / \sigma_3)_f - 1}{(\sigma_1 / \sigma_3)_f + 1} \qquad (4.50)$$

where ϕ = angle of shearing resistance (friction angle) and $(\sigma_1 / \sigma_3)_f$ = the maximum principal stress ratio, i.e. it is assumed that cohesion (c) is zero (Charles and Watts 1980). The curvature of the Mohr strength envelope and its significance at low and high stress levels are incorporated in the above Eqn. 4.50 at $c = 0$.

Therefore, a general formulation of stress dependency hypothesis can be developed using a similar approach by defining failure envelopes by values of the parameters c and ϕ, i.e. $c \neq 0$. In order to assess the range of normal stress on the critical failure surface, a series of drained triaxial tests were carried out at 100, 375, 750, 1000 and 2000kPa confining pressures (refer Section 5.2). Next, values of c and ϕ were selected to give the best approximation to the actual failure envelopes at 100-375kPa, 375-750kPa and 1000-2000kPa stress ranges. Then a statistical best-fit was obtained from these results to incorporate the stress dependency of the friction angle as a function of $(\sigma_1 / \sigma_3)_f$.

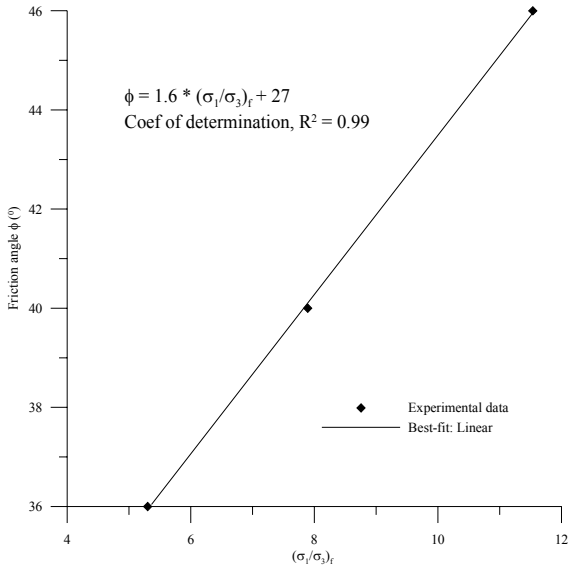

Figure 4.4 Stress dependency of the friction angle

Fig. 4.4 shows the variation in the friction angle with the increase in stress. The relationship obtained was then incorporated into the constitutive relationship given by equation 4.51.

$$\phi = 1.6\left(\frac{\sigma_1}{\sigma_3}\right)_f + 27 \qquad (4.51)$$

It is evident from Fig. 4.4 that, with the variations in the stress conditions the Mohr failure envelopes have shown pronounced curvature at low stresses. Thus as in the case of E_t, a range was imposed in the subroutine for ϕ in the form of $\phi_{min} \leq \phi \leq \phi_{max}$ where ϕ_{min} is the minimum ϕ and ϕ_{max} is the maximum ϕ which are user defined.

It is also noted that the above explicit descriptions developed in mathematical terms can not describe the actual behaviour of soils over a wide range of conditions and in fact are bound to be a drastic idealization (Chen and Mizuno 1990). Thus, when comparing the model predictions with experimental results in Chapter 5, agreement in minute detail was not expected but a satisfactory agreement in trends generally was sought.

4.4 Finite Element (FE) Analysis of SCT Setup

4.4.1 *Explicit Solution Algorithm (ABAQUS 2002)*

The Explicit time integration procedure uses a central difference rule to integrate the equations of motion explicitly in time domain using the kinematic principles successively. As a consequence of this approach, an excessive number of explicit integrations with extremely small time steps will be required. In spite of this requirement, the explicit approach remains more economical than the implicit method as the whole system stiffness matrices are not used in the solution process. The term "explicit" refers to the fact that the state at the end of the increment is based solely on the displacements, velocities and accelerations at the beginning of the increment. A summary of the explicit algorithm is provided below.

Step 1. Nodal calculations

a) Dynamic equilibrium

At the beginning of the increment the program solves for dynamic equilibrium:

$$M\,\ddot{u} = P - I \tag{4.52}$$

where M = the nodal mass matrix, P = the nodal applied force, I = the internal nodal force, and $\ddot{u}$ = the nodal accelerations. The accelerations at the beginning of the current increment (time *t*) are calculated as:

$$\ddot{u}\Big|_{(t)} = M^{-1} \cdot \left(P - I\right)\Big|_{(t)} \tag{4.53}$$

which calculates the change in velocity assuming the acceleration is constant.

b) Integrate explicitly through time

The change in velocity is added to the velocity from the middle of the previous increment to determine the velocities at the middle of the current increment:

$$\dot{u}\left|_{(t+\frac{\Delta t}{2})}\right. = \dot{u}\left|_{(t-\frac{\Delta t}{2})}\right. + \frac{\Delta t\Big|_{(t+\Delta t)} + \Delta t\Big|_{(t)}}{2}\ddot{u}\Big|_{(t)} \tag{4.54}$$

The velocities are then integrated through time and added to the displacement at the beginning of the increment to determine the displacement at the end of the increment:

$$u\Big|_{(t+\Delta t)} = u\Big|_{(t)} + \Delta t\Big|_{(t+\Delta t)}\dot{u}\left|_{(t+\frac{\Delta t}{2})}\right. \tag{4.55}$$

Step 2. Element calculations

The element calculations include determination of element strains and applying material constitutive relationships to determine element stresses and consequently the internal forces.

a) Compute element strain increment $d\varepsilon$ from the strain rate $\dot{\varepsilon}$

b) Compute stresses σ from constitutive equations

$$\sigma_{(t+\Delta t)} = \left(\sigma_{(t)}, d\varepsilon\right) \tag{4.56}$$

c) Assemble nodal internal forces $I_{(t+\Delta t)}$

Step 3. Set ($t + \Delta t$) to (t) and return to Step 1

4.4.2 *Stability Limit (ABAQUS 2002)*

The Explicit procedure integrates through time by using many small time increments. The stability limit is the maximum time increment that can be used to advance the kinematic state and still remain accurate. ABAQUS/Explicit automatically controls the time increment size throughout the analysis to maintain the stability. The central difference operator is conditionally stable and the stability limit for the operator without damping is given in terms of the highest Eigenvalue in the system as

$$\Delta t \le \frac{2}{\omega_{\max}} \tag{4.57}$$

A small amount of damping is introduced in ABAQUS/Explicit to control high frequency oscillations. With damping, the stable time increment is given by

$$\Delta t \le \frac{2}{\omega_{\max}}\left(\sqrt{1+\xi^2} - \xi\right) \tag{4.58}$$

where ξ is the fraction of critical damping in the highest mode.

An estimate of the highest Eigenvalue in the system is obtained by determining the maximum dilatational mode of the mesh. The stability limit based upon this highest frequency estimates a smaller stable time than the true stability limit based upon the

maximum frequency of the entire model. In general ABAQUS/Explicit contains a global estimation algorithm, which determines the maximum frequency of the entire model.

An approximation to the stability limit is often written as the smallest transit time of a dilatational wave across any element in the mesh given by

$$\Delta t \approx \frac{L_{\min}}{c_d} \qquad (4.59)$$

where $L_{\min}$ = the smallest element dimension in the mesh and c_d = the dilatational wave speed.

This estimate for Δt is only an approximation and in most cases is not a conservative estimate. Generally, actual stable time chosen by ABAQUS/Explicit is less than this estimate by a factor between $1/\sqrt{2}$ and 1 in a two-dimensional model. If $L_{\min}$ and c_d of the material are known, for example, if $L_{\min}$ = 5mm and c_d = 5000m/s, the stable time increment will be in the order of 1 x 10^{-6}s.

Since the stability limit is proportional to the shortest element dimension, a single small or poorly shaped element can reduce the stability limit drastically. To obtain a higher stability limit, it is advantageous to keep the element size as large as possible. However, for accurate stress results a fine mesh is necessary. Therefore, while maintaining the required level of mesh refinement, the best approach is to have a mesh that is as uniform as possible.

The material model affects the stability limit as it has an effect on c_d. In a linear material model c_d remains constant. Thus, the stability limit change during the analysis results from changes in the smallest element dimension only. In a nonlinear material model the wave speed changes as the material yields leading to reduction in the stiffness. Consequently, the stability limit will increase due to the reduction in the wave speed.

ABAQUS/Standard and ABAQUS/Explicit are separate program modules with different data structures. Therefore the Explicit dynamic procedure cannot be used in the same analysis as any of the procedures in ABAQUS/Standard. However, ABAQUS provides a capability to import a deformed mesh and associated material state from ABAQUS/Explicit into ABAQUS/Standard and vice versa. The major difference of the two methods is that ABAQUS/Standard generally uses tangent stiffness matrices while ABAQUS/Explicit allows the solution to proceed without requiring tangent stiffness matrices to be formed. Hence the ABAQUS/Explicit solution is generally obtained faster than the implicit solution in ABAQUS/Standard particularly for nonlinear dynamics/ quasi static problems. Furthermore adaptive re-meshing is only available in ABAQUS/Explicit, which prevents mesh distortion in large deformation plasticity problems such as the one we simulated in this thesis.

4.4.3 *Quasi-static Analysis (ABAQUS 2002)*

The Explicit dynamic method was originally developed for high-speed dynamic events in which inertia plays a dominant role in the solution. By definition a static problem requires long time solution. Therefore, it is computationally impractical to analyse the simulations in their natural time scale of a static or a long-time solution, which otherwise would require

an excessive number of small time increments. To obtain an economical solution the event must be accelerated in some way. If the event is accelerated, the state of static equilibrium evolves to a state of dynamic equilibrium creating dominant inertial forces. Thus, in a quasi-static analysis the speed of the analysis is increased substantially in which the inertial forces remain insignificant without severely degrading the quality of the solution. However, the solution tends to localise if the analysis speed is increased to a point at which inertial effects dominate, and the results are quite different to that of a quasi-static solution. ABAQUS/Explicit successfully uses quasi-static simulations in problems involving complex frictional contact conditions where local instabilities may form during the process. As shown in Fig. 4.5 a large deformation within the soil sample in the form of an indentation identical to the size of the loading piston was created during SCT process. This can be regarded as similar to a forming process where instabilities are prominent. The difference is that the reformed shape contains failed soil material around the vertical surfaces of the formation. Therefore, the SCT process was idealised in a similar manner as a quasi-static process in this study.

Figure 4.5 Plan view of a typical test showing the indentation created by the loading piston

4.4.4 Finite Element Model

The SCT setup used in the testing of capping layer material (Chapter 3) was modelled as an axisymmetric problem as illustrated in Fig. 4.6. A 4-node axi-symmetric quadrilateral element (CAX4R) with reduced integration was used in its modelling. A suitable mesh was adopted after trials of several meshes. The bottom of the sample was restrained in direction 2 while the two vertical sides of the sample were restrained in direction 1. An analytical rigid surface was used to define the loading piston of the actuator. It was positioned in contact with the top edge of the soil sample and constrained to translate vertically downwards over a pre-defined displacement of 100mm, such that it axially penetrated the soil sample.

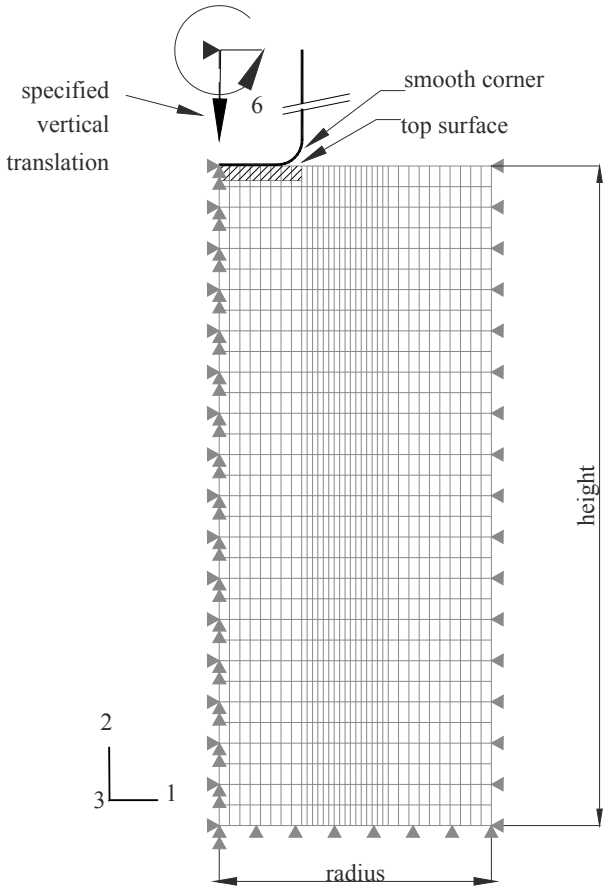

Figure 4.6 ABAQUS Finite element mesh

The predefined displacement was defined using the AMPLITUDE option, which moved the rigid body over a duration time equal to the total step time for the nonlinear analysis. To ensure an accurate, noiseless solution, the rigid surface was controlled using the SMOOTH STEP sub-option, which ensured a smooth motion without any sudden jerky movement of the rigid surface. The surface-to-surface contact between the rigid surfaces and the soil sample was defined using the finite sliding KINEMATIC based contact algorithm with contact pairs and hard contact in the normal direction and a frictionless contact in the tangential direction. The corner of the rigid surface was smoothed by a fillet curve for mathematical convenience in the finite-element analysis. ADAPTIVE MESH control option was used to avoid mesh distortion as well as to maintain a high quality mesh throughout the penetration process.

The steps used in the INPUT file are as follows: A FREQUENCY linear perturbation analysis was used to determine the step time for the quasi-static analysis. In a quasi-static analysis the lowest mode of the structure usually dominates the response. The frequency analysis provided the frequency of this mode for the specimen. The corresponding period determined the lowest limit of the step time. ABAQUS (2002) specifies that this period be multiplied by a factor of a minimum of 10 to ensure better prediction of the structural deformation characteristic of a quasi-static analysis. The VUMAT routine was called at each material calculation point for which the **MATERIALS definition included the *USER MATERIAL option, and was used to define the mechanical constitutive behaviour of the material. The number of material constants defined in this subroutine was eleven. FREQUENCY analysis and step time calculations and a typical INPUT File/User Subroutine are located in Appendix B.1 and B.3 respectively.

4.4.4.1 *Loading Rates*

The actual time taken for a physical process is called its natural time. In a static analysis the lowest mode of the structure usually dominates the response. Therefore the time required to obtain the proper static response can be estimated from the period of the lowest mode. To obtain desirable quasi-static overall structural response without significant inertial effects, ABAQUS/Explicit suggests 10 times the period of the lowest mode. As the loading rate is artificially increased, it is important that the loads are applied gradually to overcome adverse effect of any impact load on the system. The propagation of impact stress waves may produce undesirable results. Ramping up the loading rate using the SMOOTH STEP amplitude option minimizes these adverse effects.

4.4.4.2 *Steps*

An analysis history is defined in ABAQUS by dividing the problem history into steps. The step sequence provides a convenient way to capture changes in the loading and boundary conditions of the model, changes in the way parts of the model interact with each other, the removal or addition of parts, and any other changes that may occur during the course of the analysis. A step starts with *STEP option and ends with *END STEP option. For each step the user chooses an analysis procedure or type of analysis to be performed during a step. To ensure consistency and continuity, ABAQUS compares all loads and boundary conditions specified in a step with that of the previous step.

4.4.4.3 *Amplitude Curves*

An amplitude curve allows arbitrary time (or frequency) variations of load, displacement and other prescribed variables to be given throughout a step (using step time) or throughout

the analysis (using total time). By default, the values of loads, boundary conditions and pre-defined fields either change linearly with time throughout the step (ramp function) or they are applied immediately and remain constant throughout the step (step function). However when more elaborate definitions such as time variations for different loading are required, amplitude curves can be used to specify these variations.

4.4.5 *Mesh Refinement and Adaptive Meshing*

The SCT setup allows modelling the 3D test specimen as a 2D axisymmetric idealisation as shown in Fig. 4.6. Three meshes were used in ABAQUS/Explicit to assess the sensitivity of the results to mesh refinement: a coarse 10 x 6 mesh, a medium 34 x 32 mesh (which was used in the simulations) and a very fine 84 x 64 mesh of elements CAX4R (Table 4.2). The corresponding FE analysis data are given in Appendix B.2. Since considerable nonlinearity is expected in the response, including the possibility of unstable regimes below and around the rigid surface, the solution-dependent meshing (adaptive meshing) controls were assigned. This counteracts the tendency of the basic smoothing methods to reduce the mesh refinement near concave boundaries where solution accuracy is important (ABAQUS 2002).

Table 4.2 Results of mesh refinement study

Mesh Type	**Coarse**	**Medium (mesh used in the analysis)**	**Fine**
Mesh size	10 x 6	34 x 32	84 x 64
Number of Elements	60	1088	5525
Number of Nodes	77	1155	5376
CPU Time (hrs:min:sec)	00:00:01	00:00:06	00:01:22
Percentage saving in CPU Time	99%	93%	0%

Figs. 4.7 and 4.8 show the mesh configuration before commencement of penetration and after penetration of the piston to the 100mm penetration level respectively. All three

meshes clearly indicate the benefits of adaptive meshing as the mesh used showed very little distortion.

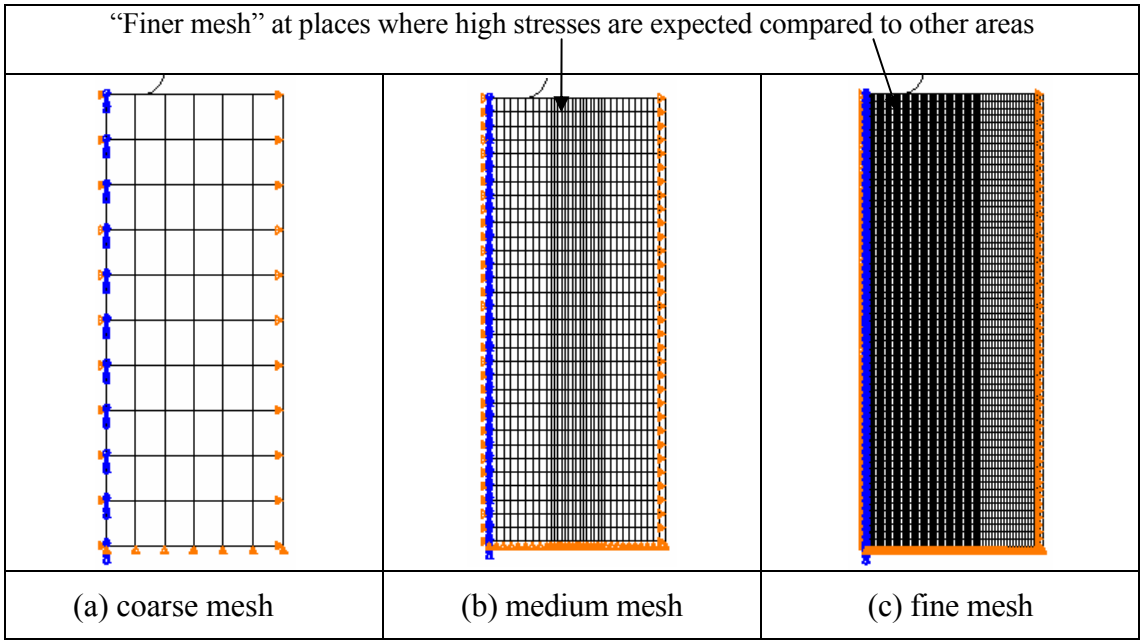

Figure 4.7 Original mesh configuration

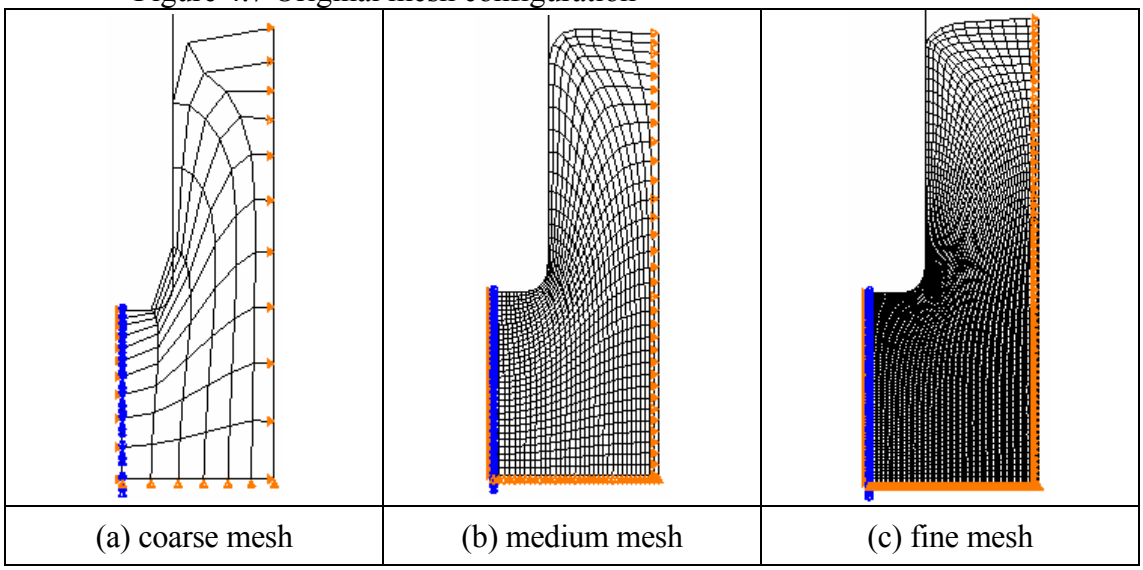

Figure 4.8 Deformed mesh configuration at 100mm penetration of the loading piston

The number of elements used in a particular mesh is referred to as the mesh density. In a stress analysis, the displacements of the nodes are the fundamental variables. For complex simulations the available computer resources often dictate a practical limit on the mesh density that can be adopted. Therefore a 'finer mesh' was used mainly in the areas of the

high stress gradients (Fig. 4.7) compared to the other areas. Fig. 4.9 shows the load-penetration response of the SCT setup for the three different mesh densities.

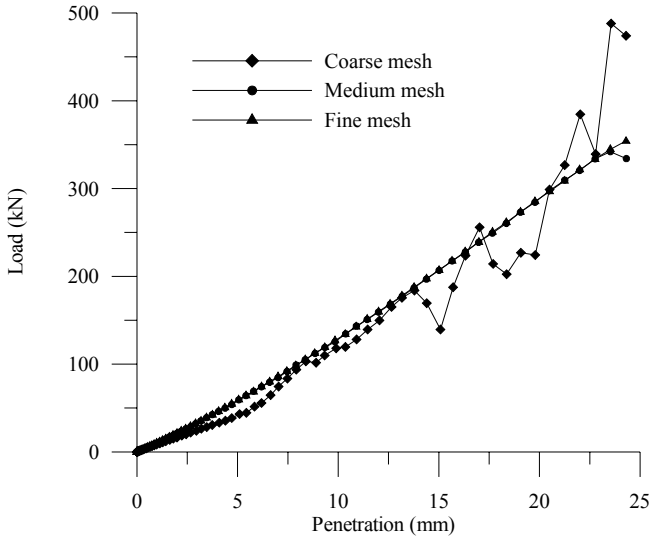

Figure 4.9 Load-penetration response of the SCT setup, ABAQUS/Explicit; influence of mesh refinement

The coarse mesh predicts a lower limit load than the medium and fine meshes do, and the limit loads for the medium and fine mesh analyses are very close. Coarse mesh also showed some noise in its predictions compared to medium and fine meshes. Since almost similar results were obtained from the medium and fine mesh analyses with the Central Processing Unit (CPU) time much reduced (Table 4.2) for the medium mesh (92% CPU time is saved than that of the fine mesh), the medium mesh was used in all the simulations of the SCT specimens.

4.4.6 *Sensitivity of the Modelling Parameters*

4.4.6.1 *Total Step Time and Energy Balance*

The AMPLITUDE option was used to simulate the penetration rate of the loading piston (rigid body) into the soil sample. The arbitrary time of the displacement amplitude was prescribed as equal to the total step time. In an analysis ABAQUS allows the total step

time to be divided into arbitrary steps (Section 4.4.4.2); in the present model 20 steps were allowed. The effect of the change in total step time on load-penetration profiles is shown in Fig. 4.10. Three total step times were considered in the analysis; 0.0128s (10 x period), 0.109s (50 x period) and 0.218s (100 x period). The period considered was obtained from the lowest mode of the model (0.00128s).

The higher the total step time the more closely the quasi-static model followed the static behavioural patterns observed in the experiments. The initial 10mm penetration of the piston had not caused significant deviations in the load irrespective of the total step time used, but a dramatic drop of the load was noticed beyond 10mm penetration.

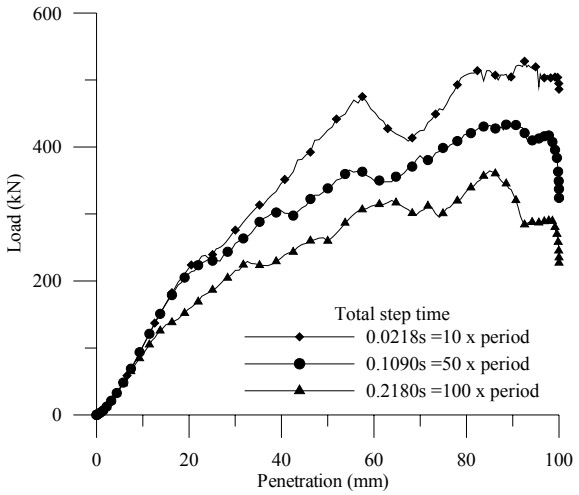

Figure 4.10 Effect of total step time on load-penetration profiles in ABAQUS model

Usually in a quasi-static analysis the monitoring of the Kinetic Energy (KE) is a must as it is used to help evaluate whether an analysis is yielding an appropriate response to reduce the computational cost by speeding up the simulation. As a general rule, the KE should be a small fraction of its Internal Energy (IE) – typically less than 10% (ABAQUS 2002).

Thus, the kinetic energy to internal energy ratio (KE/IE) was also evaluated for the three total step times considered. Fig. 4.11 shows these results with respect to time. For clarity a full graph, Fig. 4.11(a) and an enlarged initial part, Fig. 4.11(b) are shown.

It can be seen that at the initial step the KE/IE ratio had a peak but within the next step it had reduced drastically. As shown in Fig. 4.11(b), the KE/IE ratios at the peak for the three total step times were about 120% for 0.0218s, about 75% for 0.109s and about 96% for 0.218s, showing that the initial instability is primarily due to the speedup of the process which is very much in excess of the allowable KE/IE ratio of 10% expected in any analysis. However, this initial inertial instability was quickly recovered and the energy system stabilised showing expected KE/IE ratios less than 10% reached after a time interval of about 0.0014, 0.0018 and 0.0029s for the total step times of 0.0128, 0.109 and 0.218s respectively.

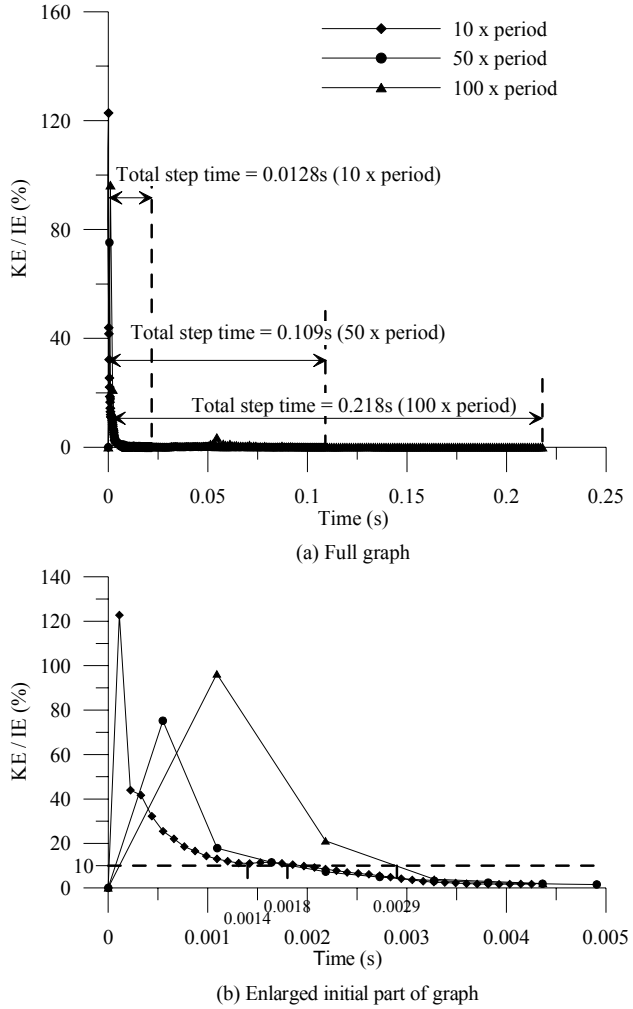

Figure 4.11 Kinetic and internal energy ratio histories for the speedups of 0.0218s, 0.109s and 0.218s

Thus, it can be concluded that use of the appropriate step is required, but for the adopted model the instability time interval at the beginning was negligible, irrespective of the total step time used. Therefore, a step time of 10 times the period of the lowest mode (ABAQUS 2002) is used in matching the load-penetration experimental results of this thesis which is considered adequate for speeding up the analysis process. The corresponding FE analysis data are located in Appendix B.4.

4.5 Output and Discussion

The deformed meshes at 10%, 25%, 50%, 75%, and 100% of the total piston penetration (100mm) are shown in Fig 4.12. The upheaval of the top surface of the sample onto the rigid piston is clearly visible from the modelling results, which indicates the benefits of adaptive meshing as the mesh used in ABAQUS/Explicit has exhibited very little distortion.

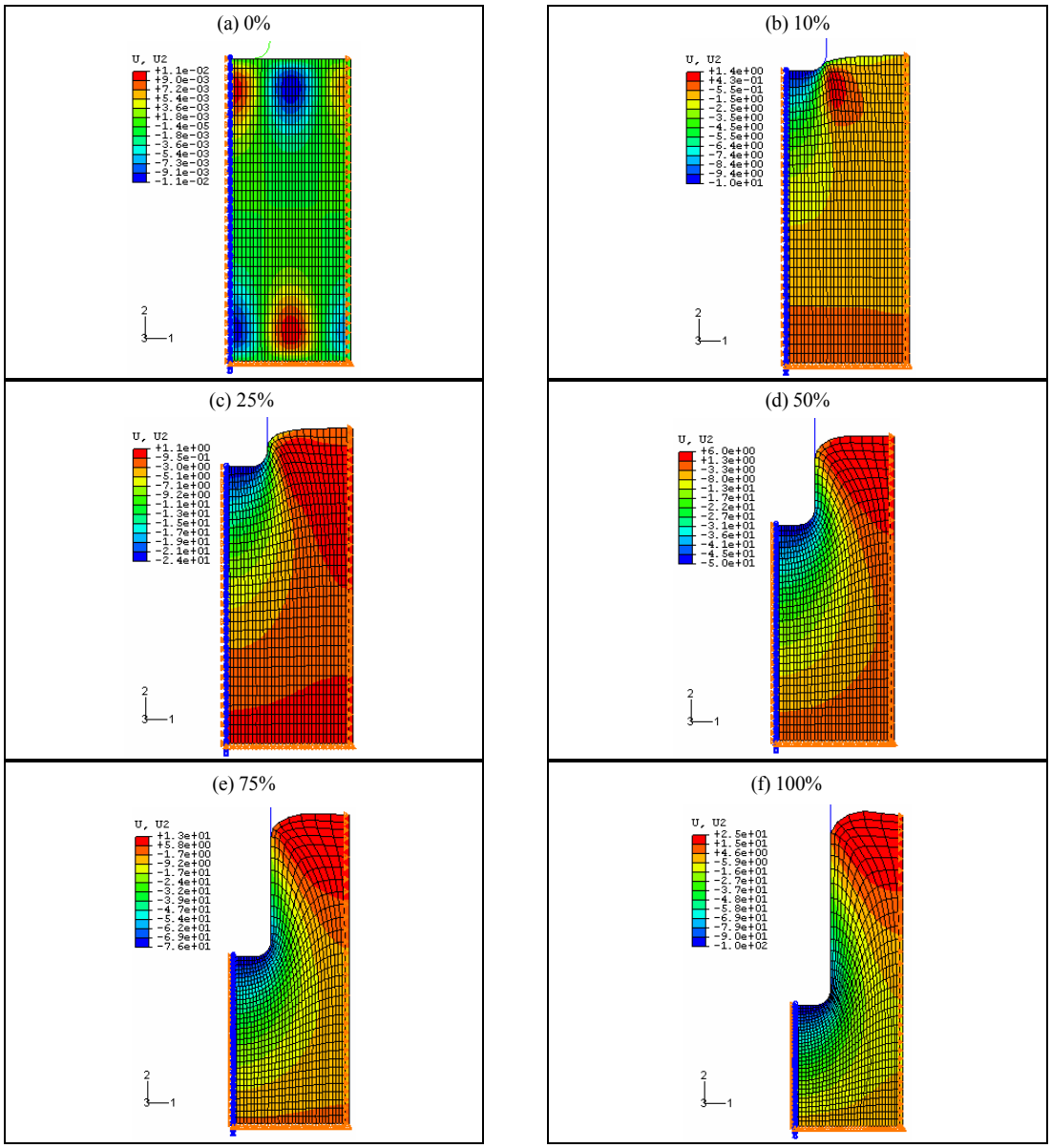

Note: U2 is the axial deformation in (mm)

Figure 4.12 Deformed configurations at different percentages of the total piston penetration of 100mm

Although the physical experimental views in Fig. 4.13 may not readily provide an exact step-by-step comparison of the modelling process, it shows the tendency for the failed sample to heave outward from the top unconstrained boundary of the mould. The simulated movement of the mesh along the vertical surfaces of the loading piston shows similarity with the experimental observations.

Figure 4.13 Physical configuration of the penetration of the piston throughout a typical test

As illustrated in Fig. 4.5, the indentation caused by the loading piston at the completion of the experiment indicates that the deformation process adopted in the model reasonably simulates the experimental process and is fairly compatible with the physical process happening in the SCT set-up. Extensive comparisons of the experimental and FE results will be presented in Chapter 5.

Figs. 4.14 and 4.15 show the change in the stress distribution within the medium with 10%, and 100% of the total piston penetration (100mm). The (+) sign in the figures show tensile stresses while the (-) sign shows compressive stresses. S11, S22 and S33 indicate the stresses in each direction 1, 2, and 3 respectively while S12 indicates the shear stress in plane '12' of the medium. Stresses in Figs. 4.14 and 4.15 are in MPa. It can be seen from these figures that high tensile stresses of magnitudes up to 15.0MPa were observed (Fig. 4.15c) in some areas within the soil compared to very low values or zero which is usually suggested in structural soil analysis. However, these high stresses were mainly observed near the curved surface of the rigid piston. Though the present user subroutine does not include a tension cut-off, such localised areas can be considered as failed due to the penetration of the piston which is observed to be physically happening in the experiments.

The Explicit solution checks for equilibrium in a global sense as detailed in Section 4.4.3 and if more accurate stress distribution is desired the ABAQUS/Explicit solution should be taken into ABAQUS/Standard for further iterations until the prescribed level of convergence is obtained. Only an approximate global behaviour was sought in the current thesis due to the practical nature of its objectives. Therefore such transfers from ABAQUS/Explicit to ABAQUS/Standard to minimise the tensile stresses were not

performed as refinement of stress state in soil was considered not essential in the context of this thesis to address all behavioural responses.

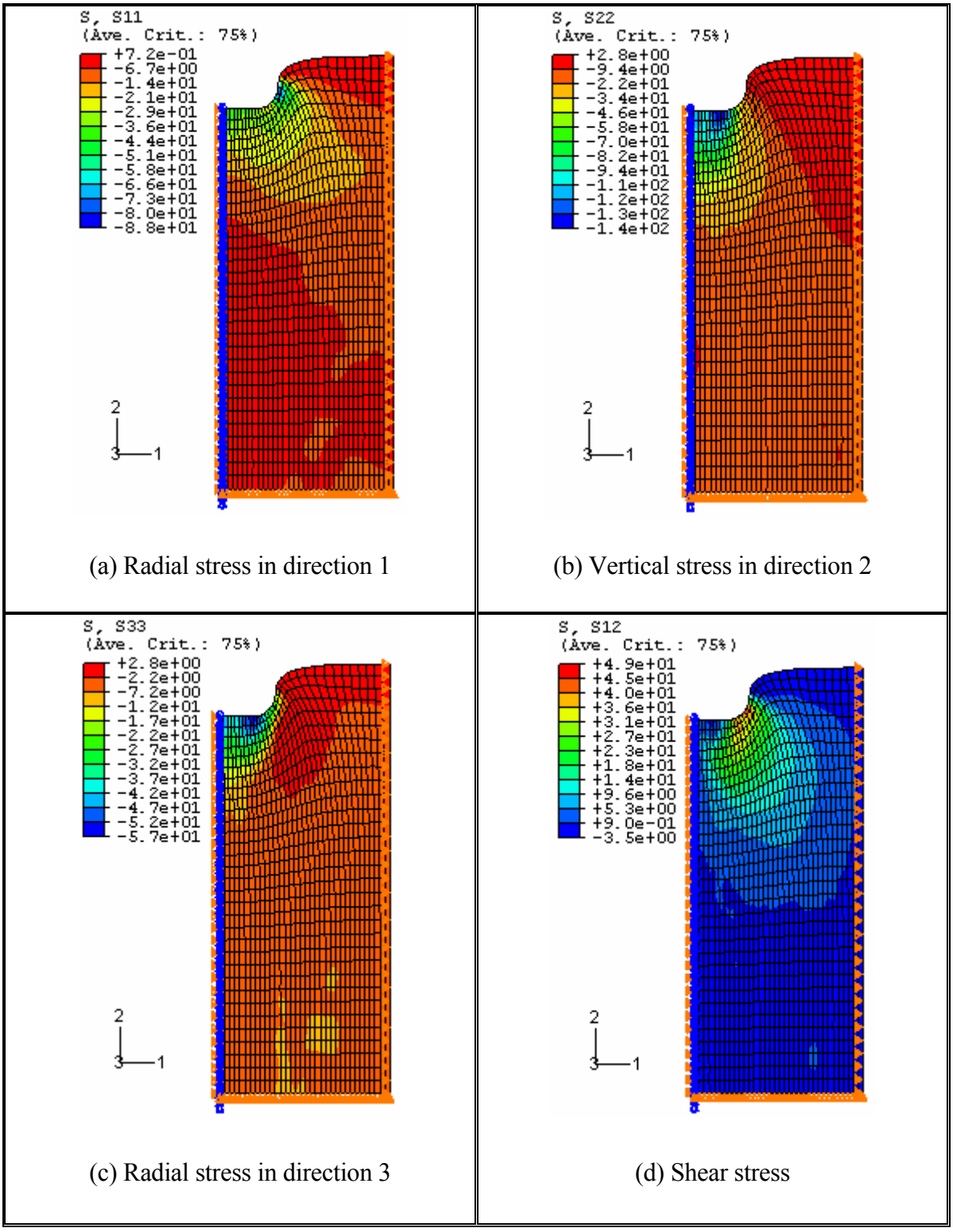

(a) Radial stress in direction 1

(b) Vertical stress in direction 2

(c) Radial stress in direction 3

(d) Shear stress

Figure 4.14 Typical stress distributions at 10% of the total piston penetration of 100mm

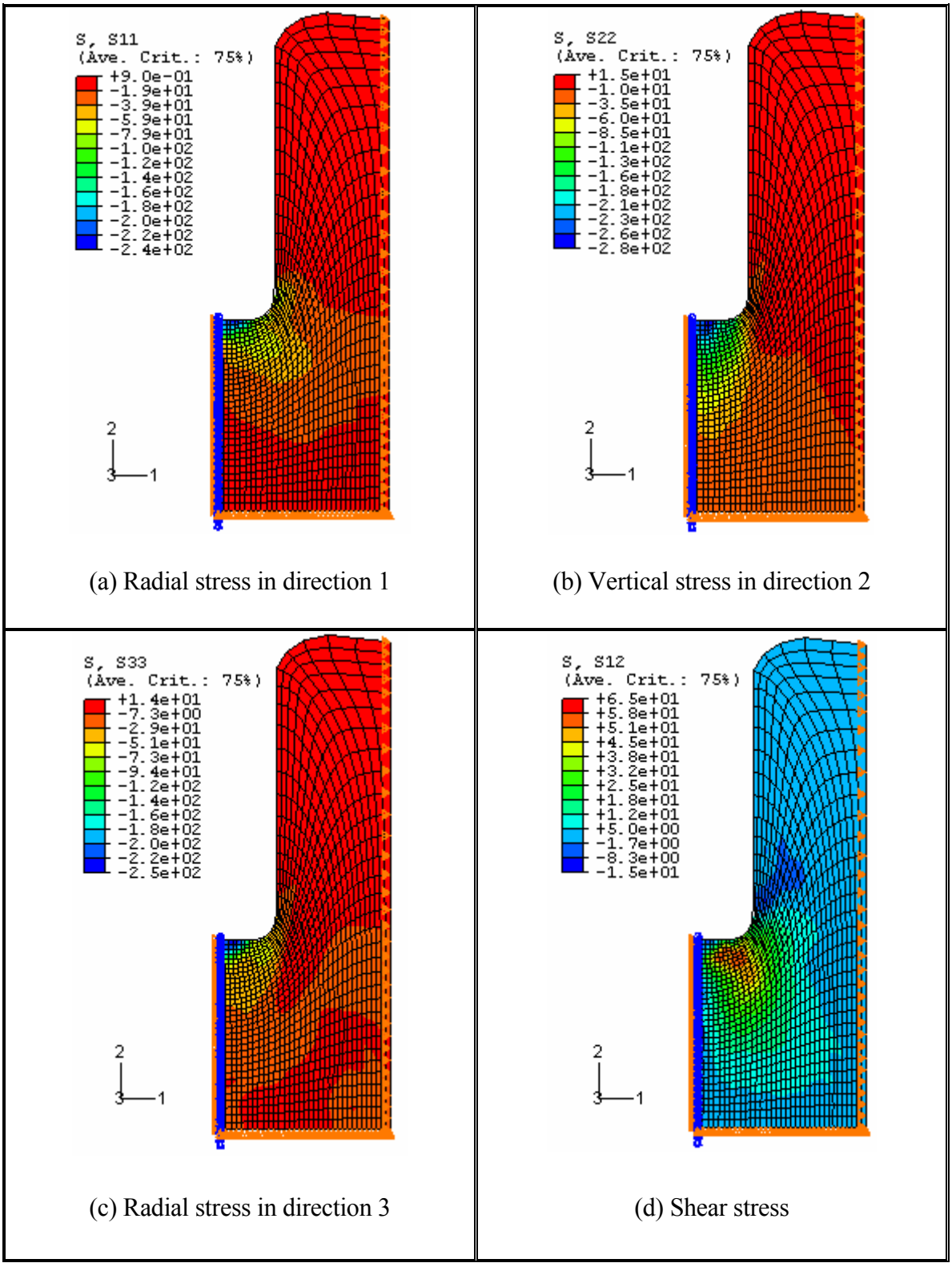

(a) Radial stress in direction 1

(b) Vertical stress in direction 2

(c) Radial stress in direction 3

(d) Shear stress

Figure 4.15 Typical stress distributions at 100% of the total piston penetration of 100mm

4.6 Summary

The constitutive model of the capping layer material tested in a SCT setup for the finite element analysis is presented in this Chapter. The FE model of the SCT setup and a qualitative analysis of the mesh refinement and adaptive meshing techniques are also presented. The stress distribution and the effect of the step time and plasticity criterion are also discussed. The application of the present model for backcalculating the properties of the capping layer material is presented in Chapter 5.

CHAPTER 5

5. BACKCALCULATION OF THE CAPPING LAYER MATERIAL PROPERTIES

5.1 Introduction

This Chapter describes the application of the finite element model defined in Chapter 4 to determine the elasto-plastic properties of the capping layer material whose response to prescribed penetration in a semi-confined cylinder test (SCT) setup had been experimentally investigated as reported in Chapter 3. The properties were determined using a trial and error approach "backcalculation" process. As described in Chapter 3, the experimental data were grouped based on the level of moisture in the test specimens and the three groups of data thus formed were used in the backcalculation process. Each group consisted of the dataset from specimens tested under varying rates (2.5 – 25mm/min) and types (monotonic/ cyclic) of loading. This Chapter first describes the backcalculation process applied to the SCT setup, and then presents the properties of the capping layer material predicted from the simulations and compares the results with the reported values in the literature as well as that evaluated from a limited number of triaxial and uniaxial tests conducted as part of this thesis. The relevant data sheets of this Chapter are provided in Appendices C.1-C.10.

APPENDIX C.1	Density and saturation calculations-triaxial test samples
APPENDIX C.2	Triaxial test data sheets
APPENDIX C.3	Modulus, cohesion and friction angle obtained from triaxial tests
APPENDIX C.4	Uniaxial test data sheets
APPENDIX C.5	Density, saturation, initial modulus and hardening modulus - uniaxial test samples
APPENDIX C.6	Establishing lower and upper boundaries of SCT data
APPENDIX C.7	Effect of moisture on SCT FEM predicted parameters

APPENDIX C.8 Sensitivity of elastic material parameters in SCT FEM

APPENDIX C.9 Sensitivity of plastic material parameters in SCT FEM

APPENDIX C.10 Stresses induced in SCT FEM

5.2 Backcalculation Process

Backcalculation process has briefly been reviewed in Chapter 2. This process is also referred to as inverse method in the literature. Inverse method is a term for the determination of material properties from structural response data. Traditionally material properties are determined from small size specimens tested under uniform state of stress, most commonly uniaxial compression or tension. The properties evaluated using such simple test methods do not always provide accurate predictions of the behaviour of structures especially under complex states of loading. Furthermore, with the advent of new materials, especially composites, it becomes increasingly difficult to use such simple test methods to determine the properties of materials. Therefore there is a growing modern trend of using inverse method (Kang et al. 2004; Lin et al. 2005) to determine material properties from structural response determined experimentally (and hence the term "inverse method"). These inverse methods invariably use FE modelling combined with some advanced search techniques for example, Genetic Algorithm or GA (Lin et al. 2005) to determine the most appropriate material dataset to satisfy the observed structural behaviour.

As soils are complex media with significant variability of their properties, it was decided not to use very sophisticated search techniques such as the GA for material dataset determination – but rather limit the search to some indicative upper and lower bound values using trial and error method known as the backcalculation procedure.

The structural behaviour observed from the SCT specimens are shown in Fig. 5.1 as three distinctive groups of dry, OMC and saturated data.

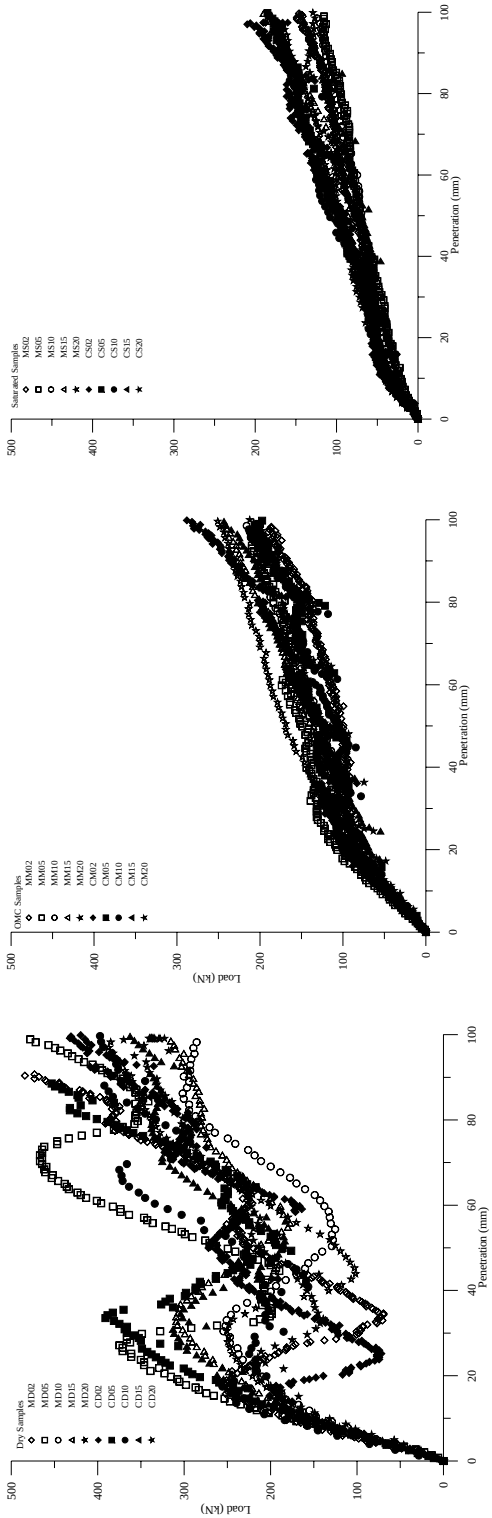

(a) Dry (D) (b) OMC (M) (c) Saturated (S)

Figure 5.1 Three distinctive groups of experimental data obtained from SCT

Estimating the upper and lower bounds of material properties for these three groups was considered sufficient given the variability in soil behaviour observed in the field. Although deformation of about 20-30mm is considered a failure in practice for railway subgrades, we have considered a penetration of up to 100mm to improve the reliability of the evaluated material property datasets.

Eleven user input parameters describe the behaviour of the capping layer material adequately. They are:

- the minimum elastic modulus (E_0),
- the maximum elastic modulus ($E_{\max}$),
- the Poisson's ratio (ν),
- the minimum friction angle ($\phi_{\min}$),
- the maximum friction angle ($\phi_{\max}$),
- the cohesion (c),
- the dilatancy angle (ψ),
- the hardening parameter (H_p),
- the factor (R_f) and
- the two material constants (K_a) and (n)

The above user inputs are then classified as elastic or plastic parameters as shown in Table 5.1. Multiple combinations of the user inputs in Table 5.1 can be applied in the simulation process, which will lead to a considerable number of trial runs in the analysis. Thus, to simplify the simulation process, values suggested in the literature and material parameters obtained from triaxial/uniaxial tests on the capping layer material were used as a guide and they were classified further as primary, secondary or tertiary parameters.

Table 5.1 User input parameters

Elastic	Plastic
$E_0 \le E_t \le E_{\max}$ (MPa)	ψ (^{0})
$\phi_{\min} \le \phi \le \phi_{\max}$ (^{0})	
c (MPa)	H_p (MPa)
ν	
K_a	R_f
n	

The direct measurement of ν is very difficult and suggested values of other references are generally considered acceptable in geotechnical engineering (Liao 2003). A value for ν of 0.3 was suggested by Croney and Croney (1992) for unbound base and sub-base materials in pavements while for sand and gravely sand the most commonly used value range for ν was between 0.3 - 0.4 (Bowles 1988). Although with the increase in stress level the Poisson's ratio, ν could increase (Croney and Croney 1992; Lambe and Whitman 1979), ν was kept a constant at 0.35 in all simulations for simplification, which is representative enough for the capping layer material used in the experiments being a mixture of very sandy gravel with a feeble plastic binder (refer Section 3.3).

The values suggested in literature specify the range of 0.7-0.9 for R_f (Desai and Christian 1977). Thus, it was decided to keep R_f constant at 0.8 simplifying the backcalculation process.

The dilatancy angle ψ was not measured for the material; it was decided to use values suggested in the literature as a guide to find a specific range in the simulations. According to Liao (2003) the values of ψ suggested by Vermeer and de Borst in 1984 are given in Table 5.2.

Table 5.2 Values of dilation angle (ψ) suggested by Vermeer and de Borst in 1984 (Liao 2003)

Dense sand	15^0
Loose sand	$<10^0$

Liao (2003) also stated that these values were broadly suggested in geotechnical computer software like FLAC^{3D} and PLAXIS, and further stated that a simple empirical equation was suggested in the programs given by:

$$\psi = \phi - 30^0 . \qquad (5.1)$$

The theoretical solutions stated by Liao (2003) are:

Maximum theoretical dilation angle suggested by Bolton (1986) for plane strain conditions

$$\sin\psi_{\max} = \left[\frac{-(d\varepsilon_1 + d\varepsilon_3)}{(d\varepsilon_1 - d\varepsilon_3)}\right]_{\max} \qquad (5.2)$$

where ε_1 = axial strain and ε_3 = lateral strain and

Maximum theoretical dilation angle suggested by Tatsuoka (1987) for triaxial conditions

$$\sin\psi_{\max} = \left[\frac{-(d\varepsilon_1/2 + d\varepsilon_3)}{(d\varepsilon_1/2 - d\varepsilon_3)}\right]_{\max} \qquad (5.3)$$

If Eqn. (5.1) is used in calculating ψ, the corresponding values for ϕ = 30^0, 35^0, and 40^0 would be 0^0, 5^0 and 10^0 respectively.

Thus, by considering the suggested values it was decided to employ $\psi < 15^0$ in the simulation process.

The two material constants K_a and n were calibrated using a limited set of drained triaxial tests taking the reference pressure p_a as 100kPa (normal practice is to choose a value close to the atmospheric pressure of 101kPa). The triaxial results were also used to

identify possible ranges for the user inputs of E_t, ϕ, and c. Uniaxial tests were carried out to find possible ranges of values for E_0 and H_p. The following describes the triaxial and uniaxial tests carried out.

Triaxial and Uniaxial Test Data

a) Triaxial tests

The triaxial tests carried out served four purposes, (i) calibration of model parameters K_a and n, (ii) deriving an equation to use in the subroutine for the stress dependent friction angle, (iii) use of extracted values E_t, c and ϕ as a preliminary guide to initial inputs in the trial simulations and (iv) comparison with model backcalculation predictions. A set of standard drained triaxial tests (AS 1289.6.4.1. 1998; AS 1289.6.4.2 1998; Bishop and Henkel 1962) for the loading rates (2.5, 5.0, 10.0, 15.0 and 20mm/min) considered in the SCT for confining pressures below 800kPa were carried out at the Central Queensland University (CQU). The tests were carried out for 100, 375 and 750kPa confining pressures. Another set of tests at 2.5mm/min for higher confining pressures of 1000 and 2000kPa were carried out at the University of Sydney (USyd). Higher levels of confining pressure were not possible at CQU and higher levels of rate of loading were not possible within the time available at USyd. Further details and data of triaxial tests are contained in Appendices C.1-C.3.

200mm high x 100mm diameter samples were used for testing. The samples were prepared using modified compactive effort (AS 1289.6.8.1 1995). The samples were compacted in five layers, each of about 40 mm thick subjected to 56 blows with the 4.9kg Proctor hammer falling a distance of 450mm.

Fig. 5.2 shows the setup used at CQU and USyd. The 2.5mm/min rate data was used in calibrating the model parameters K_a and n as the confining pressure range 100-2000kPa best represents the high confining stresses induced in the SCT. The initial modulus, cohesion and friction angle obtained from the triaxial tests are given in Table 5.3 while the average values are used in Table 5.11 for comparisons.

(a) CQU apparatus

(b) USyd apparatus

Figure 5.2 Triaxial setup

Table 5.3 Material properties obtained from triaxial tests

Material property	Confining pressure (kPa)	Deformation rate (mm/min)					Average
		2.5	5.0	10.0	15.0	20.0	
E_t (MPa)	100	88	106	111	125	112	108
	375	260	283	266	282	256	269
	750	360	414	392	372	366	381
	1000	479	-	-	-	-	479
	2000	589	-	-	-	-	589
c (kPa)	100-750	263	323	356	315	391	330
	1000-2000	534	-	-	-	-	534
ϕ^0 (deg)	100-750	38	40	38	38	39	39
	1000-2000	36	-	-	-	-	36

The calibration of K_a and n is shown in Fig. 5.3. By comparison of the best-fit power curve of the data and Eqn. (4.43) as shown in Fig. 5.3, the values evaluated and used in the analysis for K_a and n are 970 and 0.65 respectively.

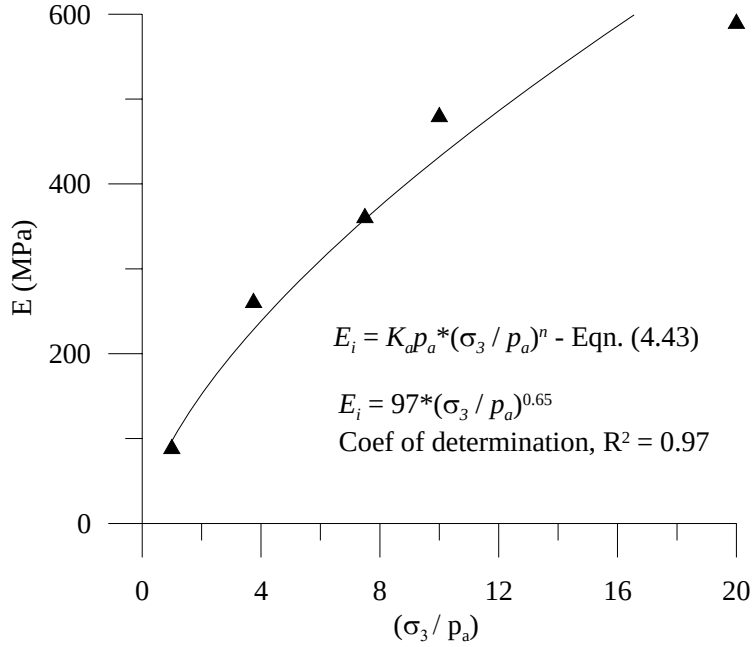

Figure 5.3 Calibration of K_a and n

Obtaining a possible relationship for the stress dependency of the friction angle was also carried out using the triaxial test results. Table 5.4 presents the data used in deriving the stress dependent friction angle (Eqn. 4.51) described in Section 4.3.2.

Table 5.4 Variation in ϕ at different stress levels

Confining pressure σ_3 (kPa)	Average. confining pressure σ_3 (kPa)	Major principal stress at failure $(\sigma_1)_f$ (kPa)	Average principal stress at failure $(\sigma_1)_f$ (kPa)	$(\sigma_1/\sigma_3)_f$	Friction angle ϕ^0 (deg)
100-375	238	1900 -3579	2739	11.5	46
375-750	563	3579-5300	4439	7.9	40
1000-2000	1500	6004-9900	7952	5.3	36

b) Uniaxial compression tests

The uniaxial compression tests (see Fig. 5.2a) were carried out to find a suitable input range for the minimum elastic modulus E_0 and the hardening modulus H_p of the

material. Two uniaxial compression tests on OMC samples were carried out (AS 1141.51 1996; AS 4133.4.2 1993). Fig. 5.4 shows the effective stress-effective strain of the material showing H_p for the material. The results obtained for E_0 and H_p are shown in Table 5.5. Accordingly for the capping layer material at OMC state, E_0 = 25MPa and H_p = 270kPa. Appendices C.4 and C.5 present the detail data of the uniaxial compression tests.

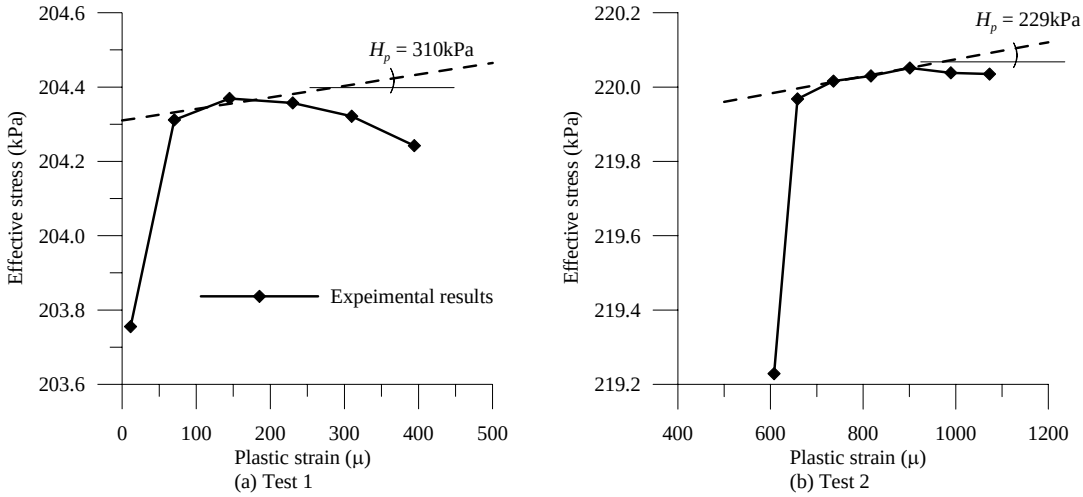

Figure 5.4 Effective stress-effective strain curves of the OMC samples

Table 5.5 E_0 and H_p of the capping layer material at OMC state

	E_0 (MPa)	H_p (kPa)
Test 1	27	310
Test 2	22	229
Average	25	270

From the triaxial and uniaxial tests data, suitable ranges for input values for numerical simulations would be E < 600MPa, ϕ between 30^0-40^0, c < 1MPa and H_p < 1MPa.

Based on the above discussion and the importance of definitions used in the constitutive relationships the above inputs were categorised as primary, secondary or tertiary parameters as shown in Table 5.6.

Table 5.6 Classification of user input parameters as primary, secondary or tertiary

Elastic Parameters		Plastic Parameters	
$E_0 \le E_t \le E_{max}$ (MPa)	Primary	ψ (^{0})	Primary
$\phi_{min} \le \phi \le \phi_{max}$ (^{0})	Primary		
c (MPa)	Secondary	H_p (MPa)	Secondary
ν	Tertiary		
K_a	Tertiary	R_f	Tertiary
n	Tertiary		

Thus, the backcalculation process was much simplified by keeping the tertiary parameters constant and varying only the primary and secondary parameters. The following summarises the final conclusions drawn on the simplification of simulation process.

- Keep K_a (= 970) and n (= 0.65) constant in all simulations obtained through triaxial tests taking the reference pressure p_a as 100kPa.
- Keep ν (= 0.35) and R_f (= 0.8) constant in all simulations considering the relevant suggestions in literature.
- Keep the secondary parameters c < 1MPa, and H_p < 1.0MPa in all simulations considering the values obtained from triaxial/uniaxial test data.
- Keep the primary parameters E < 750MPa, ϕ between 30^0 - 40^0, and ψ < 15^0 considering the triaxial test data and suggestions made in literature respectively.
- Main parameters to be changed in the simulation process to match the upper and lower bound envelopes of the experimental data are the primary elastic parameters E_t, ϕ and plastic parameter ψ.
- The values obtained for the primary parameter ϕ in matching the lower bound to be employed in matching the upper bound.
- The values employed for the secondary parameters c and H_p in matching upper bound to be kept close to the values obtained from lower bound simulations.

The flow chart for the adopted simulation process is summarised in Fig. 5.5.

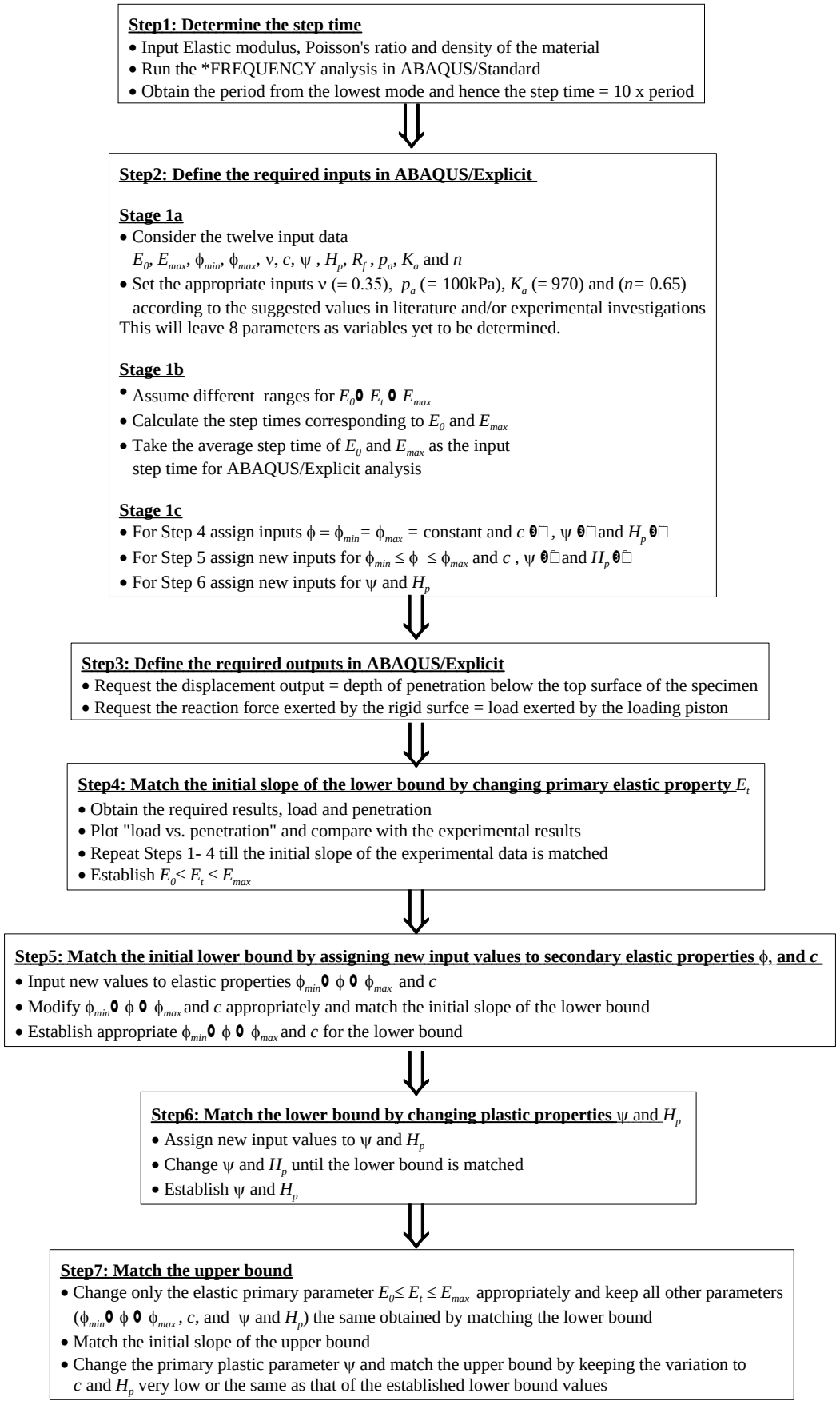

Figure 5.5 Flow chart of simulation process

5.2.1 Results of the ABAQUS Simulations

5.2.1.1 *Model Predictions – OMC State (M)*

The most representative envelopes obtained from the simulations are shown in Fig. 5.6 for OMC state specimens. The model predicted the response reasonably well for a penetration level up to 80mm which is about 45% of the total height of 177.5mm of the SCT setup. In fact the model was able to predict the properties for a broad range of confining stress levels providing more valuable data.

The inability of the model to capture the remoulding behaviour beyond 80mm penetration level was considered not very significant. Firstly the choice of 100mm is arbitrary and somewhat extreme from practical perspective. The simplified trial and error based backcalculation process could possibly have limitations in determining the appropriate dataset for the behaviour of material at highly nonlinear condition.

The model predicted properties are given in Table 5.7 for the OMC state of the material.

Table 5.7 Model predicted properties – OMC state

		Elastic Parameters			**Plastic Parameters**	
		$E_0 \le E_t \le E_{\max}$ (MPa)	$\phi_{\min} \le \phi \le \phi_{\max}$ (^{0})	c (kPa)	ψ (^{0})	H_p (kPa)
OMC	Lower bound	$30 \le E_t \le 80$	$35 \le \phi \le 38$	300	4	300
	Upper bound	$80 \le E_t \le 130$	$35 \le \phi \le 38$	350	7	350

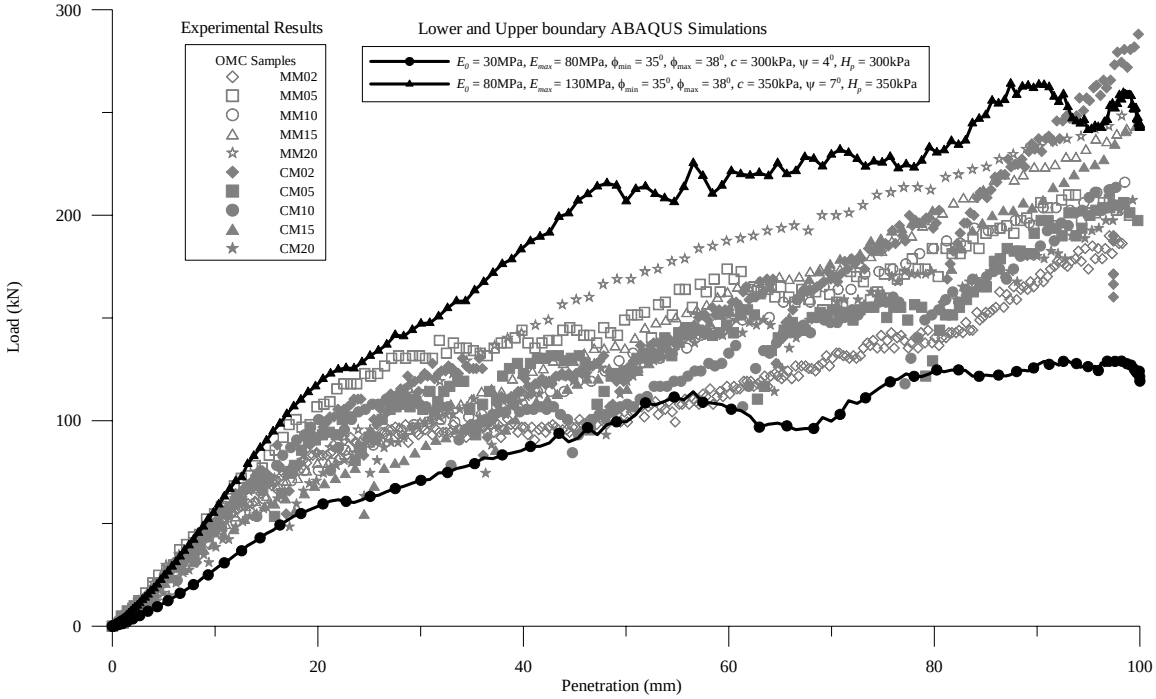

Figure 5.6 Predicted boundary envelopes of OMC state

5.2.1.2 *Model Predictions – Saturated State (S)*

Similar to the OMC state specimens the saturated state specimen properties were also predicted reasonably well up to 80mm penetration level by the FE based backcalculation process. Beyond 80mm penetration level the prediction was not completely satisfactory. The model predictions are given in Table 5.8 while Fig. 5.7 shows the predicted boundary envelopes.

Table 5.8 Model predicted properties – Saturated state

		Elastic Parameters			**Plastic Parameters**	
		$E_0 \le E_t \le E_{\max}$ (MPa)	$\phi_{\min} \le \phi \le \phi_{\max}$ (^{0})	c (kPa)	ψ (^{0})	H_p (kPa)
Saturated	Lower bound	$20 \le E_t \le 45$	$33 \le \phi \le 35$	300	7.5	300
	Upper bound	$55 \le E_t \le 80$	$33 \le \phi \le 35$	300	6.7	300

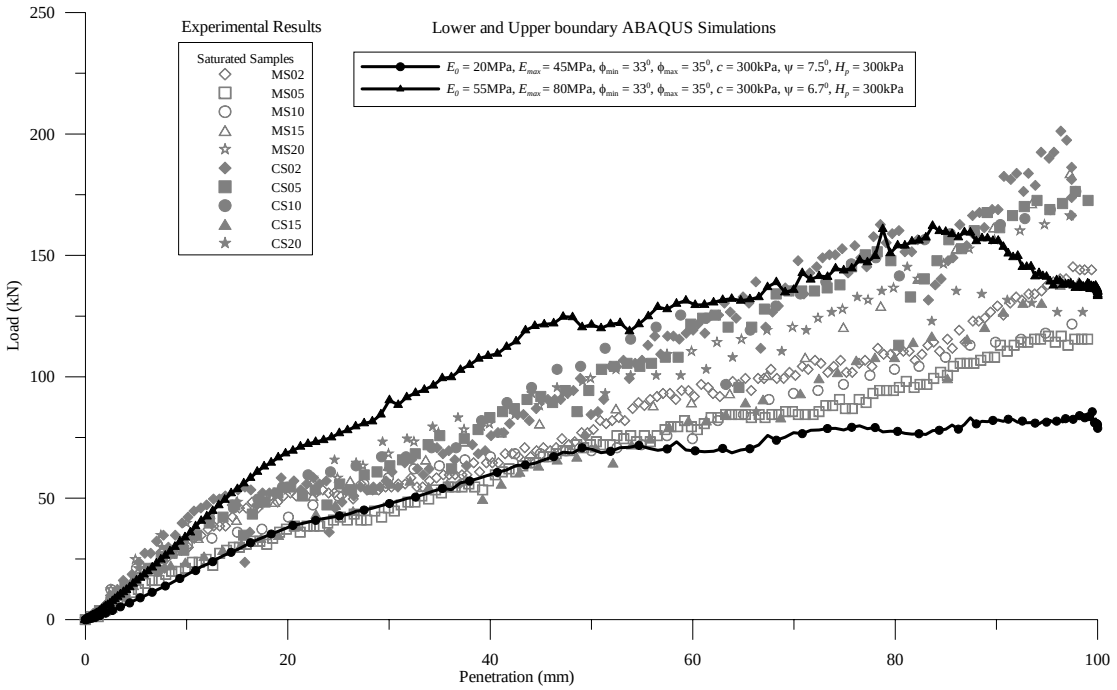

(a) Lower bound input combinations

Figure 5.7 Predicted boundary envelopes of saturated state

5.2.1.3 *Model Predictions – Dry State (D)*

The hardening-failure-remoulding behaviour of the dry state specimens was very much pronounced compared to that of the OMC and saturated states of the material. The model was not capable of predicting the zigzag behaviour observed in the experiments in its present form. The absence of moisture in dry specimens makes them a separate class as presented in Chapter 3 (see dimensional analysis and ternary plot sections). Therefore, conservative lower and upper boundaries were obtained via the backcalculation process capturing all the variations as shown in Fig. 5.8. Table 5.9 shows the results of the simulated boundaries. The broad variation (upper bound is about 4 times the lower bound) in the dataset may not represent true material behaviour and based on the limitations of the current model, the dataset presented in Table 5.9 should be considered with caution.

The increase in stiffness and brittleness suggests that the cohesion 'c' plays a more dominant role in the failure-remoulding behaviour of the dry specimens. Developing a backcalculation process for determination of dry specimen material dataset requires very intensive research and hence is not considered further in this thesis.

Table 5.9 Model predicted properties – Dry state

		Elastic Parameters			**Plastic Parameters**	
		$E_0 \le E_t \le E_{\max}$ (MPa)	$\phi_{\min} \le \phi \le \phi_{\max}$ (^{0})	c (kPa)	ψ (^{0})	H_p (kPa)
Dry	Lower bound	$80 \le E_t \le 100$	$40 \le \phi \le 43$	200	2	200
	Upper bound	$345 \le E_t \le 350$	$40 \le \phi \le 43$	200	2	200

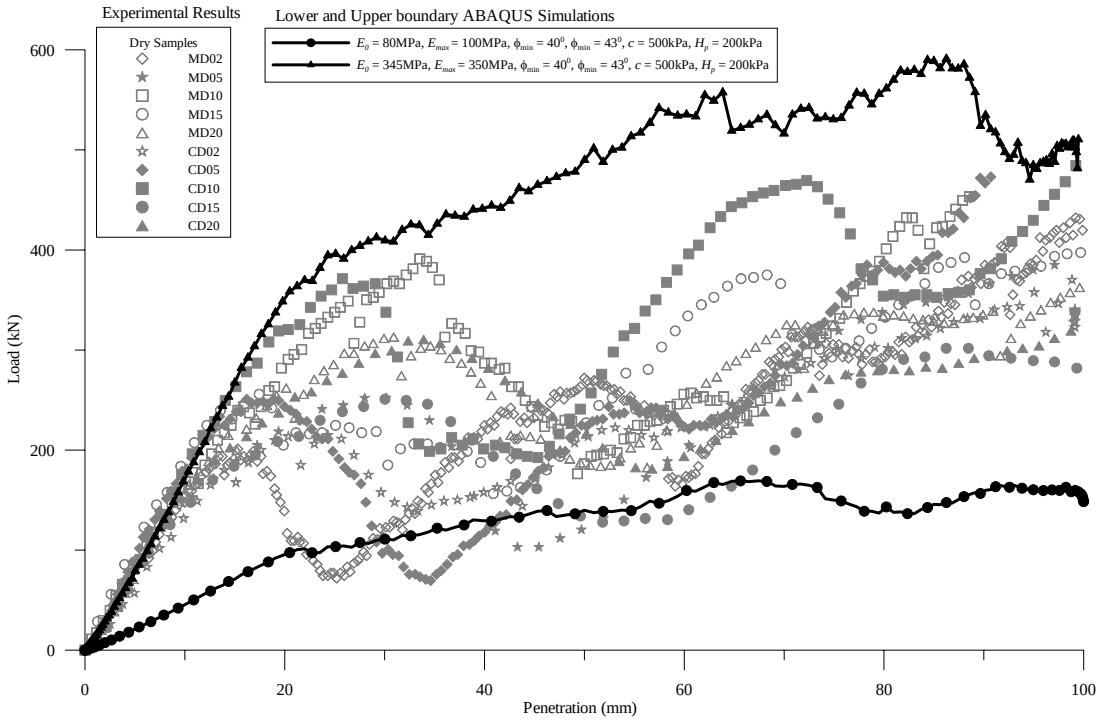

Figure 5.8 Predicted boundary envelopes of dry state

5.2.1.4 *Final Output*

Table 5.10 summarises the material properties predicted from simulations of the OMC, saturated and dry states of the experimental data. The relevant FE simulation data are provided in Appendix C.6.

Table 5.10 Predicted material properties from simulations

		Elastic Parameters			Plastic Parameters	
		$E_0 \le E_t \le E_{max}$ (MPa)	$\phi_{min} \le \phi \le \phi_{max}$ (^{0})	c (kPa)	ψ (^{0})	H_p (kPa)
Dry	Lower bound	$80 \le E_t \le 100$	$40 \le \phi \le 43$	500	2	200
	Upper bound	$345 \le E_t \le 350$	$40 \le \phi \le 43$	500	2	200
OMC	Lower bound	$30 \le E_t \le 80$	$35 \le \phi \le 38$	300	4	300
	Upper bound	$80 \le E_t \le 130$	$35 \le \phi \le 38$	350	7	350
Saturated	Lower bound	$20 \le E_t \le 45$	$33 \le \phi \le 35$	300	7.5	300
	Upper bound	$55 \le E_t \le 80$	$33 \le \phi \le 35$	300	6.7	300

As expected from the experimental results, the saturated state had the lowest values of the elastic properties, E_0, E_{max}, ϕ_{min} and ϕ_{max} for each of the lower and upper bound while the dry state showed the highest values. The plastic modulus was the same for both saturated and OMC states while dry state predictions were the lowest.

The lowest range between E_0 = 345 MPa and E_{max} = 350MPa was observed in the upper bound at the dry state while the highest range was observed in the OMC state. A similar pattern was observed in the lower bound values of E_0 and E_{max} too. These ranges show the variability expected from the simulations which are relevant to critical soil conditions, in the present case mainly the degree of saturation and the very high stress levels.

Friction angle and tangent modulus are primary strength indices for soils. The initial tangent modulus is more influential in obtaining better analytical results. Table 5.11 shows some typical values suggested in literature for E, ϕ, ν, ψ and c, for soils of similar type to the capping layer material.

Budhu (2000) and Duncan (1992) have indicated typical values of peak friction angle ϕ_p and the ultimate friction angle ϕ_{cv} for mixtures of gravel and sands with fine grained soils

(Liao 2003). Further, empirical equations of friction angle for granular soils can be found in Liao (2003). The ϕ values predicted from the model of $33^0 - 43^0$ are justifiable compared to the values suggested for mixtures of gravel and sands with fine grained soils. As discussed by Means and Parcher (1964), the angle of friction ϕ' exhibited by the naturally or artificially cemented granular soil is smaller than that of the friction angle ϕ exhibited by the same soil in an uncemented state (Fig. 5.9). They further stated that a cemented material undergoes two failures, one when the cohesive resistance is broken and again when the internal shearing resistance of the granular component is broken. The strain required to develop the full shearing resistance is much greater than that required to break the cohesive bonds. Line AD represents the strength of soil at the instant when cohesive bonds are just about to be broken and line OC shows the shearing resistance at much larger strains when complete destruction of the bonds of the cementation material has occurred and material behaviour is similar to that of a clean granular soil. As such, comparison of the current model predicted data with triaxial test data are also presented in Table 5.11.

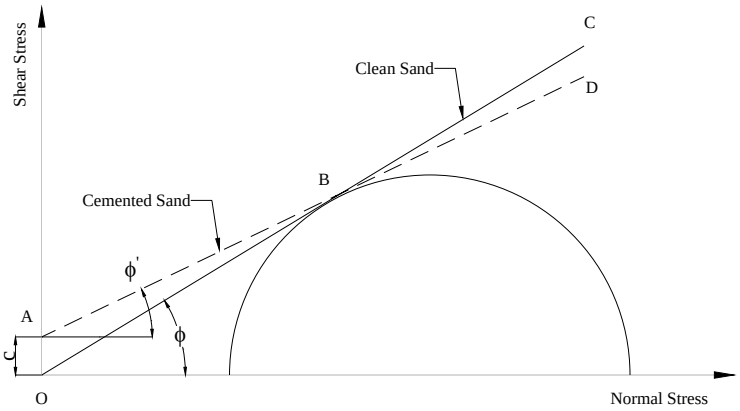

Figure 5.9 Strength line of cemented granular soils (Means and Parcher 1964)

Typical modulus values suggested for different types of soils are presented in Table 5.11. A comprehensive study of various empirical relationships suggested in literature can be

found in Liao (2003). The model predicted E_0 values of 20-55MPa for saturated state, 30-80MPa for OMC state and 80-345MPa for dry state and E_{max} values of 45-80MPa for saturated state, 80-130MPa for OMC state and 100-350MPa seem reasonable when compared with the values for sand and gravel and the values obtained from the triaxial test results in Table 5.11. Further, in comparison to the uniaxial test results of the OMC state samples, the model predictions of saturated and OMC states seem reasonable.

For sub-base and unbound base materials used in pavements, the following values were suggested by Croney and Croney (1992) as useful target values in structural analysis. An initial modulus of 150MPa with a ν of 0.3 was suggested for the unbound base and a modulus of 100-150MPa for the sub-base (Croney and Croney 1992). Sowers (1979) also discussed that ν is not a constant and is stress dependent. Sowers (1979) stated that ν exceeds 0.5 when the volume and void ratio of a dense cohesionless soil increase as the peak strength is reached. Some typical values of ν are given in Table 5.11. Accordingly, for sands and gravelly sands ν varies from 0.1 to 1.0, while the commonly used value is between 0.3- 0.4. Some empirical relationships synthesised in the past also can be found in Liao (2003). Therefore the assumed value of 0.35 is reasonable and representative enough in predicting other material parameters from the model.

As already discussed in choosing the value of $\psi < 15^0$, the predicted values $< 7.5^0$ seem reasonable.

Croney and Croney (1992) also indicated that use of high modulus values leads to the prediction of significant tensile stresses in the unbound material (< 10kPa), and suggest a

stress-dependent modulus be used so that tensile stresses in excess of 10kPa are not predicted. In order to prevent excessive tensile stresses, a tension cut-off can be incorporated in the model.

Table 5.11 Comparison of model predicted data with published, triaxial and uniaxial test data

Properties obtained from model predictions (This Thesis)

	Elastic properties					Plastic properties	
	Modulus, *E* (MPa)		Poisson's ratio, ν	Friction angle, ϕ (^{0})	Cohesion, *c* (kPa)	Dilation angle, ψ (^{0})	Hardening Modulus, H_p (kPa)
	E_0	E_{max}					
Dry state	80-345	100-350	Assumed as 0.35	40-43	~ 500	~ 2	~ 200
OMC state	30-80	80-130		35-38	300-350	4-7	300-350
Saturated state	20-55	45-80		33-35	~ 300	6.7-7.5	~ 300

Properties obtained from uniaxial test data (This Thesis)

Unconfined test	25						270

Properties obtained from triaxial test data (This Thesis)

Confining pressure	100kPa	108		39	330		
	375kPa	269					
	750kPa	381					
	1000kPa	479		36	534		
	2000kPa	589					

Published data for soils
Note: *Referenced in (Liao 2003)

	Elastic properties							Plastic properties	
	Modulus, *E* (MPa)		Poisson's ratio, ν	Friction angle, ϕ (^{0})			Cohesion, *c* (kPa)	Dilation angle, ψ (^{0})	Hardening Modulus, H_p (kPa)
Reference	*Cernica (1995)	*Bowels (1992)	Bowels (1998)	*Duncan (1992)	*Budhu (2000)			*Vermeer and de Borst (1992)	
Sand and Gravel Loose	100	50-150						<10	
Dense	150	100-200						15	
Sand, gravely sand			0.1-1.0						
Commonly used			0.3-0.4						
Mixtures of gravel and sand with fine grained soils				33-36 (peak)	28-33 (ultimate)	30-40 (peak)			

Figure 5.10 shows typical Mohr-Coulomb failure envelopes of the material tested. The material showed some cohesion and a high friction angle. By comparison, the final model backcalculation predicted results of modulus values in Table 5.11 seem well correlated

with the triaxial test results. The ϕ values of saturated samples are much lower than that obtained from the triaxial tests, the OMC and dry sample predictions are much more representative of triaxial data.

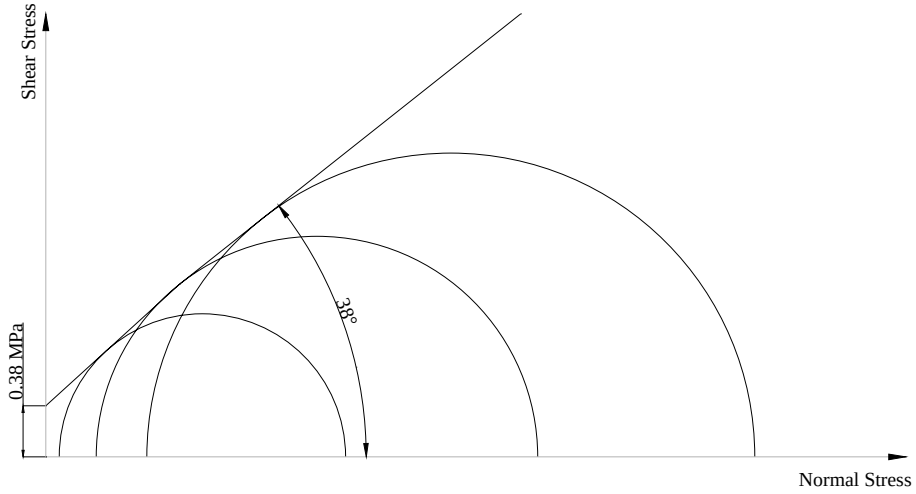

Figure 5.10 Typical Mohr-Coulomb envelopes of the material tested

From the foregoing discussion and Table 5.11 it can be concluded that the model backcalculation predictions are reasonable. The experimental and numerical investigations provided valuable qualitative and quantitative data over a wide range of stress levels.

5.2.2 Effect of Moisture Content on Predicted Parameters

From widely published data for unbound materials and all the experimental results and simulations obtained it was evident that the saturation level of the material governs the material properties. As such the effect of the moisture in dry, OMC and saturated states of the material is discussed below. The trends shown in Figs. 5.11-5.15 are very much dependant on dry state data and should be considered with caution. The relevant data sheets are located in Appendix C.7.

a) Effect on tangent modulus E_t

Fig. 5.11 shows the effect of moisture content on the predicted parameters of the material, E_0 and $E_{\max}$. The predicted parameters show a range of modulus values which narrows down at the high moisture contents. Therefore it can be concluded that the tangent modulus obtained is very much sensitive to the moisture content.

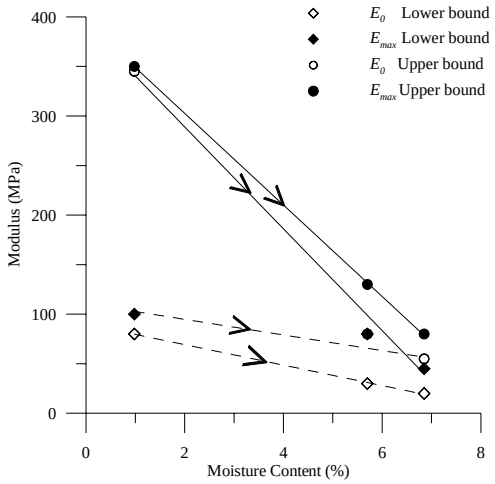

Figure 5.11 Effect of moisture on the tangent modulus

b) Effect on friction angle ϕ

Friction angle decreased with the increase in moisture, as apparent from Fig. 5.12.

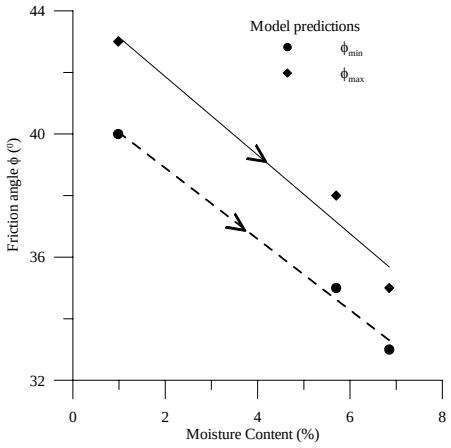

Figure 5.12 Effect of moisture on friction angle

c) Effect on cohesion c

Fig. 5.13 shows the effect of moisture on cohesion. As apparent from the model predictions the cohesion has increased with the decrease in moisture.

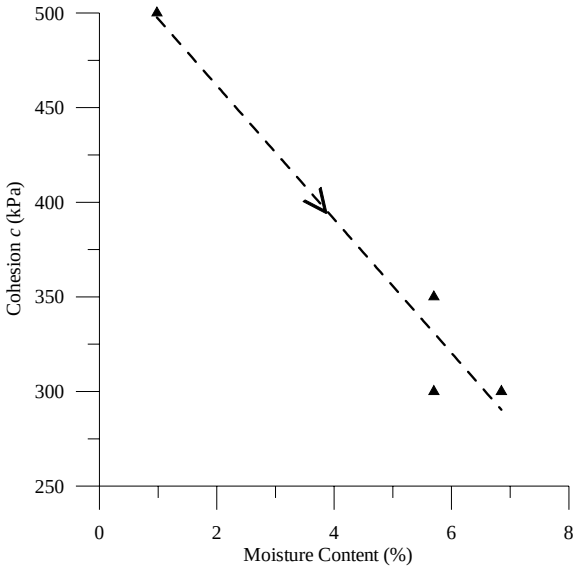

Figure 5.13 Effect of moisture on cohesion

d) Effect on dilation angle ψ

The predicted dilation angle showed an increase with the increase in the moisture content as shown in Fig. 5.14 whereas the friction angle showed the opposite trend (Fig. 5.12)

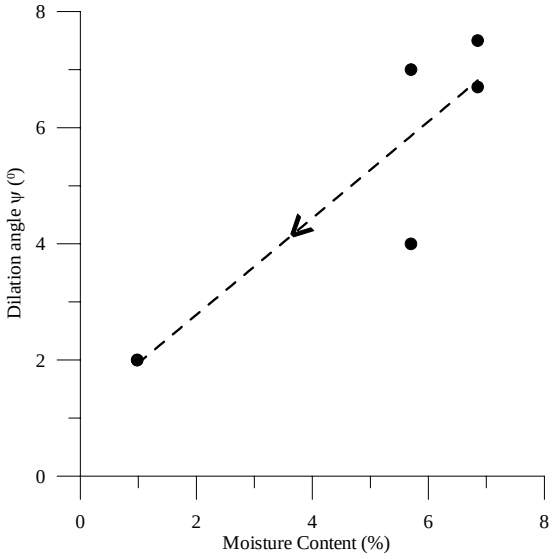

Figure 5.14 Effect of moisture on dilation angle

e) Effect on hardening modulus H_p

Hardening modulus also showed an increase with the increase in the moisture shown in Fig. 5.15. The hardening modulus itself has very low values (200-300kPa), thus its variation is not a very significant issue.

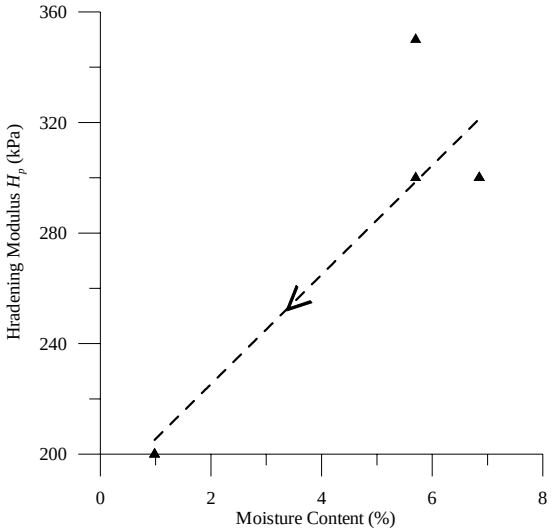

Figure 5.15 Effect of moisture on hardening modulus

Therefore it can be concluded that moisture has a greater effect on elastic material properties of tangent modulus, friction angle and cohesion, reducing them with the increase in the moisture content. On the other hand the plastic properties of dilation angle and the hardening modulus increased with the increase in the moisture. This may be caused due to the decrease in stability of the fine-grained components with the increase in moisture.

As discussed by Lambe and Whitman (1979), the friction between the mineral particles reduces with the introduction of water causing a decrease in shearing resistance as well as the friction angle. Al-Shayea (2001) has discussed that the properties of artificial clay-sand mixtures are highly influenced by the clay content and the moisture content. Al-Shayea (2001) has found that the internal frictional angle and shearing resistance generally

decreases with increasing water content or clay contents. This was very much observed in the experimental results (Fig. 5.1) as well as in the model prediction properties.

5.2.3 Parametric Study

In order to investigate the various assumptions made in the constitutive relationship and in modelling, a parametric study was performed considering the OMC predictions from the SCT model. The sensitivity analysis was performed individually for the primary parameters (E_t, ψ and ϕ) and the secondary parameters (c and H_p) to observe their degree of influence and significance on the variability of the load-penetration profiles obtained from the simulations of the SCT results. The medium mesh described in Section 4.1.7 was used in all the sensitivity analyses. The sensitivity of each selected parameter was analysed while keeping the input values of all other parameters at a prescribed level taken as the average for upper and lower bound of OMC state envelopes (Table 5.10) for simplicity here. The parameters varied in the sensitivity analysis are shown in the diagonal of Table 5.12 while the rest are the parameters whose values were fixed for the sensitivity studies. The relevant FE analysis data are provided in Appendices C.8 and C.9.

Table 5.12 Average parameter values of OMC state used in sensitivity analysis

$E_0 \le E_t \le E_{max}$ (MPa)	$\phi_{min} \le \phi \le \phi_{max}$ (^{0})	c (kPa)	ψ (^{0})	H_p (kPa)
E_t	$35 \le \phi \le 38$	325	5.5	325
$55 \le E_t \le 105$	ϕ	325	5.5	325
$55 \le E_t \le 105$	$35 \le \phi \le 38$	c	5.5	325
$55 \le E_t \le 105$	$35 \le \phi \le 38$	325	ψ	325
$55 \le E_t \le 105$	$35 \le \phi \le 38$	325	5.5	H_p

1) Elastic parameters

The elastic parameters considered for the sensitivity analysis are E_t, ϕ and c.

The effect of tangent modulus E_t on the load-penetration response was investigated by:

(i) keeping E_t (for two cases) as constant by considering the lowest and highest OMC state predictions of 30 and 130MPa respectively, i.e. $E_0 = E_{\max} =$ 30/130MPa and

(ii) varying E_t for two cases of $30 \le E_t \le 80$ MPa and $80 \le E_t \le 130$ MPa.

Fig. 5.16 shows the results of these four cases examined. Accordingly, it can be concluded that model output is very sensitive to E_0 and $E_{\max}$. Whilst the effect of increasing E_0 is to increase the initial stiffness of the specimen, the effect of increasing $E_{\max}$ appears to be an increase in the remoulding capability of resistance to penetration.

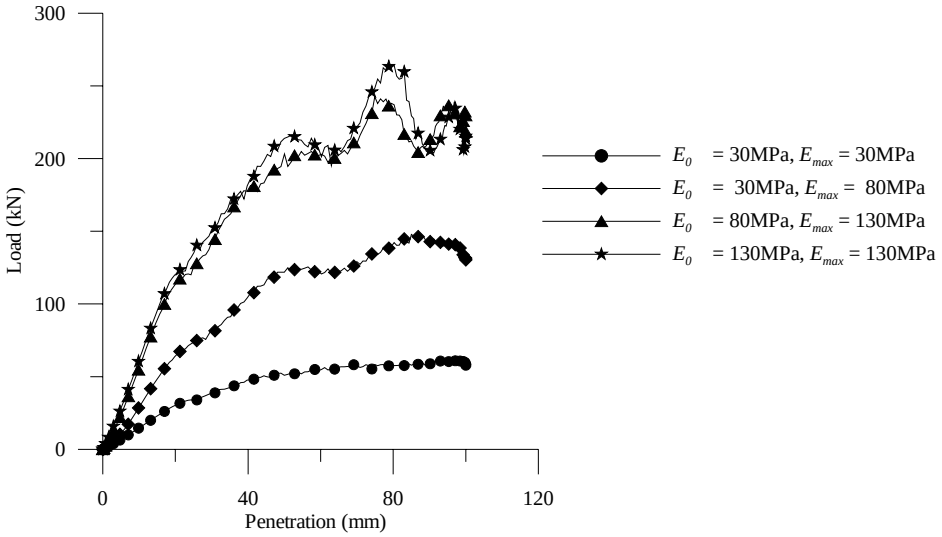

Figure 5.16 Effect of E_t : SCT Specimen Behaviour

As the variation in $35^0 \le \phi \le 38^0$ for the OMC state was 3^0, to understand the effect of friction angle ϕ to the load-penetration behaviour following cases were studied:

(i) keeping ϕ as a constant, i.e. $\phi_{\max} = \phi_{\min} = 35^0$, and

(ii) using two different ranges of ϕ, $25^0 \le \phi \le 35^0$ and $35^0 \le \phi \le 45^0$.

As the variation in the friction angle for one particular material cannot show very high values (more than 10^0), the difference between ϕ_{max} and ϕ_{min} were kept at 10^0. It can be seen from the load-penetration profiles shown in Fig. 5.17, that there is not much variation in load-penetration profiles compared to the effect caused by E_t. Therefore, ϕ in its present form of usage as a pressure sensitive property is not a very sensitive input parameter for the current FE model. This may be considered as an advantage of the FE model as we do not have to pay significant attention in determining the values of ϕ_{min} and ϕ_{max}.

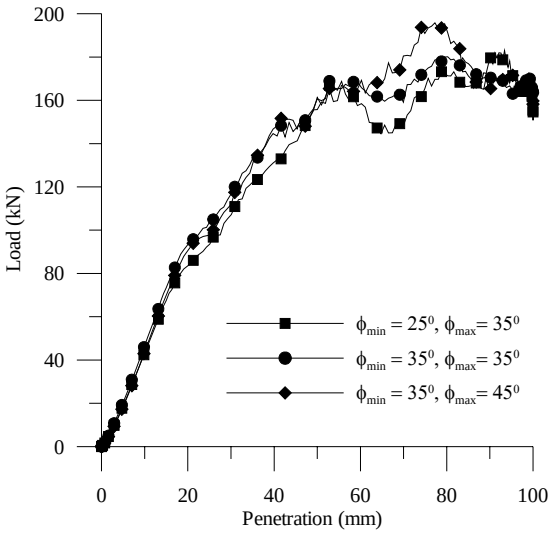

Figure 5.17 Effect of changes to ϕ : SCT Specimen Behaviour

Fig. 5.18 shows the effect of c. As the OMC state predictions showed low values for c (300 and 350kPa), three cases for the sensitivity were considered namely the average value of c = 325kPa, c = 0.1kPa, i.e. almost zero and c =1000kPa. The effect was not prominent in the load-penetration profiles. Therefore, c is regarded as not particularly sensitive to the behaviour of capping layer.

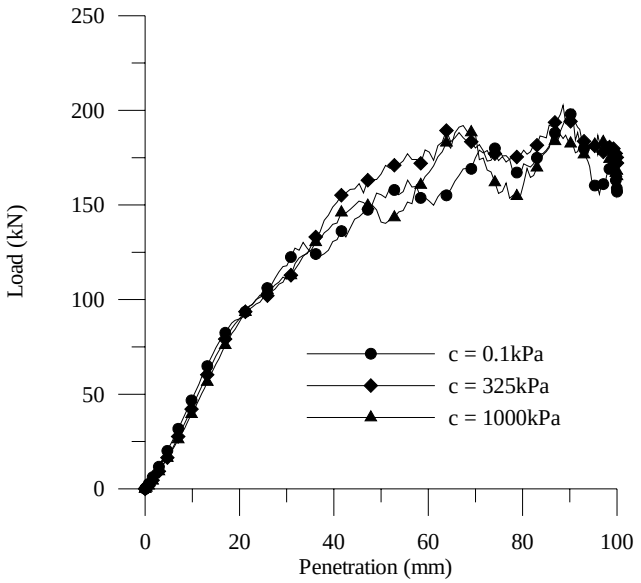

Figure 5.18 Effect of c : SCT Specimen Behaviour

Thus, from the sensitivity analysis of the elastic parameters it can be concluded that the tangent modulus is the most sensitive parameter; the friction angle and cohesion are very much less sensitive parameters. Care must therefore be taken in chracterising the material properties E_0 and $E_{\max}$.

2) Plastic parameters

The plastic parameters considered in the sensitivity analysis are ψ and H_p.

For associated flow rule $\phi = \psi$ and for non-associated flow rule $\phi \neq \psi$. If it is assumed that $35^0 \leq \phi \leq 38^0$, then for the non-associated flow rule the ψ will have to be set as $0 \leq \psi \leq 35^0$ and for associated flow rule ψ has to be set as $35^0 \leq \psi \leq 38^0$. Fig. 5.20 shows the load-penetration behaviour for non-associated flow rule for the cases of $\psi = 0^0$, $\psi = 5.5^0$ and $\psi = 34^0$. The higher the value of ψ, the higher is the resistance to penetration. Also note that the lower the difference between ϕ and ψ the higher is the

initial slope of the load-penetration profiles. Therefore ψ is regarded as a very sensitive plastic parameter.

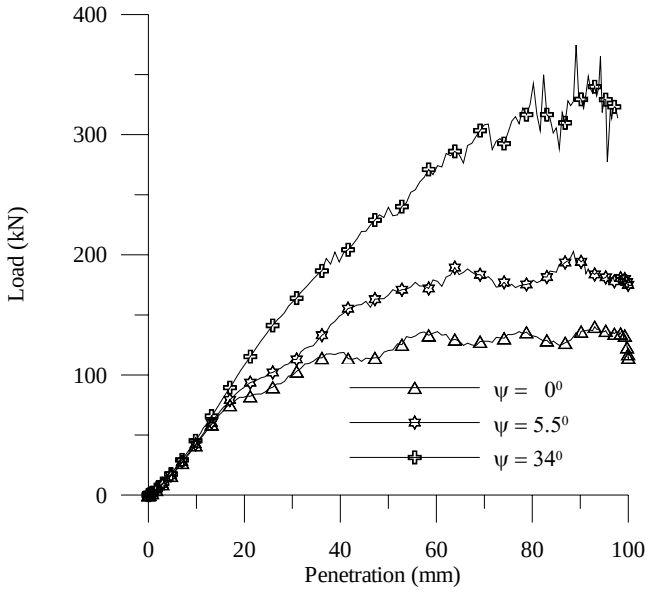

Figure 5.19 Effect of changes to ψ : SCT Specimen Behaviour

The sensitivity of H_p was observed by comparing the responses when H_p = 0.0, 325, and 1000kPa considering values lower/higher than the average of the OMC state of 325kPa. As shown in Fig. 5.21 the effect is not prominent compared to the sensitivity in ψ. Therefore, H_p is considered not a very sensitive parameter.

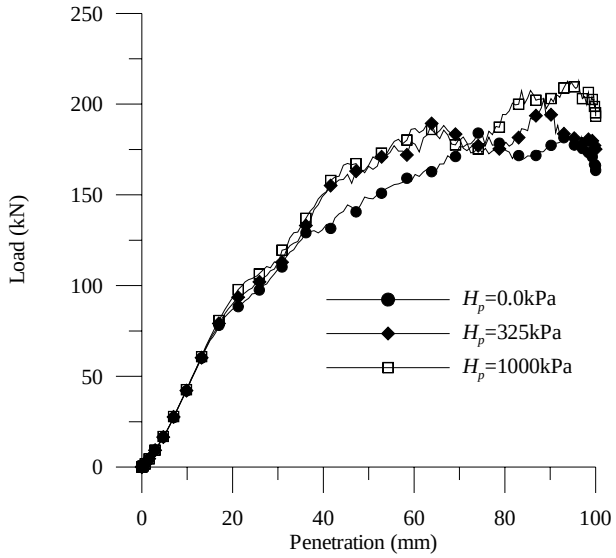

Figure 5.20 Effect of H_p : SCT Specimen Behaviour

Therefore, from the plastic parameters considered in the sensitivity analysis, the dilation angle was the most sensitive while hardening modulus is less sensitive in influencing predicted load-penetration profiles.

From the sensitivity analyses of the five input parameters considered in the backcalculation process it can be concluded that E_t and ψ are the most sensitive parameters. All other parameters showed insignificant sensitivity. Therefore care should be taken in the determination of the E_t and ψ values.

It can be further concluded from this parametric study that when performing an analysis of complex phenomenon like the nonlinear capping layer behaviour, care should be taken when assigning input values to the model. Though the above analysis was carried out varying only one parameter at a time so that its influence could be separated, care must be taken when assigning the model inputs as some parameters not considered to be sensitive (ϕ, c, H_p) when looked at individually may have a greater influence in the outcome of a combination.

5.3 Viability of the Model

The other main consideration is the viability of the model given the very high axial stress and confining stress induced in the semi-confined small scale mould used in the SCT. The normal and confining stresses induced at various penetration levels of the loading cylinder for a typical simulation are shown in Figs. 5.21 and 5.22 respectively. The corresponding FE analysis data are given in Appendix C.10.

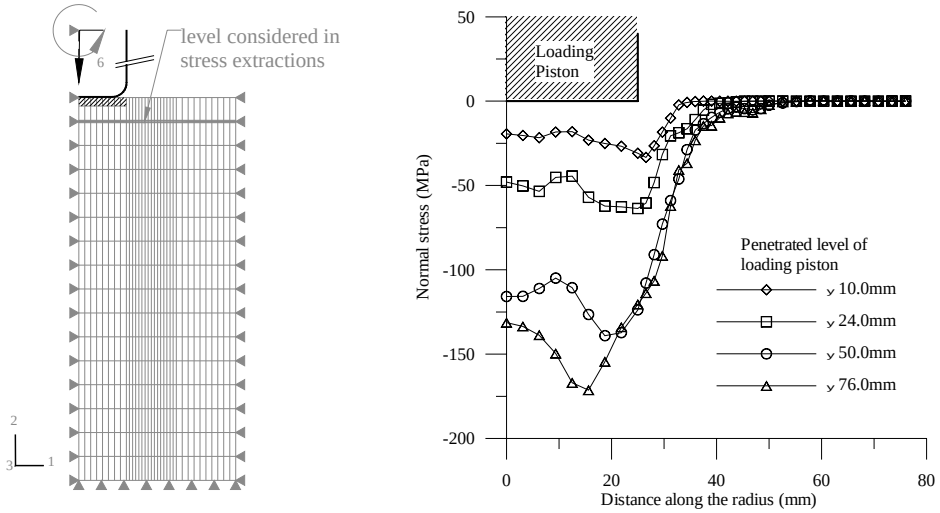

Figure 5.21 Normal stress development along a selected level with the penetration of the loading piston

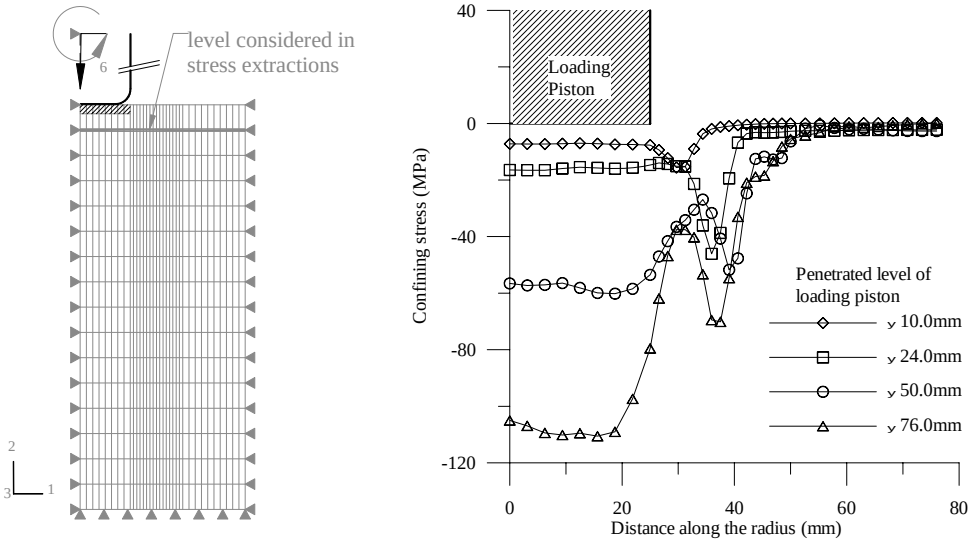

Figure 5.22 Confining stress development along a selected level with the penetration of the loading piston

It can be seen that even at a small penetration level of 10mm, the confining stresses are in excess of 1.0MPa. Even though the induced normal and confining stresses are high, by controlling E_0 and $E_{\max}$ suitably, reasonable material properties have been obtained using the backcalculation technique, thus vindicating the approach. Therefore it can be stated that the model is viable and can be used as a tool for the prediction of material properties.

The viability of the model for application to actual practical cases in the field will differ as the confining stresses induced in an infinite soil mass will be very much smaller compared to the stresses induced in the small scale SCT setup where the boundary effects influence the material behaviour. This issue is dealt with in Chapter 6 which discusses how the model was changed to suit plane strain conditions, and its behaviour is tested in a purpose built large scale experimental setup.

5.4 Summary

This Chapter has described a new user defined material routine for ABAQUS/Explicit simulations which incorporates a pressure dependent modulus and a friction angle. The capping layer material has successfully been characterised by the ABAQUS/Explicit model. The backcalculated material parameters have been compared with general soil properties published and triaxial/uniaxial test data.

The model was able to predict the material properties considering a wider range of stress levels as well as saturation levels adopted in the testing. Thus, it provided valuable representation of data more broadly than for a single stress-level/saturation condition or restricted narrow ranges of stress-levels/saturation conditions.

Six material parameters (the tangent modulus, Poisson's ratio, friction angle, cohesion, dilation angle and hardening modulus) were obtained from the backcalculation process whereas the current level of knowledge in inverse technique could not predict more than four parameters successfully. The model was able to predict satisfactory ranges for the

"engineering material parameters" rather than predicting singular values as soil is a very complex medium with a great level of variability.

The saturation level has the most significant effect on material properties. The elastic material properties of tangent modulus, friction angle and cohesion reduced with the increase in the moisture content. The plastic properties of dilation angle and the hardening modulus increased with the increase in the moisture.

The parametric study showed that tangent modulus and dilation angle are the most sensitive when looked at individually. However, choice of appropriate input parameters is of importance for any numerical analysis and sound knowledge of the effect of input parameters on the expected results will considerably improve the sensibility and reliability of the results.

It is expected that the implementation of the ABAQUS/Explicit model for advanced railway substructure structural response analysis will lead to better understanding of railway substructure and will be presented in Chapter 6.

CHAPTER 6

6. APPLICATION OF THE FE MODEL FOR CAPPING LAYER IN PRACTICE

6.1 Introduction

The preceding Chapters have demonstrated the development of a FE model based backcalculation process to predict the properties of the capping layer material coupled with the testing of the soil specimens in semi confined condition using CBR mould. The predicted properties have been shown to lie within the range of the expected values and/or the values reported in the literature for similar materials. Prior to applying the FE model based backcalculation process and the associated Semi Confined Tests (SCT) for practical cases, it is necessary to show the process is robust enough, especially for changes to boundary conditions. This is especially important as the SCT specimens were subjected to extreme levels of lateral stresses due to the rigid boundaries of the CBR mould.

The capping layer of railway subgrade, however, will normally not have such rigid lateral boundaries and hence under vertical penetration (for example, due to ballast pocket formation mechanism) their behaviour might differ to that of the specimens tested using SCT process. Furthermore, the SCT specimens have had axi-symmetric response whilst most rail tracks are normally analysed using plane strain idealisation. Therefore, it was necessary to examine the behaviour of the capping layer with reduced level of lateral confinement under plane strain condition by suitably modifying the FE model developed in Chapters 4 and 5. It was also necessary to carry out verification tests to validate the predictions of the modified FE model.

Basically, capping layers act to improve subgrade load bearing capability by protecting weak underlying layers that may prevail in the natural conditions. Given that all the deformations during construction and operation of the railway lines will be focussed on the behaviour of the cross sectional planes yz shown in Fig. 6.1, a plane strain model is most appropriate. The major (σ_1) and minor (σ_3) principal stresses occur in these cross sectional planes while the intermediate (σ_2) principal stress is parallel to the x-axis.

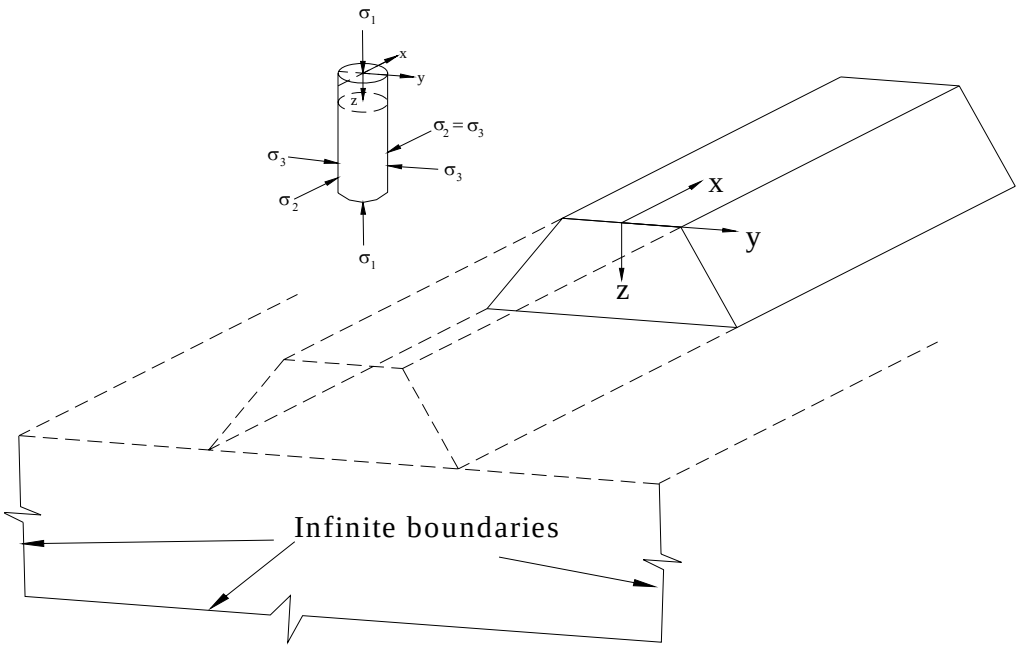

Figure 6.1 Plane strain conditions in a railway embankment

In order to validate that the results from the proposed technique described in Chapters 3, 4 and 5 are representative of the in-service performance of the capping layer material in railway subgrade, further modifications to the FE model as well as validation experiments under plane strain conditions are required. In order to keep the whole process much simpler, it is prudent to consider only the capping layer in the FE modelling and analysis although the capping layer in practice is sandwiched between several other layers of complex materials.

It should be noted that the major objective of the thesis is to develop an economical method of testing and establishing a process for calculating the properties of the capping layer material only, and not to involve detailed analysis of the rail track behaviour. *It is believed the procedure developed in the thesis to characterise the materials using a simpler testing process coupled with FE modelling based backcalculation can be used for any material used in track construction and the properties predicted could then be used in the analysis of track substructures.*

This Chapter presents the modified FE model, its predictions of the behaviour of capping layer under plane strain conditions subjected to vertical penetration and the validation of such predictions. The corresponding data relevant to this Chapter are located in Appendices D.1-D.3.

APPENDIX D.1	Convergence studies of the plane strain FE model
APPENDIX D.2	Application of SCT predicted properties to the plane strain FEM
APPENDIX D.3	Large-scale experiments data sheets

6.2 Design of Experiments for Plane Strain Conditions

To facilitate the testing of the capping layer material under plane strain conditions with much reduced levels of confining stress, a large scale experimental setup was designed. This required testing of a large volume of the capping layer material. Furthermore, as final validation experiments were sought, the large volume testing was required to be carefully designed by considering the constraints of costs, time and the laboratory limitations on space and loading/ deformation levels. The size of the box was selected to accommodate low levels of lateral stresses. The design has resulted in rigid steel boxes of internal dimensions 1.6m x 1.6m x 1.2m. The box consisted of 32mm thick base plate, 6mm thick

walls with 12 mm thick vertical gussets in two opposite sides, and 10mm thick vertical and horizontal gussets in the other two opposite sides of which one was designed with a 10mm thick clear polycarbonate sheet for viewing purposes (Fig. 6.2).

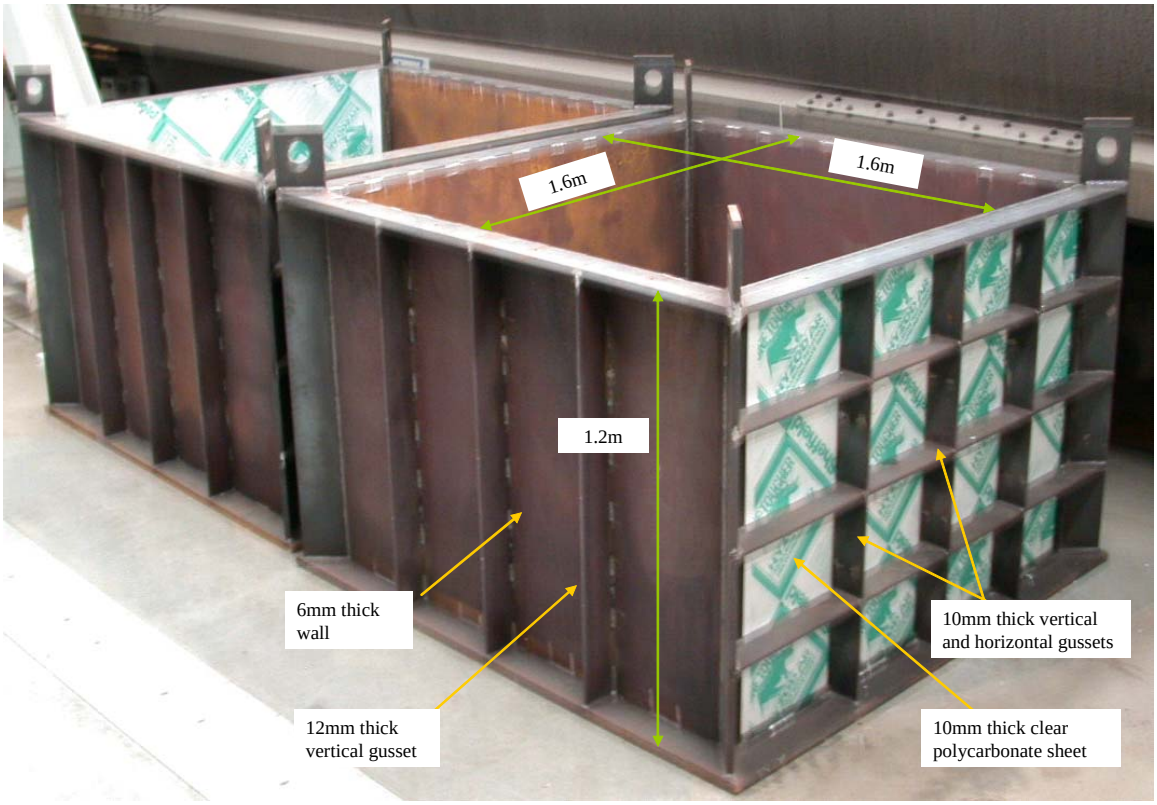

Figure 6.2 Boxes used for the testing of large scale capping layer material

Capping layer thicknesses recommended for improvement of in-situ conditions are often in the range from 300 to 600mm. Therefore, two thicknesses of the capping layer material were considered in the validation tests; 300 and 600mm.

Design of loading plate

A loading plate of 350mm x 700mm was considered large enough not to cause excessive stresses and small enough not to distribute the imposed loading to the side walls of the boxes. The length to width ratio of the loading plate was kept as two primarily to ensure that the load was transferred as a strip load incorporating the plane strain conditions sought

in the FE model. Secondly it ensured that the effect of load transferred through the soil mass to the vertical faces of the box would be minimal based on a vertical load spread slope of 1:1 (Fig. 2.11). In order to achieve a uniform load distribution over the entire plate area, a stack of 50mm thick plates were also designed to transfer the load uniformly to the specimen as shown in Fig. 6.3 (a), (b) and (c).

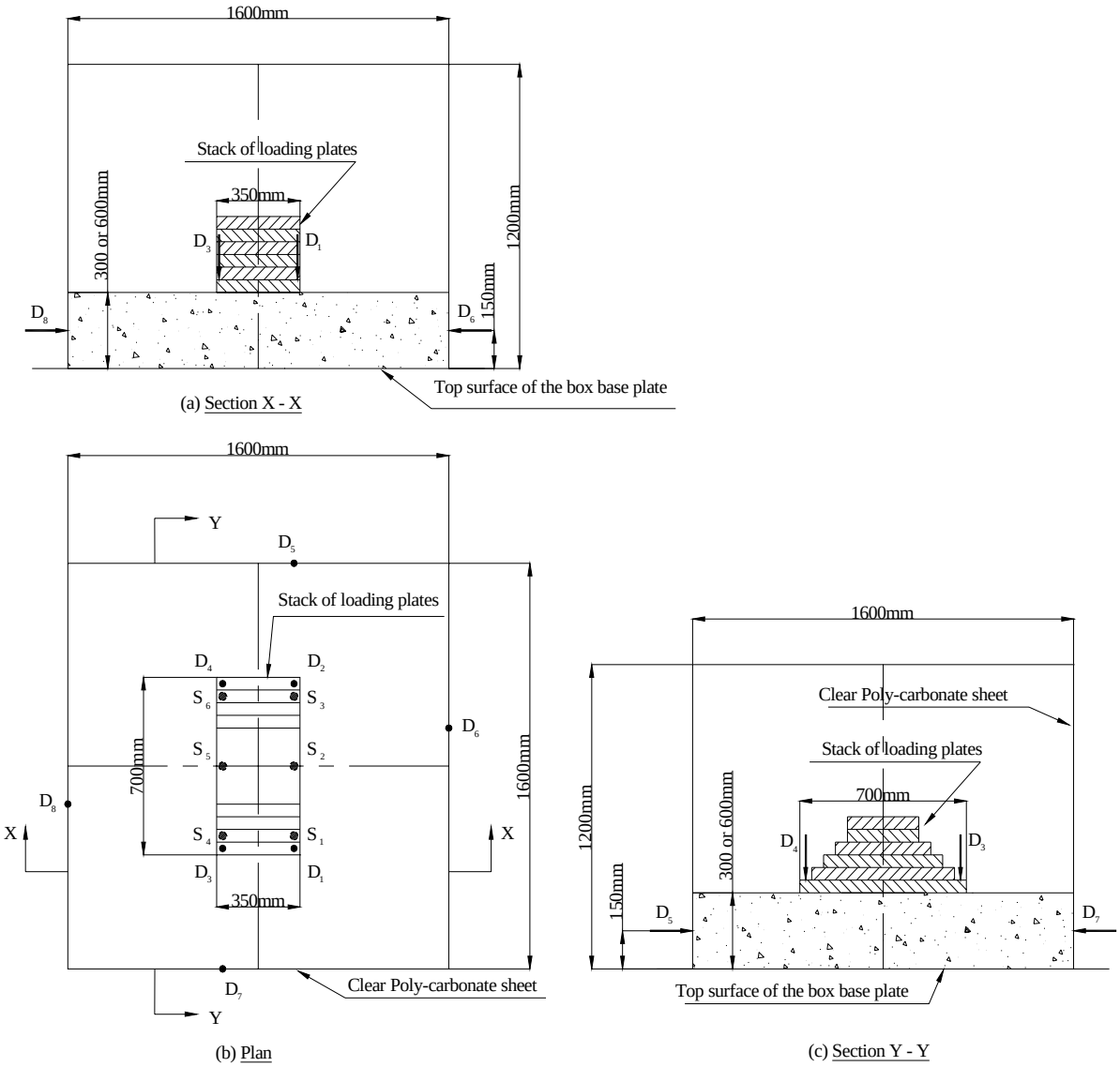

Note:
D denotes displacement transducers and S denotes strain gauges
Only the internal dimensions of the box are shown for clarity

Figure 6.3 Load distribution method and instrumentation layout

Design of Instrumentation

To obtain reliable results desired from the experimental investigations, it was required to locate all instrumentation independent of the box or the loading frame. An independent framework was therefore designed to hold the displacement transducers and the framework was attached to the concrete floor. The vertical deformation of the specimens was measured using two sets of displacement transducers D_1/D_3 and D_2/D_4 at the corners of the bottom plate shown in Fig. 6.3 (b) and the average displacement of these transducers were taken as the deformation of the capping layer. Another two sets of displacement transducers, D_5/D_7 and D_6/D_8 on the walls shown in Fig. 6.3 (b) were used to measure any horizontal movements during loading. The displacement transducers D_5/D_7 and D_6/D_8 were located at 150mm above the bottom plate of the box as depicted in Fig. 6.3 (a) and (c).

As shown in Fig. 6.3 (b), by locating three sets of strain gauges S_1/S_4, S_2/S_5 and S_3/S_6 on the bottom plate, any uneven movements due to warping or bending of the plate during loading were measured.

Method of compaction

In practice, capping layers are compacted in horizontal layers *not exceeding* 200mm loose thickness and the minimum density to be achieved is 95% of the maximum dry density by modified compaction.

Thus, in order to achieve the required uniform density in the experiments it was decided to compact the material in horizontal layers of 150mm thickness. To ensure that a uniform density was achieved in each layer, a pre-calculated mass of the required volume was used

for each layer. Given the limited work space within the box it was necessary to use a small 40kg plate compactor of plate size 420 x 292mm for the compaction of the material. It was also decided to measure the as-compacted density by weighing the compacted material boxes just after compaction and to measure the moisture content using a small portion of the material sample used. At the completion of the test the density of the samples was measured using a Surface Moisture-Density Gauge (SMDG).

6.3 FE Modelling of the Capping Layer under Plane Strain Conditions

6.3.1 FE Model

The capping layer material modelled as a plane strain problem is illustrated in Fig. 6.4. The model in ABAQUS/Explicit used 4-node plane strain quadrilateral elements (CPE4R) with reduced integration. A suitable mesh was adopted after convergence studies using several trials of mesh densities. The bottom of the sample was restrained in direction 2 while the two vertical sides were restrained in direction 1. An analytical rigid surface was used to define the loading plate, positioned in contact with the top edge of the soil sample. The rigid surface was constrained to translate vertically downwards through a pre-defined displacement history. The displacement of the rigid surface was defined using the AMPLITUDE option using the SMOOTH STEP sub-option. The surface-to-surface contact between the rigid surface and the soil sample was defined using the finite sliding KINEMATIC based contact algorithm with contact pairs. Hard contact was defined in the vertical direction while a frictionless contact was defined in the tangential direction. ADAPTIVE MESH control option was used to avoid mesh distortion. The analysis was performed using ABAQUS/Explicit and the VUMAT routine was called at each material calculation point.

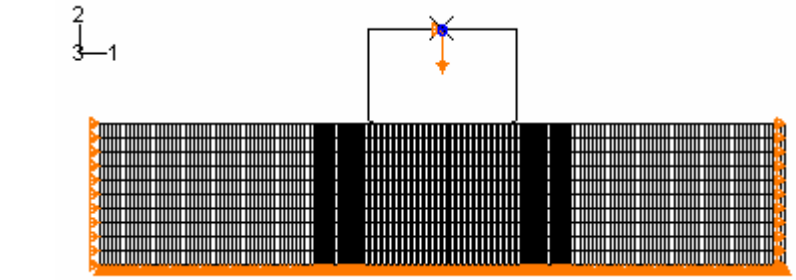

(a) 300mm layer model

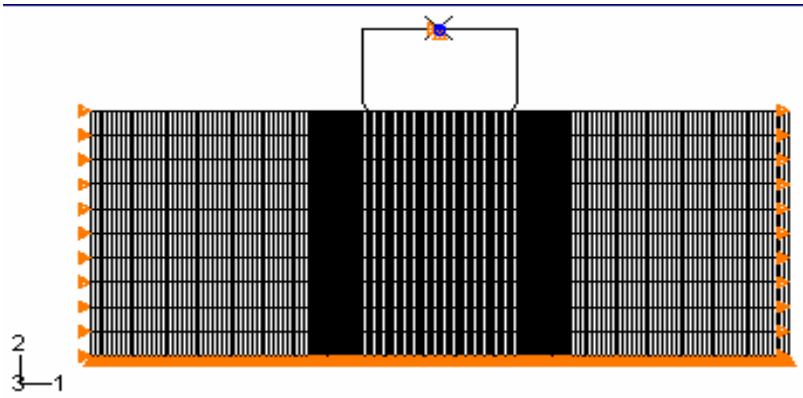

(b) 600mm layer model

Figure 6.4 ABAQUS plane strain model

6.3.2 Mesh Convergence Studies

As before, a mesh refinement was carried out to assess the sensitivity of the model predictions to the mesh density. Figs. 6.5 and 6.6 show three different mesh densities used in 300 and 600mm thick layers respectively.

Fig. 6.7 shows load-displacement profiles obtained, indicating that the medium meshes predicted similar results to that of fine meshes. Therefore the medium density meshes were used for both 300mm and 600mm layer specimens in the simulations for optimising the CPU time (Table 6.1). The coarse meshes were avoided due to noisy results. The relevant FE analysis data are given in Appendix D.1.

Table 6.1 Mesh refinement results

	300mm layer			600mm layer		
Mesh density	Coarse	Medium	Fine	Coarse	Medium	Fine
Mesh size	10x36	10x200	10x360	15x60	10x200	10x360
Number of elements	360	2000	3600	976	2000	3600
Number of nodes	407	2211	3971	900	2211	3971
CPU Time (hrs:min:sec)	00:00:03	00:00:44	00:02:46	00:00:08	00:00:41	00:02:31

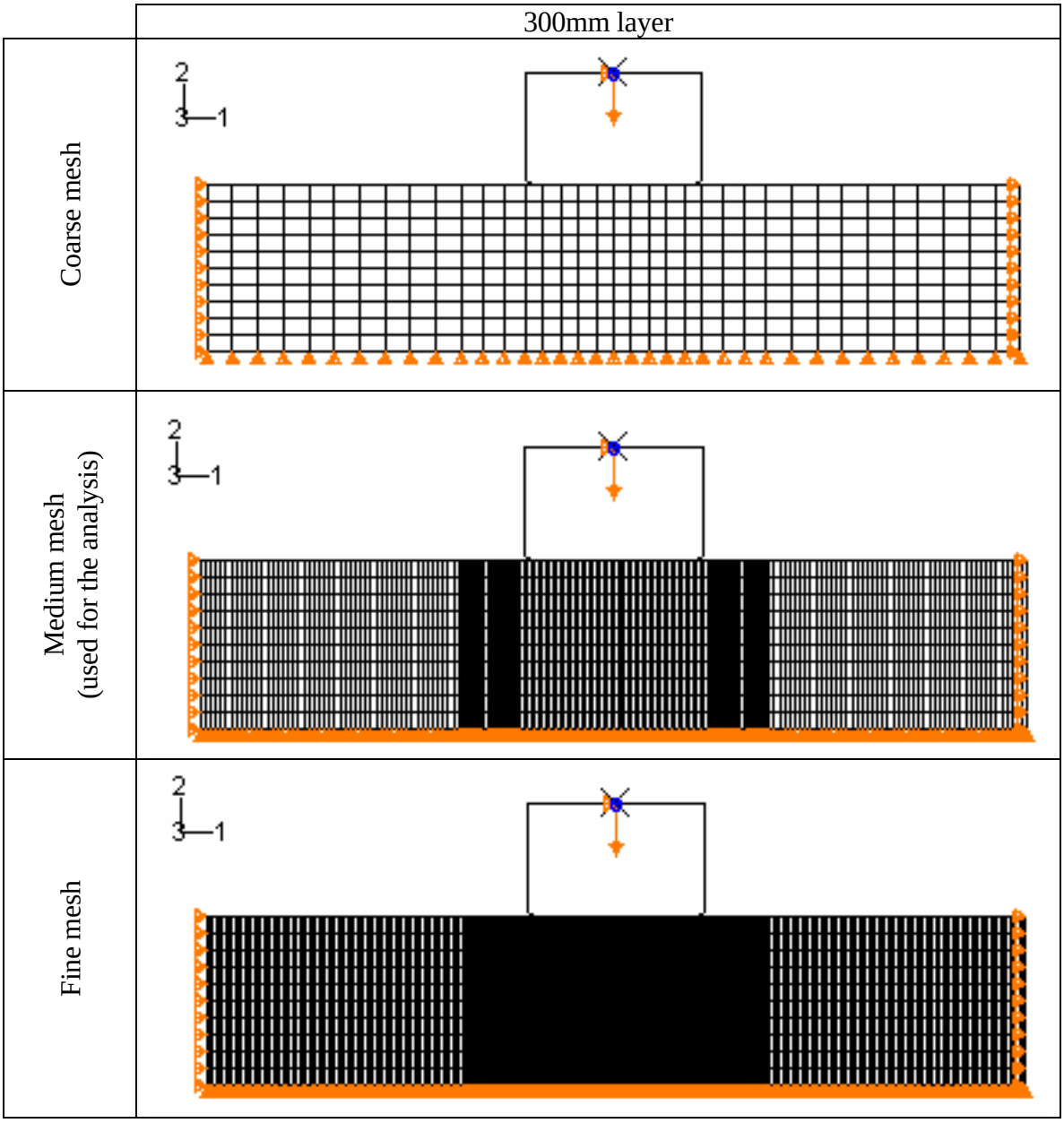

Figure 6.5 Original mesh configurations at different mesh densities of 300mm layer

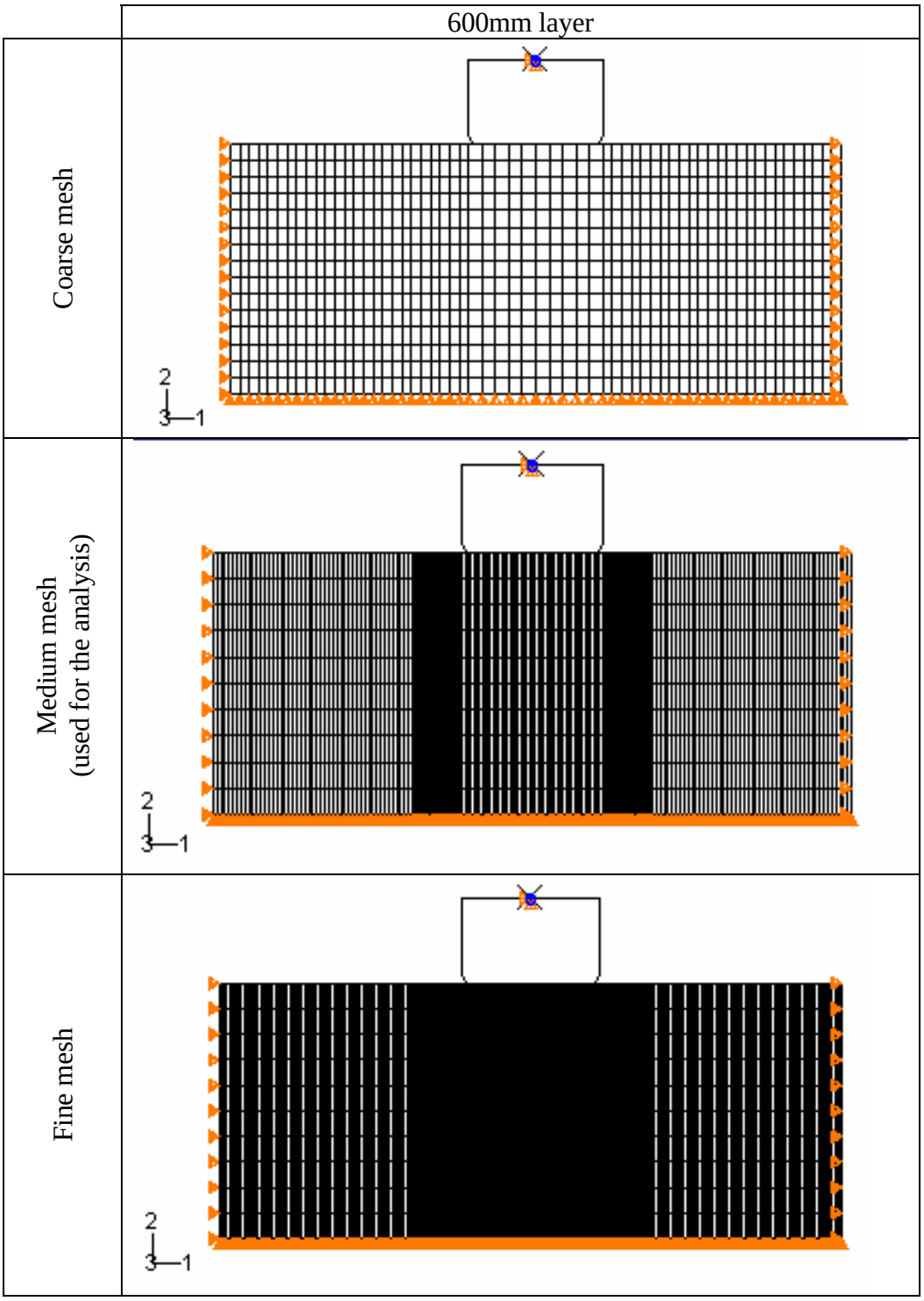

Figure 6.6 Original mesh configurations at different mesh densities of 600mm layer

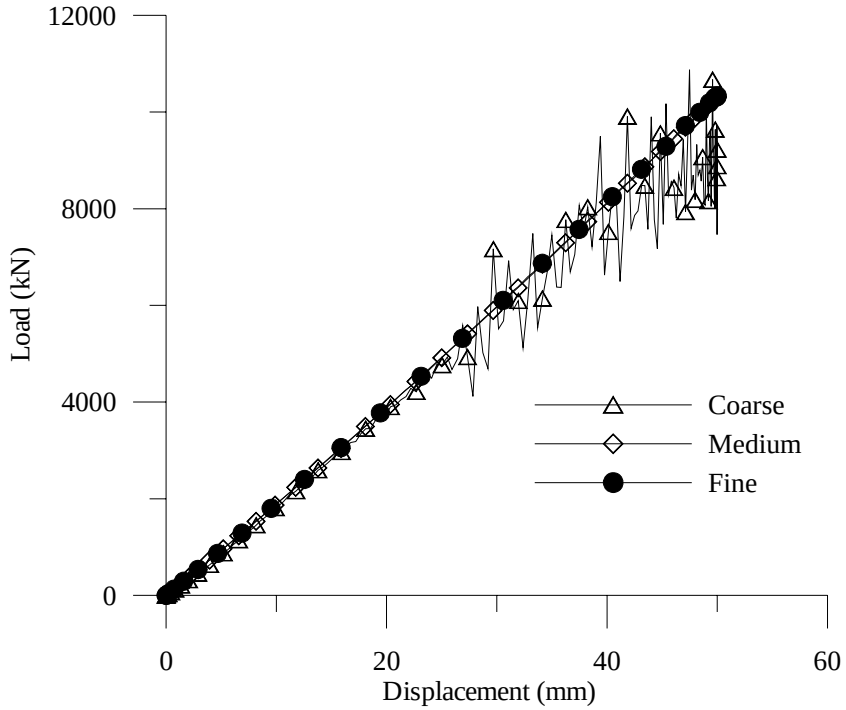

(a) 300mm layer

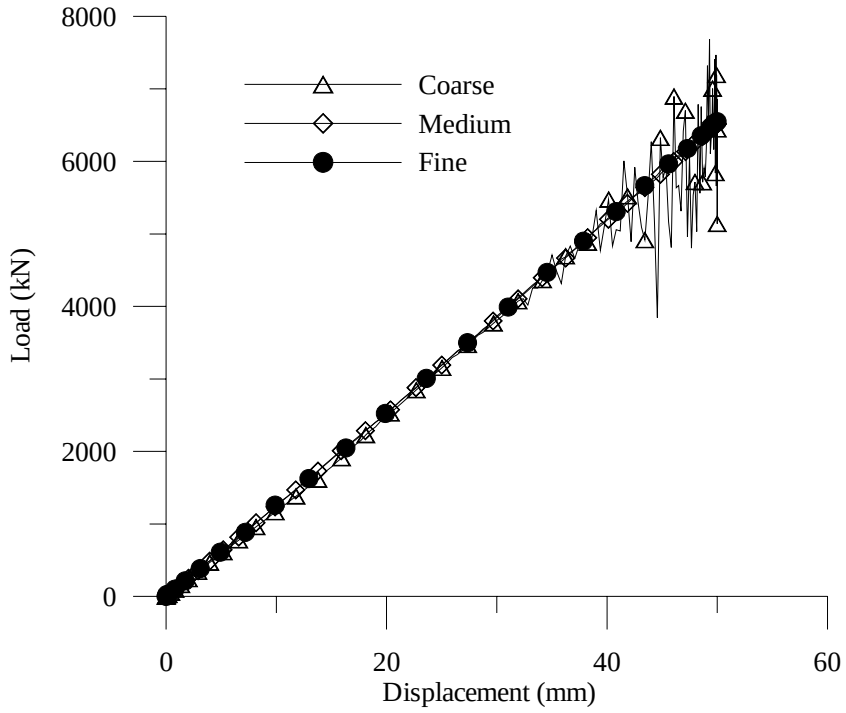

(b) 600mm layer

Figure 6.7 Load-displacement profiles of the large-scale set-up, ABAQUS/Explicit; influence of mesh refinement

6.3.3 Analysis, Results and Discussions

The purpose of the analysis was to demonstrate that the material data obtained from the axisymmetric FE modelling based backcalculation coupled with the semi confined tests could be used for the prediction of the capping layer behaviour under plane strain condition with much reduced level of lateral confinement. Although the axisymmetric analyses were carried out for specimens containing three different moisture levels, it was decided to carry out the plane strain analyses for only specimens under OMC condition. The material data obtained from the axisymmetric model for OMC state (Table 6.2) were used in the analysis of the plane strain model of the capping layer material.

Table 6.2 Model predictions of SCT setup for OMC state

		Elastic			**Plastic**	
		$E_0 \le E_t \le E_{max}$ (MPa)	$\phi_{min} \le \phi \le \phi_{max}$ (^{0})	c (kPa)	ψ (^{0})	H_p (kPa)
OMC	Lower bound	$30 \le E_t \le 80$	$35 \le \phi \le 38$	300	4	300
	Upper bound	$80 \le E_t \le 130$	$35 \le \phi \le 38$	350	7	350

The relevant FE analysis data sheets are located in Appendix D.2.

Fig. 6.8 (a) and (b) show the plane strain model predictions for upper and lower bounds obtained from the analysis respectively. It can be seen from the graphs that the 300mm layer showed an initial stiffer response than the 600mm layer. This has changed in the upper bound response beyond 15mm deformation where the 600mm layer started to gain a stiffer response while the 300mm layer started to show some failure with the increase in imposed penetration. At the lower bound, both layers have showed initial failure beyond 25mm deformation. The 600mm layer has totally failed after about 40mm deformation while the 300mm layer was able to increase its load carrying capacity due to remoulding response.

From the predictions of the plane strain model for a wheel load of 500kN (representing a 25t axle load subjected to a dynamic load factor of 4.0), the lower bound deformations obtained were 13mm and 17.5mm for 300 and 600mm layers respectively as shown in Fig. 6.8 (a). At the corresponding upper bound the deformations obtained were 5.0mm for the 300mm layer while for the 600mm layer it was about 6.5mm depicted from Fig. 6.8(b). The margin between the deformations of 300 and 600mm layers was higher at the lower bound (4.5mm) compared to that of the upper bound (1.5mm). This shows that if good quality stiffer materials are used for a capping layer, the ability to withstand settlements is much enhanced irrespective of their layer thicknesses, 300 or 600mm, at normally expected dynamic loading conditions.

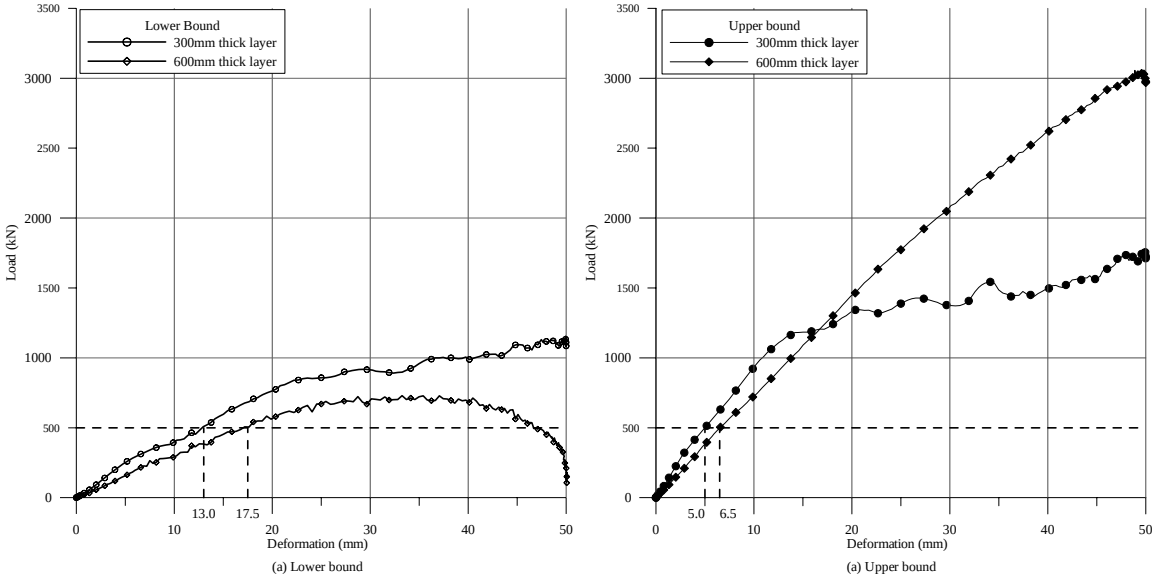

Figure 6.8 Plane strain model predictions and deformations at a 500kN wheel load

In service conditions for railway practices the allowable deformations are usually about 20mm. As shown in Fig. 6.9 (a), at a deformation of 20mm the limit loads obtained for the lower bound were 755kN for the 300mm layer and 565kN for the 600mm layer. At the upper bound the limit loads obtained were 1330kN and 1445kN for 300mm and 600mm layers respectively (Fig. 6.9 (b)). These wheel loads correspond to very high dynamic

impact factor and might not be experienced in practice. However a progressive accumulation of damage leading to 20mm deformation at much lower levels of load would be possible; a fatigue analysis would be required to predict such failures. The margin between the loads obtained for the 300 and 600mm layers from the current analysis were higher for the lower bound (190kN) than for the upper bound (115kN). As discussed before this once again confirms that the higher the quality of the material, the larger is the ability to withstand imposed loads than the less stiff material irrespective of their thicknesses.

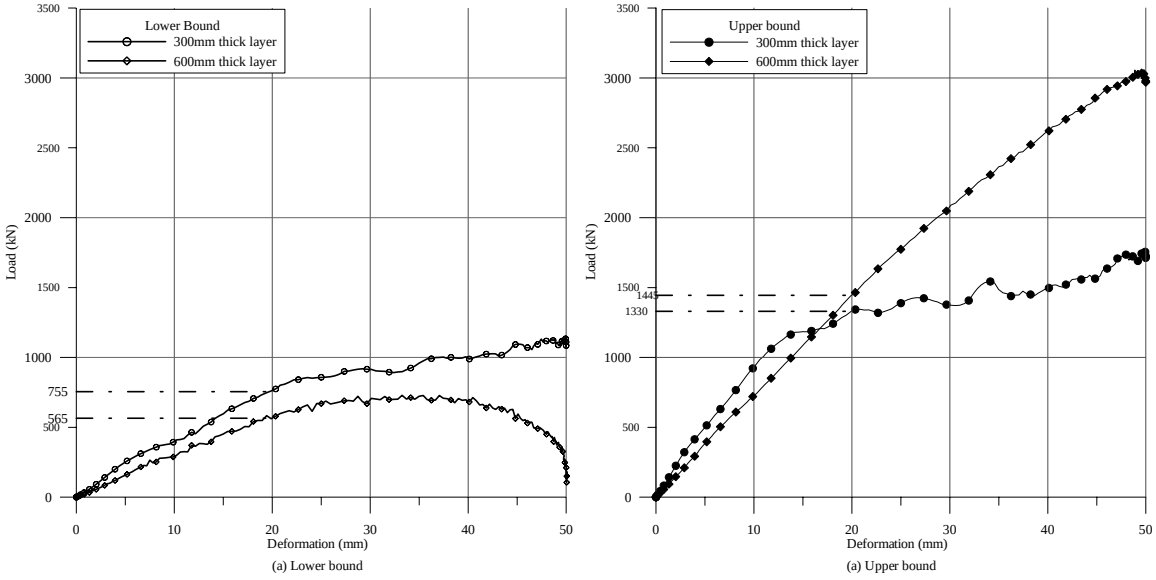

Figure 6.9 Plane strain model predictions and limit loads at a 20mm deformation

Therefore, it can be concluded that if a lower quality (less stiff) material cannot be avoided in the construction of capping layers, a thicker layer would not necessarily be appropriate. However, if a good quality (stiff) material is available then detailed thickness design of the capping layer is less critical. This judgement should be cautiously applied to any practical situations where the boundary conditions are not the same as considered in the limited experimental environment based simulations reported in this thesis. The load-deformation

relationship of the capping layer might be significantly affected due to the presence of poor layers below affecting the boundary conditions. Further research would be warranted to examine such effects.

As a general rule it can be concluded that *specifying a good quality material for the capping layer for railway substructure appears more important in practice than improved thickness design criteria or models*. The importance of characterisation of the material advocated in this thesis could be re-emphasised based on this conclusion.

6.4 Validation Experiments

The plane strain FE predictions discussed in the previous section have been validated using full-scale testing. Fig. 6.10 shows the experimental setup.

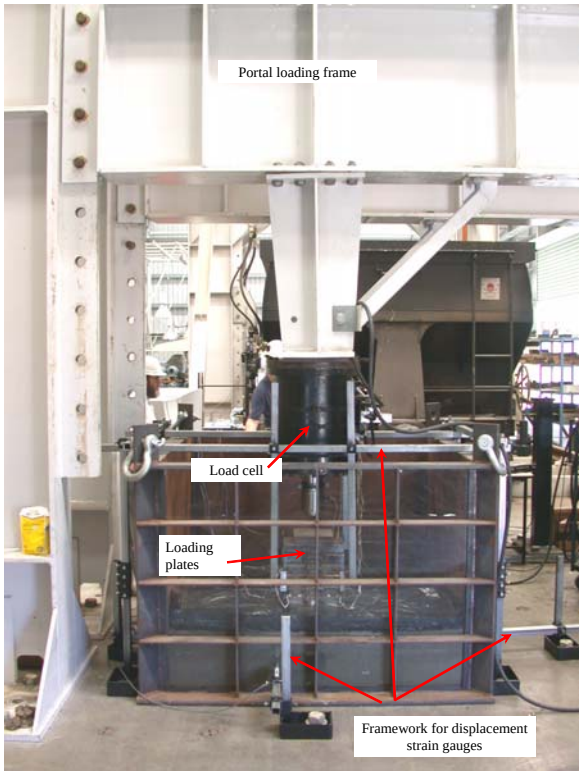

Figure 6.10 Experimental setup

6.4.1 Test Procedure

The axial penetration was imposed by a servo-hydraulic actuator with a load cell (capacity of 2000kN) fitted to a rigid portal frame. The load cell was centred over the capping layer sample and load was transferred via a stack of 50mm thick loading plates as shown in Fig. 6.10. The resisting load to penetration was measured directly via the loading actuator.

The movement of the actuator was also recorded. This is a precautionary measure which is useful in detecting any substantial differences of the movement of the plates to that of the loading actuator that might have occurred during testing.

All instrumentation was connected to separate frames or supports that were independent of the box or loading frame (Fig. 6.10). The strain gauges and displacement transducers located on the bottom loading plate are shown in Fig. 6.11. The average displacement of these displacement transducers was taken as the deformation of the capping layer.

Two sets of displacement transducers were located on the walls of the box to measure any horizontal movements during loading (Fig. 6.10) discussed in Section 6.4. These were located at 150mm height from the top surface of the bottom plate of the box.

To prohibit any substantial amount of moisture loss from the sample after compaction, it was covered with plastic sheets during and after the testing as shown in Fig. 6.11.

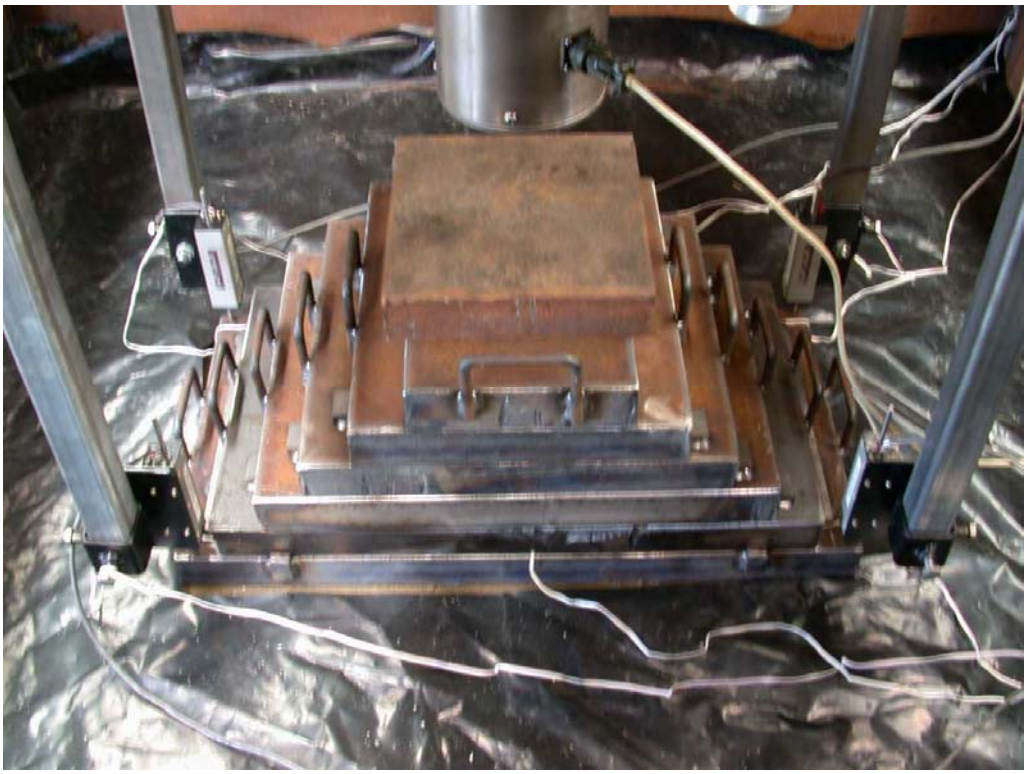

Figure 6.11 Loading plates stack with deformation transducers and strain gauges

The testing procedure is summarised below in detail.

Step 1. The capping layer material was first sieved through a 19mm sieve ensuring that oversize materials were removed. Due to the large material volume (about 8 tons) involved it was sieved through a motor driven sieve as shown in Fig. 6.12.

Step 2. Next, it was mixed using a back hoe at the required moisture level and kept for a minimum of 2hrs allowing water to permeate thoroughly in the mix (Fig. 6.13).

Figure 6.12 Sieving large material volumes using a motor driven sieve

Figure 6.13 Mixing at required moisture level using a back hoe

Step 3. The required compacted layer thickness of 150mm was first marked on the walls of the boxes (Fig. 6.14). The weight of the empty box was recorded as W.

Step 4. To ensure that each layer was of required uniform density, a pre-calculated mass of the required volume was put in to the box and levelled as shown in Fig. 6.14.

Step 5. The layer was then compacted using the 40kg plate compactor (Fig. 6.15) until the required compaction thickness of 150mm was achieved. The specifications of the compactor are plate size 420mm x 292mm, centrifugal force 630kgf (6.2kN), frequency 6200vpm (103Hz), and travel speed 20-22m/min.

Step 6. A layer of chalk dust was then applied on to the surface as shown in Fig. 6.16. This was carried out in each layer with a view to visually observing the deformation profiles after the completion of the test. (However this objective was not realised as samples extracted after testing crumbled without the ability of retaining their shapes.)

Step 7. Once all the required layers were compacted the weight of the box was measured and the density of the compacted sample was obtained. The moisture content of the material used was also measured.

Figure 6.14 150mm thick layers marked on the walls of the box and a levelled material layer ready for compaction

Figure 6.15 Compaction using a 40kg plate compactor

Figure 6.16 Application of a thin layer of chalk dust

Step 8. Loading plates were then located on the centre of the surface (Fig. 6.17).

Step 9. Next the top surface was covered to minimise evaporation of moisture from the top surface (Fig. 6.18).

Step 10. The box was then centred under the load cell (Fig. 6.19).

Step 11. All the instrumentations were positioned at the required locations (Fig. 6.20).

Step 12. The load was applied at a deformation rate of 5mm/min and the load-displacement data were acquisitioned.

Figure 6.17 Centred loading plates

Figure 6.18 Covered top surface hindering moisture evaporation

Figure 6.19 Centred sample under the load cell ready for instrumentation

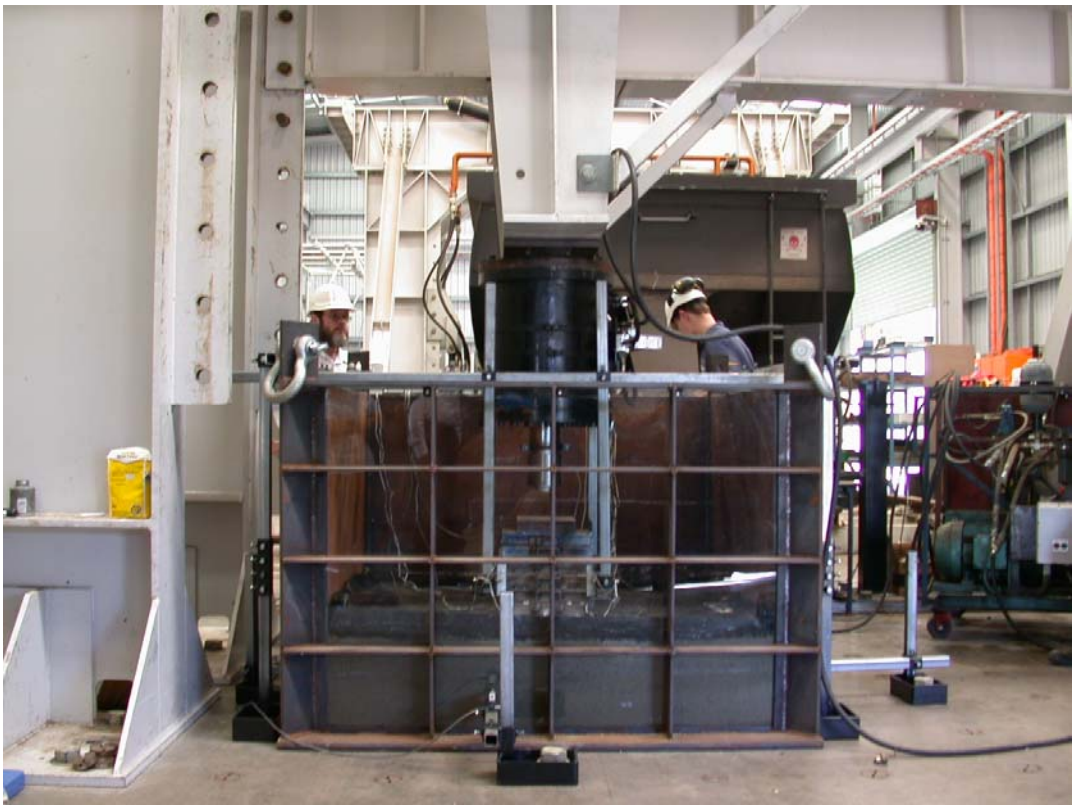

Figure 6.20 Instrumented setup ready for testing

Step 13. At the completion of the test, density of the samples was recorded using a Surface Moisture-Density Gauge (SMDG) as shown in Figs. 6.21 and 6.22.

Step 14. With a view of obtain a deformation profile, some core samples along the centre line of the specimen were obtained (Fig. 6.23).

(a) Using scraper plate/drill rod guide to prepare the test site and aiding the drill rod into the soil

(b) Drilled holes layout ready for taking measurements of density

Figure 6.21 Preparation for the Moisture-density gauge measurement taking

(a) The source rod containing Cesium-137 (8mCi/0.3GBq) is lowered to the desired depth

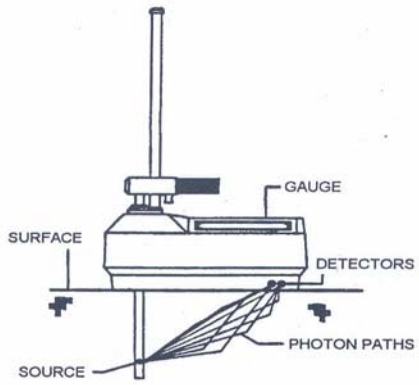

(b) The detectors in the gauge base measure the radiation emitted by the source rod and records the density at the specified depth

Figure 6.22 Obtaining the Moisture-density gauge measurement from SMDG (Troxler Electronic Laboratories Inc 1990-2001)

Figure 6.23 Obtaining core samples along the centre line of the specimen using a 50mm diameter sampler

6.4.2 Failure Mechanism

Fig. 6.24 (a) shows how the sample was heaved and moved towards the walls of the box when subjected to vertical penetration. In practice similar behaviour occurs on an operating railway as soil mass is subjected to many thousands of loading, unloading and re-loading cycles as well as repetitive wetting and drying. Such movements may not readily be visible due to the presence of the ballast layer. Instances when water is trapped within the soil mass often cause heaving at the edge of ballast which make visible such movements (Fig. 6.24(b)). Therefore, it can be stated that the application of the load will cause movement of the soil mass not only in the vertical direction (z direction, Fig. 6.1) but

also in the horizontal direction (y direction, Fig. 6.1) until equilibrium is achieved. The movements in the longitudinal direction (x direction, Fig. 6.1) will be less prominent.

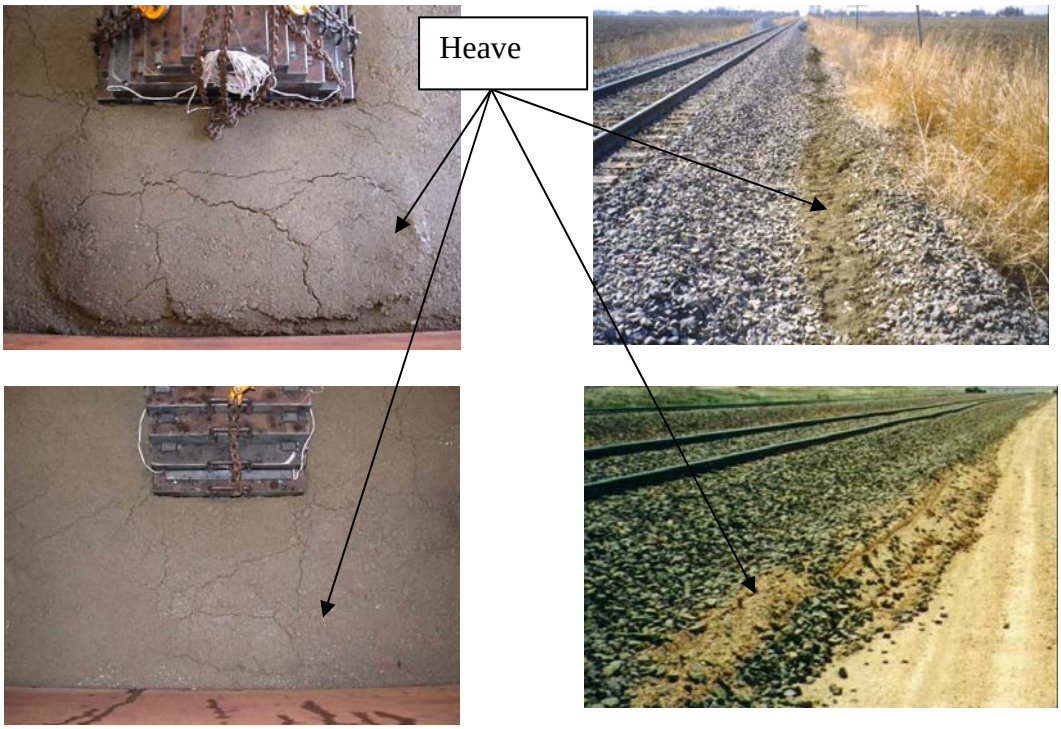

(a) in experiments (b) in practice

Figure 6.24 Heaving and pushing of material due to applied loading

6.4.3 Deformations and Strains

The data obtained from the displacement transducers (D_1, D_2, D_3 and D_4) and strain gauges (S_1, S_2, S_3, S_4, S_5 and S_6) located on the loading plate (Fig. 6.3) of the two tests is plotted against the load in Fig. 6.25. The relevant experimental data are located in Appendix D.3.

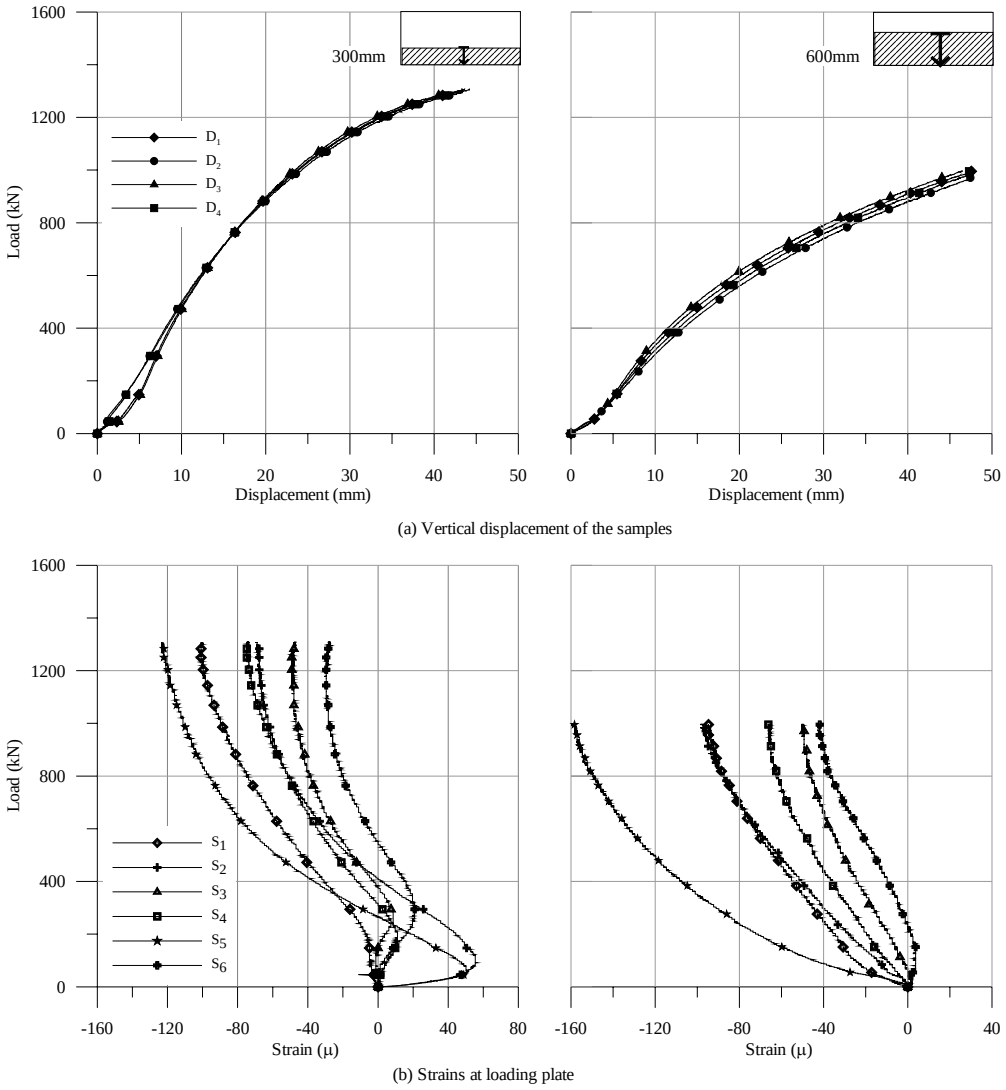

Figure 6.25 Displacement transducer (D_1-D_4) and strain gauge (S_1-S_6) readings relative to the normal load applied on the plate

It can be seen that the displacement transducers D_1-D_4 in the 300mm thick sample test showed almost the same deformation throughout, though below 10mm some discrepancies were observed. This might have been caused by some bedding errors between the load plates and the sample top surface. This is also highlighted in the strain gauge readings S_1-S_6 showing tensile strains (+) induced by the normal force below a load of 400kN. Subsequently all strain gauges showed compressive strains (-) induced by the normal force showing a uniform contact between the plates and the soil. In the 600mm thick sample test the bedding errors were minimal below 400kN as observed in the strain gauge readings S_1-

S_6. The deformation transducers, D_1-D_4 also gave similar results showing parallel movements in relation to each other.

Fig. 6.26 shows the relative movement of the side walls from their original position with load at 150mm from the base top surface as indicated in Fig. 6.2. The steel walls showed movement of less than 1.0mm for 300mm layer and less than 2.0mm for 600mm layer. The polycarbonate sheet wall moved by a maximum of just under 6.0mm.

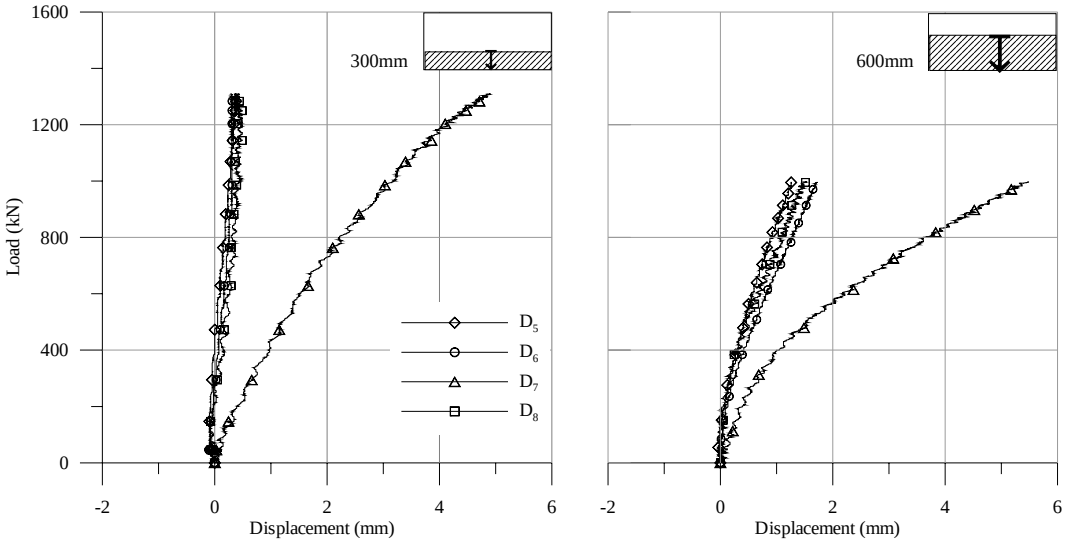

Figure 6.26 Vertical displacement profiles of the side walls

The behavioural pattern of the polycarbonate sheet indicates the flexibility required in the out-of-plane direction of the plane strain specimens (both 300 and 600mm) has indeed been achieved. Movable steel walls have been designed for ballast testing in plane strain conditions by Ionescu et al (2004) which is considerably more complex than the box described in this thesis. The steel wall (measuring in-plane deformation in the lateral direction) movement warranted adjusting the lateral boundary conditions of the vertical faces of the specimens (Figs. 6.5 and 6.6). Spring elements of various stiffness were attached and simulations repeated. No significant difference to the global behaviour of the specimens were observed and hence the work is not reported.

6.4.4 Spatial Variation of Density

Table 6.3 shows the in-situ density of the compacted samples and moisture content of the mix used. The density measurements were obtained by weighing the samples as at the completion of compaction.

Table 6.3 Density and moisture content of the layers

Layer thickness (mm)	300	600
In-situ bulk density (t/m^3)	2.20	2.21
Moisture content (%)	6.3	6.3

By considering the density of the compacted samples before testing it can be stated that overall an average compaction of 95% of the maximum dry density of 2.31t/m^3 (Table 3.1) was achieved by the compaction. This is well within the in-practice specification of 95% modified compaction. After testing, the density is expected to vary spatially and this has occurred as shown in Fig. 6.27 where the data measured by the Surface Moisture-Density Gauge (SMDG) at the completion of the tests are presented. Using the SMDG the densities were recorded at a depth of 150mm from the surface. Fig. 6.27 shows the densities within the loaded area and its outskirts. As expected, it was observed that the density within the loaded areas were higher than that of the outskirts.

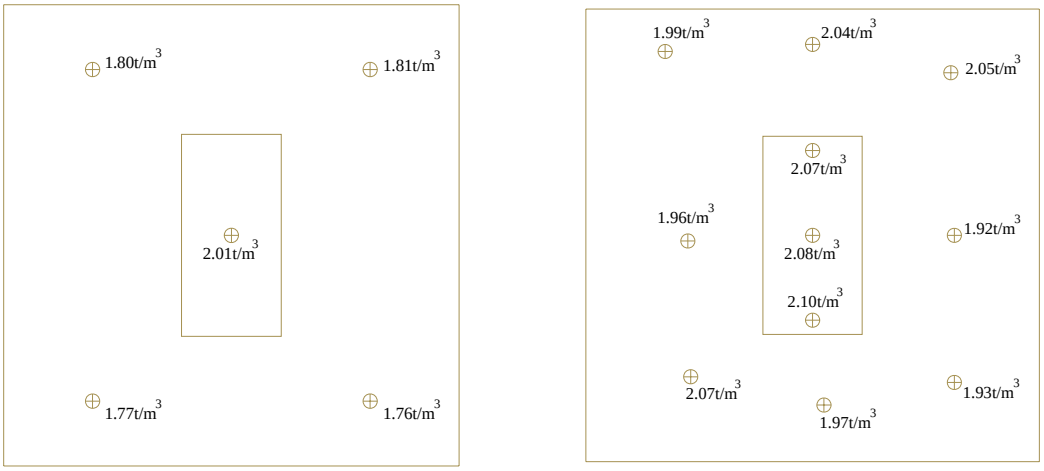

(a) 300mm layer (b) 600mm layer

Figure 6.27 Dry density recordings obtained from SMDG

The average modified compaction of the 300mm layer within the loading plate area was 87%. In the 600mm layer an average modified compaction of 90% had been achieved. The average modified compaction of the outskirts of the loaded area was 79% (300mm layer) and 86% (600mm layer). The reduction in the densities were obvious at a level of 150mm below the top surface as already the application of load has caused failure of the sample, loosened due to tensile stresses as shown in Fig. 6.24 (a).

Core sample data

Though the core samples were obtained (Fig. 6.23) with the view of obtaining the deformed profile, they were unable to be removed properly from the sampler without disturbing them. In fact, already loosened core samples were not intact and collapsed when removed from the sampler. Therefore, the expected deformed profiles could not be drawn.

6.5 Results and Discussions

Fig. 6.28 shows the final load-deformation profiles obtained from the experiments for capping layer thicknesses of 300 and 600mm. The average of displacement transducers (D_1, D_2, D_3 and D_4) was taken as the total deformation of the sample in the experimental results. It can be seen that a substantial progressive stiffness reduction had occurred with the increase in layer thicknesses. The gradual development of the ultimate load is indicative of progressive failure rather than a sudden brittle failure. This can be described as gradual transfer of load from failed zones to unfailed zones where the ultimate load will be reached as a combination of failed, nearly failed and other stresses. It is evident from the results that capping layer failures are progressive over a finite area rather than a singular stress value.

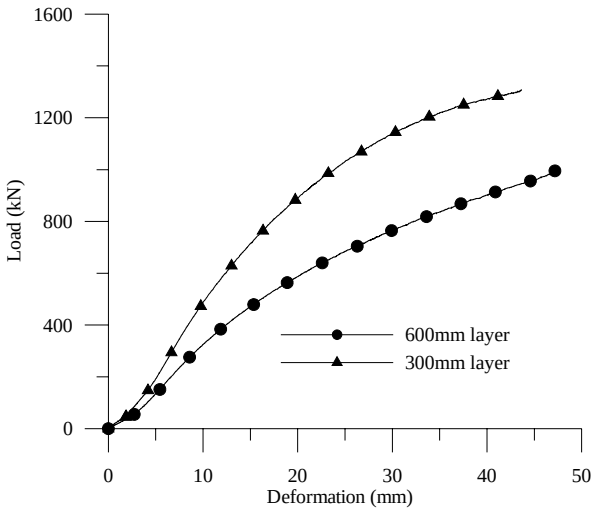

Figure 6.28 Comparison of load-displacement profiles of varying thicknesses

Figure 6.29 shows the experimental results together with the FE simulations carried out using the upper and lower bounds of the SCT predictions. It can be seen from the graphs that the experimental predictions tend towards the very extreme to the lower bound. Given the variability in the properties of the soils like the capping layer material considered in this thesis, the ability of the FE model to predict the capping layer material behaviour under plane strain conditions using constitutive properties obtained from axisymmetric FE modelling based backcalculation method coupled with SCT, is considered satisfactory.

Furthermore, although the properties of the capping layer material have been obtained from specimens under high levels of confining stresses, the constitutive material modelling developed in this thesis based on Drucker-Prager theory of plasticity including pressure dependent tangent modulus and angle of friction has worked well in adapting itself for situations that are vastly different to that of the original conditions from which they have been developed. Conversely it could be stated that although material data more representative of the field condition could be obtained by testing the capping layer materials in large boxes under plane strain condition with small levels of lateral

confinement, given the costs and time required for such tests, it is reasonable to estimate the properties of the materials using much smaller size specimens (SCT) contained in the CBR mould.

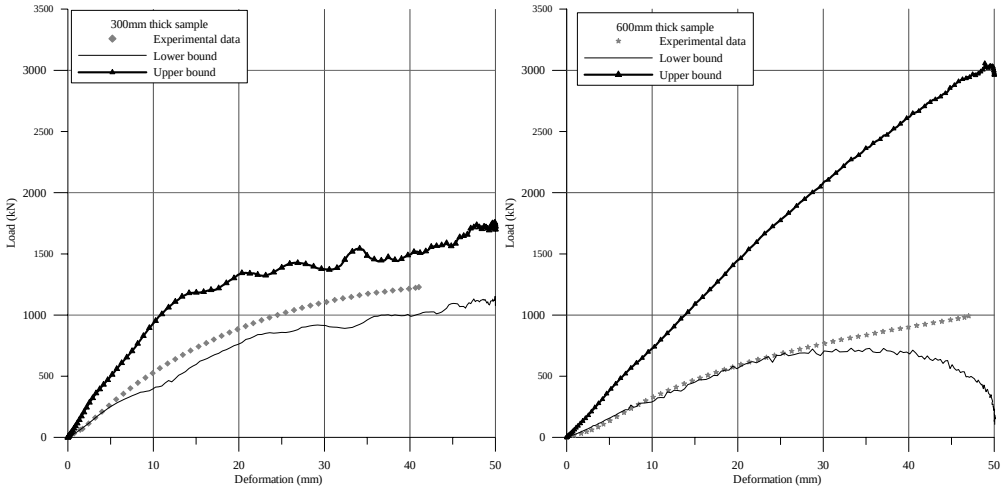

Figure 6.29 Comparison of experimental data with FEM predictions

From the two tests carried out it can be concluded that,

- The SCT predicted material properties were able to simulate the experimental behaviour of the capping layer under different conditions of stress states and FE idealisations.
- By successfully incorporating the pressure dependent tangent modulus and the angle of friction into the constitutive relationship, the model was able to predict the required material properties using the developed small-scale semi confined test which was much easier and economical to perform and less time consuming than cyclic triaxial tests.
- The use of the present model and the limited number of validated experiments does not guarantee that the SCT predictions can be used “generally” for either other materials or significantly different layer thicknesses of capping layer materials.

- The two validation tests had fixed base boundary conditions instead of the in service conditions of underlying soils of variable quality. Therefore, more experimental validation with an underlying layer of soil is required to prove the reliability of the present model in predicting behaviour in actual situations.

6.6 Summary

The development of a new small-scale experimental method (SCT) based FE backcalculation simulations of non-cohesive granular material has been reasonable in predicting the required properties that can be used for in-situ plane strain conditions prevailing in railway substructure and in road pavement. It is proved that data predicted from axisymmetric FE simulations can be successfully applied to plane strain conditions.

Large scale testing of capping layer in a purpose built testing apparatus has proved that the SCT predictions were reasonable and that this inexpensive method can be used as an alternate method to the conventional cyclic triaxial tests that are time consuming and expensive.

The development of a constitutive relationship that accounts for the pressure dependency of the properties of the non-cohesive capping soils has been successfully utilised in predicting material properties as well as permanent deformations based on theory of plasticity, whereas most models developed in past decades incorporated only the theory of elasticity of the material as described in detail in Chapter 2.

Though the limited number of validation tests (two) showed promising results, more experimental data are needed to generalise the findings prior to field applications.

CHAPTER 7

7. SUMMARY, CONCLUSIONS AND RECOMMENDATIONS

7.1 Summary

Capping layers are used in railway/pavement substructures to improve the structural stability where the in-situ materials can not sustain the imposed loads adequately especially without undue permanent deformations. It is essential that these capping layers be properly characterised for use in any design practices.

Methods of characterising railway substructure materials have first been reviewed in detail in this thesis. An economical method, both in terms of testing effort and cost of evaluating the capping layer material properties using penetration tests on specimens contained in a California Bearing Ratio (CBR) test mould coupled with a finite element modelling based backcalculation technique has been developed. The finite element based backcalculation of material properties has been achieved by incorporating stress-dependent tangent modulus and friction angle to modify the Drucker-Prager model. An explicit finite element code coupled with adaptive re-meshing technique was used to model the large vertical penetration relative to the height of the specimen without mesh distortion or any other form of numerical instability. However, whilst the explicit algorithm models the global behaviour adequately, it does not provide an accurate measure of the distribution of internal stresses within the specimens. Although more involved methods of importing the explicit solution into implicit algorithms for achieving acceptable internal stress distribution are available, such a procedure was not adopted as the main objective of the thesis was to evaluate representative upper and lower bound values of the properties of capping layer material only. Furthermore the backcalculation

method used was also a trail and error approach, although there is an emerging trend of using genetic algorithm search techniques for such inverse problems. Once again the adoption of approximate methods in preference to advanced techniques/ procedures is due to the practical objective of the thesis for developing a simple and economical method to determine the upper and lower bound properties of the capping layer materials which allow the practitioner to make reasonable assessments of the likely field performance of capping material.

The robustness of the evaluated material properties has been examined by applying the data to unfamiliar situation where the material layer was kept under plane strain condition with limited lateral confinement. The predicted behaviour of the capping layer material under plane strain condition has been validated using large-scale tests.

7.2 Major Conclusions

The following are some important conclusions made from this thesis:

(1) The simple penetration test termed 'Semi Confined Test (SCT)' coupled with the explicit finite element technique based backcalculation procedure is capable of characterising the material well. Methodology proposed in this thesis could be used to determine broad characteristics of the capping material for assessing their suitability.

(2) For this procedure to work well, both the tangent moduli and friction angle should be regarded as confining pressure dependent. A limited number (3) of drained

triaxial tests and uniaxial tests are required for the determination of initial trial values of elastic moduli, coefficient of friction, cohesion, and hardening modulus to be used in the backcalculation procedure. Capping layer material could be modelled as an elasto-plastic continuum represented by the Drucker-Prager failure criterion modified for the pressure dependent tangent modulus and friction angle to determine the level of permanent deformation under loading.

(3) Acceptable predictions of upper and lower bounds of capping layer tangent moduli, friction angles, cohesion, dilation angle and hardening modulus were obtained from the simulations using the constitutive model based on Drucker-Prager theory of plasticity coupled with a stress dependent tangent modulus and a friction angle.

(4) Other than the degree of compaction, the main external parameter that affects the properties of material is the level of moisture. Moisture level in capping layers adversely affects their properties more than the effects of load cycle or loading rate. Saturation tends to soften the material and dryness tends to stiffen the material relative to the behaviour of the material with optimum moisture content (OMC) in the low level of penetration ($\leq$ 20mm). Beyond this level, the softening – remoulding – hardening behaviour of the capping layer within the highly confined CBR mould is less pronounced for saturated specimens and significantly highly pronounced for dry specimens.

(5) From the limited number of large scale plane strain modelling of capping layer material carried out, it may be inferred that specifying a good quality material for

the capping layer for railway substructure is more important in practice than improved thickness design criteria or models. The importance of characterisation of the material advocated in this thesis could be re-emphasised based on this conclusion.

(6) Although large scale plane strain testing could be used for backcalculating the properties of the capping layer materials as they more closely resemble the field condition than the CBR mould test, considering the costs and efforts associated with the large scale testing, it can be concluded the semi confined testing in CBR mould is the most economical testing base although the testing generates very high levels of confining stresses that do not get generated in practice.

7.3 Specific Conclusions

The following conclusions are specific to the capping layer material tested in this thesis:

1. Three distinctive groups of properties were predicted from the experimental based finite element backcalculation process for dry, OMC and saturated state of the capping layer material given in Table 7.1.

Table 7.1 Summary of predicted capping layer properties

		Elastic			**Plastic**	
		$E_0 \le E_t \le E_{\max}$ (MPa)	$\phi_{\min} \le \phi \le \phi_{\max}$ (^{0})	c (kPa)	ψ (^{0})	H_p (kPa)
Dry	Lower bound	$80 \le E_t \le 100$	$40 \le \phi \le 43$	500	2	200
	Upper bound	$345 \le E_t \le 350$	$40 \le \phi \le 43$	500	2	200
OMC	Lower bound	$30 \le E_t \le 80$	$35 \le \phi \le 38$	300	4	300
	Upper bound	$80 \le E_t \le 130$	$35 \le \phi \le 38$	350	7	300
Saturated	Lower bound	$20 \le E_t \le 45$	$33 \le \phi \le 35$	300	7.5	300
	Upper bound	$55 \le E_t \le 80$	$33 \le \phi \le 35$	300	6.7	300

2. For the capping layer material considered in the thesis, it was found that with the increase in moisture content the tangent moduli, friction angle (all elastic properties) and cohesion decreased whilst the dilation angle and hardening modulus (both plastic properties) increased.

3. The large scale plane strain testing, modelling and analysis carried out indicated that

    (i) the 300mm capping layer resisted the penetration with higher resistance than the 600mm layer did

    (ii) the 300mm layer sustained failure beyond 15mm penetration irrespective of the quality of the material (upper bound or high quality & lower bound or poor quality)

    (iii) the 600mm layer made from lower bound material sustained failure beyond 30mm penetration whilst the 600mm layer made from upper bound material did not fail up to 50mm penetration for which the analysis was made.

4. Although thicker capping layer reduce the stresses in the layers below; it was evident from the above results that the thicker capping layers made from lower bound materials do not provide better behaviour than a corresponding thinner layer. Therefore, anticipated improvements by providing a thicker layer may not be the right approach in a rail track design where low quality materials are to be used.

7.4 Recommendations for Future Studies

There is much scope for further advancement of the modelling details. Some potential future improvements to the analytical procedures and to our overall understanding of capping layer behaviour are presented below.

- Extension to SCT – In the SCT, only granular materials were tested. It is worthwhile to further investigate the behaviour of cohesive material using the current experimental method and extend the constitutive model. As more knowledge becomes available, the constitutive model can be improved to describe what has been observed in the laboratory and in engineering practice.
- Extensions to constitutive model – The present material constitutive relationships consider an *isotropic hardening model* where the loading surface expands uniformly (or isotropically), and it cannot account for the Bauschinger effect (Chen and Mizuno 1990) exhibited by material subjected to cyclic loading. Therefore the present constitutive model might usefully be extended to a *kinematic hardening model* which can predict cyclic loading which is more relevant to railway loading conditions.
  The friction angle is also a stress-dependent parameter (Selig and Waters 2000), therefore the present material constitutive relationships can be improved by incorporating a yield function that includes first and third stress invariants which are related to soil shear strength or friction angle (Yang and Elgamal 2004).
  The material strength parameters were drastically changed according to the degree of saturation, from dry to fully saturated. As much as they depend on the stress conditions, they also depend on the moisture levels. Therefore, this study can be improved by incorporating a factor for the moisture levels in the constitutive model.

- Extensions to validation experiments – The validation experiments can be extended for more realistic situations, especially by varying the base boundary conditions as capping layers are provided when natural ground or fill has lower strength parameters than the capping layer. Extending experiments to such scenarios will provide valuable information on the behaviour of the capping layer and the applicability of SCT predicted material parameters via finite element modelling.
- Parameter data base and design charts – Little is known of the capping layer materials used in Australia. Typically, broadly graded sandy gravel with a feeble plastic binder is used as a capping layer. Further research is required to examine the effect of these materials simulating in-service conditions. After extensive investigations a data base or design charts can be produced using different boundary conditions.

BIBLIOGRAPHY

ABAQUS. (2002). *Analysis User's Manual Version 6.4*, Hibbitt, Karlsson & Sorensen, Inc., USA.

Adegoke, C. W., Chang, C. S., and Selig, E. T. (1979). "Study of analytical models for track support systems." *Transportation Research Record 733*, TRB, 12-20.

Al-Shayea. (2001). "The combined effect of clay and moisture content on the behaviour of remolded unsaturated soils." *Engineering Geology*, 62, 319-342.

AS 1141.51. (1996). "Methods for sampling and testing aggregates, Method 51: Unconfined compressive strength of compacted materials." *Standards Australia, NSW, Australia*.

AS 1289.3.4.1. (1995). "Methods of testing soils for engineering purposes, Method 3.4.1: Soil classifications tests - Determination of the linear shrinkage of a soil - Standard method." *Standards Australia, NSW, Australia*.

AS 1289.3.9.1. (2002). " Methods of testing soils for engineering purposes, Method 3.9.1: Soil classifications tests - Determination of the cone liquid limit of a soil." *Standards Australia, NSW, Australia*.

AS 1289.5.2.1. (2003). "Methods of testing soils for engineering purposes, Method 5.2.1: Soil classifications tests - Determination of the dry density/moisture content relation of a soil using modified compactive effort." *Standards Australia, NSW, Australia*.

AS 1289.6.4.1. (1998). "Methods of testing soils for engineering purposes, Method 6.4.1: Soil strength and consolidation tests - Determination of compressive strength of soil - Compressive strength of a specimen tested in undrained triaxial

compression without measurement of pore water pressure." *Standards Australia, NSW, Australia*.

AS 1289.6.4.2. (1998). "Methods of testing soils for engineering purposes, Method 6.4.2: Soil strength and consolidation tests - Determination of compressive strength of soil - Compressive strength of a specimen tested in undrained triaxial compression with measurement of pore water pressure."

AS 1289.6.6.1. (1998). "Methods of testing soils for engineering purposes, Method 6.6.1: Soil strength and consolidation properties of a soil - Determination of the one-dimensional consolidation properties of a soil - Standard method." *Standards Australia, NSW, Australia*.

AS 1289.6.7.2. (2001). "Methods of testing soils for engineering purposes, Method 6.7.2: Soil strength and consolidation tests - Determination of permeability of a soil - Falling head method for a remoulded specimen." *Standards Australia, NSW, Australia*.

AS 1289.6.8.1. (1995). "Methods of testing soils for engineering purposes, Method 6.8.1: Soil strength and consolidation tests - Determination of the resilient modulus and permanent deformation of granular unbound pavement material." *Standards Australia, NSW, Australia*.

AS 4133.4.2. (1993). "Methods of testing rocks for engineering purposes, Method 4.2: Rock strength tests - Determination of uniaxial compressive strength." *Standards Australia, NSW, Australia*.

Bishop, A. W., and Henkel, D. J. (1962). *The measurement of soil properties in the triaxial test*, Edward Arnold (Publishes) Ltd., London, UK.

Bolton, M. D. (1986). "The strength and dilatancy of sand." *Geotechnique*, 36(No. 1), 65 - 78.

Boulbibane, M., Collins, I. F., Weichert, D., and Raad, L. (2000). "Shakedown analysis of anisotropic asphalt pavements with clay subgrade." *Can. Geotech. J.*, 37, 882 - 889.

Bowles, J. E. (1979). *Physical and geotechnical properties of soil*, McGraw-Hill Book Company, USA.

Bowles, J. E. (1988). *Foundation analysis and design*, McGraw-Hill Book Co., Singapore.

Boyce, J. R. (1980). "A non-linear model for the elastic behaviour of granular materials under repeated loading." International symposium on soils under cyclic and transient loading, G. N. Pande and O. C. Zienkiewicz, eds., Brookfield Pub Co, Swansea.

Brown, S. F., Lashine, A. K. F., and Hyde, A. F. L. (1975). "Repeated load triaxial testing of a silty clay." *Geotechnique*, 25(1), 95 - 114.

Cai, Z., and Raymond, G. P. (1993). "Responses of railway track to dynamic and static loading." *5th International Heavy Haul Railway Conference, Beijing, China*, 362 - 368.

Chang, C. S., Adegoke, C. W., and Selig, E. T. (1980). "GEOTRACK model for railroad track performance." *Journal of the Geotechnical Engineering Division*, 106(GT11), 1201 - 1218.

Charles, J. A., and Watts, K. S. (1980). "The influence of confining pressure on the shear strength of compacted rockfill." *Geotechnique*, 30(No. 4), 353 - 367.

Chen, W. F., and Han, D. J. (1988). *Plasticity for structural engineers*, Springer-Verlag, NY.

Chen, W. F., and Mizuno, E. (1990). *Nonlinear analysis in soil mechanics*, Elsevier, 1990.

Chen, D.-H., Zaman, M., Laguros, J., and Soltani, A. (1995). "Assessment of computer programs for analysis of flexible pavement structures." *Transportation Research Record 1482, TRB.*

Cho, Y.-H., McCullough, B. F., and Weissmann, J. (1996). "Considerations on finite-element method application in pavement structural analysis." *Transportation Research Record 1539*, TRB.

Collins, I. F., and Boulbibane, M. (2000). "Geomechanical analysis of unbound pavements based on shake down theory." *Journal of Geotechnical and Geoenvironmental Engineering, ASCE*, 126(1), 50 - 59.

Collop, A. C., and Cebon, D. (1996). "Stiffness reduction of flexible pavements due to cumulative fatigue damage." *Journal of Transportation Engineering, ASCE*, 122(2), 131-139.

Craig, R. F. (1997). *Soil Mechanics*, E & FN Spon, London, UK.

Crisfield, M. A. (1991). *Non-linear finite element analysis of solids and structures*, John Wiley & Sons Ltd., England.

Croney, D., and Croney, P. (1992). *The design and performance of road pavements*, McGraw-Hill, Singapore.

Dahlberg, T. (2001). "Some railroad settlement models - a critical review." *Proceedings Institution of Mechanical Engineers*, 215 Part F, 289 - 300.

Desai, C. S., and Abel, J. F. (1972). *Introduction to the finite element method; a numerical method for engineering analysis*, Van Nostrand Reinhold Co., New York .

Desai, C. S., and Christian, J. T. (1977). *Numerical Methods in Geotechnical Engineering*, McGraw-Hill Book Company.

Desai, C. S., and Siriwardane, H. J. (1982). "Numerical models for track support structure." *Journal of the Geotechnical Engineering Division*, 108(GT3), 461 - 480.

Douglas, J. F. (1969). *An introduction to Dimensional Analysis for Engineers*, Sir Isaac Pitman & Sons Ltd., London.

Dowding, C. H. (2000). "Effects of Ground Motions from High Speed Trains on Structures, Instruments, and Humans." Wave 2000: Wave Propagation, Moving Load, Vibration Reduction, Proceedings of International Workshop Wave 2000, Bochum, Germany, December 13-14, 2000, N. Chouw and D. Schmid, eds., A.A. Balkema, Rotterdam, 269 - 288.

Drucker, D. C., and Prager, W. (1952). "Soil mechanics and plastic analysis or limit design." *Quart. Appl. Math*, 10, 157 - 165.

Drumm, E. C., Boateng-Poku, Y., and Pierce, J. T. (1990). "Estimation of subgrade resilient modulus from standard tests." *Journal of Geotechnical Engineering*, 116(5), 774 - 789.

Drumm, E. C., Li, Z., Reeves, J. S., and Madgett, M. R. (1996). "Alternative test method for resilient modulus of fine-grained subgrades." *Geotechnical Testing Journal*, 19(2), 141 - 154.

Drumm, E. C., Reeves, J. S., Madgett, M. R., and Trolinger, W. D. (1997). "Subgrade resilient modulus correction for saturation effects." *Journal of Geotechnical and Geoenvironmental Engineering*, 123(7), 663 - 670.

Esveld, C. (2001). *Modern Railway Track*, MRT-Productions, West Germany.

Frohling, R. D. (1997). "Deterioration of railway track due to dynamic vehicle loading and spatially varying track stiffness," PhD Thesis, University of Pretoria, Pretoria.

Foun, D., and Williams, S. (2003). "RTAA 4 - QR's trackbed investigation methodology." AusRail Plus 2003, Informa Australia Pty Ltd, Sydney, Australia, 1 -11.

Gazetas, G. (1991). "Foundation Vibrations." Foundation Engineering Handbook, H. Y. Fang, ed., Van Nostrand Reinhold, New York, 553 - 593.

Hagaman, B. R. (1997). "Railway Track Design." Civil Engineering Course, Queensland Rail, Australia.

Hall, L. (2003). "Simulations and analyses of train-induced ground vibrations in finite element models." *Soil Dynamics and Earthquake Engineering*, 23, 403 - 413.

Harison, J. A. (1989). "Technical Note: In situ CBR determination by DCP testing using a laboratory-based correlation." *Australian Road Research*, 19(4), 313 - 317.

Heath, D. L., Shenton, M. J., and Sparrow, R. W. (1972). "Design of conventional rail track foundations." *Proc. Instn Civ. Engrs*, 51, 251 - 267.

Hendriks, R. (2002). "Transportation related earthborne vibrations." *TAV-02-01-R9601*, California Department of Transportaion, Division of Environmental Analysis, Office of Noise, Air Quality, and Hazardous Waste Management, Sacramento, CA.

Hicks, R. G., and Monismith, C. L. (1971). "Factors Influencing the resilient properties of granular materials." *Transportation Research Record 345*, TRB.

Hjelmstad, K. D., and Taciroglu, E. (2000). "Analysis and Implementation of resilient modulus models for granular solids." *Journal of Engineering Mechanics, ASCE*, 126(8), 821 - 830.

Ionescu, D., Indraratna, B., and Christie, D. (2004). "Construction potential of recycled railway ballast based on large-scale triaxial tests." *Conference on Railway Engineering, Darwin 20-23 June 2004*, 29.1 - 29.11.

Janssen, D. J., and Dempsey, B. J. (1981). "Soil-moisture properties of subgrade soils."

Jeffs, T., and Tew, G. P. (1991). *A review of track design procedures, Volume 2, Sleepers and Ballast*, Railways of Australia.

Jirasek, M., and Bazant, Z. (2002). *Inelastic analysis of structures*, John Wiley & Sons, Ltd, West Sussex, England.

Kang, Y. L., Lin, X. H., and Qin, Q. H. (2004). "Inverse/generic method and its application in identification of mechanical parameters of interface in composite." *Composite Structures*, 66, 449 - 458.

Kim, D. S., Kweon, G. C., and Lee, K. H. (2001a). "Alternative method of determining resilient modulus of subgrade soils using a static triaxial test." *Can. Geotech. J.*, 38, 107 - 116.

Kim, D. S., Kweon, G. C., and Rhee, S. (2001b). "Alternative method of determining resilient modulus of subbase soils using a static triaxial test." *Can. Geotech. J.*, 38, 117 - 124.

Knothe, K., and Wu, Y. (1998). "Receptance behaviour of railway track and subgrade." *Archive of Applied Mechanics*, 68(7-8), 457-470.

Ksaibati, K., Armaghani, J., and Fisher, J. (2000). "Effect of moisture on modulus values of base and subgrade materials." *Transportation Research Record 1716, TRB.*

Lambe, T. W., and Whitman, R. V. (1979). *Soil Mechanics*, John Wiley & sons, Inc., New York.

Lay, M. G. (1990). *Handbook of road technology*, Gordon and Breach Science Publishes.

Lee, W., Bohra, N. C., Altschaeffl, A. G., and White, T. D. (1997). "Resilient modulus of cohesive soils." *Journal of Geotechnical and Geoenvironmental Engineering*, 123(2), 131 - 136.

Lei, X. (2001). "Dynamic analysis of the track structure of a high-speed railway using finite elements." *Proceedings Institution of Mechanical Engineers*, 215 Part F, 301 - 309.

Lekarp, F., and Dawson, A. (1997). "Analysis of permanent deformation behaviour of unbound granular material." *International Symposium on Thin Pavements, Surface Treatment, Unbound Roads, Fredericton, New Brunswick, Canada*, 91 - 99.

Lekarp, F., and Dawson, A. (1998). "Modelling permanent deformation behaviour of unbound granular materials." *Construction and Buildings Materials, Elsevier Science Ltd.*, 12(1), 9 - 18.

Lekarp, F., Isacsson, U., and Dawson, A. (2000). "State of the Art II: Permanent strain response of unbound aggregates." *Journal of Transportation Engineering, ASCE*, 126(1), 76 - 83.

Li, D., and Selig, E. T. (1994). "Resilient modulus for fine grained subgrade soils." *Journal of Geotechnical Engineering*, 120(6), 939 - 957.

Li, D., and Selig, E. T. (1996). "Cumulative plastic deformation for fine-grained subgrade soils." *Journal of Geotechnical Engineering, ASCE*, 122(12), 1006 - 1013.

Li, D., and Selig, E. T. (1998a). "Method for railroad track foundation design I: development." *Journal of Geotechnical and Geoenvironmental Engineering*, 124(4), 316 - 322.

Li, D., and Selig, E. T. (1998b). "Method for railroad track foundation design II: Applications." *Journal of the Geotechnical and Geoenvironmental Engineering*, 124(4), 323 - 329.

Liao, N.-H. (2003). "Assessment empirical soil properties and its applications in performance analysis," Masters Thesis, National Cheng Kung University, Taiwan.

Lin, X. H., Kang, Y. L., Qin, Q. H., and Fu, D. H. (2005). "Identification of interfacial parameters in a particle reinforced metal matrix composite Al6061-10%Al_2O_3 by hybrid method and generic algorithm." *Computational Materials Science*, 32, 47 - 56.

Main Roads MRS11.05. (1999). "Main Roads Standard Specifications-Unbound Pavements." *Queensland Department of Main Roads*.

May, R. W., and Von Quintus, H. L. (1994). "The quest for a standard guide to NDT backcalculation." Nondestructive testing of pavements and backcalculation of moduli (Second Volume), ASTM STP 1198, H. L. Von Quintus, A. J. Bush, and G. Y. Baladi, eds., American Society for Testing and Materials, Philadelphia, 505 - 520.

Means, R. E., and Parcher, J. V. (1964). *Physical properties of soils - Their determination, interpretation, and significance*, Constable and Company Limited, UK.

Menzies, B. K. (1988). "A computer controlled hydraulic triaxial system." Advanced Triaxial Testing of Soil and Rock, ASTM STP 977, R. T. Donaghe, R. C. Chaney, and M. L. Silver, eds., American Society for Testing Materials, Philadelphia, 82 - 94.

Muhanna, A. S., Rahman, M. S., and Lambe, P. C. (1999). "Resilient modulus measurements of fine-grained subgrade soils." *Transportation Research Record 1687*, TRB.

Murphy, D. J. (1987). "Stress, degradation, and shear strength of granular material." Geotechnical modeling and applications, M. S. Sayed, ed., Gulf Publishing Company, Texas, USA, 181 - 211.

Nazarian, S., and Boddapati, K. M. (1995). "Pavement-Falling weight deflectometer interaction using dynamic finite element analysis." *Transportation Research Record 1482*, TRB.

Okada, K., and Ghataora, G. S. (2002). "Use of cyclic penetration test to estimate the stiffness of railway subgrade." *NDT & E international*, 35, 65 -74.

Potts, D. M., and Zdravkovic, L. (1999). *Finite element analysis in geotechnical engineering, Theory*, Thomas Telford, London.

Profillidis, V. A. (1985). "Three-dimensional Elasto-plastic finite element analysis for track bed structures." *Civil engineering for practicing and design engineers*, 4, 685 - 701.

Profillidis, V. A. (1986). "Application of finite element analysis in the rational design of track bed structures." *Computers & structures*, 22(3), 439 - 443.

Profillidis, V. A. (2000). *Railway Engineering*, Avebury Technical, Ashgate Publishing Limited, England.

Puppala, A. J., Mohammad, L. N., and A, A. (1999). "Permanent deformation characterization of subgarde soils from RLT test." *Journal of Materials in Civil Engineering, ASCE*, 11(4), 274 - 282.

Quantachrome Corporation. (1996). "Multi-pycnometer user manual."

Queensland Rail - Civil Engineering Section. (1998). "Civil engineering standard specification - Earthworks." Part No. 6(Revision C).

Raad, L., Weichert, D., and Haidar, A. (1989). "Shakedown and fatigue of pavements with granular bases." *Transportation Research Record 1227*, TRB.

Raymond, G. P. (1978). "Design for railroad ballast and subgrade support." *Journal of the Geotechnical Engineering Division*, 104(GT1), 45 - 60.

Selig, E. T., and Waters, J. M. (2000). *Track geotechnology and substructure management*, Thomas Telford Publications, London.

Shackel, B. (1973). "Repeated loading of soils." *Australian Road Research*, 5(3), 22 - 49.

Shahu, J. T., Rao, N. S. V. K., and Yudhbir. (1999). "Parametric study of resilient response of tracks with a sub-ballast layer." *Can. Geotech. J.*, 36, 1137 - 1150.

Sharp, R. W., and Booker, J. R. (1984). "Shakedown of pavement under moving surface loads." *Journal of Transportation Engineering, ASCE*, 110(1), 1 -14.

Shuo, L., Fwa, T. F., and Tan, K. H. (1998). "Parameters back-calculation for concrete pavement with two slab layers." *Journal of Transportation Engineering, ASCE*, 124(6), 567 - 572.

Smith, I. M., and Griffiths, D. V. (1988). *Programming the finite element method*, John Wiley & Sons Ltd., U.K.

Sowers, G. F. (1979). *Introductory soil mechanics and foundations: Geotechnical Engineering*, Macmillan Publishing Co., Inc., USA.

Stolle, D. F. E. (1990). "Effect of mechanical model on back-calculated pavement modulus." *Can. Geotech. J.*, 17, 494 - 496.

Sun, L. (2002). "A closed-form solution of beam on viscoelastic subgrade subjected to moving loads." *Computers & structures*, 80, 1 - 8.

Sussmann, T. R., and Selig, E. T. (2000). "Resilient modulus backcalculation techniques for track." *ASCE Special Publication No. 94*, 401 - 410.

Svec, O. J., and Raymond, G. P. (1976). "Nonlinear analysis rail track and support." *Second International Conference on Mumerical Methods in Geomechanics, ASCE, New York, USA*, 540 - 550.

Tayabji, S. D., and Marshall, T. (1977). "Considerations in the analysis of conventional railway track support system." *Transportation Engineering Journal, ASCE*, 103(TE2), 279 - 292.

Taylor, E. S. (1974). *Dimensional analysis for engineers*, Clarendon Press, Oxford.

Thompson, M. R., and Robnett, Q. L. (1979). "Resilient properties of subgrade soils." *Transportation Engineering Journal, ASCE*, 105(TE1), 71 - 89.

Thompson, M. R., Tutumluer, E., and Bejarano, M. (1998). "Granular material and soil moduli - Review of the literature." *COE Report No. 1*, Center of Excellence for Airport Pavement Research, Dept. of Civil Engineering, University of Illinois, Illinois, USA.

Tian, P., Zaman, M., and Laguros, J. G. (1998). "Variation of resilient modulus of aggregate base and its influence on pavement performance." *Journal of Testing and Evaluation, JTEVA*, 26(4), 329 - 335.

Troxler Electronic Laboratories Inc. (1990-2001). "Manual of operations and instructions, Surface moisture-density gauge." USA.

Uddin, W., Hackett, R. M., Joseph, A., Pan, Z., and Crawley, A. B. (1995). "Three-dimensional finite-element analysis of jointed concrete pavement with discontinuities." *Transportation Research Record 1482*, TBR.

Uzan, J. (1985). "Characterization of granular materials." *Transportation Research Record 1022*, TRB.

Uzan, J. (1994). "Advanced backcalculation techniques." Nondestructive testing of pavements and backcalculation of moduli (Second Volume), ASTM STP 1198, H. L. Von Quintus, A. J. Bush, and G. Y. Baladi, eds., American Society for Testing and Materials, Philadelphia, 3 - 37.

Vucetic, M., and Dobry, R. (1991). "Effect of soil plasticity on cyclic response." *Journal of Geotechnical Engineering, ASCE*, 117(1), 89 - 107.

Wang, G., and Sitar, N. (2004). "Numerical analysis of piles in elasto-plastic soils under axial loading." 17th ASCE Engineering Mechanics Conference, University of Delaware, Newark, DE.

Yang, Z., and Elgamal, A. (2004). "A multi-surface plasticity sand model including the lode angle effect." 17th ASCE Engineering Mechanics Conference, University of Delaware, Newark, DE, June 13-16, 2004.

Zhang, Y. J. (2000). "An Integrated Rail Track Degradation Model," PhD Thesis, Queensland University of Technology, Australia.

Zicha, J. H. (1989). "High-speed rail track design." *Journal of Transportation Engineering*, 115(1), 68 - 83.

Zienkiewicz, O. C., and Taylor, R. L. (2002). *The finite element method, 5th ed.*, Butterworth-Heinemann, Oxford ; Boston.

APPENDICES

APPENDIX A.1 Basic properties of the capping layer material

APPENDIX A.2 Density and saturation calculations- Semi Confined Test (SCT) samples

APPENDIX A.3* SCT experimental data sheets

APPENDIX A.4 Stiffness and penetrated depth against moisture, penetration rate and number of cycles in SCT

APPENDIX A.5* Dimensional analysis data sheets

APPENDIX A.6 Coefficients of the orthogonal polynomials

APPENDIX A.7 Ternary plot calculations

APPENDIX B.1 Frequency analysis and step time calculations

APPENDIX B.2* Mesh refinement of SCT FEM

APPENDIX B.3 Typical ABAQUS/Explicit INPUT file

APPENDIX B.4* Sensitivity of modelling parameters in SCT FEM

APPENDIX C.1 Density and saturation calculations-triaxial test samples

APPENDIX C.2* Triaxial test data sheets

APPENDIX C.3 Modulus, cohesion and friction angle obtained from triaxial tests

APPENDIX C.4* Uniaxial test data sheets

APPENDIX C.5 Density, saturation, initial modulus and hardening modulus -uniaxial test samples

APPENDIX C.6* Establishing lower and upper boundaries of SCT data

APPENDIX C.7 Effect of moisture on SCT FEM predicted parameters

APPENDIX C.8* Sensitivity of elastic material parameters in SCT FEM

Note: * - A sample data sheet is provided for clarity. All other data sheets in EXCEL files

APPENDIX C.9* Sensitivity of plastic material parameters in SCT FEM

APPENDIX C.10 Stresses induced in SCT FEM

APPENDIX D.1* Convergence studies of the plane strain FE model

APPENDIX D.2* Application of SCT predicted properties to the plane strain FEM

APPENDIX D.3* Large-scale experiments data sheets

In the relevant appendices the user input properties are represented by either

*Elastic
250., 0.3,

or

*User Material, constants=12
250., 0.3, 0.2, 39., 5., 0.01, 760., 0.9
0.1, 0.735, 400., 42.

The above inputs are of the following order.

Props(1) Elastic modulus, E (MPa)

Props(2) Poisson's ratio, ν

or

Props(1) Initial modulus, E_0 (MPa)

Props(2) Poisson's ratio, ν

Props(3) Cohesion, c (MPa)

Props(4) Minimum friction angle ϕ_{min} (^{0})

Props(5) Dilation angle, ψ (^{0})

Props(6) Hardening modulus, H_p (MPa)

Note: * - A sample data sheet is provided for clarity. All other data sheets in EXCEL files

Props(7)	Material constant, K_a
Props(8)	Material constant, R_f
Props(9)	Atmospheric pressure, p_a (MPa)
Props(10)	Power n of modulus formulation
Props(11)	Maximum modulus E_{max} (MPa)
Props(12)	Maximum friction angle ϕ_{max} (^{0})

The step time of the analysis is indicated by

*Step, name=Step-1
*Dynamic, Explicit
,0.0282

where the step time 0.0282 is given in seconds.

APPENDIX A.1 Basic properties of the capping layer material

Material tested **Type 2.4 Unbound Material**
Source **CSR Quarry, Nerimbera, Queensland, Australia**

Table A.1-1 Specific gravity – Multipycnometer test

Sample Wt (g)			79.86
Reference Volume (V_R) (cm^3)			91.293
Cell Volume (Vc) (cm^3)			149.019
Operational Equation $Vp = Vc-V_R[(P1/P2)-1]$ Vp = Volume of powder (cm^3) Vc = Volume of sample cell (cm^3) V_R = Reference volume (cm^3) P1 = Pressure reading after pressurizing the reference volume P2 = Pressure reading after including Vc			
	Run1	Run2	Run3
P1	17.696	17.455	17.012
P2	7.615	7.565	7.367
Vp	28.162	29.668	29.497
Specific Gravity	2.836	2.692	2.707
Ave Specific Gravity	2.75		

Table A.2-2 Modified compaction test data

Moisture contents and dry density of the sample tested				
Mould No	1	2	3	4
Wt of Mould +Base (g)	5699.2	5699.2	5699.2	5699.2
Wt of M+B+ Wet Sample (g)	7962.7	8141.5	8127	8098.6
Wt of Wet Sample (g)	2263.5	2442.3	2427.8	2399.4
Wt of Tray (g)	987.2	262.7	353.7	263.6
Wt of Tray + Dry Sample (g)	3177.2	2575.5	2613.9	2475
Wt of Dry Sample (g)	2190	2312.8	2260.2	2211.4
Wt of Water (g)	73.5	129.5	167.6	188.0
Volume (m^3)	9.96E-04	9.96E-04	9.96E-04	9.96E-04
Moisture Content (%)	3.36	5.60	7.42	8.50
Dry Density (kg/m^3)	2190	2312.8	2260.2	2211.4

Table A.1-3 Zero Air Void (ZAV) line using the specific gravity of 2.75

Moisture Content (%)	Dry density at ZAV (kg/m^3)
4	2469
5	2410
6	2353
7	2299
8	2247
8.9	2203
10	2151
11	2105

Table A.1-4 Maximum Dry Density ($\gamma_{d\,max}$) and Optimum Moisture Content (OMC)

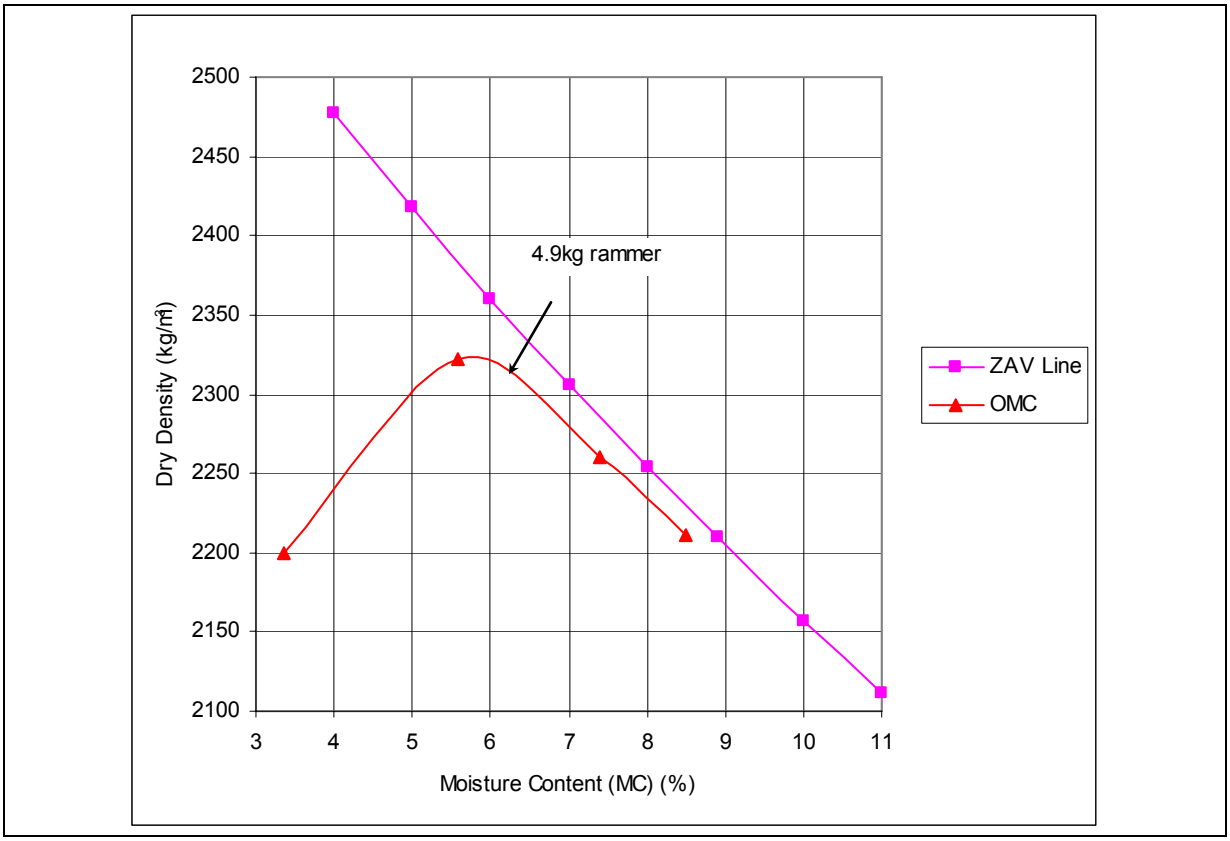

From the best-fit the polynomial equation obtained is

$\gamma_{d\,max}$ (kg/m^3) = -16.701*MC^2 (%) + 198.25*MC (%) + 1724.6

R^2 = 0.95

OMC = 5.9%

Therefore, $\gamma_{d\,max}$ = 2312 kg/m^3

Table A.1-5 Linear Shrinkage

Container number	10	8
Length of container (mm)	125	125
Length of sample (mm)	122	122
Linear Shrinkage (%)	2.4	2.4
Average Linear Shrinkage (%)	2.4	

Table A.1-6 Liquid Limit

Moisture content (%)	Penetration (mm)
18.21924	12.1
19.10615	15.5
20.17585	20.05
20.93178	24.2

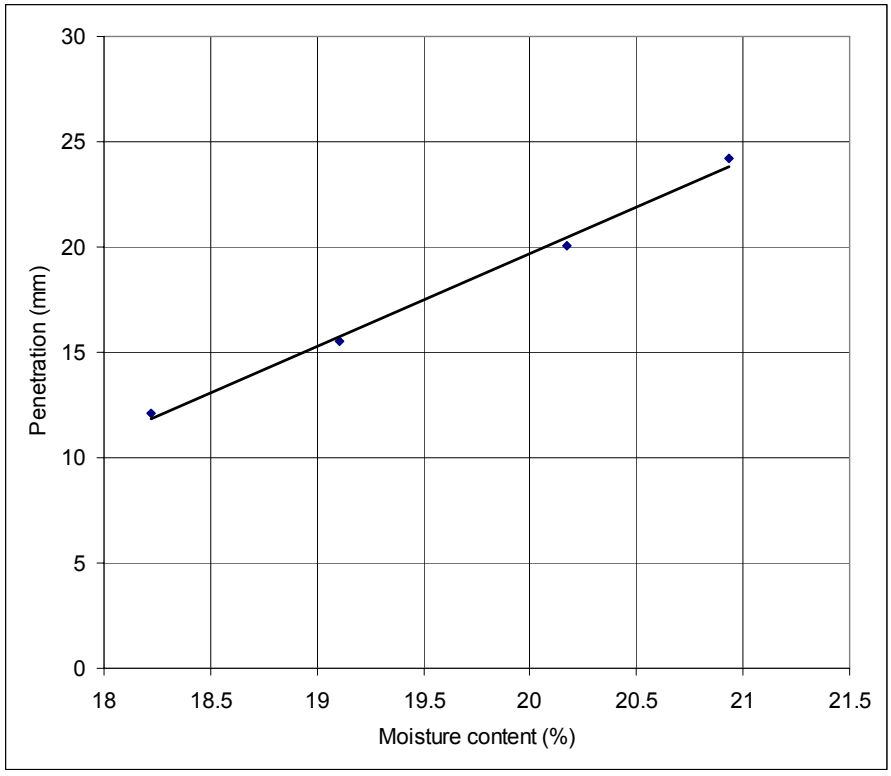

From the Best-fit linear equation
Penetration (mm) = 4.4226 *MC(%) - 68.758
R^2 = 0.9945
Therefore Liquid Limit at 20mm penetration = 20%

Table A.1-7 California Bearing Ratio (CBR) test data (modified compacted and 96hrs saturated)

Test No.	CBR1	CBR2
Weight of mould without base plate and collar (g)	4525.0	5149.6
Weight of mould and compacted soil and the steel plate without base plate and collar (g)	9635.6	10225.8
Weight of the steel plate (g)	240	240
Volume of mould (m^3)	2.12E-03	2.12E-03
Wet density (kg/m^3)	2294.14	2277.94
Dry density (kg/m^3)	2129.20	2114.48
Laboratory density Ratio = Dry density/MDD x100 < 1% MDD	101.4	100.7
Laboratory moisture ratio = m/c immediately prior to compaction/OMC x 100< 5% OMC	101.4	100.7

Table A.1-8 Moisture contents of the samples tested

Test No.	CBR1	CBR2	CBR1			CBR2		
Container No.	224	219	Top 205	Mid 103	End 221	Top 217	Mid 226	End 134
Mass of container + wet soil (g)	90.7	99.7	166.3	184.3	193.7	198.1	182.8	170.9
Mass of container + dry soil (g)	86.8	95.2	158.5	175.4	182.5	188.3	174.2	161.6
Mass of container (g)	36.0	36.2	35.6	38.4	35.6	35.0	35.8	30.5
Mass of water (g)	3.9	4.6	7.8	9.0	11.2	9.8	8.6	9.4
Mass of dry soil (g)	50.8	59.0	122.9	137.0	146.9	153.2	138.5	131.0
Moisture content (%)	7.7	7.7	6.3	6.5	7.6	6.4	6.2	7.1
Average moisture content (%)	7.7		6.8			6.6		

Table A.1-9 CBR test data – CBR1

Load (kN)	Penetration (mm)	Load kN)	Penetration (mm)	Load (kN)	Penetration (mm)	Load (kN)	Penetration (mm)	Load (kN)	Penetration (mm)	Load (kN)	Penetration (mm)
0.00	0.00	14.90	1.76	25.27	4.02	35.73	6.31	45.71	8.61	54.65	10.93
0.00	0.00	15.14	1.81	25.46	4.07	35.97	6.36	46.00	8.66	54.84	10.98
0.05	0.02	15.38	1.86	25.70	4.12	36.21	6.41	46.19	8.71	55.03	11.03
0.14	0.06	15.57	1.91	25.94	4.17	36.40	6.46	46.43	8.75	55.22	11.08
0.19	0.09	15.81	1.95	26.13	4.22	36.64	6.50	46.62	8.80	55.36	11.13
0.19	0.09	16.00	2.00	26.42	4.26	36.83	6.55	46.81	8.85	55.55	11.18
0.33	0.14	16.24	2.05	26.61	4.31	37.07	6.60	47.00	8.90	55.74	11.23
0.53	0.18	16.48	2.09	26.75	4.36	37.31	6.65	47.24	8.95	55.98	11.28
0.67	0.21	16.67	2.14	26.99	4.41	37.55	6.70	47.39	9.00	56.17	11.33
0.91	0.25	16.91	2.19	27.23	4.46	37.78	6.75	47.58	9.05	56.37	11.38
1.19	0.28	17.15	2.24	27.47	4.51	37.98	6.80	47.82	9.10	56.56	11.43
1.48	0.31	17.24	2.29	27.71	4.56	38.17	6.84	47.96	9.15	56.75	11.48
1.82	0.35	17.48	2.34	27.94	4.61	38.41	6.89	48.10	9.20	56.94	11.52
2.20	0.38	17.67	2.38	28.18	4.65	38.69	6.94	48.34	9.25	57.13	11.57
2.63	0.41	17.91	2.43	28.42	4.70	38.88	6.99	48.53	9.29	57.27	11.63
3.10	0.44	18.15	2.48	28.61	4.75	39.07	7.04	48.68	9.34	57.46	11.68
3.63	0.48	18.39	2.53	28.85	4.80	39.31	7.09	48.87	9.39	57.66	11.73
4.25	0.51	18.63	2.58	29.14	4.85	39.55	7.14	49.06	9.44	57.85	11.78
4.82	0.54	18.87	2.62	29.38	4.89	39.79	7.19	49.34	9.49	58.09	11.83
5.45	0.58	18.77	2.68	29.62	4.94	40.03	7.23	49.49	9.54	58.23	11.88
6.11	0.61	19.06	2.72	29.85	4.99	40.27	7.28	49.68	9.59	58.37	11.92
6.74	0.64	19.30	2.77	30.09	5.04	40.46	7.33	49.82	9.65	58.52	11.97
7.36	0.68	19.54	2.82	30.33	5.09	40.70	7.38	50.01	9.69	58.66	12.03
7.93	0.72	19.78	2.87	30.52	5.14	40.94	7.43	50.25	9.74	58.85	12.08
8.50	0.75	20.01	2.92	30.76	5.19	41.13	7.48	50.49	9.79	59.04	12.13
9.03	0.79	20.25	2.96	31.00	5.24	41.37	7.53	50.68	9.84	59.23	12.18
9.51	0.83	20.49	3.01	31.19	5.29	41.56	7.58	50.87	9.89	59.38	12.23
9.94	0.88	20.68	3.06	31.43	5.33	41.80	7.62	51.02	9.94	59.57	12.28
10.27	0.92	20.92	3.11	31.67	5.39	41.99	7.67	51.21	9.98	59.76	12.32
10.65	0.96	21.16	3.16	31.81	5.43	42.23	7.72	51.40	10.03	59.95	12.37
10.94	1.01	21.35	3.21	32.05	5.48	42.42	7.78	51.54	10.08	60.09	12.42
11.27	1.05	21.59	3.26	32.24	5.53	42.61	7.82	51.73	10.13	60.28	12.47
11.56	1.10	21.83	3.30	32.43	5.58	42.85	7.87	51.92	10.18	60.47	12.53
11.85	1.15	22.07	3.35	32.63	5.63	43.04	7.92	52.11	10.23	60.66	12.58
12.09	1.19	22.31	3.40	32.86	5.68	43.23	7.97	52.31	10.28	60.86	12.63
12.32	1.24	22.55	3.45	33.10	5.73	43.42	8.02	52.45	10.33	61.00	12.68
12.56	1.28	22.74	3.50	33.29	5.78	43.56	8.07	52.64	10.38	61.24	12.72
12.80	1.33	22.98	3.55	33.53	5.83	43.80	8.12	52.78	10.43	61.38	12.77
13.04	1.38	23.22	3.59	33.72	5.87	43.99	8.17	52.97	10.48	61.57	12.82
13.33	1.42	23.45	3.64	33.96	5.92	44.19	8.21	53.21	10.53	61.76	12.87
12.95	1.45	23.69	3.69	34.15	5.97	44.33	8.26	53.40	10.58	61.95	12.92
13.47	1.48	23.88	3.74	34.39	6.02	44.47	8.31	53.55	10.63	62.15	12.97
13.76	1.52	24.12	3.79	34.63	6.07	44.71	8.36	53.69	10.68	62.34	13.02
14.00	1.57	24.36	3.83	34.82	6.12	44.95	8.41	53.93	10.73		
14.23	1.62	24.60	3.88	35.06	6.17	45.14	8.46	54.12	10.78		
14.47	1.67	24.79	3.93	35.30	6.21	45.33	8.51	54.31	10.83		
14.66	1.72	25.03	3.97	35.49	6.26	45.52	8.56	54.50	10.88		

Table A.1-10 CBR test data – CBR2

Load (kN)	Penetration (mm)	Load (kN)	Penetration (mm)	Load (kN)	Penetration (mm)	Load (kN)	Penetration (mm)	Load (kN)	Penetration (mm)	Load (kN)	Penetration (mm)
0.00	0.00	2.48	2.18	9.65	4.41	19.39	6.66	29.81	9.00	39.93	11.38
0.05	0.02	2.58	2.22	9.84	4.46	19.63	6.71	30.00	9.05	40.17	11.43
0.10	0.08	2.67	2.27	10.03	4.51	19.87	6.76	30.19	9.10	40.41	11.48
0.10	0.13	2.77	2.32	10.22	4.55	20.01	6.81	30.38	9.16	40.65	11.53
0.14	0.18	2.91	2.37	10.41	4.60	20.21	6.87	30.52	9.21	40.84	11.58
0.14	0.23	3.01	2.42	10.60	4.65	20.40	6.91	30.76	9.26	41.08	11.63
0.14	0.28	3.15	2.47	10.80	4.70	20.64	6.96	30.95	9.31	41.27	11.68
0.19	0.33	3.25	2.51	10.99	4.75	20.87	7.01	31.19	9.36	41.46	11.73
0.19	0.38	3.39	2.55	11.18	4.80	21.11	7.06	31.38	9.41	41.70	11.78
0.24	0.43	3.49	2.60	11.37	4.84	21.35	7.11	31.62	9.46	41.94	11.84
0.24	0.48	3.63	2.65	11.56	4.89	21.54	7.16	31.91	9.51	42.13	11.89
0.29	0.53	3.77	2.70	11.75	4.94	21.78	7.21	32.10	9.56	42.32	11.94
0.33	0.58	3.92	2.75	11.99	4.99	21.97	7.26	32.34	9.61	42.56	11.99
0.38	0.63	4.01	2.79	12.18	5.04	22.21	7.31	32.53	9.66	42.75	12.04
0.38	0.68	4.16	2.84	12.37	5.09	22.40	7.36	32.72	9.71	42.99	12.09
0.43	0.73	4.30	2.89	12.61	5.13	22.59	7.41	33.01	9.76	43.18	12.14
0.48	0.78	4.44	2.93	12.75	5.18	22.79	7.46	33.20	9.81	43.37	12.19
0.53	0.83	4.59	2.98	12.61	5.22	22.98	7.51	33.44	9.86	43.61	12.24
0.53	0.88	4.73	3.03	12.85	5.24	23.22	7.56	33.68	9.91	43.80	12.29
0.57	0.93	4.87	3.08	13.18	5.29	23.41	7.61	33.92	9.96	43.99	12.35
0.62	0.97	5.02	3.12	13.42	5.34	23.60	7.66	34.06	10.01	44.19	12.40
0.67	1.02	5.16	3.17	13.61	5.39	23.84	7.71	34.20	10.07	44.42	12.45
0.72	1.07	5.30	3.22	13.85	5.44	24.03	7.76	34.44	10.12	44.62	12.49
0.72	1.10	5.45	3.27	14.04	5.49	24.31	7.81	34.68	10.17	44.85	12.55
0.67	1.10	5.64	3.32	14.33	5.53	24.41	7.86	34.92	10.22	45.04	12.60
0.76	1.15	5.78	3.36	14.52	5.58	24.65	7.91	35.11	10.27	45.24	12.65
0.86	1.19	5.92	3.41	14.76	5.63	24.89	7.96	35.35	10.32	45.47	12.70
0.91	1.24	6.07	3.46	14.95	5.68	25.13	8.01	35.59	10.37	45.67	12.75
0.96	1.29	6.21	3.51	15.19	5.73	25.36	8.06	35.83	10.42	45.90	12.80
1.00	1.33	6.40	3.55	15.43	5.78	25.60	8.11	36.06	10.47	46.05	12.85
1.10	1.38	6.54	3.60	15.62	5.83	25.84	8.16	36.30	10.52	46.29	12.91
1.15	1.43	6.74	3.64	15.81	5.87	26.03	8.21	36.54	10.57	46.53	12.96
1.19	1.47	6.93	3.69	16.05	5.92	26.27	8.26	36.78	10.62	46.81	13.00
1.29	1.52	7.07	3.74	16.29	5.97	26.51	8.31	36.88	10.68	47.00	13.05
1.39	1.57	7.26	3.79	16.53	6.02	26.75	8.36	37.12	10.72	47.15	13.11
1.43	1.62	7.45	3.84	16.77	6.07	26.94	8.41	37.31	10.77	47.34	13.16
1.48	1.67	7.60	3.89	16.96	6.12	27.23	8.46	37.55	10.82	47.53	13.21
1.58	1.72	7.79	3.93	17.20	6.17	27.47	8.51	37.74	10.88	47.77	13.26
1.67	1.76	7.98	3.98	17.39	6.22	27.71	8.55	37.98	10.93	48.01	13.31
1.72	1.81	8.17	4.03	17.63	6.27	27.94	8.60	38.21	10.98	48.20	13.36
1.82	1.85	8.36	4.08	17.87	6.32	28.14	8.65	38.45	11.03	48.44	13.41
1.91	1.90	8.55	4.12	18.10	6.37	28.42	8.70	38.64	11.08	48.68	13.46
1.96	1.95	8.69	4.17	18.30	6.42	28.61	8.75	38.84	11.13	48.87	13.51
2.10	1.99	8.88	4.22	18.53	6.47	28.85	8.80	39.07	11.18	49.11	13.56
2.20	2.04	9.08	4.27	18.72	6.52	29.04	8.85	39.27	11.23		
2.29	2.09	9.27	4.32	18.96	6.57	29.28	8.91	39.55	11.28		
2.39	2.13	9.46	4.36	19.15	6.61	29.57	8.95	39.74	11.33		

Table A.1-11 Calculations of the CBR of the material

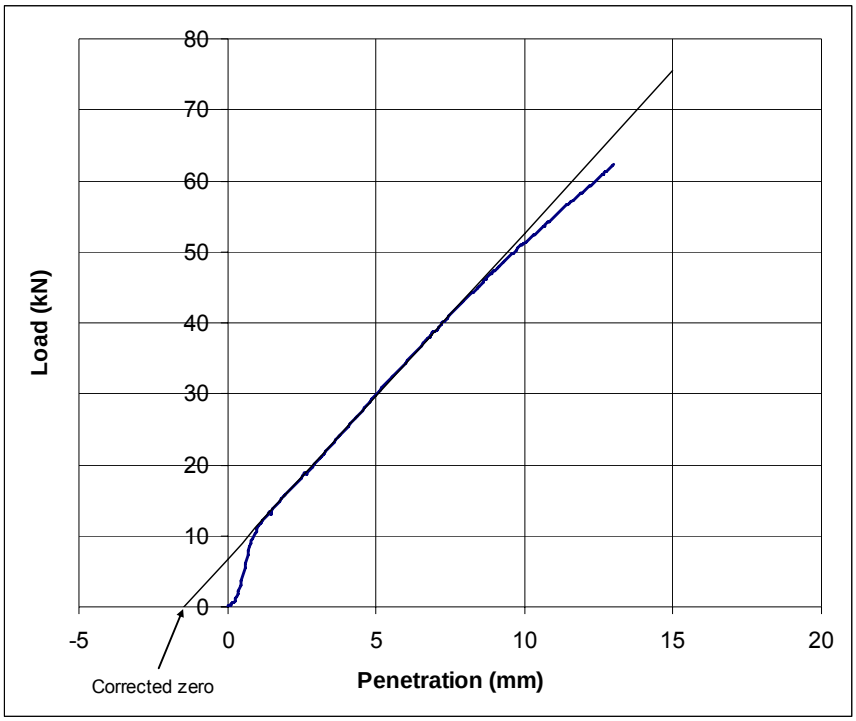

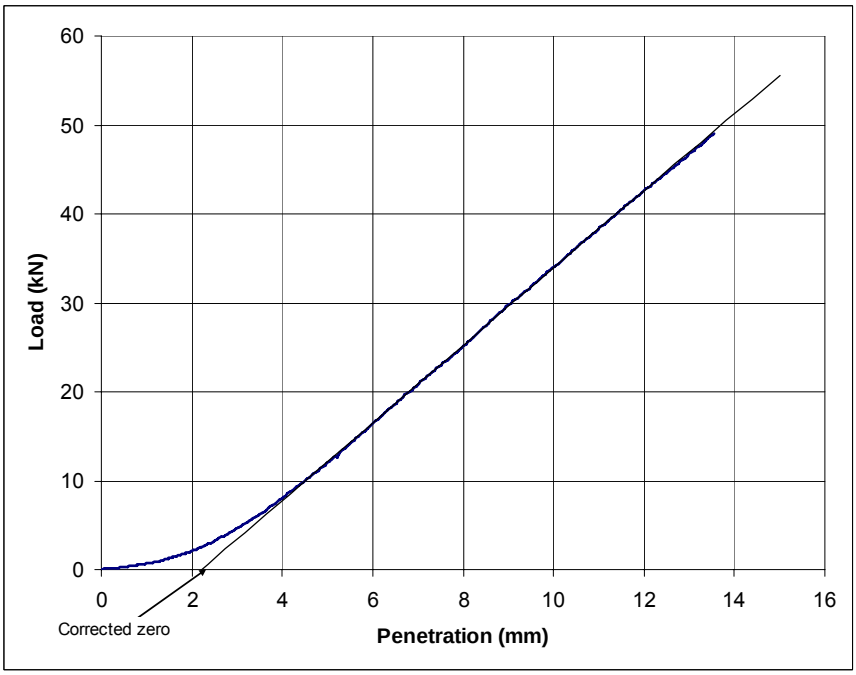

CBR Values	At 2.5mm	At 5.0mm
CBR1	87	116
CBR2	82	110
CBR of the material	110 at 5.0mm penetration	

Table A.1-12 Coefficient of permeability

The coefficient of permeability is calculated using the following formula:

$K_T = 2.303*La/tA*log_{10}(h_1/h_2)$

where

K_T =coefficient of permeability at test temperature (mm/s)

L = specimen length (mm)

A = cross-sectional area of flow (mm^2)

h_1 & h_2 = initial and final standpipe levels (mm)

a = internal cross-sectional area of the standard pipe used (mm^2)

t = time of fall in standpipe water level from h_1 to h_2 (sec)

The coefficient of permeability must be corrected to 20^0C by using the following formula:

$K = K_T *(n_T/n_{20})$

K = permeability at 20^0 C

n_T = viscosity of water at test temperature

n_{20} = viscosity of water at 20^0 C

Trial No	1	2	3
L mm	125	125	125
A mm^2	9331.316	9331.316	9331.316
a mm^2	37.39281	37.39281	37.39281
h_1 mm	1320	1220	1120
h_2 mm	1220	1120	1020
t sec	2235	2593	3191
K_T mm/sec	0.015086	0.011978	0.0089
Test temperature ^{0}C	23		
n_T/n_{20}	0.9311		
K mm/sec	0.01405	0.01115	0.00829
Average K mm/sec at 20^0 C	0.0112		

Table A.1-13 Particle size distribution

Sieve size (mm)	Mass Retained (g)	% Retained	Cumulative % Retained	% Passing
19	0.0	0.0	0.0	100.0
9.5	457.0	17.2	17.2	82.8
4.75	513.3	19.3	36.5	63.5
2.36	702.5	26.5	63.0	37.0
0.425	732.6	27.6	90.6	9.4
0.075	199.2	7.5	98.1	1.9
pan	50.6	1.9	100.0	0.0

APPENDIX A.2 Density and saturation calculations-Semi Confined Test (SCT) samples

Table A.2 -1 Density and saturation of SCT samples /Monotonic tests

Penetration Rate	**2.5mm/min**	**5.0mm/min**	**10mm/min**	**15mm/min**	**20mm/min**	**Average**
04/09/2003 - Saturated Samples	**MS02**	**MS05**	**MS10**	**MS15**	**MS20**	
Mould+Base (g)	7193.3	8766.1	7158	7205.3	7535	
M+B+Wet Sample (96hrs saturated) (g)	14727.2	16242.4	15001.7	15125	15467.1	
Wt of moist sample (g)	7533.9	7476.3	7843.7	7919.7	7932.1	
Wet density kg/m3	2339.1	2321.2	2435.3	2458.9	2462.7	
Water content before saturation %	5.41	5.27	5.42	5.45	5.64	
M+B+Wet Sample (96hrs saturated) (g)	14842.5	12765.2	15131	15213	15553.2	
Wt of Saturated Sample (g)	7649.2	7620.8	7973	8007.7	8018.2	
Density of 96hrs saturated sample kg/m3	***2375***	***2366***	***2475***	***2486***	***2489***	***2438***
Water content after saturation %	***7.03***	***7.30***	***7.16***	***6.62***	***6.79***	***6.98***
Wt of Dry Sample (g)	7147.1	7102.2	7440.3	7510.6	7508.7	
Dry Density kg/m3	2219.0	2205.0	2310.0	2331.8	2331.3	
Increase in water content %	1.61	2.03	1.74	1.17	1.15	
Water content w %	0.07	0.07	0.07	0.07	0.07	
Void ratio e = $Gs(1+w)\rho_w/\rho-1$	0.2393	0.2471	0.1905	0.1793	0.1796	
Porosity n=e/(1+e)	0.1931	0.1982	0.1600	0.1521	0.1523	
Degree of saturation Sr=wGs/e	0.8228	0.7365	0.9797	1.0150	1.0388	
Air content n(1-Sr)	0.0342	0.0522	0.0032	-	-	
09/09/2003 - Oven dried Samples	**MD02**	**MD05**	**MD10**	**MD15**	**MD20**	
Mould+Base (g)	7192.5	5146.4	7158	7195	7535	
M+B+Wet Sample 24hrs oven dried (g)	15211.1	12863.5	15098.3	15141.8	15463.5	
Wt of moist sample (g)	8018.6	7717.1	7940.3	7946.8	7928.5	
Wet density kg/m3	2489.6	2396.0	2465.3	2467.3	2461.6	
Water content before drying in oven %	5.76	6.09	5.86	5.79	5.65	
M+B+Wet Sample 24hrs oven dried (g)	14808.3	12475.1	14780.8	14792.8	15125.8	
Wt of sample after 24hrs drying (g)	7615.8	7328.7	7622.8	7597.8	7590.8	
Density of 24hrs oven dried sample	***2365***	***2275***	***2367***	***2359***	***2357***	***2344***
Water content after 24hrs drying %	***0.45***	***0.75***	***1.63***	***1.14***	***1.15***	***1.02***
Wt of Dry Sample (g)	7581.7	7274.4	7500.5	7512.1	7504.5	
Dry Density kg/m3	2353.9	2258.5	2328.7	2332.3	2329.9	
Water content w %	0.0045	0.01	0.02	0.01	0.01	
Void ratio e = $Gs(1+w)\rho_w/\rho-1$	0.1683	0.2176	0.1809	0.1791	0.1803	
Porosity n=e/(1+e)	0.1440	0.1787	0.1532	0.1519	0.1527	
Degree of saturation Sr=wGs/e	0.0735	0.1442	0.1748	0.1572	0.1754	
Air content n(1-Sr)	0.1334	0.1530	0.1264	0.1280	0.1260	

Table A.2 -1 Density and saturation of SCT samples /Monotonic tests (contd..)

Penetration Rate	**2.5mm/min**	**5.0mm/min**	**10mm/min**	**15mm/min**	**20mm/min**	**Average**
11/09/2003 -OMC Samples	**MM02**	**MM05**	**MM10**	**MM15**	**MM20**	
Mould+Base (g)	7531.8	5146.4	7158	7195	7535	
M+B+Wet Sample (g)	15469.3	12787.7	15130.8	15121.8	15456.7	
Wt of moist sample (g)	7937.5	7641.3	7972.8	7926.8	7921.7	
Density of OMC sample kg/m3	***2464***	***2372***	***2475***	***2461***	***2459***	***2447***
Water content %	***5.93***	***5.66***	***5.74***	***5.53***	***5.46***	***5.66***
Wt of Dry Sample (g)	7492.9	7231.9	7539.8	7511.6	7511.7	
Dry Density kg/m3	2326.3	2245.3	2340.9	2332.2	2332.2	
Water content w %	0.06	0.06	0.06	0.06	0.05	
Void ratio $e = Gs(1+w)\rho_w/\rho-1$	0.1821	0.2248	0.1748	0.1792	0.1792	
Porosity n=e/(1+e)	0.1541	0.1835	0.1488	0.1519	0.1519	
Degree of saturation Sr=wGs/e	0.8960	0.6763	0.8589	0.0000	0.8378	
Air content n(1-Sr)	0.0160	0.0594	0.0210	0.1519	0.0246	

Table A.2 -2 Density and saturation of SCT samples /Cyclic tests

Penetration Rate	**2.5mm/min**	**5.0mm/min**	**10mm/min**	**15mm/min**	**20mm/min**	**Average**
21/08/2003 - Saturated Samples	**CM02**	**CM05**	**CM10**	**CM15**	**CM20**	
Mould+Base (g)	7194.8	5146.4	7170.8	7195	8766.1	
M+B+Wet Sample (96hrs saturated) (g)	14876.4	12855.4	15152	15027.8	16480.1	
Wt of moist sample (g)	7681.6	7709	7981.2	7832.8	7714	
Wet density kg/m3	2384.9	2393.4	2478.0	2431.9	2395.0	
Water content before saturation %	5.83	5.52	5.76	5.56	6.11	
M+B+Wet Sample (96hrs saturated) (g)	14940.5	12913.4	15209	15154.5	12911.5	
Wt of Saturated Sample (g)	7745.7	7767	8038.2	7959.5	7765.1	
Density of 96hrs saturated sample kg/m3	***2405***	***2411***	***2496***	***2471***	***2411***	***2439***
Water content after saturation %	***6.71***	***6.31***	***6.51***	***7.27***	***6.82***	***6.72***
Wt of Dry Sample (g)	7258.7	7305.8	7546.6	7420	7269.5	
Dry Density kg/m3	2253.6	2268.3	2343.0	2303.7	2257.0	
Increase in water content %	0.88	0.79	0.76	1.71	0.70	
Water content w %	0.07	0.06	0.07	0.07	0.07	
Void ratio $e = Gs(1+w)\rho_w/\rho-1$	0.2203	0.2124	0.1737	0.1937	0.2184	
Porosity n=e/(1+e)	0.1805	0.1752	0.1480	0.1623	0.1793	
Degree of saturation Sr=wGs/e	0.8377	0.8174	1.0313	1.0321	0.8583	
Air content n(1-Sr)	0.0293	0.0320	-	-	0.0254	

Table A.2 -2 Density and saturation of SCT samples /Cyclic tests (contd..)

Penetration Rate	**2.5mm/min**	**5.0mm/min**	**10mm/min**	**15mm/min**	**20mm/min**	**Average**
26/08/2003 - Oven Dried Samples	**CD02**	**CD05**	**CD10**	**CD15**	**CD20**	
Mould+Base (g)	7154.8	7539.7	7192.5	7170.8	5146.4	
M+B+Wet Sample 24hrs oven dried (g)	15108.5	15524.7	15202.5	15160.7	12769.7	
Wt of moist sample (g)	7953.7	7985	8010	7989.9	7623.3	
Wet density kg/m3	2469.4	2479.1	2486.9	2480.7	2366.8	
Water content before drying in oven %	5.91	5.90	6.12	5.54	5.38	
M+B+Wet Sample 24hrs oven dried (g)	14702.5	15117.6	14791.7	14841.2	12476.7	
Wt of sample after 24hrs drying (g)	7547.7	7577.9	7599.2	7670.4	7330.3	
Density of 24hrs oven dried sample	***2332***	***2353***	***2343***	***2381***	***2276***	***2337***
Water content after 24hrs drying %	***0.50***	***0.51***	***0.68***	***1.32***	***1.33***	***0.87***
Wt of Dry Sample (g)	7509.8	7539.8	7547.9	7570.2	7233.9	
Dry Density kg/m3	2331.6	2340.9	2343.4	2350.3	2245.9	
Water content w %	0.01	0.01	0.01	0.01	0.01	
Void ratio $e = Gs(1+w)\rho_w/\rho-1$	0.1854	0.1748	0.1815	0.1700	0.2244	
Porosity n=e/(1+e)	0.1564	0.1488	0.1536	0.1453	0.1833	
Degree of saturation Sr=wGs/e	0.0749	0.0795	0.1030	0.2141	0.1633	
Air content n(1-Sr)	0.1447	0.1369	0.1378	0.1142	0.1534	
28/08/2003 - OMC Samples	**CM02**	**CM05**	**CM10**	**CM15**	**CM20**	
Mould+Base (g)	7194.8	5146.4	7170.8	7205.3	7539.7	
M+B+Wet Sample (g)	14904.5	12863.2	15227.9	15163.9	15517.2	
Wt of moist sample (g)	7709.7	7716.8	8057.1	7958.6	7977.5	
Density of OMC sample kg/m3	***2394***	***2396***	***2502***	***2471***	***2477***	***2448***
Water content %	***5.86***	***5.70***	***5.69***	***5.71***	***5.74***	***5.74***
Wt of Dry Sample (g)	7283.1	7300.5	7623.2	7528.6	7544.3	
Dry Density kg/m3	2261.2	2266.6	2366.8	2337.4	2342.3	
Water content w %	0.06	0.06	0.06	0.06	0.06	
Void ratio $e = Gs(1+w)\rho_w/\rho-1$	0.2162	0.2133	0.1619	0.1765	0.1741	
Porosity n=e/(1+e)	0.1777	0.1758	0.1393	0.1500	0.1483	
Degree of saturation Sr=wGs/e	0.7452	0.7353	0.9668	0.8899	0.9072	
Air content n(1-Sr)	0.0453	0.0465	0.0046	0.0165	0.0138	

APPENDIX A.3 SCT experimental data sheets

Table A.3 -1 Load - penetration results of dry specimens - Monotonic

2.5mm/min		5.0mm/min		10.0mm/min		15.0mm/min		20.0mm/min	
MD02		MD05		MD10		MD15		MD20	
Penetration (mm)	Load (kN)	Penetration (mm)	Load (kN)	Penetration (mm)	Load (kN)	Penetration (mm)	Load (kN)	Penetration (mm)	Load (kN)
0.00	0.00	0.00	0.00	0.00	0.00	0.00	0.00	0.00	0.00
0.19	1.24	0.19	1.24	0.10	1.24	0.10	2.48	0.19	3.73
0.19	1.24	0.19	1.24	0.19	3.73	0.29	3.73	0.39	4.97
0.19	0.00	0.29	2.48	0.39	4.97	0.39	4.97	0.58	7.45
0.19	1.24	0.39	2.48	0.58	7.45	0.58	6.21	0.68	8.69
0.19	2.48	0.48	3.73	0.68	8.69	0.68	7.45	0.87	9.93
0.39	3.73	0.58	3.73	0.87	11.18	0.78	8.69	1.07	12.42
0.39	2.48	0.58	6.21	0.97	14.90	0.97	11.18	1.26	14.90
0.39	2.48	0.68	7.45	1.26	16.14	0.97	11.18	1.36	17.39
0.48	4.97	0.78	8.69	1.36	17.39	1.16	13.66	1.55	18.63
0.48	3.73	0.87	8.69	1.55	18.63	1.26	14.90	1.65	22.35
0.48	3.73	0.97	9.93	1.65	22.35	1.36	16.14	1.84	24.84
0.58	6.21	0.97	9.93	1.94	24.84	1.55	18.63	2.03	27.32
0.68	7.45	1.16	9.93	2.03	26.08	1.65	19.87	2.23	29.80
0.68	7.45	1.26	13.66	2.23	28.56	1.74	19.87	2.42	33.53
0.68	6.21	1.36	13.66	2.33	31.05	1.94	24.84	2.52	36.01
0.78	7.45	1.36	16.14	2.52	36.01	2.03	26.08	2.71	39.74
0.78	7.45	1.45	17.39	2.71	38.50	2.13	28.56	2.81	40.98
0.87	8.69	1.45	17.39	2.91	40.98	2.23	31.05	3.10	45.95
0.87	8.69	1.55	18.63	3.00	42.22	2.42	33.53	3.20	48.43
0.87	8.69	1.65	19.87	3.10	44.71	2.52	37.25	3.39	50.91
0.97	12.42	1.74	24.84	3.29	49.67	2.62	38.50	3.58	54.64
0.97	11.18	1.94	24.84	3.49	52.16	2.81	40.98	3.68	57.12
0.97	9.93	1.94	27.32	3.68	54.64	2.91	43.46	3.88	58.37
1.07	13.66	2.03	24.84	3.88	58.37	3.10	45.95	3.97	62.09
1.16	13.66	2.13	27.32	3.97	60.85	3.10	49.67	4.17	64.57
1.16	13.66	2.13	29.80	4.26	58.37	3.29	49.67	4.36	68.30
1.16	14.90	2.33	31.05	4.26	64.57	3.39	53.40	4.46	70.78
1.36	17.39	2.33	33.53	4.46	69.54	3.49	54.64	4.65	74.51
1.26	14.90	2.42	36.01	4.65	70.78	3.68	58.37	4.84	75.75
1.26	14.90	2.52	33.53	4.84	74.51	3.78	59.61	5.04	78.23
1.36	13.66	2.62	40.98	5.04	78.23	3.88	63.33	5.13	81.96
1.36	17.39	2.71	38.50	5.13	80.72	4.07	64.57	5.33	83.20
1.45	17.39	2.81	40.98	5.33	81.96	4.07	67.06	5.52	86.93
1.45	19.87	2.91	44.71	5.52	83.20	4.26	69.54	5.72	89.41
1.55	22.35	2.91	45.95	5.72	88.17	4.36	72.03	5.81	91.89
1.55	21.11	3.00	49.67	5.81	89.41	4.46	74.51	5.91	93.14
1.65	21.11	3.10	50.91	6.01	94.38	4.65	76.99	6.20	96.86
1.65	19.87	3.20	48.43	6.20	96.86	4.75	79.48	6.30	99.35

APPENDIX A.4 Stiffness and penetrated depth against moisture, penetration rate and number of cycles in SCT

Table 4.1-1 Calculated initial stiffness from load-penetration curves

Test No.	Moisture Content (%)	Initial stiffness (kN/mm)	Test No	Moisture Content (%)	Initial stiffness (kN/mm)	Test No	Moisture Content (%)	Initial stiffness (kN/mm)
MD02	0.45	20.7	MM02	5.93	4.7	MS02	7.03	2.9
MD05	0.75	20.8	MM05	5.66	5.7	MS05	7.30	3.0
MD10	1.63	16.4	MM10	5.74	5.2	MS10	7.16	5.2
MD15	1.14	19.3	MM15	5.53	5.8	MS15	6.62	4.0
MD20	1.15	18.3	MM20	5.46	6.2	MS20	6.79	5.0
CD02	0.50	16.13	CM02	5.86	5.80	CS02	6.71	5.05
CD05	0.51	16.7	CM05	5.70	4.70	CS05	6.31	3.90
CD10	0.68	21.8	CM10	5.69	4.50	CS10	6.51	3.60
CD15	1.32	18.7	CM15	5.71	4.60	CS15	7.27	4.70
CD20	1.33	15.4	CM20	5.74	5.20	CS20	6.82	5.10

Table 4.2-2 Calculated reloading stiffness at each cycle number from load-penetration curves

	Reloading stiffness (kN/mm)					
Cycle No. / Test No	CD02	CM02	CS02	CD15	CM15	CS15
1	29.64	9.93	11.77	31.45	8.90	10.14
2	38.82	14.97	13.99	36.86	11.96	10.49
3	50.47	23.94	20.96	48.85	19.81	15.02
4	39.82	22.65	16.27	48.85	19.80	16.10
5	43.56	28.84	19.15	49.85	21.38	18.62
6	52.66	30.75	23.94	47.15	23.72	19.69
7	40.42	30.88	28.59	45.50	31.35	23.33
8	58.16	35.78	34.08	54.10	34.06	24.34
Cycle No. / Test No	CD05	CM05	CS05	CD20	CM20	CS20
1	28.08	7.61	9.30	30.19	10.02	9.15
2	36.49	12.30	11.69	35.94	11.88	11.67
3	49.27	23.11	14.09	44.41	17.46	15.54
4	54.82	22.59	13.97	45.74	20.95	15.69
5	60.65	27.67	18.98	39.31	21.39	21.21
6	58.72	27.67	24.99	45.00	24.83	21.71
7	48.22	27.83	26.37	42.93	28.14	24.03
8	50.16	33.43	30.14	49.28	32.83	29.92
Cycle No. / Test No.	CD10	CM10	CS10			
1	37.64	7.17	6.82			
2	42.50	10.77	9.88			
3	46.86	19.22	12.20			
4	48.10	21.03	16.30			
5	47.76	23.20	17.95			
6	40.34	22.68	23.40			
7	53.07	28.61	27.18			
8	55.01	33.00	30.22			

Table A.4-3 Penetration with cycle number

		Penetration, δ (mm)		
Penetration Rate (mm/min)	Cycle No	Dry	Saturated	OMC
2.5	1	3.6	5.58	4.59
	2	6.05	8.99	8.08
	3	12.67	16.84	16.06
	4	19.11	24.74	23.16
	5	30.51	37.23	35.02
	6	41.36	49.36	46.78
	7	56.3	66.05	63.1
	8	71.25	82.4	78.99
5.0	1	3.67	5.28	4.1
	2	6	8.6	7.49
	3	12.06	16.2	15.32
	4	17.28	23.6	22.2
	5	26.5	35.82	33.94
	6	35.12	47.6	45.11
	7	48.8	62.65	61.34
	8	64.36	79.62	77.4
10.0	1	3.22	4.62	4.34
	2	5.11	7.9	6.87
	3	10.9	17.07	14.65
	4	16.6	22.64	21.36
	5	26.94	34.68	32.88
	6	37.07	46.29	44.48
	7	51.66	62.58	60.94
	8	65.8	78.48	86.91
15.0	1	3.44	4.1	4.12
	2	5.78	7.77	7.34
	3	12.11	16.33	15.4
	4	17.56	24.28	22.48
	5	27.5	36.77	34.13
	6	37.8	48.99	45.68
	7	52.4	65.73	61.83
	8	68.1	82.03	77.37
20.0	1	3.67	4.32	4.54
	2	6.2	7.77	7.61
	3	12.6	15.68	15.27
	4	18	22.91	22.39
	5	29.9	35.15	33.93
	6	41.36	46.96	45.39
	7	56.92	63.64	61.51
	8	72.14	79.94	77.48

APPENDIX A.5 Dimensional analysis data sheets

Table A.5 -1 Dimensional analysis results of dry specimens - Monotonic

2.5mm/min		5.0mm/min		10.0mm/min		15.0mm/min		20.0mm/min	
MD02		MD05		MD10		MD15		MD20	
$V^2\rho_d\delta^2$ (kN)	Load (kN)	$V^2\rho_d\delta^2$ (kN)	Load (kN)	$V^2\rho_d\delta^2$ (kN)	Load (kN)	$V^2\rho_d\delta^2$ (kN)	Load (kN)	$V^2\rho_d\delta^2$ (kN)	Load (kN)
0.00E+00	0	0.00E+00	0	0.00E+00	0	0.00E+00	0	0.00E+00	0
3.80E-16	1.242	1.53E-15	1.242	6.11E-15	1.242	1.38E-14	2.484	9.37E-14	3.725
3.80E-16	1.242	6.10E-15	1.242	2.44E-14	3.725	1.24E-13	3.725	3.75E-13	4.967
3.80E-16	1.242	1.37E-14	2.484	9.78E-14	4.967	2.21E-13	4.967	8.43E-13	7.451
3.42E-15	2.484	2.44E-14	2.484	2.20E-13	7.451	4.96E-13	6.209	1.15E-12	8.693
3.42E-15	2.484	2.44E-14	3.725	2.99E-13	8.693	6.76E-13	7.451	1.90E-12	9.935
3.42E-15	2.484	5.49E-14	4.967	4.95E-13	11.18	8.82E-13	8.693	2.83E-12	12.42
6.08E-15	3.725	5.49E-14	4.967	6.11E-13	14.9	1.38E-12	11.18	3.96E-12	14.9
6.08E-15	2.484	9.77E-14	6.209	1.03E-12	16.14	1.38E-12	11.18	4.59E-12	17.39
6.08E-15	2.484	9.77E-14	6.209	1.20E-12	17.39	1.99E-12	13.66	6.00E-12	18.63
9.50E-15	3.725	1.24E-13	7.451	1.56E-12	18.63	2.33E-12	14.9	6.77E-12	22.35
9.50E-15	3.725	1.53E-13	7.451	1.77E-12	22.35	2.70E-12	16.14	8.46E-12	24.84
9.50E-15	3.725	1.85E-13	8.693	2.44E-12	24.84	3.53E-12	18.63	1.03E-11	27.32
1.86E-14	4.967	2.20E-13	8.693	2.69E-12	26.08	3.98E-12	19.87	1.24E-11	29.8
1.86E-14	4.967	2.20E-13	11.18	3.23E-12	28.56	4.47E-12	19.87	1.46E-11	33.53
1.86E-14	4.967	2.58E-13	12.42	3.52E-12	31.05	5.51E-12	24.84	1.58E-11	36.01
1.86E-14	4.967	2.99E-13	13.66	4.13E-12	36.01	6.08E-12	26.08	1.84E-11	39.74
3.08E-14	7.451	3.43E-13	13.66	4.79E-12	38.5	6.67E-12	28.56	1.97E-11	40.98
3.08E-14	7.451	3.91E-13	14.9	5.50E-12	40.98	7.29E-12	31.05	2.40E-11	45.95
3.08E-14	6.209	3.91E-13	14.9	5.87E-12	42.22	8.62E-12	33.53	2.55E-11	48.43
3.08E-14	6.209	4.94E-13	14.9	6.26E-12	44.71	9.32E-12	37.25	2.87E-11	50.91
3.08E-14	7.451	5.51E-13	18.63	7.06E-12	49.67	1.01E-11	38.5	3.21E-11	54.64
3.80E-14	8.693	6.10E-13	18.63	7.92E-12	52.16	1.16E-11	40.98	3.38E-11	57.12
4.60E-14	8.693	6.10E-13	21.11	8.82E-12	54.64	1.24E-11	43.46	3.75E-11	58.37
4.60E-14	8.693	6.73E-13	22.35	9.78E-12	58.37	1.41E-11	45.95	3.94E-11	62.09
4.60E-14	8.693	6.73E-13	22.35	1.03E-11	60.85	1.41E-11	49.67	4.33E-11	64.57
4.60E-14	8.693	7.38E-13	23.59	1.18E-11	58.37	1.59E-11	49.67	4.74E-11	68.3
6.42E-14	9.935	8.07E-13	24.84	1.18E-11	64.57	1.69E-11	53.4	4.96E-11	70.78
6.42E-14	9.935	8.79E-13	29.8	1.29E-11	69.54	1.79E-11	54.64	5.40E-11	74.51
6.42E-14	8.693	1.03E-12	29.8	1.41E-11	70.78	1.99E-11	58.37	5.86E-11	75.75
6.42E-14	9.935	1.03E-12	32.29	1.53E-11	74.51	2.10E-11	59.61	6.33E-11	78.23
6.42E-14	11.18	1.11E-12	29.8	1.65E-11	78.23	2.21E-11	63.33	6.58E-11	81.96
8.55E-14	12.42	1.20E-12	32.29	1.72E-11	80.72	2.43E-11	64.57	7.09E-11	83.2
8.55E-14	11.18	1.20E-12	34.77	1.85E-11	81.96	2.43E-11	67.06	7.61E-11	86.93

APPENDIX A.6 Coefficients of the orthogonal polynomials

Table A.6-1 Coefficients of the orthogonal polynomial - monotonic tests

Numerical	***Rate (mm/min)***				
Coefficients	***2.5***	***5***	***10***	***15***	***20***
Dry specimens					
B	47.08	46.35	56.99	67.04	49.04
p	3.25E+13	8.13E+12	1.00E+12	44.5	3.34E+11
q	-1.71E+24	-7.42E+22	-1.77E+21	-2.80E+20	-1.81E+20
r	3.58E+34	2.80E+32	1.37E+30	7.70E+28	4.05E+28
s	-3.77E+44	-5.42E+41	-5.85E+38	-1.10E+37	-4.73E+36
t	2.19E+54	5.89E+50	1.51E+47	1.00E+45	3.17E+44
u	7.14E+63	-3.67E+59	-2.33E+55	-5.60E+52	-1.23E+52
v	1.22E+73	1.22E+68	1.98E+63	1.80E+60	2.59E+59
w	-8.58E+81	-1.71E+76	-7.09E+70	-2.60E+67	-2.29E+66
R^2	***0.98***	***0.97***	***0.97***	***0.96***	***0.98***
Monotonic specimens					
B	11.94	18.66	18.6	21.82	23.58
p	6.31E+12	2.26E+12	3.63E+11	1.51E+11	8.44E+10
q	-1.73E+23	-1.70E+22	-6.42E+20	-1.14E+20	-3.05E+19
r	2.35E+33	6.46E+31	6.00E+29	4.83E+28	6.80E+27
s	-1.74E+43	-1.33E+41	-3.09E+38	-1.12E+37	-8.65E+35
t	7.54E+52	1.58E+50	9.19E+46	1.50E+45	6.36E+43
u	-1.89E+62	1.07E+59	-1.56E+55	-1.14E+53	-2.67E+51
v	2.55E+71	3.89E+67	1.42E+63	4.59E+60	5.98E+58
w	-1.44E+80	-5.83E+75	-5.31E+70	-7.60E+67	-5.48E+65
R^2	***0.99***	***0.99***	***0.99***	***0.99***	***0.99***
Saturated specimens					
B	13.9	9.61	16.47	15.5	16.66
p	3.82E+12	6.38E+11	1.44E+11	7.64E+10	6.03E+10
q	-1.29E+23	-4.51E+21	-1.73E+20	-4.62E+19	-2.75E+19
r	2.17E+33	1.85E+31	1.06E+29	1.67E+28	6.88E+27
s	-1.92E+43	-4.15E+40	-3.54E+37	-3.61E+36	-9.31E+35
t	9.56E+52	5.24E+49	6.52E+45	4.64E+44	7.15E+43
u	-2.70E+62	-3.74E+58	-6.33E+53	-3.45E+52	-3.12E+51
v	4.04E+71	1.40E+67	2.58E+61	1.36E+60	7.22E+58
w	-2.50E+80	-2.17E+75	-7.23E+67	-2.19E+67	-6.88E+65
R^2	***0.99***	***0.99***	***0.99***	***0.99***	***0.99***

Table A.6-2 Coefficients of the orthogonal polynomial - cyclic tests

Numerical	***Rate (mm/min)***				
Coefficients	***2.5***	***5***	***10***	***15***	***20***
Dry specimens					
B	101.55	48.33	92.39	56.19	54.16
p	1.65E+12	4.72E+12	1.07E+12	5.55E+11	2.75E+11
q	2.41E+21	-1.79E+22	-2.55E+21	-4.19E+20	-1.76E+20
r	-1.86E+31	1.99E+30	2.47E+30	1.36E+29	4.85E+28
s	-1.07E+42	1.10E+41	-1.19E+39	-2.32E+37	-6.89E+36
t	1.06E+52	-2.55E+50	3.16E+47	2.26E+45	5.50E+44
u	-3.93E+61	2.57E+59	-4.69E+55	-1.27E+53	-2.48E+52
v	6.56E+70	-1.25E+68	3.66E+63	3.91E+60	5.91E+59
w	-4.14E+79	2.39E+76	-1.16E+71	-5.02E+67	-5.78E+66
R^2	***0.88***	***0.97***	***0.94***	***0.97***	***0.95***
OMC specimens					
B	10.81	12.72	7.18	16.73	12.61
p	7.72E+12	1.58E+12	4.69E+11	1.25E+11	8.26E+10
q	-2.15E+23	9.85E+21	-7.95E+20	-8.83E+19	-3.22E+19
r	2.96E+33	3.15E+31	6.40E+29	3.44E+28	6.93E+27
s	-2.22E+43	-5.50E+40	-2.79E+38	-7.36E+36	-8.45E+35
t	9.67E+52	5.47E+49	7.08E+46	9.15E+44	6.02E+43
u	-2.42E+62	-3.07E+58	-1.04E+55	-6.60E+52	-2.48E+51
v	3.26E+71	9.05E+66	8.32E+62	2.56E+60	5.49E+58
w	-1.82E+80	-1.08E+75	-2.78E+70	-4.16E+67	-5.02E+65
R^2	***0.98***	***0.97***	***0.98***	***0.98***	***0.98***
Saturated specimens					
B	13.07	11.13	8.91	11.68	17.22
p	4.13E+12	8.04E+11	2.58E+11	6.59E+10	5.10E+10
q	-1.42E+23	-4.83E+21	-4.99E+20	-4.09E+19	-1.78E+19
r	2.51E+33	1.66E+31	5.16E+29	1.36E+28	3.71E+27
s	-2.33E+43	-3.13E+40	-2.82E+38	-2.50E+36	-4.60E+35
t	1.22E+53	3.39E+49	8.60E+46	2.65E+44	3.43E+43
u	-3.63E+62	-2.11E+58	-1.47E+55	-1.63E+52	-1.49E+51
v	5.74E+71	7.09E+66	1.31E+63	5.42E+59	3.47E+58
w	-3.72E+80	-9.92E+74	-4.80E+70	-7.55E+66	-3.29E+65
R^2	***0.97***	***0.95***	***0.98***	***0.98***	***0.97***

APPENDIX A.7 Ternary plot calculations

Table A.7-1 Values used for ternary plot of monotonic tests

	Load kN	Rate mm/min	Sample m/c %	δ mm	Q	F	L	NQ	NF	NL	Sum NQ+NF+NL
Dry	25	2.5	0.45	2.38	0.125	0.07	0.09	42.1	25.7	32.1	100.0
	50	2.5	0.45	3.84	0.125	0.07	0.15	35.2	21.5	43.3	100.0
	25	5	0.75	2.21	0.25	0.12	0.08	53.7	27.3	19.0	100.0
	50	5	0.75	3.50	0.25	0.12	0.14	48.3	24.6	27.1	100.0
	25	10	1.63	2.07	0.5	0.27	0.08	58.2	32.2	9.7	100.0
	50	10	1.63	3.28	0.5	0.27	0.13	55.1	30.4	14.5	100.0
	25	15	1.14	2.00	0.75	0.19	0.08	73.3	18.9	7.8	100.0
	50	15	1.14	3.30	0.75	0.19	0.13	69.8	18.0	12.3	100.0
	25	20	1.15	1.89	1	0.19	0.07	78.7	15.3	6.0	100.0
	50	20	1.15	3.34	1	0.19	0.13	75.3	14.7	10.1	100.0
OMC	25	2.5	5.93	7.54	0.125	1.00	0.30	8.7	70.2	21.1	100.0
	50	2.5	5.93	12.18	0.125	1.00	0.48	7.7	62.1	30.1	100.0
	25	5	5.66	4.73	0.25	0.95	0.18	17.9	68.6	13.5	100.0
	50	5	5.66	8.77	0.25	0.95	0.35	16.0	61.5	22.5	100.0
	25	10	5.74	5.11	0.5	0.97	0.20	29.8	58.0	12.2	100.0
	50	10	5.74	10.73	0.5	0.97	0.42	26.3	51.1	22.6	100.0
	25	15	5.53	4.53	0.75	0.93	0.18	40.1	50.2	9.7	100.0
	50	15	5.53	10.14	0.75	0.93	0.40	35.8	44.8	19.4	100.0
	25	20	5.46	4.39	1	0.92	0.17	47.6	44.0	8.4	100.0
	50	20	5.46	9.42	1	0.92	0.37	43.4	40.2	16.4	100.0
Saturated	25	2.5	7.03	8.05	0.125	1.19	0.32	7.6	72.7	19.7	100.0
	50	2.5	7.03	17.64	0.125	1.19	0.70	6.2	58.9	34.9	100.0
	25	5	7.3	11.42	0.25	1.23	0.45	12.9	63.6	23.5	100.0
	50	5	7.3	32.82	0.25	1.23	1.31	8.9	44.2	46.9	100.0
	25	10	7.16	6.24	0.5	1.21	0.24	25.5	61.8	12.7	100.0
	50	10	7.16	24.96	0.5	1.21	0.99	18.4	44.7	36.8	100.0
	25	15	6.62	7.40	0.75	1.12	0.29	34.6	51.7	13.7	100.0
	50	15	6.62	20.29	0.75	1.12	0.81	27.9	41.8	30.2	100.0
	25	20	6.79	6.15	1	1.15	0.24	41.7	48.0	10.3	100.0
	50	20	6.79	17.86	1	1.15	0.71	34.9	40.2	24.9	100.0

Table A.7-2 Values used for ternary plot of cyclic tests

	Load kN	Rate mm/min	Sample m/c %	δ mm	Q	F	L	NQ	NF	NL	Sum NQ+NF+NL
Dry	25	2.5	0.5	2.58	0.125	0.08	0.10	39.9	27.1	33.0	100.0
	50	2.5	0.5	4.01	0.125	0.08	0.16	33.8	22.9	43.3	100.0
	25	5	0.51	2.48	0.25	0.09	0.10	57.4	19.8	22.8	100.0
	50	5	0.51	4.37	0.25	0.09	0.17	48.9	16.9	34.2	100.0
	25	10	0.68	1.21	0.5	0.12	0.05	75.3	17.4	7.3	100.0
	50	10	0.68	2.30	0.5	0.12	0.09	70.7	16.3	13.0	100.0
	25	15	1.32	2.10	0.75	0.22	0.08	70.9	21.1	8.0	100.0
	50	15	1.32	3.60	0.75	0.22	0.14	67.1	20.0	12.9	100.0
	25	20	1.33	2.45	1	0.23	0.10	75.6	17.0	7.4	100.0
	50	20	1.33	4.00	1	0.23	0.16	72.2	16.3	11.6	100.0
OMC	25	2.5	5.86	6.38	0.125	0.99	0.26	9.1	72.3	18.6	100.0
	50	2.5	5.86	11.29	0.125	0.99	0.45	8.0	63.3	28.8	100.0
	25	5	5.7	6.67	0.25	0.97	0.27	16.9	65.2	18.0	100.0
	50	5	5.7	11.27	0.25	0.97	0.45	15.0	58.0	27.0	100.0
	25	10	5.69	7.40	0.5	0.96	0.30	28.4	54.8	16.8	100.0
	50	10	5.69	12.02	0.5	0.96	0.48	25.7	49.6	24.7	100.0
	25	15	5.71	6.41	0.75	0.97	0.26	38.0	49.0	13.0	100.0
	50	15	5.71	12.82	0.75	0.97	0.51	33.6	43.4	23.0	100.0
	25	20	5.74	6.79	1	0.97	0.27	44.6	43.3	12.1	100.0
	50	20	5.74	13.15	1	0.97	0.53	40.0	38.9	21.0	100.0
Saturated	25	2.5	6.71	7.67	0.125	1.14	0.31	8.0	72.5	19.5	100.0
	50	2.5	6.71	14.30	0.125	1.14	0.57	6.8	62.0	31.2	100.0
	25	5	6.31	9.08	0.25	1.07	0.36	14.9	63.6	21.6	100.0
	50	5	6.31	19.52	0.25	1.07	0.78	11.9	50.9	37.2	100.0
	25	10	6.51	8.76	0.5	1.10	0.35	25.6	56.5	17.9	100.0
	50	10	6.51	19.60	0.5	1.10	0.78	20.9	46.2	32.8	100.0
	25	15	7.27	10.71	0.75	1.23	0.43	31.1	51.1	17.8	100.0
	50	15	7.27	25.41	0.75	1.23	1.02	25.0	41.1	33.9	100.0
	25	20	6.7	6.77	1	1.14	0.27	41.6	47.2	11.3	100.0
	50	20	6.7	15.47	1	1.14	0.62	36.3	41.2	22.5	100.0

APPENDIX B.1 Frequency analysis and step time calculations

Table B.1-1 Frequency analysis output for different mesh densities

	Frequency (cycles/sec)		
Elastic Modulus (MPa)	Coarse Mesh	Medium Mesh	Fine Mesh
50	193.29	255.27	255.29
300	473.45	625.27	625.32
500	611.22	807.23	807.19

Table B.1-1 A typical calculation of steptime using the obtained frequencies

	Elastic Modulus (MPa)	Frequency using the equations obtained (cycles/sec)	Period (sec)	Step Time (s) = 10*period
Coarse Mesh	150	334.81	0.0030	0.0299
Medium Mesh	150	442.15	0.0023	0.0226
Fine Mesh	150	442.26	0.0023	0.0226

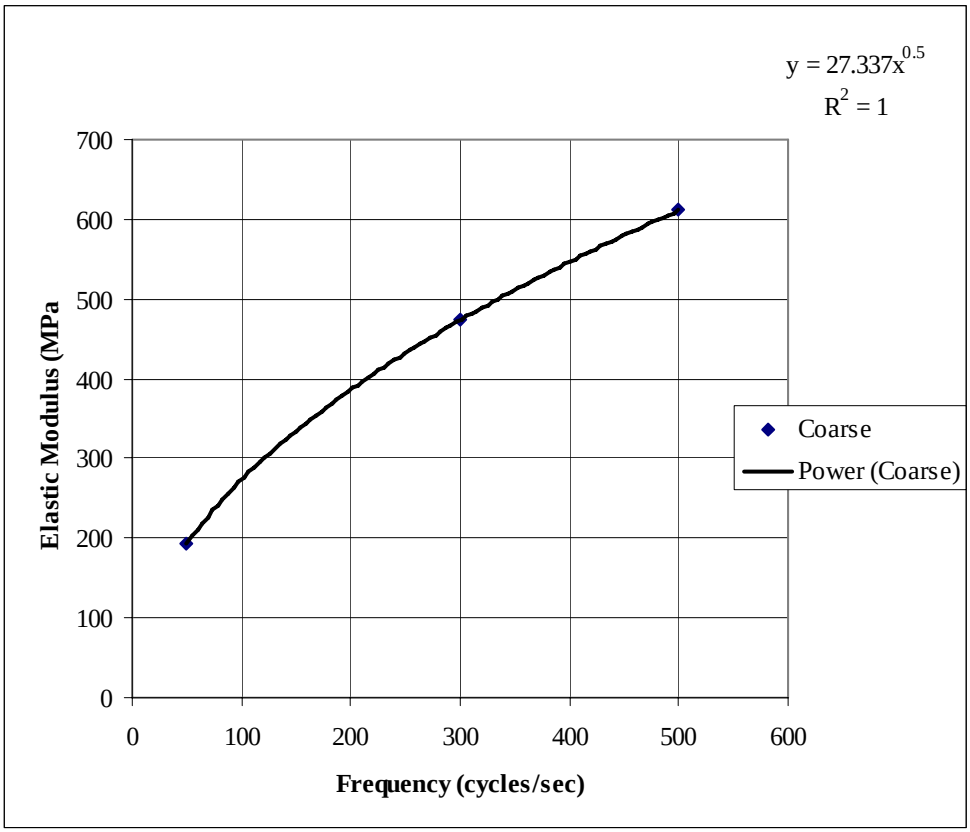

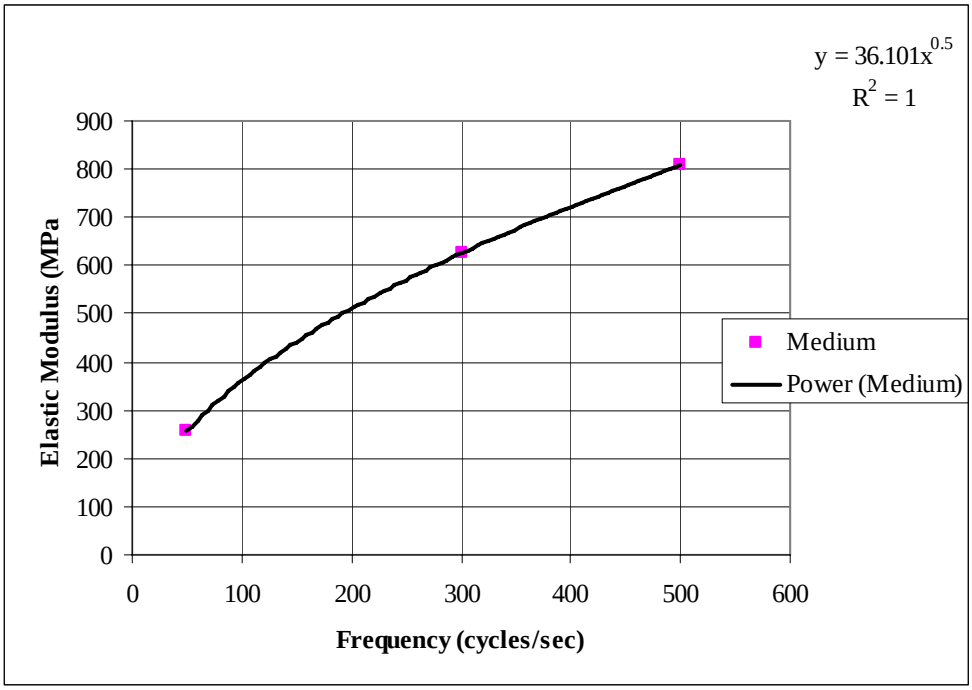
y = 36.101x^0.5
R^2 = 1
Elastic Modulus (MPa
900
800
700
600
500
400
300
200
100
0
0
100
200
300
400
500
600
Frequency (cycles/sec)
Medium
Power (Medium)

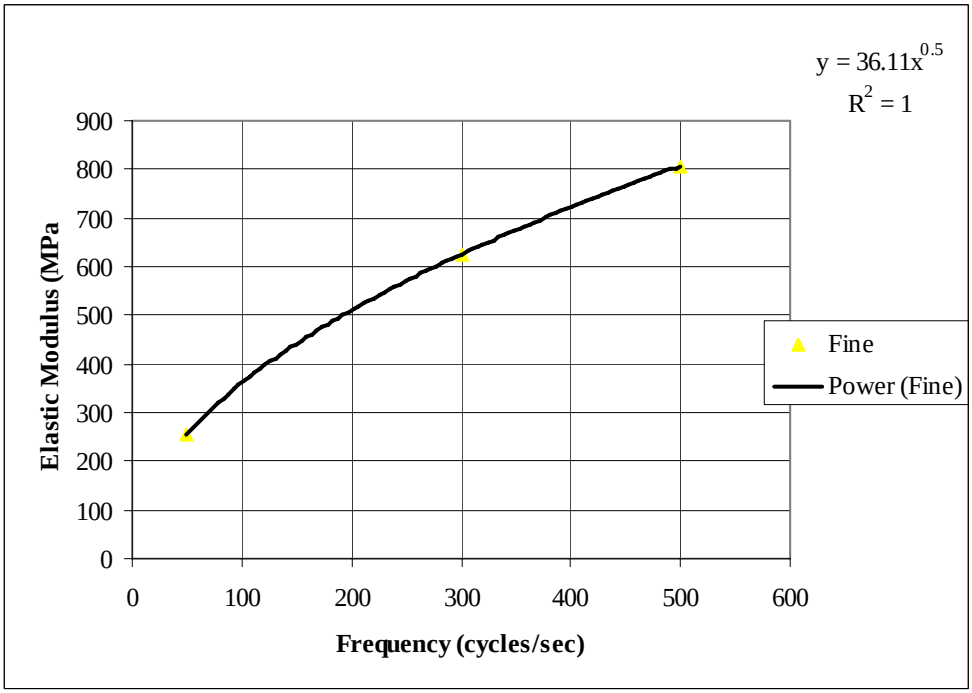
y = 36.11x^0.5
R^2 = 1
Elastic Modulus (MPa
900
800
700
600
500
400
300
200
100
0
0
100
200
300
400
500
600
Frequency (cycles/sec)
Fine
Power (Fine)

APPENDIX B.2 Mesh refinement of SCT FEM

Table B.2-1 Mesh refinement

*Elastic 250., 0.35			*Elastic 250., 0.35			*Elastic 250., 0.35		
*Dynamic, Explicit , 0.0231			*Dynamic, Explicit , 0.0175			*Dynamic, Explicit , 0.0175		
Penetration (mm)	Load (N)	Load (kN)	Penetration (mm)	Load (N)	Load (kN)	Penetration (mm)	Load (N)	Load (kN)
0	0	0	0	0	0	0	0	0
0.0011	14.9	0.014928	0.0010	15.6	0.015586	0.0010	4.3	0.004274
0.0034	43.3	0.043339	0.0034	47.6	0.047627	0.0033	47.9	0.04788
0.0086	100.3	0.10031	0.0080	121.6	0.121557	0.0078	206.4	0.206426
0.0159	171.8	0.171847	0.0150	196.2	0.19624	0.0152	92.5	0.092489
0.0264	266.4	0.26635	0.0258	289.4	0.28944	0.0259	299.6	0.299634
0.0435	429.0	0.428973	0.0414	444.2	0.444162	0.0407	449.3	0.449281
0.0628	603.4	0.603391	0.0611	658.8	0.658786	0.0605	651.8	0.651802
0.0870	824.9	0.824866	0.0860	876.7	0.876712	0.0852	712.5	0.712493
0.1166	1084.4	1.08439	0.1165	1165.6	1.16555	0.1161	1242.5	1.2425
0.1586	1447.2	1.44722	0.1532	1534.3	1.53425	0.1535	1633.2	1.63317
0.2014	1818.9	1.8189	0.1987	1907.1	1.90707	0.1972	1954.2	1.95422
0.2511	2233.7	2.23367	0.2494	2375.8	2.37581	0.2490	2581.3	2.58125
0.3080	2725.2	2.72516	0.3102	3165.3	3.16534	0.3088	3177.4	3.17737
0.3841	3372.9	3.37285	0.3767	3817.9	3.81793	0.3761	3844.3	3.84426
0.4581	3999.3	3.99926	0.4552	4541.0	4.54102	0.4533	4637.2	4.63716
0.5406	4705.2	4.70517	0.5393	5487.8	5.48779	0.5397	5524.7	5.52465
0.6480	5623.0	5.62295	0.6367	6512.3	6.51226	0.6346	6587.5	6.58751
0.7501	6513.6	6.51362	0.7445	7649.6	7.64958	0.7409	7537.1	7.53713
0.8616	7444.6	7.44461	0.8576	8744.9	8.74491	0.8561	8891.6	8.8916
0.9831	8446.3	8.44631	0.9864	9952.6	9.95256	0.9837	10287.0	10.287
1.1376	9782.0	9.78198	1.1266	11334.7	11.3347	1.1227	11610.6	11.6106
1.2808	10879.8	10.8798	1.2718	12874.5	12.8745	1.2710	13295.6	13.2956
1.4348	12204.6	12.2046	1.4350	14891.1	14.8911	1.4332	14936.9	14.9369
1.6284	13785.5	13.7855	1.6106	16959.8	16.9598	1.6076	16982.0	16.982
1.8062	15165.9	15.1659	1.7987	19063.6	19.0636	1.7917	19141.0	19.141

APPENDIX B.3 Typical ABAQUS/Explicit INPUT file & User Subroutine

ABAQUS/Explicit INPUT file

```
*Heading
** Job name: d-1 Model name: Model-1
*Preprint, echo=NO, model=NO, history=NO, contact=NO
**
** PARTS
**
*Part, name="Loading cylinder"
*End Part
*Part, name="Soil sample"
*End Part
**
** ASSEMBLY
**
*Assembly, name=Assembly
**
*Instance, name="Soil sample-1", part="Soil sample"
*Node
      1,         37.5,           0.
      2,         37.5,        88.75
      …          …             …
    595,        21.875,     11.09375
*Element, type=CAX4R
 1,   1,  19, 190,  46
 2,  19,  20, 191, 190
 ..   ..     ..      ..     ..
..   ..     ..      ..     ..
543, 594, 595,  39,  38
544, 595, 189,   4,  39
** Region: (SoilSample:Picked)
*Elset, elset=_PickedSet6, internal, generate
   1,  544,    1
** Section: SoilSample
*Solid Section, elset=_PickedSet6, material=RoadBase
1.,
*End Instance
**
*Instance, name="Loading cylinder-1", part="Loading cylinder"
          0.,        -22.5,           0.
*Node
      1,           0.,         800.,           0.
*Nset, nset="Loading cylinder-1-RefPt_", internal
1,
*Surface, type=SEGMENTS, name=Surf-1
START,          25.,         800.
 LINE,          25.,         210.
 CIRCL,          15.,         200.,          15.,         210.
 LINE,           0.,         200.
*Rigid Body, ref node="Loading cylinder-1-RefPt_", analytical
surface=Surf-1
*End Instance
**
```

```
*Nset, nset=Center, instance="Soil sample-1"
  10,  11,  14,  85,  86,  87,  88,  89,  90,  91, 118, 119, 120, 121,
122, 123
 124,
*Elset, elset=Center, instance="Soil sample-1"
 153, 154, 155, 156, 157, 158, 159, 160, 217, 218, 219, 220, 221, 222,
223, 224
*Nset, nset=End, instance="Soil sample-1"
  15,  16,  18, 141, 142, 143, 144, 145, 146, 147, 173, 174, 175, 176,
177, 178
 179,
*Elset, elset=End, instance="Soil sample-1"
 298, 308, 318, 328, 338, 348, 358, 368, 369, 379, 389, 399, 409, 419,
429, 439
*Nset, nset=N1, instance="Soil sample-1"
  12,  13,  14, 112, 113, 114, 115, 116, 117
*Elset, elset=N1, instance="Soil sample-1"
 161, 169, 177, 185, 200, 208, 216, 224
*Nset, nset=ALL, instance="Soil sample-1", generate
   1,  595,    1
*Elset, elset=ALL, instance="Soil sample-1", generate
   1,  544,    1
*Nset, nset=M1, instance="Soil sample-1"
 14,
*Nset, nset=Bot, instance="Soil sample-1"
   1,   4,   8,  11,  17,  18,  40,  41,  42,  43,  44,  45,  46,  92,
93,  94
 164, 165, 166, 167, 168, 169, 170, 171, 172, 180, 181, 182, 183, 184,
185, 186
 187, 188, 189
*Elset, elset=Bot, instance="Soil sample-1"
   1,   9,  17,  25,  33,  41,  49,  57, 129, 137, 145, 153, 439, 440,
441, 442
 443, 444, 445, 446, 447, 448, 456, 464, 472, 480, 488, 496, 504, 512,
520, 528
 536, 544
*Nset, nset=REF, instance="Loading cylinder-1"
 1,
*Nset, nset=N2, instance="Soil sample-1"
  12,  13, 112, 113, 114
*Elset, elset=N2, instance="Soil sample-1", generate
 161,  185,    8
*Elset, elset=_Surf-2_S4, internal, instance="Soil sample-1"
  65,  73,  81,  89,  97, 105, 113, 121, 161, 169, 177, 185
*Elset, elset=_Surf-2_S2, internal, instance="Soil sample-1", generate
 200,  288,    8
*Elset, elset=_Surf-2_S3, internal, instance="Soil sample-1", generate
 359,  368,    1
*Surface, type=ELEMENT, name=Surf-2
_Surf-2_S4, S4
_Surf-2_S2, S2
_Surf-2_S3, S3
*End Assembly
*
*Amplitude, name=Amp-1, definition=SMOOTH STEP
0., 0., 0.021214283, 1.
**
```

```
** MATERIALS
**
*Material, name=RoadBase
*Density
 2.4425e-09,
*Depvar
      7,
*User Material, constants=12
350.,  0.3,   0.2,   38.,  0.6,    0.01,  760., 0.9
0.1, 0.735, 370., 40
**
** INTERACTION PROPERTIES
**
*Surface Interaction, name=IntProp-1
*Friction
0.,
*Surface Behavior, pressure-overclosure=HARD
**
** BOUNDARY CONDITIONS
**
** Name: BC-1 Type: Symmetry/Antisymmetry/Encastre
*Boundary
Center, XSYMM
** Name: BC-2 Type: Displacement/Rotation
*Boundary
Bot, 2, 2
** Name: BC-3 Type: Displacement/Rotation
*Boundary
End, 1, 1
** Name: BC-4 Type: Displacement/Rotation
*Boundary
REF, 1, 1
REF, 2, 2
REF, 6, 6
** ----------------------------------------------------------------
**
** STEP: Step-1
**
*Step, name=Step-1
*Dynamic, Explicit
,0.021214283
*Bulk Viscosity
0.06, 1.2
**
** BOUNDARY CONDITIONS
**
** Name: BC-1 Type: Symmetry/Antisymmetry/Encastre
*Boundary, op=NEW
Center, XSYMM
** Name: BC-2 Type: Displacement/Rotation
*Boundary, op=NEW
Bot, 2, 2
** Name: BC-3 Type: Displacement/Rotation
*Boundary, op=NEW
End, 1, 1
** Name: BC-4 Type: Displacement/Rotation
*Boundary, op=NEW
REF, 1, 1
```

```
REF, 6, 6
** Name: BC-6 Type: Displacement/Rotation
*Boundary, op=NEW, amplitude=Amp-1
REF, 2, 2, -100.
*Adaptive Mesh Controls, name=Ada-1
1., 0., 0.
*Adaptive Mesh, elset=ALL, controls=Ada-1, initial mesh sweeps=100, mesh
sweeps=3, op=NEW
**
** INTERACTIONS
**
** Interaction: Int-1
*Contact Pair, interaction=IntProp-1, mechanical constraint=KINEMATIC,
cpset=Int-1
Surf-2, "Loading cylinder-1".Surf-1
**
** OUTPUT REQUESTS
**
*Restart, write, number interval=1, time marks=NO
*Print, etotal=YES, dmass=YES
*Monitor, dof=2, node=M1
**
** FIELD OUTPUT: F-Output-1
**
*Output, field, variable=PRESELECT
**
** HISTORY OUTPUT: H-Output-1
**
*Output, history, variable=PRESELECT
**
** HISTORY OUTPUT: H-Output-2
**
*Output, history
*Node Output, nset=N1
U2,
**
** HISTORY OUTPUT: H-Output-3
**
*Node Output, nset=REF
RF2,
*End Step
**
```

User subroutine VUMAT for axisymmetric conditions

For plane strain conditions, the relevant friction and dilation angles should be included.

```
C
C     User subroutine VUMAT
      subroutine vumat (
C     Read only - for definations of variables in program
     *     nblock, ndir, nshr, nstatev, nfieldv, nprops, lanneal,
     *     stepTime, totalTime, dt, cmname, coordMp, charLength,
     *     props, density, strainInc, relSpinInc,
     *     tempOld, stretchOld, defgradOld, fieldOld,
     *     stressOld, stateOld, enerInternOld, enerInelasOld,
     *     tempNew, stretchNew, defgradNew, fieldNew,
C     Write only - for update variables in program
     *     stressNew, stateNew, enerInternNew, enerInelasNew )
C
      include 'vaba_param.inc'
C
      dimension coordMp(nblock,*), charLength(nblock), props(nprops),
     1     density(nblock), strainInc(nblock,ndir+nshr),
     2     relSpinInc(nblock,nshr), tempOld(nblock),
     3     stretchOld(nblock,ndir+nshr),
     4     defgradOld(nblock,ndir+nshr+nshr),
     5     fieldOld(nblock,nfieldv), stressOld(nblock,ndir+nshr),
     6     stateOld(nblock,nstatev), enerInternOld(nblock),
     7     enerInelasOld(nblock), tempNew(nblock),
     8     stretchNew(nblock,ndir+nshr),
     9     defgradNew(nblock,ndir+nshr+nshr),
     1     fieldNew(nblock,nfieldv),
     2     stressNew(nblock,ndir+nshr), stateNew(nblock,nstatev),
     3     enerInternNew(nblock), enerInelasNew(nblock)
C
      character*80 cmname
      DIMENSION SP(3), sigNEW(nblock,4)
C
C     real*8 an,ppa,emax,vk,hard,dang,fang,coh,xnu,e0
      parameter ( zero = 0.d0, one = 1.d0, two = 2.d0,three = 3.d0,
     *     third = 1.d0 / 3.d0, half = 0.5d0, op5 = 1.5d0,
     *     two_thirds = 2.d0 /3.d0,threeHalfs = 1.5d0,six = 6.0d0,
     *     pi = 3.1415926d0,oety = 180.d0)
C
C     Under axisymmetric conditions the state variable is stored as:
C
C
C     User needs to input
C     props(1)    initial young's modulus, E0
C     props(2)    Poisson's ratio
C     props(3)    Cohesion
C     props(4)    Friction angle (Minimum)
C     props(5)    Dilation angle
C     props(6)Slope of the uniaxial yield stress versus plastic strain
      curve
C     props(7)    Material constant,Ka
C     props(8)    Material constant Rf
C     props(9)    Atmospheric pressure, Pa
C     props(10)   Power n of E formulation
```

```
C     props(11)   Maximum E
C     props(12)   Maximum Friction Angle
C
      e0    = props(1)
      xnu   = props(2)
      coh   = props(3)
      phi0  = props(4)
      dang  = props(5)
      hard  = props(6)
      vk    = props(7)
      rf    = props(8)
      ppa   = props(9)
      an    = props(10)
      emax  = props(11)
      phiMX = props(12)

C     If steptime equals to zero, assume the material as pure elastic and
      use inital elastic modulus

      twomu  = e0 / ( one + xnu )
      alamda = xnu * twomu / ( one - two * xnu )
      thremu = op5 * twomu
      bulk   = alamda + twomu/three

      if (stepTime .eq. zero) Then
C

      do i = 1, nblock
      trace = strainInc(i,1) + strainInc(i,2) + strainInc(i,3)
C
      stressNew(i,1) = stressOld(i,1)
     *                 + twomu * strainInc(i,1) + alamda * trace
C
      stressNew(i,2) = stressOld(i,2)
     *                 + twomu * strainInc(i,2) + alamda * trace
C
      stressNew(i,3) = stressOld(i,3)
     *                 + twomu * strainInc(i,3) + alamda * trace
C
      stressNew(i,4) = stressOld(i,4) + twomu * strainInc(i,4)
C
      sigNEW(i,1) = stressNew(i,1)
C
      sigNEW(i,2) = stressNew(i,2)
C
      sigNEW(i,3) = stressNew(i,3)
C
      sigNEW(i,4) = stressNew(i,4)
C
      end do

      else

      do i = 1, nblock
C
C
C
```

```
C     Plasticity Calculations in Block Form
C
C     Defination of material stiffness
C
C**** DI1, DI2 and DI3 stand for the first invariant of stresses

      DI1 = sigNEW(i,1) + sigNEW(i,2) + sigNEW(i,3)
      DI2 = sigNEW(i,1) * sigNEW(i,2) + sigNEW(i,1) *
     *      sigNEW(i,3) + sigNEW(i,2) * sigNEW(i,3) - sigNEW(i,4)**2
      DI3 = sigNEW(i,1) * sigNEW(i,2) * sigNEW(i,3) -
      1sigNEW(i,3) * sigNEW(i,4)**2
      R = (1.0 / 3.0) * DI1**2 - DI2
      T = SQRT(1.0 / 27.0 * R**3)
      Q = (1.0 / 3.0) * DI1 * DI2 - DI3 - (2.0 / 27.0) * DI1**3
      ST= SQRT(1.0/3.0*R)
      ALPHA = ACOS(-Q / (2.0 * T))
C
C**** The array SP() stands for three principal stresses: SP(1) > SP(2) >
SP(3)
      SP(1) = 2.0 * ST * COS( ALPHA / 3.0) + 1.0 / 3.0 * DI1
      SP(2) = 2.0 * ST * COS((ALPHA / 3.0) + 2.0944) + 1.0 / 3.0 * DI1
      SP(3) = 2.0 * ST * COS((ALPHA / 3.0) + 4.1888) + 1.0 / 3.0 * DI1
C
C**** Sort the principal stresses
      DO 50 II = 1, 2
      DO 40 JJ = II, 3
      IF(abs(SP(II)) .LT. abs(SP(JJ)))GO TO 30
      GO TO 40
30    TEMP = SP(II)
      SP(II) = SP(JJ)
      SP(JJ) = TEMP
40    CONTINUE
50    CONTINUE
C
C****
C
      des   = abs(SP(1)) - abs(SP(3))
      if (des .gt. zero.and. abs(sp(1)) .gt. zero ) then
      ve1   = vk * ppa
      ve2   = abs(SP(3)) / ppa
      va1   = an * log(ve2)
      va2   = exp(va1)
      ve0   = abs(ve1 * va2)
      fang = phi0
      fang  = 1.6*((abs(SP(1))/abs(SP(3))))+27.
111   Format (6f12.4//)
      If (fang.le.phi0) fang = phi0
      If (fang.gt.phi0.and.fang.le.phiMX) fang = fang
      If (fang.gt.phiMX) fang = phiMX
      etop  = rf * (one - sin(fang))
      ebot  =two*coh * cos(fang) + two *abs(SP(3))*sin(fang)
      ve    = ve0 * (one - etop * des / ebot)**2
      if (ve .gt. e0 .and. ve .le. emax) e = ve
      if (ve .gt. emax) e = emax
      if (ve .le. e0) e = e0
      else
      e = e0
      end if
```

```
C
      twomu  = e / ( one + xnu )
      alamda = xnu * twomu / ( one - two * xnu )
      thremu = op5 * twomu
      bulk   = alamda + twomu/three
C
C
      trace = strainInc(i,1) + strainInc(i,2) + strainInc(i,3)
C
      s11 = stressOld(i,1)
     *      + twomu * strainInc(i,1) + alamda * trace
C
      s22 = stressOld(i,2)
     *      + twomu * strainInc(i,2) + alamda * trace
C
      s33 = stressOld(i,3)
     *      + twomu * strainInc(i,3) + alamda * trace
C
      s12 = stressOld(i,4) + twomu * strainInc(i,4)
C
C
C     Deviatoric part of trial stress measured from the back stress
C
      smean = third*(s11+s22+s33)
C
      ds1 = s11 - smean
      ds2 = s22 - smean
      ds3 = s33 - smean
C
C
      varj2 = sqrt(one/two*(ds1**2 + ds2**2 + ds3**2
     *            + two*s12**2))
C
C
C     Check for yield by determining the factor for plasticity,
C     Zero for elastic, one for yield
C     Drucker Prager yield surface
C
      agl   = fang*pi/oety
      alf   = two*sin(agl)/(sqrt(three)*(three -sin(agl)))
      hardk = three*two*coh*cos(agl)/(sqrt(three)*(three-sin(agl)))
C
C
      vari1  = alf*(s11 + s22 + s33)
C
      surf = vari1 + varj2 - hardk
C
      facyld = zero


      if (surf.gt. zero) then
      facyld = one
      aglb  = dang*pi/oety
      alfd   = two*sin(aglb)/(sqrt(three)*(three -sin(aglb)))
      endif
C
C
```

```
C
C     1. Update the stress
C
      varj2 = varj2 + one - facyld

      efs = sqrt(three)*(alf*three*smean + varj2)/(one+sqrt(three)*alf)

      efk = (one + sqrt(three)*alf)*efs/sqrt(three)

      ehh1 = (alfd*(three*smean) + varj2)/(three*efk)
      ehh2 = (one + sqrt(three)*alf)**2

      hh = half*twomu + three*three*bulk*alf*alfd
     *     +ehh1*ehh2*hard
      ft1 = facyld/hh
      ft2 = half*twomu/varj2
      ftd = three*bulk*alfd
      ftf = three*bulk*alf
C
      stressNew(i,1) = s11 - ft1*((ftd + ft2*ds1)*(ftf + ft2*ds1)
     *                           *strainInc(i,1)
     *                      +(ftd + ft2*ds1)
.....*.....................
      stressNew(i,2) = s22 - ft1*((ftd + ft2*ds2)*(ftf + ft2*ds2)
     *                         *strainInc(i,2)
     *                      +(ftd + ft2*ds2)
.....*.....................

      stressNew(i,3) = s33 - ft1*((ftd + ft2*ds3)*(ftf + ft2*ds3)
     *                           *strainInc(i,3)
     *                      +(ftd + ft2*ds3)
.....*.....................

      stressNew(i,4) = s12 - ft1*((ft2*s12)**2*strainInc(i,4)
     *                      +(ft2*s12)*(ftf + ft2*ds1)
.....*.....................
C
      sigNEW(i,1) = stressNew(i,1)
      sigNEW(i,2) = stressNew(i,2)
      sigNEW(i,3) = stressNew(i,3)
      sigNEW(i,4) = stressNew(i,4)
C
C     2. Update the plastic strain variable
C
      cont1 = one/(two*varj2)
C
      ep11 = (alfd + cont1*ds1)*ft1
     *                        *((ft2*ds1 + ftf)*strainInc(i,1)
     *                          +(ft2*ds2 + ftf)*strainInc(i,2)
.....*.....................
      ep22 = (alfd + cont1*ds2)*ft1
     *                        *((ft2*ds1 + ftf)*strainInc(i,1)
     *                          +(ft2*ds2 + ftf)*strainInc(i,2)
.....*.....................
            ep33 = (alfd + cont1*ds3)*ft1
     *                        *((ft2*ds1 + ftf)*strainInc(i,1)
     *                          +(ft2*ds2 + ftf)*strainInc(i,2)
```

```
      ep12 = (cont1*s12)*ft1
     *                          *((ft2*ds1 + ftf)*strainInc(i,1)
     *                            +(ft2*ds2 + ftf)*strainInc(i,2)
.....*.......................
C
C    3. Update the specific internal energy
C
C
      stressPower = half*((stressOld(i,1)
     *              + stressNew(i,1))*strainInc(i,1)
     *              + (stressOld(i,2) + stressNew(i,2))*strainInc(i,2)
     *              + (stressOld(i,3) + stressNew(i,3))*strainInc(i,3))
     *              + (stressOld(i,4) + stressNew(i,4))*strainInc(i,4)
      enerInternNew(i) = enerInternOld(i)
     *                   + stressPower/density(i)
C
C    4. Update the dissipated inelastic specific energy
C
C
      plasticWorkInc = s11*ep11 + s22*ep22 + s33*ep33 + two*s12*ep12
C
      enerInelasNew(i) = enerInelasOld(i)
     *                   + plasticWorkInc/density(i)
C
C


      end do

      end if
C
      return
      end
C
C
```

APPENDIX B.4 Sensitivity of modelling parameters in SCT FEM

Table B.4-1 Effect of step time

Step time =10*period			**Step time =50*period**			**Step time =100*period**		
*User Material, constants=12 100., 0.35, 0.5, 35., 8.0, 0.5, 970., 0.8 0.1, 0.65, 300.,38.			*User Material, constants=12 100., 0.3, 0.5, 40., 8., 0.5, 970., 0.8 0.1, 0.65, 300.,60.			*User Material, constants=12 100., 0.3, 0.5, 40., 8., 0.5, 970., 0.8 0.1, 0.65, 300.,60.		
*Dynamic, Explicit , 0.0218			*Dynamic, Explicit , 0.109			*Dynamic, Explicit , 0.218		
Penetration (mm)	Load (N)	Load (kN)	Penetration (mm)	Load (N)	Load (kN)	Penetration (mm)	Load (N)	Load (kN)
0	0	0	0	0	0	0	0	0
0.001096	9.53052	0.009531	0.000998	4.13356	0.004134	0.001052	5.17041	0.00517
0.003377	21.927	0.021927	0.003378	13.0664	0.013066	0.0033	23.8634	0.023863
0.007898	44.2043	0.044204	0.007814	41.6825	0.041683	0.00775	36.3538	0.036354
0.015528	89.8267	0.089827	0.015077	54.2241	0.054224	0.015129	42.9056	0.042906
0.026392	123.146	0.123146	0.025888	91.9842	0.091984	0.025863	90.3373	0.090337
0.040796	218.512	0.218512	0.040719	144.187	0.144187	0.040756	128.378	0.128378
0.060266	262.147	0.262147	0.060372	213.019	0.213019	0.060317	210.399	0.210399
0.086206	380.666	0.380666	0.085229	295.038	0.295038	0.085197	296.632	0.296632
0.116358	489.792	0.489792	0.115991	403.949	0.403949	0.115898	396.875	0.396875
0.153345	630.304	0.630304	0.1531	543.645	0.543645	0.153114	532.262	0.532262
0.198023	826.197	0.826197	0.197427	704.904	0.704904	0.197082	699.685	0.699685
0.249597	1031.38	1.03138	0.248635	943.624	0.943624	0.248573	927.537	0.927537
0.309717	1364.01	1.36401	0.308076	1169.72	1.16972	0.308044	1191.3	1.1913
0.377771	1601.38	1.60138	0.376008	1444.38	1.44438	0.375976	1459.35	1.45935
0.452722	1936.81	1.93681	0.453218	1764.15	1.76415	0.452689	1761.96	1.76196
0.53927	2331.91	2.33191	0.538644	2143.62	2.14362	0.53865	2127.41	2.12741
0.637293	2786.34	2.78634	0.634225	2477.7	2.4777	0.6342	2492.1	2.4921
0.740442	3168.85	3.16885	0.740289	2895.47	2.89547	0.739929	2941.83	2.94183
0.857935	3659.19	3.65919	0.856683	3463.24	3.46324	0.856361	3411.44	3.41144

Table B.4-2 Kinetic and internal energy histories

Step time =10*period				**Step time =50*period**				**Step time =100*period**			
*User Material, constants=12				*User Material, constants=12				*User Material, constants=12			
100., 0.35, 0.5, 35., 8, 0.5, 970., 0.8 0.1, 0.65, 300.,38.				100., 0.3, 0.5, 40., 8., 0.5, 970., 0.8 0.1, 0.65, 300.,60.				100., 0.3, 0.5, 40., 8., 0.5, 970., 0.8 0.1, 0.65, 300.,60.			
*Dynamic, Explicit , 0.0218				*Dynamic, Explicit , 0.109				*Dynamic, Explicit , 0.218			
Time (s)	Internal Energy, IE (kJ)	Kinetic Energy, KE (kJ)	KE/IE (%)	Time (s)	Internal Energy, IE (kJ)	Kinetic Energy, KE (kJ)	KE/IE (%)	Time (s)	Internal Energy, IE (kJ)	Kinetic Energy, KE (kJ)	KE/IE (%)
0	0	0	0	0	0	0	0	0	0	0	0
0.0001	1E-10	1E-10	122.776	0.000548	2E-10	1E-10	75.21668	0.001091	2E-10	2E-10	96.27046
0.0002	3E-09	1E-09	43.951	0.001095	2E-09	4E-10	17.86657	0.002182	2E-09	4E-10	21.15783
0.0003	3E-08	1E-08	41.700	0.00164	2E-08	2E-09	11.46586	0.003274	2E-08	7E-10	3.891411
0.0004	1E-07	5E-08	32.235	0.002184	1E-07	8E-09	7.256061	0.004365	1E-07	2E-09	1.98363
0.0006	5E-07	1E-07	25.471	0.002727	4E-07	2E-08	4.934262	0.005453	4E-07	5E-09	1.30688
0.0007	1E-06	3E-07	22.085	0.003274	1E-06	4E-08	3.198176	0.006543	1E-06	1E-08	0.822019
0.0008	3E-06	6E-07	18.606	0.003816	3E-06	7E-08	2.359923	0.007634	3E-06	2E-08	0.677967
0.0009	7E-06	1E-06	16.561	0.004363	6E-06	1E-07	1.856276	0.008723	6E-06	3E-08	0.474558
0.0010	1E-05	2E-06	14.356	0.004907	1E-05	2E-07	1.500043	0.009814	1E-05	5E-08	0.368361
0.0011	3E-05	3E-06	13.027	0.005452	2E-05	3E-07	1.181956	0.010902	2E-05	7E-08	0.307224
0.0012	5E-05	5E-06	11.978	0.005997	4E-05	4E-07	0.956277	0.011994	4E-05	1E-07	0.239311
0.0013	7E-05	8E-06	11.133	0.006544	7E-05	6E-07	0.901467	0.01308	7E-05	2E-07	0.260939
0.0014	1E-04	1E-05	10.950	0.007086	1E-04	1E-06	0.991986	0.01417	1E-04	3E-07	0.278681
0.0015	2E-04	2E-05	11.405	0.007631	2E-04	2E-06	0.978881	0.01526	2E-04	3E-07	0.171718
0.0016	3E-04	3E-05	11.470	0.008176	3E-04	2E-06	0.696224	0.016352	3E-04	5E-07	0.192062
0.0017	4E-04	4E-05	11.010	0.008724	4E-04	2E-06	0.503955	0.017442	4E-04	5E-07	0.133352
0.0019	6E-04	6E-05	10.456	0.009266	6E-04	2E-06	0.448049	0.018532	6E-04	7E-07	0.125958
0.0020	8E-04	8E-05	9.817	0.00981	8E-04	4E-06	0.450586	0.01962	8E-04	8E-07	0.105533
0.0021	1E-03	1E-04	9.192	0.010357	1E-03	4E-06	0.3946	0.020711	1E-03	9E-07	0.085597
0.0022	1E-03	1E-04	8.462	0.010903	1E-03	4E-06	0.278379	0.021803	1E-03	1E-06	0.075141
0.0023	2E-03	2E-04	7.725	0.011447	2E-03	4E-06	0.212763	0.022892	2E-03	1E-06	0.0574
0.0024	3E-03	2E-04	6.968	0.011991	3E-03	6E-06	0.239681	0.023982	3E-03	2E-06	0.078064
0.0025	3E-03	2E-04	6.501	0.012535	3E-03	1E-05	0.328691	0.02507	3E-03	2E-06	0.075181
0.0026	4E-03	3E-04	6.094	0.013083	4E-03	1E-05	0.293672	0.026163	4E-03	3E-06	0.059326

APPENDIX C.1 Density and saturation calculations-triaxial samples

Table C.1-1 Density and saturation of triaxial test samples

Penetration Rate (mm/min)	**2.5**			**5**		
Sample No	**S1**	**S2**	**S3**	**S4**	**S5**	**S6**
During Sample Preparation						
Mould+Base (g)	7236	7236.4	7238.2	7235.6	7236.4	7232.3
M+B+Wet Sample (g)	11267.9	11291.5	11265	11286.4	11277.4	11245.4
Wt of moist Sample (g)	4031.9	4055.1	4026.8	4050.8	4041	4013.1
Density kg/m3	2479.0	2493.3	2475.9	2490.6	2484.6	2467.5
Water content of the compacted sample %	5.86	5.84	5.14	5.86	5.97	5.08
During Triaxial testing						
Wt before saturation (g)	3902.9	3933.9	3828	3915.2	3898.4	3837.2
Wt of Saturated Sample (g)	4041.0	4077	4018.3	4075	4037.1	4026
Wet density of saturated sample kg/m3	2484.6	2506.8	2470.7	2505.5	2482.2	2475.4
Wt of Dry Sample (g)	3808.6	3831.3	3830	3826.4	3813.2	3819
Dry Density kg/m3	2353.3	2355.7	2354.9	2352.7	2344.6	2348.1
Water content after saturation %	6.10	6.41	4.92	6.50	5.87	5.42
Water content after saturation	0.06	0.06	0.05	0.06	0.06	0.05
Void ratio $e = Gs(1+w)\rho_w/\rho-1$	0.1770	0.1737	0.1653	0.1759	0.1718	0.1749
Porosity $n=e/(1+e)$	0.1504	0.1480	0.1419	0.1496	0.1466	0.1489
Degree of saturation $Sr=wGs/e$	0.9481	1.0153	0.8178	1.0159	0.9399	0.8522
Air content $n(1-Sr)$	0.0078	-	0.0258	-	0.0088	0.0220
Penetration Rate (mm/min)	**10**			**15**		
Sample No	**S7**	**S8**	**S9**	**S10**	**S11**	**S12**
During Sample Preparation						
Mould+Base (g)	7236.4	7236.7	7235	7235.2	7234.7	7232
M+B+Wet Sample (g)	11289.3	11298.2	11247	11293.0	11293.1	11233.3
Wt of moist sample (g)	4052.9	4061.5	4012	4057.8	4058.4	4001.3
Density kg/m3	2491.9	2497.2	2466.8	2495.0	2495.3	2460.2
Water content of the compacted sample %	5.94	5.93	5.34	5.99	6.04	5.46
During Triaxial testing						
Wt before saturation (g)	3938.5	3935.3	3834.0	3927.8	3901.5	3830.0
Wt of Saturated Sample (g)	4057.6	4043	4035.1	4101.6	4048.7	3994.8
Wet density of saturated sample kg/m3	2494.8	2485.9	2481.0	2521.9	2489.4	2456.2
Wt of Dry Sample (g)	3825.5	3834.1	3808.6	3828.6	3827.3	3794
Dry Density kg/m3	2352.1	2357.4	2341.7	2354.0	2353.2	2332.8
Water content after saturation %	6.07	5.45	5.95	7.13	5.78	5.29
Water content after saturation	0.06	0.05	0.06	0.07	0.06	0.05
Void ratio $e = Gs(1+w)\rho_w/\rho-1$	0.1705	0.1612	0.1811	0.1808	0.1658	0.1769
Porosity $n=e/(1+e)$	0.1457	0.1388	0.1533	0.1531	0.1422	0.1503
Degree of saturation $Sr=wGs/e$	0.9785	0.9294	0.9030	1.0844	0.9594	0.8225
Air content $n(1-Sr)$	0.0031	0.0098	0.0149	-	0.0058	0.0267

Note: *The errors in experimental measurements may have caused degree of saturation more than 100%.*

Table C.1-1 Density and saturation of triaxial test samples (contd..)

Penetration Rate (mm/min)	**20**		**2.5**	
Sample No	**S13**	**S14**	**S15**	**S16**
During Sample Preparation				
Mould+Base (g)	7233.6	7233.5	7232	7228
M+B+Wet Sample (g)	11299.2	11286.5	11247	11243.1
Wt of moist sample (g)	4065.6	4053	4009	4010
Density kg/m3	2499.7	2492.0	2464.9	2465.6
Water content of the compacted sample %	7.70	6.03	6.49	4.86
During Triaxial testing				
Wt before saturation (g)	3919.4	3906.3	3819.3	4002.3
Wt of Saturated Sample (g)	4046.5	4076.3	3981.3	4074
Wet density of saturated sample kg/m3	2488.0	2506.3	2447.9	2504.9
Wt of Dry Sample (g)	3774.8	3822.4	3764.8	3824
Dry Density kg/m3	2320.9	2350.2	2314.8	2351.2
Water content after saturation %	7.20	6.64	5.75	6.54
Water content after saturation	0.07	0.07	0.06	0.07
Void ratio $e = Gs(1+w)\rho_w/\rho-1$	0.1793	0.1768	0.1798	0.1883
Porosity $n=e/(1+e)$	0.1520	0.1503	0.1524	0.1585
Degree of saturation $Sr=wGs/e$	1.1040	1.0330	0.8795	0.9549
Air content $n(1-Sr)$	-	-	0.0184	0.0072

Note: *The errors in experimental measurements may have caused degree of saturation more than 100%.*

APPENDIX C.2 Triaxial test data sheets

Table C.2 -l Triaxial test data (2.5mm/min)

Confining Pressures 100kPa, 375kPa and 750kPa								
S1 (2.5mm/min)			**S2 (2.5mm/min)**			**S3 (2.5mm/min)**		
Axial stress (kN/m2)	Axial strain (ε) ΔL/L0	Cell Pressure (kPa)	Axial stress (kN/m2)	Axial strain (ε) ΔL/L0	Cell Pressure (kPa)	Axial stress (kN/m2)	Axial strain (ε) ΔL/L0	Cell Pressure (kPa)
0.0	0.0000	99.2	0.0	0.0000	100.9	0.0	0.0000	99.8
74.8	0.0008	99.2	36.0	0.0004	100.9	12.2	0.0002	99.8
99.5	0.0010	99.2	63.2	0.0007	100.8	37.8	0.0005	99.8
126.0	0.0013	99.1	100.5	0.0011	100.7	60.9	0.0008	99.7
153.5	0.0016	99.1	135.7	0.0015	100.9	81.6	0.0011	99.7
182.1	0.0019	99.2	166.5	0.0018	100.8	102.9	0.0014	99.7
212.1	0.0022	99.1	197.6	0.0021	100.9	126.1	0.0017	99.7
243.2	0.0024	99.1	228.7	0.0025	100.8	149.2	0.0020	99.8
275.0	0.0028	99.2	257.2	0.0028	100.9	173.6	0.0023	99.8
308.2	0.0032	99.2	288.6	0.0031	100.7	196.1	0.0026	99.7
342.1	0.0036	99.1	319.6	0.0035	100.7	218.6	0.0029	99.7
377.5	0.0040	99.1	351.3	0.0039	100.8	236.4	0.0032	99.7
413.5	0.0044	99.1	384.4	0.0043	100.5	258.8	0.0036	99.7
450.9	0.0048	99.1	418.3	0.0047	100.5	280.6	0.0039	99.6
488.0	0.0052	99.2	452.8	0.0051	100.7	303.1	0.0042	99.7
526.5	0.0056	99.2	487.3	0.0055	100.8	327.3	0.0045	99.6
566.7	0.0060	99.2	522.8	0.0059	100.3	352.3	0.0049	99.7
606.9	0.0064	99.1	560.5	0.0063	100.1	378.7	0.0053	99.6
647.1	0.0068	99.1	596.8	0.0067	100.9	407.6	0.0056	99.6
688.0	0.0071	99.2	635.5	0.0071	100.6	436.2	0.0060	99.6
728.4	0.0076	99.2	673.8	0.0075	100.1	465.1	0.0063	99.6
770.3	0.0080	99.2	712.1	0.0079	100.3	493.9	0.0067	99.6

APPENDIX C.3 Modulus, cohesion, friction angle obtained from triaxial tests

Table C.3 -1 Modulus of the capping layer material

Confining Pressures 100kPa, 375kPa and 750kPa - Tests S1-S15

Confining Pressures 1000 and 2000kPa - Test S16

Rate (mm/min)	Confining Pressure (kPa)	Modulus (MPa)				
		S1	**S2**	**S3**	**Average**	**S16**
2.5	100	98	92	74	88	-
	375	305	296	179	260	
	750	391	399	291	360	
	1000	-	-	-	-	479
	2000	-	-	-	-	589
		S4	**S5**	**S6**		
5.0	100	73	82	161	106	
	375	235	244	370	283	
	750	380	364	497	414	
		S7	**S8**	**S9**		
10.0	100	86	101	144	111	
	375	225	252	321	266	
	750	348	399	430	392	
		S10	**S11**	**S12**		
15.0	100	133	110	133	125	
	375	295	256	295	282	
	750	384	348	384	372	
		S13	**S14**	**S15**		
20.0	100	96	99	139	112	
	375	250	262	255	256	
	750	355	383	360	366	

Table C.3 -2 Average modulus from the tests

Rate (mm/min)	Confining Pressure (kPa)	Modulus (MPa)	
		S1-S15	**S16**
2.5-20.0	100-750	**108**	-
		269	
		381	
2.5	1000 -2000	-	**479**
			589

Table C.3 -3 Calibration of *K* and *n*

Reference pressure p_a = 100kPa

Confining Pressure P (kPa)	P/p_a	Modulus (MPa)
100	1	88
375	3.75	260
750	7.5	360
1000	10	479
2000	20	589

Table C.3 -4 Cohesion of the capping layer material

Confining Pressures 100kPa, 375kPa and 750kPa - Tests S1-S15

Confining Pressures 1000 and 2000kPa - Test S16

Rate (mm/min)	Confining Pressure (kPa)	Cohesion (MPa)			
		S1	**S2**	**S3**	**Average**
2.5	100-750	278	288	222	263
	1000-2000				534
		S4	**S5**	**S6**	
5.0	100-750	283	282	405	323
		S7	**S8**	**S9**	
10.0	100-750	380	321	368	356
		S10	**S11**	**S12**	
15.0	100-750	242	369	335	315
		S13	**S14**	**S15**	
20.0	100-750	405	380	387	391

Table C.3 -5 Average cohesion from the tests

Rate (mm/min)	Confining Pressure (kPa)	Modulus (MPa)	
		S1-S15	S16
2.5-20.0	100-750	**330**	-
2.5	1000 -2000	**-**	**534**

Table C.3 -6 Friction angle of the capping layer material

Confining Pressures 100kPa, 375kPa and 750kPa - Tests S1-S15

Confining Pressures 1000 and 2000kPa - Test S16

Rate (mm/min)	Confining Pressure (kPa)	Friction Angle (^{0})			
		S1	S2	S3	Average
2.5	100-750	40	39	36	38
	1000-2000				36
		S4	**S5**	**S6**	
5.0	100-750	39	39	43	40
		S7	**S8**	**S9**	
10.0	100-750	38	38	39	38
		S10	**S11**	**S12**	
15.0	100-750	37	38	38	38
		S13	**S14**	**S15**	
20.0	100-750	42	38	37	39

Table C.3 -7 Average friction angle from the tests

Rate (mm/min)	Confining Pressure (kPa)	Modulus (MPa)	
		S1-S15	**S16**
2.5-20.0	100-750	**39**	-
2.5	1000 -2000	**-**	**36**

APPENDIX C.4 Uniaxial test data sheets

Table C.4 -1 Uniaxial test data-OMC samples
Unconfined test

Test1 (0.5mm/min)		**Test2 (0.5mm/min)**	
Axial stress (kN/m2)	Axial strain (ε) ΔL/L0	Axial stress (kN/m2)	Axial strain (ε) ΔL/L0
0	0	0	0
15.475864	0.0004414	0.853565	7.98873E-05
16.769605	0.0004963	1.7583351	0.000158118
18.352666	0.0005613	2.6629629	0.000236343
19.679745	0.0006245	3.5503886	0.000312902
20.844711	0.0006861	4.4376776	0.000389466
21.984237	0.0007427	5.3588965	0.00047102
23.166271	0.0007993	6.2715482	0.000547583
24.476074	0.0008559	7.2437974	0.000627475
25.904685	0.0009191	8.2074853	0.000702373
27.367534	0.0009774	9.2050159	0.000783926
29.051329	0.0010439	10.193938	0.000862157
30.658509	0.0011055	11.199898	0.000937054
32.341411	0.0011788	12.205652	0.001013618
33.990436	0.0012453	13.245313	0.001093505
35.672855	0.0013186	14.267836	0.001170069
37.338469	0.0013851	15.273177	0.001244966
38.978168	0.0014534	16.329552	0.001321529
40.702599	0.0015249	17.436944	0.001399755
42.27367	0.0015932	18.330798	0.001474652
44.091205	0.0016664	19.199161	0.001542892

APPENDIX C.5 Density, saturation, initial modulus and hardening modulus-uniaxial samples

Table C.5-1 Density and saturation - uniaxial test samples

Penetration Rate (mm/min)	0.5	
Sample No	Test1	Test2
During Sample Preparation		
Mould+Base (g)	7231	7229
M+B+Wet Sample (g)	11244	11226
Wt of moist Sample (g)	4013	3997
Density of Sample kg/m3	2467.4	2457.6
Container No	**112**	**211**
Wt of the container (g)	37.8	35.9
Wt of wet sample + container (g)	121.4	132.343
Wt of dry sample + container (g)	117.0	127.1
Water content of the compacted sample %	5.57	5.70

Table C.5-2 Initial and Hardening Moduli

Penetration Rate (mm/min)	0.5		
Sample No	Test1	Test2	Average
Initial modulus (MPa)	27	22	25
Hardening modulus (MPa)	310	229	270

APPENDIX C.6 Establishing lower and upper boundaries of SCT data

Table C.6-1 Establishing suitable ranges for Modulus keeping a constant friction angle, ϕ

30<E<50MPa, ϕ=20^0			**30<E<50MPa, ϕ=30^0**		
*User Material, constants=12 30., 0.35, 0.0001, 20., 0., 0.3, 970., 0.8 0.1, 0.65, 50., 20.			*User Material, constants=12 30., 0.35, 0.0001, 30., 0., 0.3, 970., 0.8 0.1, 0.65, 50., 30.		
*Dynamic, Explicit , 0.0448			*Dynamic, Explicit , 0.0448		
Penetration (mm)	Load (N)	Load (kN)	Penetration (mm)	Load (N)	Load (kN)
0.00E+00	0	0	0.00E+00	0	0
9.97E-04	2.04136	0.002041	0.0009929	2.05261	0.002053
0.0034419	4.67289	0.004673	0.0034343	5.83696	0.005837
0.0078931	13.9149	0.013915	0.0078913	11.5646	0.011565
0.0150982	13.8739	0.013874	0.0153317	20.015	0.020015
0.0262066	24.3171	0.024317	0.0261419	30.3359	0.030336
0.040794	28.5376	0.028538	0.0409124	56.2291	0.056229
0.0608746	42.7563	0.042756	0.0602606	72.0311	0.072031
0.0851666	56.8419	0.056842	0.0855291	92.1174	0.092117
0.116233	77.2273	0.077227	0.116718	125.153	0.125153
0.153892	92.6795	0.09268	0.153095	156.063	0.156063
0.198509	119.245	0.119245	0.198208	207.503	0.207503
0.250328	168.469	0.168469	0.250332	277.107	0.277107
0.308517	211.683	0.211683	0.308925	341.898	0.341898
0.3759	254.946	0.254946	0.377407	471.711	0.471711
0.453781	289.174	0.289174	0.452846	578.518	0.578518
0.538681	361.243	0.361243	0.540493	715.818	0.715818
0.634201	427.305	0.427305	0.637356	866.34	0.86634
0.743026	489.044	0.489044	0.741115	979.216	0.979216
0.859665	569.629	0.569629	0.858852	1149.86	1.14986
0.985275	676.145	0.676145	0.9855	1346.4	1.3464
1.12407	734.416	0.734416	1.12499	1571.27	1.57127
1.27159	907.75	0.90775	1.27227	1818.89	1.81889

APPENDIX C.7 Effect of moisture on SCT FEM predicted parameters

Table C.7-1 Effect of moisture on predicted parameters

	Tangent modulus (MPa)				Friction angle for both lower and upper bounds (^{0})		Cohesion (kPa)		Dilation angle (^{0})		Hardening modulus (kPa)	
	Lower bound		Upper bound				Lower bound	Upper bound	Lower bound	Upper bound	Lower bound	Upper bound
Moisture content (%)	E_0	E_{max}	E_0	E_{max}	ϕ_{min}	ϕ_{max}	c		ψ		H_p	
0.98	80	100	345	350	40	43	500	500	2	2	200	200
5.7	30	80	80	140	35	38	300	350	4	7	300	350
6.85	20	45	55	80	33	35	300	300	7.5	6.7	300	300

APPENDIX C.8 Sensitivity of elastic material parameters in SCT FEM

Table C.8-1 Effect of modulus

$E_0 = E_{max}$=30MPa			E_0 =30MPa, E_{max}=80MPa		
*User Material, constants=12			*User Material, constants=12		
30., 0.35, 0.325, 35., 5.5, 0.325, 970., 0.8 0.1, 0.65, 30., 38.			30., 0.35, 0.325, 35., 5.5, 0.325, 970., 0.8 0.1, 0.65, 80., 38		
*Dynamic, Explicit , 0.05057			*Dynamic, Explicit , 0.04077		
Penetration (mm)	Load (N)	Load (kN)	Penetration (mm)	Load (N)	Load (kN)
0.00E+00	0	0	0.00E+00	0	0
0.00104557	2.12049	0.00212	0.00104535	2.28986	0.00229
0.00342928	5.7301	0.00573	0.00342757	9.22035	0.00922
0.00800691	12.2104	0.01221	0.00794417	13.2709	0.013271
0.0153922	21.8709	0.021871	0.0150853	28.4791	0.028479
0.0261344	35.2338	0.035234	0.0263158	40.4397	0.04044
0.0409049	53.0857	0.053086	0.0408421	55.335	0.055335
0.0611075	78.8185	0.078819	0.0602513	80.7795	0.08078
0.0855826	107.134	0.107134	0.0861302	108.872	0.108872
0.117077	139.786	0.139786	0.117136	147.147	0.147147
0.153576	180.24	0.18024	0.154673	191.207	0.191207
0.198376	232.257	0.232257	0.197764	241.129	0.241129
0.250637	292.119	0.292119	0.250315	309.463	0.309463
0.308315	375.857	0.375857	0.309214	392.062	0.392062
0.376858	453.377	0.453377	0.376703	474.383	0.474383
0.454311	550.449	0.550449	0.455378	583.894	0.583894
0.540981	664.683	0.664683	0.539606	698.198	0.698198
0.637356	778.186	0.778186	0.637079	803.686	0.803686
0.743618	911.367	0.911367	0.74029	939.184	0.939184
0.860317	1046.34	1.04634	0.857904	1113.12	1.11312
0.987758	1196.35	1.19635	0.987299	1298.44	1.29844
1.12619	1344.71	1.34471	1.12615	1568.82	1.56882
1.27609	1555.61	1.55561	1.27184	1848.69	1.84869
1.43777	1795.56	1.79556	1.43572	2270.08	2.27008
1.61155	2032.55	2.03255	1.60992	2705.2	2.7052
1.79765	2291.13	2.29113	1.7963	3143.13	3.14313
1.99577	2564.11	2.56411	1.99442	3593.94	3.59394
2.20121	2843.7	2.8437	2.202	4083.87	4.08387
2.42649	3113.84	3.11384	2.42642	4577.78	4.57778
2.66313	3421.71	3.42171	2.66202	5143.17	5.14317
2.91209	3837.96	3.83796	2.9144	5770.67	5.77067
3.18467	4240.76	4.24076	3.17905	6369.73	6.36973
3.46226	4618.1	4.6181	3.46024	7126.18	7.12618
3.75138	5041.86	5.04186	3.75054	7793.99	7.79399

APPENDIX C.9 Sensitivity of plastic material parameters in SCT FEM

Table C.9-1 Effect of dilation angle, ψ

$\psi = 0^0$			$\psi = 15^0$			$\psi = 30^0$		
*User Material, constants=12			*User Material, constants=12			*User Material, constants=12		
50., 0.35, 0.5, 30., 0., 0.5, 970., 0.8 0.1, 0.65, 150., 40.			50., 0.35, 0.5, 30., 15., 0.5, 970., 0.8 0.1, 0.65, 150., 40.			50., 0.35, 0.5, 30., 30., 0.5, 970., 0.8 0.1, 0.65, 150., 40.		
*Dynamic, Explicit , 0.031			*Dynamic, Explicit , 0.031			*Dynamic, Explicit , 0.031		
Penetartion (mm)	Load (N)	Load (kN)	Penetartion (mm)	Load (N)	Load (kN)	Penetartion (mm)	Load (N)	Load (kN)
0.00E+00	0	0	0.00E+00	0	0	0.00E+00	0	0
0.0001433	1.25175	0.001252	0.0001433	1.25175	0.001252	0.0001433	1.25175	0.001252
0.0010597	0.29718	0.000297	0.0010597	0.29718	0.000297	0.0010597	0.29718	0.000297
0.0034993	11.2942	0.011294	0.0034993	11.2942	0.011294	0.0034993	11.2942	0.011294
0.008077	22.4905	0.022491	0.008077	22.4905	0.022491	0.008077	22.4905	0.022491
0.015096	40.874	0.040874	0.015096	40.874	0.040874	0.015096	40.874	0.040874
0.0263875	54.6259	0.054626	0.0263875	54.6259	0.054626	0.0263875	54.6259	0.054626
0.0413411	87.3583	0.087358	0.0413411	87.3583	0.087358	0.0413411	87.3583	0.087358
0.0612996	138.645	0.138645	0.0612996	138.645	0.138645	0.0612996	138.645	0.138645
0.0851644	183	0.183	0.0851644	183	0.183	0.0851644	183	0.183
0.116292	253.386	0.253386	0.116292	253.386	0.253386	0.116292	253.386	0.253386
0.154073	310.967	0.310967	0.154073	310.967	0.310967	0.154073	310.967	0.310967
0.198507	398.782	0.398782	0.198507	398.782	0.398782	0.198507	398.782	0.398782
0.249593	520.488	0.520488	0.249593	520.488	0.520488	0.249593	520.488	0.520488
0.310537	676.777	0.676777	0.310537	676.777	0.676777	0.310537	676.777	0.676777
0.376638	810.017	0.810017	0.376638	810.017	0.810017	0.376638	810.017	0.810017
0.454702	972.656	0.972656	0.454702	972.656	0.972656	0.454702	972.656	0.972656
0.540273	1127.68	1.12768	0.540273	1127.68	1.12768	0.540273	1127.68	1.12768
0.634206	1369.49	1.36949	0.634206	1369.49	1.36949	0.634206	1369.49	1.36949
0.740102	1573.53	1.57353	0.740102	1573.53	1.57353	0.740102	1573.53	1.57353

APPENDIX C.10 Stresses induced in SCT FEM

Table C.10-1 Normal stresses induced in SCT FEM

*User Material, constants=12 50., 0.35, 0.5, 30., 10., 0.5, 970., 0.9 0.1, 0.65, 150., 40.							
*Dynamic, Explicit , 0.031							
Penetrated level of loading cylinder (mm)							
≈ 10.0mm		≈ 24.0mm		≈ 50.0mm		≈ 76.0mm	
Distance along the radius (mm)	Normal stress S_{33}(MPa)	Distance along the radius (mm)	Normal stress S_{33}(MPa)	Distance along the radius (mm)	Normal stress S_{33}(MPa)	Distance along the radius (mm)	Normal stress S_{33}(MPa)
0	-19.3747	0	-47.9946	0	-115.835	0	-131.3
3.125	-20.3383	3.125	-50.2292	3.125	-115.732	3.125	-133.544
6.25	-21.7008	6.25	-53.4365	6.25	-111.073	6.25	-138.723
9.375	-18.3078	9.375	-45.2575	9.375	-104.91	9.375	-149.607
12.5	-18.1367	12.5	-44.419	12.5	-110.615	12.5	-166.999
15.625	-23.1437	15.625	-57.0096	15.625	-126.506	15.625	-171.359
18.75	-25.0675	18.75	-62.1646	18.75	-139.044	18.75	-154.492
21.875	-26.7471	21.875	-62.6842	21.875	-137.267	21.875	-134.032
25	-30.8716	25	-63.6555	25	-123.742	25	-120.482
26.5625	-33.3138	26.5625	-60.365	26.5625	-107.856	26.5625	-113.801
28.125	-26.4702	28.125	-48.2407	28.125	-91.0247	28.125	-106.483
29.6875	-18.379	29.6875	-31.6995	29.6875	-72.9297	29.6875	-91.6703
31.25	-10.0899	31.25	-20.5882	31.25	-58.9371	31.25	-62.1515
32.8125	-2.25445	32.8125	-18.7382	32.8125	-46.1759	32.8125	-40.7629
34.375	-0.74159	34.375	-16.3966	34.375	-28.7525	34.375	-36.7814
35.9375	-0.27185	35.9375	-10.9462	35.9375	-17.1082	35.9375	-23.2075
37.5	0.061516	37.5	-5.27917	37.5	-13.3757	37.5	-14.6448
39.0625	0.028847	39.0625	-1.90121	39.0625	-9.59581	39.0625	-14.5196
40.625	-0.04114	40.625	-1.3164	40.625	-6.60076	40.625	-9.81014
42.1875	-0.04236	42.1875	-1.13933	42.1875	-4.5388	42.1875	-7.21023
43.75	-0.03762	43.75	-0.48015	43.75	-3.44118	43.75	-6.29041
45.3125	-0.03762	45.3125	-0.04223	45.3125	-4.44545	45.3125	-6.52643
46.875	-0.04523	46.875	-0.05934	46.875	-5.18669	46.875	-6.78853
48.4375	-0.01688	48.4375	-0.01553	48.4375	-4.37189	48.4375	-4.76618
50	0.001312	50	0.033366	50	-2.40059	50	-2.18176
52.6	-0.00069	52.6	0.033984	52.6	-1.09719	52.6	-0.65839
55.2	0.007603	55.2	-0.00288	55.2	-0.25842	55.2	-0.29422
57.8	-0.01351	57.8	-0.01148	57.8	0.195684	57.8	0.391292
60.4	-0.02964	60.4	0.009158	60.4	0.012369	60.4	0.405139
63	-0.02099	63	0.02374	63	0.086146	63	-0.16506
65.6	-0.00821	65.6	0.010096	65.6	0.184545	65.6	0.033532
68.2	-0.00673	68.2	-0.01873	68.2	0.04125	68.2	0.160968
70.8	-0.01975	70.8	-0.0175	70.8	-0.03415	70.8	-0.00958
73.4	-0.01346	73.4	0.04327	73.4	0.074129	73.4	-0.13761
76	-0.00523	76	0.08887	76	0.138026	76	-0.1445

Table C.10-2 Confining stresses induced in SCT FEM

*User Material, constants=12
50., 0.35, 0.5, 30., 10., 0.5, 970., 0.9
0.1, 0.65, 150., 40.

*Dynamic, Explicit
, 0.031

Penetrated level of loading cylinder (mm)							
≈ 10.0mm		≈ 24.0mm		≈ 50.0mm		≈ 76.0mm	
Distance along the radius (mm)	Confining stress S_{11}(MPa)	Distance along the radius (mm)	Confining stress S_{11}(MPa)	Distance along the radius (mm)	Confining stress S_{11}(MPa)	Distance along the radius (mm)	Confining stress S_{11}(MPa)
0	-7.21601	0	-16.4541	0	-56.5604	0	-105.003
3.125	-7.25338	3.125	-16.5332	3.125	-57.2622	3.125	-106.902
6.25	-7.28185	6.25	-16.5078	6.25	-57.075	6.25	-109.407
9.375	-7.12926	9.375	-15.9369	9.375	-56.438	9.375	-110.146
12.5	-6.98018	12.5	-15.4351	12.5	-58.1375	12.5	-109.508
15.625	-7.1312	15.625	-15.6971	15.625	-59.9316	15.625	-110.577
18.75	-7.39268	18.75	-15.9806	18.75	-60.1803	18.75	-108.994
21.875	-7.42018	21.875	-15.6406	21.875	-58.4723	21.875	-97.3633
25	-7.62462	25	-14.6782	25	-53.5247	25	-79.5188
26.5625	-9.34102	26.5625	-13.9681	26.5625	-47.0333	26.5625	-61.8529
28.125	-12.2451	28.125	-14.3152	28.125	-41.6188	28.125	-46.8538
29.6875	-15.5807	29.6875	-15.1343	29.6875	-36.5614	29.6875	-37.5485
31.25	-15.289	31.25	-15.1886	31.25	-34.1809	31.25	-37.5492
32.8125	-8.97981	32.8125	-21.3631	32.8125	-30.4984	32.8125	-40.244
34.375	-3.62541	34.375	-36.0379	34.375	-26.9001	34.375	-53.2925
35.9375	-1.9221	35.9375	-46.0796	35.9375	-31.6675	35.9375	-69.4669
37.5	-1.23479	37.5	-38.6863	37.5	-40.7036	37.5	-70.1227
39.0625	-0.91583	39.0625	-19.4081	39.0625	-51.7435	39.0625	-54.6686
40.625	-0.6427	40.625	-6.75215	40.625	-47.6878	40.625	-32.9582
42.1875	-0.39403	42.1875	-3.54127	42.1875	-24.7067	42.1875	-20.9028
43.75	-0.21807	43.75	-3.11926	43.75	-12.5324	43.75	-18.7626
45.3125	-0.11798	45.3125	-3.24096	45.3125	-11.7414	45.3125	-18.365
46.875	-0.05303	46.875	-3.17771	46.875	-12.7517	46.875	-13.2767
48.4375	-0.00983	48.4375	-2.9811	48.4375	-12.2492	48.4375	-8.10057
50	-0.00149	50	-2.71537	50	-6.33381	50	-5.4325
52.6	0.004143	52.6	-2.57166	52.6	-1.80475	52.6	-4.22467
55.2	0.035552	55.2	-2.5631	55.2	-0.62013	55.2	-3.22493
57.8	0.086245	57.8	-2.52622	57.8	-1.56937	57.8	-1.28385
60.4	0.126706	60.4	-2.42026	60.4	-2.03971	60.4	-0.99335
63	0.150954	63	-2.33735	63	-1.87123	63	-1.5002
65.6	0.167378	65.6	-2.3188	65.6	-2.13147	65.6	-1.21336
68.2	0.184124	68.2	-2.31392	68.2	-2.4284	68.2	-0.63136
70.8	0.196538	70.8	-2.28612	70.8	-2.62951	70.8	-0.30063
73.4	0.202167	73.4	-2.2454	73.4	-2.69647	73.4	-0.11555
76	0.206009	76	-2.2192	76	-2.69617	76	0.035027

APPENDIX D.1 Convergence studies of the plane strain FE model

Table D.1-1 Mesh refinement 300mm thick sample

*Elastic 150,0.35			*Elastic 150,0.35			*Elastic 150,0.35		
*Dynamic, Explicit , 0.12332			*Dynamic, Explicit , 0.12325			*Dynamic, Explicit , 0.12326		
Coarse			Medium			Fine		
Displacement (mm)	1/2 Load (N)	Full Load(kN)	Displacement (mm)	1/2 Load (N)	Full Load(kN)	Displacement (mm)	1/2 Load (N)	Full Load(kN)
0	0	0	0	0	0	0	0	0
9.16E-05	5.93E-02	0.041477	1.68E-04	0	0	0.0004273	0	0
0.00051768	0.217115	0.151981	0.0005081	0.20133	0.140931	0.0009418	0	0
0.00173839	0.674749	0.472324	0.0016714	0.218695	0.153087	0.0017466	0	0
0.00390514	1.23555	0.864885	0.0039671	0.080628	0.05644	0.0038885	1.36155	0.953085
0.00781139	2.19214	1.534498	0.0075396	2.9311	2.05177	0.0075660	2.91108	2.037756
0.0129383	3.49066	2.443462	0.012937	3.9299	2.75093	0.0130121	1.08266	0.757862
0.0209034	5.32531	3.727717	0.0204138	7.33767	5.136369	0.020359	14.6074	10.22518
0.0302113	7.45741	5.220187	0.0303167	10.0895	7.06265	0.0301377	3.11802	2.182614
0.043517	10.4374	7.30618	0.0428595	11.9938	8.39566	0.0426812	15.3104	10.71728
0.0581044	13.7139	9.59973	0.0579657	17.3826	12.16782	0.058011	7.55931	5.291517
0.0779103	18.2412	12.76884	0.0767645	22.2917	15.60419	0.0767107	20.6835	14.47845
0.0987843	22.9707	16.07949	0.0991339	28.1488	19.70416	0.0986223	32.6094	22.82658
0.126281	29.1059	20.37413	0.124677	33.6533	23.55731	0.124593	33.3811	23.36677
0.154448	35.439	24.8073	0.154096	41.4918	29.04426	0.154195	47.6404	33.34828
0.190612	43.5917	30.51419	0.188581	49.4223	34.59561	0.187932	50.0152	35.01064
0.226928	51.6946	36.18622	0.226514	60.5847	42.40929	0.226567	54.1341	37.89387
0.272673	62.0096	43.40672	0.270185	73.3798	51.36586	0.269322	71.5533	50.08731
0.317962	72.0461	50.43227	0.317518	84.5628	59.19396	0.317479	84.5086	59.15602
0.374236	84.5832	59.20824	0.371259	98.8294	69.18058	0.370061	98.1434	68.70038
0.429198	96.6986	67.68902	0.428724	113.745	79.6215	0.428533	113.568	79.4976
0.496734	111.775	78.2425	0.491498	130.213	91.1491	0.491673	136.316	95.4212
0.56198	126.392	88.4744	0.561628	148.542	103.9794	0.561223	148.5	103.95
0.641539	144.009	100.8063	0.635572	168.008	117.6056	0.635594	168.109	117.6763

APPENDIX D.2 Application of SCT predicted properties to the plane strain FEM

Table D.2-1 Application of SCT predicted parameters 300mm thick sample

*User Material, constants=12 30., 0.35, 0.3, 35., 4., 0.3, 970., 0.8 0.1, 0.65, 80., 38.			*User Material, constants=12 80., 0.35, 0.35, 35., 7.0, 0.35, 970., 0.8 0.1, 0.65, 140., 38.		
*Dynamic, Explicit , 0.22219			*Dynamic, Explicit , 0.14817		
Lower boundary			Upper boundary		
Displacement (mm)	1/2 Load (N)	Full Load(kN)	Displacement (mm)	1/2 Load (N)	Full Load(kN)
0	0	0	0	0	0
5.96E-05	0.00E+00	0	1.70E-04	0	0
0.000525139	0.055866	0.039106	0.000535141	0	0
0.00170199	0.215247	0.150673	0.00166311	0.09472	0.066304
0.00386838	0.42282	0.295974	0.0039113	1.07032	0.749224
0.0075732	0.809048	0.566334	0.00756139	1.13769	0.796383
0.0130886	0.760769	0.532538	0.0130076	2.18118	1.526826
0.0206569	1.83938	1.287566	0.0204825	3.36278	2.353946
0.0301784	2.11588	1.481116	0.0303092	4.75547	3.328829
0.0426601	2.58736	1.811152	0.0428061	6.55636	4.589452
0.0586818	3.79171	2.654197	0.0582786	8.77303	6.141121
0.0766872	5.37244	3.760708	0.0769858	11.4438	8.01066
0.0986599	6.13503	4.294521	0.0985618	14.8538	10.39766
0.124813	7.44864	5.214048	0.12441	18.1498	12.70486
0.15469	8.96039	6.272273	0.15447	22.4001	15.68007
0.188137	10.7684	7.53788	0.188894	27.2295	19.06065
0.227597	13.0934	9.16538	0.226858	33.3668	23.35676
0.270413	15.7967	11.05769	0.270406	38.7878	27.15146
0.318722	17.4809	12.23663	0.318151	46.4421	32.50947
0.371029	19.8711	13.90977	0.370397	52.9347	37.05429
0.429287	25.014	17.5098	0.429143	61.7675	43.23725
0.491604	28.081	19.6567	0.493078	70.5737	49.40159
0.560879	31.5061	22.05427	0.560705	80.6181	56.43267
0.636868	36.5979	25.61853	0.635442	93.1562	65.20934
0.718441	41.0786	28.75502	0.716497	104.726	73.3082

APPENDIX D.3 Large-scale experiments data sheets

Table D.3 Experimental data large-scale test - 300mm thick sample

	Displacement transducers on the loading plate					Displacement transducers on side walls			
Load (kN)	D1 (mm)	D2 (mm)	D3 (mm)	D4 (mm)	Average D (mm)	D5 (mm)	D6 (mm)	D7 (mm)	D8 (mm)
0.000	0	0	0	0	0	0	0	0	0
0.353	0.012	0.024	0.037	0	0.01825	0	0	0	0.024
0.707	0.012	0.048	0.025	0.037	0.0305	0	0	0	0.024
1.414	0.012	0.048	0.037	0.049	0.0365	0	0	0	0
1.767	0.061	0.073	0.074	0.074	0.0705	0	0	0	0
2.121	0.048	0.097	0.086	0.098	0.08225	0	-0.012	0	0
2.828	0.073	0.097	0.11	0.098	0.0945	0	-0.012	0	0
3.181	0.097	0.134	0.122	0.135	0.122	0	-0.012	0	0
3.181	0.109	0.146	0.135	0.135	0.13125	0	-0.012	-0.025	0
4.242	0.122	0.146	0.171	0.184	0.15575	0	-0.025	-0.025	-0.025
4.949	0.146	0.195	0.183	0.184	0.177	0	-0.025	0	0
6.009	0.146	0.183	0.183	0.184	0.174	0	-0.025	0	0
6.363	0.195	0.17	0.22	0.22	0.20125	0	-0.025	0	0
7.069	0.195	0.232	0.22	0.232	0.21975	0	-0.025	0	-0.025
7.777	0.195	0.232	0.232	0.232	0.22275	-0.012	-0.025	0	0
8.130	0.244	0.232	0.269	0.269	0.2535	-0.012	-0.025	0	0
8.837	0.232	0.28	0.269	0.281	0.2655	-0.012	-0.025	0	0
9.544	0.28	0.28	0.318	0.318	0.299	-0.024	-0.025	0	0
9.897	0.28	0.329	0.318	0.318	0.31125	-0.024	-0.025	0	0
10.605	0.293	0.329	0.354	0.342	0.3295	-0.024	-0.012	0	-0.025
11.311	0.329	0.329	0.366	0.354	0.3445	-0.024	-0.025	0	-0.025
11.665	0.329	0.341	0.366	0.367	0.35075	-0.036	-0.025	0.024	-0.025
12.372	0.378	0.366	0.415	0.403	0.3905	-0.036	-0.025	0	-0.025